Modelling feedback processes, star formation and outflows in high-redshift galaxies

Orianne Roos

To cite this version:

Orianne Roos. Modelling feedback processes, star formation and outflows in high-redshift galaxies . Cosmology and Extra-Galactic Astrophysics [astro-ph.CO]. Université Paris 7 - Denis Diderot, 2016. English. NNT : . tel-01389843

HAL Id: tel-01389843
https://theses.hal.science/tel-01389843

Submitted on 30 Oct 2016

UNIVERSITÉ SORBONNE PARIS CITÉ

Thèse préparée
à l'UNIVERSITÉ PARIS DIDEROT
École doctorale STEP'UP – ED N°560
CEA-Saclay, Service d'Astrophysique
(Laboratoire de Cosmologie et Évolution des Galaxies)

Modelling feedback processes, star formation and outflows in high-redshift galaxies

par
Orianne ROOS

présentée et soutenue publiquement le
8 septembre 2016

Thèse de doctorat de Physique de l'Univers dirigée par
Frédéric BOURNAUD

devant un jury composé de :

Isabelle GRENIER Présidente
Professeure (Université Paris Diderot – France)
Romain TEYSSIER Rapporteur
Professeur (Université de Zurich – Suisse)
Françoise COMBES Rapporteuse
Professeure (Collège de France – France)
Jérémy BLAIZOT Examinateur
Astronome-adjoint (Université Claude Bernard, Lyon 1 – France)
Marta VOLONTERI Examinatrice
Directrice de recherche (Institut d'Astrophysique de Paris – France)
Frédéric BOURNAUD Directeur de thèse
Chercheur (CEA Saclay – France)
Stéphanie JUNEAU Co-encadrante de thèse
Chercheure (CEA Saclay – France)

Remerciements *Acknowledgements*

Je voudrais tout d'abord remercier mon directeur, *Frédéric*. Tu m'as dit un jour que le meilleur directeur de thèse qu'on pouvait avoir, c'était celui dont on ne savait jamais quand il serait là, car cela nous apprend à chercher par nous-même. C'est vrai, et tu m'as laissé toute l'autonomie que je voulais, tout en étant présent aux moments où j'en avais vraiment besoin. Merci pour cette expérience de vie qu'est la thèse, merci pour les longues discussions scientifiques où j'ai appris tant de choses, merci aussi pour le Teide et la Californie. Je sais que ces trois années n'ont pas toujours été faciles pour certaines raisons extérieures, que ce soit pour toi ou pour moi… mais je suis contente d'avoir fait cette thèse avec toi, et quand j'y repenserai dans quelques années, les bons moments auront éclipsé les moins bons.

Jérémy, tu sais déjà tout ce que tu vas lire ensuite, mais pour guérir un peu ton manque patent de confiance en toi, je vais enfoncer le clou. Merci de m'avoir soutenue pendant ces années, de m'avoir remonté le moral, de m'avoir raconté des anecdotes jusqu'à trop tard dans la nuit. Merci pour tes blagues pas drôles, pour tous les bouquins que tu m'as prêtés, pour toutes les conversations philosophiques, littéraires, métaphysiques, pour toutes les fois où on a refait le monde.

Olivier, tout aurait pu mal commencer quand tu m'as pris le stage que je voulais… mais finalement ce stage n'était que le premier sur la longue liste de nos points communs. Nous avons partagé bien plus qu'un bureau et un Bureau (et même un appartement, pour deux petits jours particulièrement pluvieux, merci !). Je te remercie pour ton soutien, pour nos coups de gueules, pour nos discussions (typographiques, philosophiques et autres), pour ton AUDDAS en dernière année (même si en tant que Trésorière, c'était aussi un peu la mienne). Merci pour ton délicieux hummus, dont je rêve encore, et merci aussi pour les blagues sur les murs de mon bureau, qui, rappelons-le, ont commencé suite à une des tiennes. En neuf mots plutôt qu'en un : merci pour la vie, l'Univers et le reste.

Rémi, merci pour ton enthousiasme et pour ta joie de vivre. Merci de m'avoir remonté le moral pendant la rédaction, et d'être passé prendre de mes nouvelles presque chaque jour. Merci aussi d'avoir osé chanter à ma soirée karaoké d'après soutenance. Le meilleur duo jamais entendu de *Casser la voix*, c'est définitivement le nôtre. Je te souhaite de bien t'amuser à Munich. Bonne continuation dans la vie et dans la recherche !

Dear *Kyle*, I wish I knew you before. Thank you for everything and thank you for being you. I will miss you a lot. *Francesco e Anita*, grazie a voi… pour les repas au restaurant et surtout chez vous, pour les films et pour le Cinéma Bonaparte, pour les échanges culturels et les longues conversations. *Tao*, 谢谢 for your kindness, for our conversations on anything from religion to Angela Baby, for the nice evenings we spent laughing. *Emin*, thanks for the Polidor ! Thank you also for the movies and for your happy and relaxed mood.

Merci à tous ceux qui ont un jour partagé mon bureau de m'avoir supportée (dans tous les sens du terme), d'avoir partagé avec moi vos passions, votre philosophie, merci pour les discussions parfois sans queue ni tête mais souvent très profondes. Dans l'ordre chronologique : merci aux occupants de l'Aquarium : *Olivier* (encore toi !) et *Yueh-Ning*, puis aux occupants successifs du bureau 225 : *Marc* et *Héloïse*, *Valeska*, *Aloÿs*, *Romaric*, et (last but not least) *Antoine*... *Marc*, merci de m'avoir donné le virus AUDDAS, de m'avoir éclairée sur tant de sujets, et de m'avoir soutenue dans les moments difficiles. *Valeska*, merci pour tes bons conseils, pour ta bonne humeur, pour les moments de détente au milieu de nos longues journées de travail, et surtout pour ce savoureux Pisco Sour à mon pot de soutenance ! *Aloÿs* et *Romaric*, vous êtes des OVNIS, ne changez rien. Et *Aloÿs*, merci évidemment pour le trou noir en crochet ! *Antoine*, tu as emménagé dans le bureau 225 à la fin de ma troisième année (la période la moins supportable pour des co-bureau !), et tu as contribué pour beaucoup à l'élaboration de ce manuscrit, en me soutenant au jour le jour, et en m'offrant des interludes bienvenus. Merci pour ton compte-à-rebours qui restera dans les annales, merci pour les chansons, les vidéos, les blagues, les discussions. J'espère que tu te souviendras longtemps de l'histoire de la souris et du Kit-Kat, même quand tu seras retourné pour de bon sur ton île loin là-bas. Moi, je m'en souviendrai.

La liste est encore longue... *Florent*, mine de rien, on partage pas mal de choses. Alors merci pour tout ce que tu sais, et je te souhaite tout le meilleur. *David*, merci pour tes mots. Il est vrai qu'on ne s'est pas côtoyés très longtemps, mais je suis ravie d'avoir fait ta connaissance et d'avoir pu partager un peu de tes expériences. *Bilal*, tu es le meilleur remonteur de moral de tout le labo ! Merci pour ça. Je voudrais aussi remercier *David* et *Jérôme* pour leur soutien dans les moments compliqués, et pour avoir su préserver la science avant tout le reste.

Je remercie également tous les autres thésards de la promotion 2013-2016 : *Sarah*, *Fred*, *Alan*, *Mélanie*, *Linc*, *Mathieu*, *Victor*, *Quentin*, *Pierre*, avec qui j'ai partagé à un moment ou à un autre des rires ou des coups de gueule. *Sarah*, si j'avais un exact opposé, ce serait toi. Merci de m'avoir appris tant de choses. Bonne continuation à tous.

Merci à tous ceux qui étaient là pendant mon stage ou à un moment de ma thèse et que je n'ai pas oubliés : *Benoît*, évidemment, *Manu*, aussi, *Raphaël*, bien sûr, et *Jared*, *Corentin*, *Laure*, *Matthieu*, *Ana*, *Maurilio*, *Véronica*, *Xin-Wen*, *Mark*, *Katarina*, *Amandine*, *Remco*, *Maëlle*, *Bruno*, *Thomas*, *Dai-Zhong*, *Yu-Yen*, *Shuo-Wen*, *Fiorella*, *Sam*, *Mathilde*, *Patrick*, *Pierre-Alain*, *Émeric*, *Emmanuele*, *Koryo*, *Alizée*, *Cédric*. *Corentin*, merci pour ton soutien, tes relectures et tes commentaires avisés, pour ton écoute, et pour les soirées inoubliables tous ensemble.

Merci à *Thibaud*, *Florie*, *Carole* et *Sarah* (encore une fois), parce que le Master, c'était le bon temps.

Pour finir, je remercie *mes parents et ma sœur*, qui m'ont toujours soutenue et ont toujours cru en moi. Je suis fière de vous avoir rendus fiers de moi toutes ces années, et si j'en suis là aujourd'hui, c'est grâce à vous. Je vous aime.

Modelling feedback processes, star formation and outflows in high-redshift galaxies

Abstract:

The purpose of this thesis is to give clues to answer two key questions that still remain today in the field of galaxy evolution: why do some galaxies suddenly stop forming stars? Why do models predict galaxies too massive compared to observations? Powerful outflows could be responsible, since they seem to be a promising mechanism to remove gas from galaxies, and suppress their star formation.

Even though the mass budget of baryons in today's Universe is well-known, models accounting for it create galaxies which are too massive and produce too many stars, compared to observations (see e.g. Croton et al., 2006). Some of these "missing" baryons, which account in total for about 80 % of the total mass budget, are located *around* the most massive galaxies, rather than *inside* them (e.g. Sommer-Larsen, 2006). In this thesis, we consider efficient expelling mechanisms such as galactic outflows, in the models, and study the amount of baryons they can remove from their hosts.

From observations, we know that such outflows are ubiquitous in star-forming galaxies up to high redshift (Steidel et al., 2010). They are generated by (1) young stars and supernovæ (high mass outflow rate, but limited velocity of 100 – 500 km.s^{-1}, e.g. Bournaud et al., 2014), and (2) active galactic nuclei (AGNs, with velocities up to 3,000 – 30,000 km.s^{-1} but small gas densities and outflow rates, e.g. Chartas et al., 2014; Gabor & Bournaud, 2014). Nonetheless, while the mass outflow rate of stellar outflows may be consistent with the huge fraction of baryons located around galaxies, their velocities are often too small to escape the dark matter halo, and vice-versa for AGN outflows. The coupling of AGN and stellar winds could however create powerful winds with velocities above the escape velocity of the dark matter halo, together with mass outflow rates of a few times the star formation rate of the galaxy, in potential agreement with the amount of baryons around galaxies.

This thesis focuses on the evolution of typical galaxies of the Main Sequence of star formation at redshift ~ 2, i.e.: the apogee of cosmic star formation (e.g. Madau et al., 1998; Madau & Dickinson, 2014) and quasar activity (e.g. Richards et al., 2006; Madau & Dickinson, 2014). During three years, I used simulations of such galaxies to study how they form stars and produce outflows, in relation to their small-scale (sub-pc) internal processes: stellar and AGN feedback, black hole accretion, etc.

The first chapter of this thesis explains the key notions to understand the problematic of the research I have been doing: the local and distant Universe, typical galaxies at low and high redshift, supermassive black holes and active galactic nuclei, stars and star formation, and the way both AGNs and stars *feed back* on their host galaxy, as well as how they drive galactic outflows.

In a second chapter, I describe the numerical techniques used during this thesis. First, I explain

the basic principles of numerical simulations: the grid, the initial conditions, and the equations and models used to study the time evolution of galaxies. I particularly focus on the code RAMSES (Teyssier, 2002) and describe some aspects of it, in comparison to other codes used in astrophysics. The second section of this chapter presents the radiative transfer code I used to compute the large-scale photo-ionization due to the AGN in a typical galaxy of the Main Sequence of star formation at redshift 2 (Cloudy, see Ferland et al., 1998, 2013).

Chapter 3 presents the study of the coupling between AGN winds and AGN photo-ionization in high-resolution (6 pc) galaxy simulations. As AGN photo-ionization is too costly in computation time to be computed on-the-fly, I developed a method to derive the ionization state of an entire galaxy a posteriori (published as Roos et al., 2015): lines are traced in the simulation box, radiative transfer is computed along them with Cloudy, and the ionization state of the whole galaxy is reconstructed by assembling the lines. Together with Gabor & Bournaud (2013, 2014), we showed thanks to high resolution (6 pc) and accurate radiation modelling that neither AGN outflows nor AGN photo-ionization are able to quench star formation in typical Main Sequence galaxies on a time scale of a few hundreds of million years, and that they expel hot and diffuse gas with a moderate outflow rate.

Following this work, I was granted 11 million hours of computation time as the PI of the POGO Project, with which I study the Physical Origins of Galactic Outflows at high resolution (down to 1.5 pc). With this project (described in Chapter 4, and made possible thanks to a Tier-0 PRACE allocation on the Curie super-computer), I studied the coupling between the outflows generated by the AGN and the stars (including young stars and supernovæ), and their impact at large scale in terms of outflow rate and star formation activity of the host. I showed that, even though the AGN is the main driver of the outflows at all masses studied, it is important to accurately account for stellar feedback processes. Indeed, AGN and stellar feedback couple non-linearly and can either enhance the strength of the global outflow (in the low-mass galaxy studied) or reduce it (in the intermediate-mass galaxy studied). Powerful winds generated by the AGN and the stars in the low-mass galaxy we studied may thus explain a fraction of the 80 % of baryons located around galaxies, even though it remains to quantify how much.

The last chapter of this thesis gives a state-of-the-art about AGN feedback before and during my thesis, gathers the conclusions of my work (briefly described above) and gives some future perspectives to enlarge the scope of the research I have been conducting. Finally, I include two appendices at the end of the manuscript (see Appendix A and Appendix B), in which I present the codes I used and/or developed for my research, and a beginners' guide to simulating star-forming galaxies including AGNs, using RAMSES.

Keywords:
Numerical simulations, galaxy evolution, supermassive black hole, active galactic nucleus, star formation, feedback, galactic outflows.

Modélisation des processus de rétro-action, de la formation stellaire et des vents dans les galaxies à haut redshift

Résumé étendu en français :

L'Univers observable contient plusieurs centaines de milliards de galaxies, dont la nôtre : la Voie Lactée. Comme celle-ci, les galaxies sont de gigantesques structures faites de gaz, d'étoiles, de poussières et de matière noire, des composants liés entre eux par la gravitation. Au cours de leur vie, elles transforment le gaz qu'elles contiennent en étoiles, et, par analogie, la fin des processus de formation stellaire s'apparente à leur "mort".

Depuis la découverte par l'astronome Américain Edwin Hubble que la Voie Lactée n'était pas la seule galaxie dans l'Univers (Hubble, 1925), l'astrophysique a connu de grands progrès scientifiques : nous savons maintenant que l'Univers n'est pas immobile, mais qu'il est au contraire en expansion accélérée, et que les galaxies qu'il contient s'éloignent les unes des autres d'autant plus vite qu'elles sont distantes. Pour étudier les galaxies, les astrophysiciens les observent principalement en collectant la lumière émise par les étoiles, et celle diffusée par le milieu interstellaire, mais l'évolution des galaxies est un domaine de recherche complexe et il y reste encore de nombreuses zones d'ombre. Cette thèse a pour but de donner des éléments de réponse à deux des grandes questions que les astrophysiciens se posent encore aujourd'hui : pourquoi certaines galaxies arrêtent-elles subitement de former des étoiles ? Pourquoi les modèles actuels prédisent-ils des galaxies trop massives par rapport aux galaxies observées dans l'Univers ?

La distribution en masse actuelle des baryons (la matière ordinaire, sous forme de gaz, d'étoiles, de poussière, etc.) dans l'Univers est bien connue, et est dérivée notamment de la nucléosynthèse primordiale (e.g. Olive et al., 2000) — selon laquelle la plupart des éléments légers (tels que l'hydrogène, le deutérium, l'hélium et le lithium) ont été produits entre quelques secondes et quelques minutes après le Big Bang. Toutefois, les modèles basés sur ce contenu en masse produisent des galaxies trop massives et contenant trop d'étoiles par rapport aux galaxies observées dans l'Univers (e.g. Croton et al., 2006). En effet, les lois de la gravitation prédisent que tous les baryons devraient maintenant se trouver à l'intérieur des galaxies. Au contraire, on observe que seulement 20 % des baryons se trouvent à l'intérieur des galaxies (Sommer-Larsen, 2006), une petite fraction des 80 % manquants se trouvant *autour* des galaxies les plus massives. Cette tension entre les modèles et les observations est connue sous le nom de "problème des baryons manquants". Comme aucun mécanisme physique connu à ce jour n'est capable d'empêcher efficacement les baryons de tomber dans les galaxies à long terme (presque l'âge de l'Univers), les astrophysiciens se tournent vers des processus physiques capables d'éjecter rapidement la plus grande partie du contenu des galaxies dans le milieu intergalactique afin d'améliorer leurs modèles. Les conséquences directes de cette éjection subite sont la fin de la formation d'étoiles faute de gaz, et la diminution lente de luminosité des galaxies, du fait du vieillissement des étoiles déjà formées.

Plus le processus d'éjection du gaz est subit, plus l'arrêt des processus de formation stellaire est rapide. C'est cet arrêt rapide de la formation stellaire que l'on appelle, faute d'un mot adapté en français, le "quenching". Ce mot, qui signifie à la fois étanchement (de la soif) et trempe (du métal), décrit un processus qui fait passer instantanément (relativement aux échelles de temps caractéristiques) un système d'un état à un autre, comme un métal en fusion qui se refroidit instantanément quand on le trempe dans de l'eau froide. Comme l'activité de formation stellaire est associée à la vie des galaxies, le "quenching" peut être compris comme leur étouffement, ou leur étranglement.

Toutefois, d'autres scénarios que le quenching sont envisagés par les théoriciens pour expliquer la mort des galaxies, notamment l'arrêt de leur alimentation en gaz, menant à leur mort lente par inanition. Les astrophysiciens n'ont donc pas encore identifié avec certitude le ou les phénomènes physiques qui sont à l'origine de l'existence des galaxies ne formant plus, ou presque plus, d'étoiles. Pour apporter des éléments de réponse à cette question, je me suis penchée durant mon doctorat sur l'étude de phénomènes qui pourraient jouer un rôle dans la mort subite des galaxies lointaines, à savoir les processus de rétro-action provenant des étoiles et des trous noirs supermassifs en phase active, la formation stellaire, et les vents galactiques.

Le premier chapitre présente toutes les notions astrophysiques nécessaires à la compréhension du problème : la notion d'Univers proche, d'Univers lointain et de décalage vers le rouge (ou redshift) cosmologique (utilisé pour mesurer le temps cosmologique depuis le temps présent, voir Section 1.1.1) ; les caractéristiques des galaxies typiques de l'Univers proche et lointain (voir Section 1.1.2) ; les vents galactiques (voir Section 1.1.3) ; la mort des galaxies (voir Section 1.1.4) ; les composants essentiels que sont les trous noirs supermassifs en phase active (aussi appelés noyaux actifs de galaxies ou AGN, voir Section 1.2) et les étoiles (voir Section 1.3) ; ainsi que les effets que ceux-ci ont en retour sur la galaxie qui les abrite (la rétro-action). De façon résumée, je m'intéresse aux galaxies de l'Univers lointain (ou galaxies à haut redshift), qui, comme leurs analogues plus proches, sont des galaxies en forme de disque produisant des étoiles à un taux élevé. La principale différence entre les galaxies de ces deux époques[1] est le rapport entre la masse de gaz et la masse d'étoiles. Les galaxies lointaines contiennent ainsi beaucoup moins d'étoiles par rapport à leur masse de gaz, simplement parce que la majorité d'entre elles n'ont pas encore eu le temps de naître. Les galaxies de l'Univers lointain ont donc une forte fraction de gaz, qui rend les disques plus instables et empêche la formation des bras spiraux caractéristiques des galaxies locales. Ainsi, je m'intéresse aux galaxies lointaines plutôt qu'aux galaxies locales car leur forte instabilité implique une plus forte activité de formation stellaire au niveau cosmologique (e.g. Madau et al., 1998; Madau & Dickinson, 2014) et des phases actives plus fréquentes pour les trous noirs supermassifs (e.g. Richards et al., 2006; Madau & Dickinson, 2014). De la même façon que la galaxie agit sur les étoiles et le trou noir supermassif en entretenant la formation des premières et l'activité du second avec le gaz qu'elle contient, les étoiles et le trou noir en phase active *rétro-agissent* sur la galaxie, notamment par l'intermédiaire des photons qu'ils émettent. La rétro-

---

[1] En astrophysique, plus un objet est lointain par rapport à la Terre, plus il est situé loin dans le passé. On le voit aujourd'hui comme il était quand les photons qui nous parviennent l'ont quitté, parfois il y a plusieurs milliards d'années.

action provenant des étoiles et du trou noir actif peut prendre différentes formes, parmi lesquelles l'ionisation du gaz et son éjection via de puissants vents à l'échelle galactique (pour plus de détails, voir les Sections 1.2.5, 1.2.6, 1.3.3 et 1.3.4). Cette rétro-action sous ses différentes formes est soupçonnée de jouer un rôle dans la mort des galaxies-hôtes.

Dans un deuxième chapitre, je présente les techniques numériques utilisées lors de ces trois années de thèse : tout d'abord, les simulations numériques astrophysiques en général (voir Section 2.1), le code de simulations astrophysiques Ramses en particulier (voir Section 2.1.1 et Teyssier, 2002) et d'autres codes utilisés par la communauté (voir Section 2.1.2) ; puis des éléments pour comprendre ce que sont les simulations numériques : les conditions initiales (voir Section 2.1.3) et les équations et modèles dont l'évolution temporelle est résolue pas à pas afin de calculer l'état d'une galaxie (voir Section 2.1.4). En second lieu, ce chapitre présente le code de transfert radiatif Cloudy (voir Section 2.2 et Ferland et al., 1998, 2013), que j'ai utilisé pour développer une méthode de post-traitement afin de calculer l'état d'ionisation d'une galaxie.

Le troisième chapitre détaille le travail qui a occupé la première partie de ma thèse et a mené à la publication de l'article Roos et al. (2015). Il s'agit de post-traiter une simulation de galaxie lointaine à haute résolution (6 pc), afin d'y étudier les effets de la rétro-action des trous noirs supermassifs en phase active sous deux forme : thermique, et radiative. Alors que la rétro-action thermique était déjà prise en compte de façon récurrente au début de ma thèse, les modèles étaient principalement arbitraires, car encore mal contraints. Afin de mieux les contraindre mais aussi d'étudier les effets à grande échelle de la photo-ionisation par le trou noir en phase active — qui était peu étudiée précisément car complexe et coûteuse en temps de calcul, j'ai développé une méthode pour traiter de façon précise le transfert radiatif dans une simulation de galaxie et ainsi calculer la distribution du gaz ionisé par le trou noir actif. Il en ressort qu'à haute résolution (i.e. avec un milieu interstellaire présentant de forts contrastes de densité), la radiation et la rétro-action thermique d'un trou noir supermassif typique en phase active — même couplées — sont incapables de stopper la formation stellaire de façon soudaine, et ne sont par conséquent pas responsables du “quenching” des galaxies.

Cependant, des galaxies ne formant plus, ou presque plus, d'étoiles sont observées dans l'Univers, et leur existence doit être expliquée. Une des pistes pour y arriver est de s'intéresser au couplage entre les différentes sources de rétro-action que sont les trous noirs actifs et les étoiles. Le quatrième chapitre présente les résultats du projet POGO (Physical Origins of Galactic Outflows — Origines Physiques des Vents Galactiques), avec lequel j'ai étudié l'interaction entre la rétro-action des étoiles et celle des trous noirs actifs. J'ai montré que même si les trous noirs actifs sont la source principale des vents galactiques, il est important de prendre en compte la rétro-action stellaire de façon précise. En effet, la présence de celle-ci change les caractéristiques des vents galactiques en fonction de la masse de l'hôte : à la masse la plus basse que nous avons étudiée, les rétro-actions des étoiles et du trou noir actif donnent lieu à des vents plus forts que ceux générés par la seule rétro-action des trous noirs actifs. À la masse intermédiaire, au contraire, la combinaison des deux rétro-actions génère des vents plus faibles qu'avec la seule rétro-action du trou noir actif. Toutefois, même pour la plus petite galaxie

étudiée, les vents ne sont pas assez forts pour tuer subitement la galaxie hôte. En conclusion, même si j'ai pu donner des éléments de réponse aux deux grandes questions qui ont motivé cette thèse, il y a encore beaucoup à faire dans le domaine pour trouver une réponse définitive.

Pour résumer, durant cette thèse, j'ai montré que les trous noirs actifs abrités par des galaxies lointaines typiques n'étaient pas en mesure de tuer subitement leur hôte, même en prenant en compte la rétro-action des étoiles. J'ai également montré que les vents provenant des étoiles et des trous noirs actifs dans les galaxies moyennement massives n'expliquent pas la présence de 80 % des baryons dans le milieu intergalactique, puisque leur couplage a au contraire tendance à réduire les vents. Toutefois, les vents générés par le couplage de la rétro-action des étoiles et de celle du trou noir actif dans les galaxies peu massives peuvent en expliquer une partie, même s'il reste à en déterminer quelle fraction. Le cinquième et dernier chapitre fait un état de l'art du domaine avant et pendant mon doctorat, reprend les conclusions de cette thèse et donne quelques perspectives à ce travail, notamment en ce qui concerne le rôle additionnel des rayons cosmiques dans la mort des galaxies, et la présence de tant de baryons autour d'elles.

Deux annexes s'ajoutent à ce manuscrit : la première (voir Annexe A) présente les différentes routines que j'ai développées et/ou utilisées au cours de cette thèse (en bash, Python, Fortran 90 et IDL), tant pour exploiter les résultats des simulations RAMSES que pour le post-traitement avec Cloudy. La deuxième annexe (voir Annexe B) est destinée aux personnes voulant débuter dans l'art de simuler des galaxies avec RAMSES (incluant un trou noir supermassif actif, des étoiles, de la formation stellaire, etc.). Cette section retrace les différentes étapes physiques et techniques à respecter pour simuler une galaxie proprement, et détaille les techniques de raffinement, ainsi que les modèles de formation stellaire, de trous noirs (en phase active ou non) et de rétro-action. Une section spéciale est dédiée aux mots-clés liés aux trous noirs actifs dans les `namelists` de RAMSES : ils sont listés de façon exhaustive avec leur signification et leur valeur recommandée. La dernière partie détaille la marche à suivre pour générer simplement un film à l'exécution d'une simulation.

Mots-clés:
Simulations numériques, évolution des galaxies, trou noir supermassif, noyau actif de galaxie, formation stellaire, rétro-action, vents galactiques.

Contents

List of Figures

List of Tables

List of Equations

CHAPTER 1

Introduction

Contents

The observable Universe contains several hundred billions of galaxies, including ours — the Milky Way, and we observe them by collecting the light they emit. Nowadays, telescopes such as the Very Large Telescope (VLT) in the Atacama desert and the Hubble Space Telescope (HST) are so powerful (see Figure 1.1) that the details they are able to probe inside galaxies can only be explained by accurately modelling their internal physics. This leads to simulations that are so complex that astrophysicists need the most recent high performance computing (HPC) and massively parallel computation techniques to be able to execute them. During my thesis, I ran high resolution simulations (12 to 1.5 pc) of galaxy evolution on one of the most powerful super-computers in Europe, Curie, to give clues to solve two of the key problems that still remain today in the field of galaxy evolution. What physical mechanism kills galaxies, i.e. makes them suddenly stop forming stars? Why do models predict galaxies which are too massive compared to observations? The following sections describe the key notions to understand these questions: typical galaxies in the local and distant Universe, supermassive black holes and active galactic nuclei (AGNs), stars, feedback processes and galactic outflows.

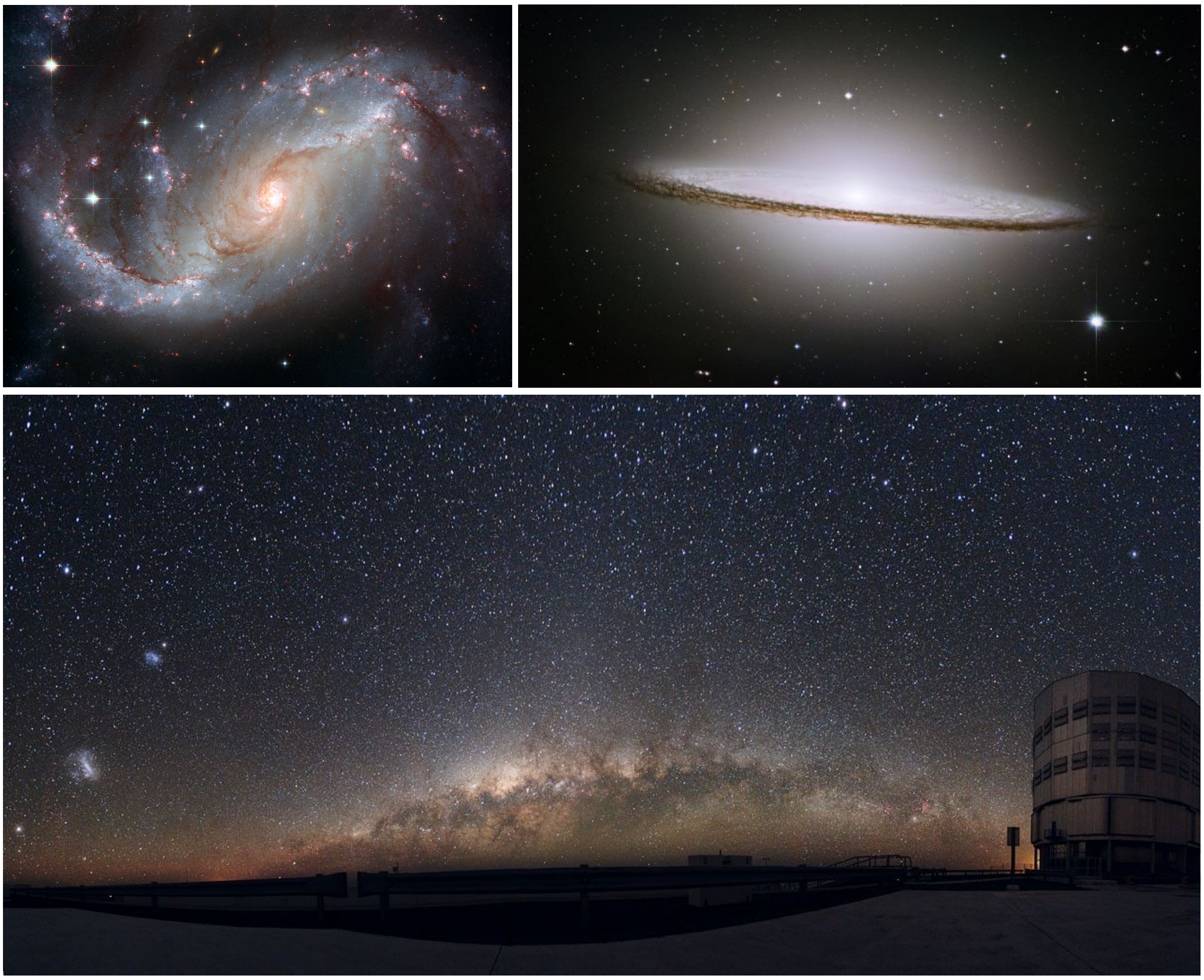

Figure 1.1: *Top left:* An observation of the spiral galaxy NGC 1672, taken with the Hubble Space Telescope (HST). Credit: NASA. *Top right:* An observation of the spiral galaxy of the Sombrero (M104), with the Very Large Telescope (VLT). Credit: ESO. *Bottom:* The VLT at night, with the Milky Way. Credit: ESO/Beletsky.

1.1 Typical galaxies in the Universe

Galaxies are very common in the observable Universe, since there are more than a hundred billions of them. As our own Milky Way, they are gigantic, gravitationally-bound structures of dark matter, stars, gas and dust. Most of them are disks, while the remainder are spheroids and ellipticals. By analogy, astronomers say that galaxies are “alive” as long as they are turning the gas they contain into stars. When the star formation process stops, galaxies "die", and their luminosity drecreases as their old stars slowly fade away.

The components of galaxies are distributed as follows: a thin disk of gas, dust and stars is surrounded by a thick disk of stars. At the center of the galaxy, there is a concentration of light coming from a bound spherical structure of stars, called the bulge. Globular clusters of old stars surround the disk, in a halo of diffuse gas and stars (see Figure 1.2). In the Standard Model of Cosmology ΛCDM (Λ Cold Dark Matter, where Λ is the cosmological constant), this halo is surrounded by a much more extended one, composed of dark matter.

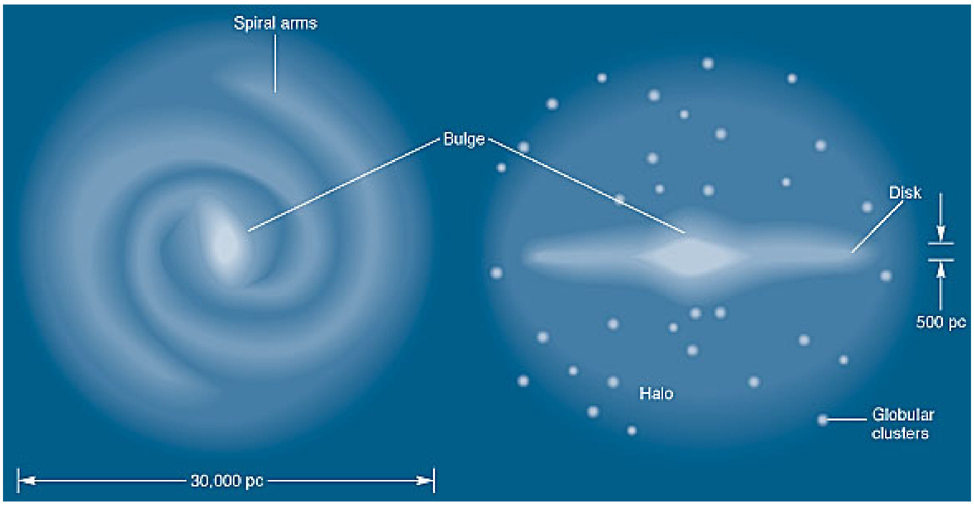

Figure 1.2: Schematic view of a spiral galaxy with its components. In the Standard Model of Cosmology, the gaseous and stellar halo is surrounded by a much more extended halo (a few hundreds of kpc) of dark matter. 1 pc = $3.09 \,.\, 10^{16}$ m. Credit: Durham University/Schombert.

The relative importance of each component can vary along the "life" of the galaxy, and the complete sequence of evolution — from spherical galaxies without disk to very thin disks without bulge — is called the Hubble Sequence, or the Hubble Tuning Fork (see Figure 1.3 and Hubble, 1936). Interestingly, this sequence shows structuration from left (no structures) to right (various features such as spiral arms, bars, etc.), but it is not a time sequence. Indeed, galaxies form as rotating disks due to the law of gravitation, while the later redistribution of angular momentum due to major mergers can create elliptical galaxies and spheroids. The distribution of galaxies between disks and ellipticals is bimodal, not only in terms of morphology but also in terms of stellar population and colors (see e.g. Schawinski et al., 2014). Typically, disk galaxies are blue because they form stars at a high rate (they are on the "Main Sequence" of star formation, see e.g. Noeske et al., 2007; Daddi et al., 2007; Elbaz et al., 2007; Schreiber et al., 2015), whereas elliptical galaxies are red because they have (almost) no star formation anymore (see e.g. Fumagalli et al., 2014). This thesis focuses on feedback processes, star formation and outflows in typical disk galaxies of the distant Universe.

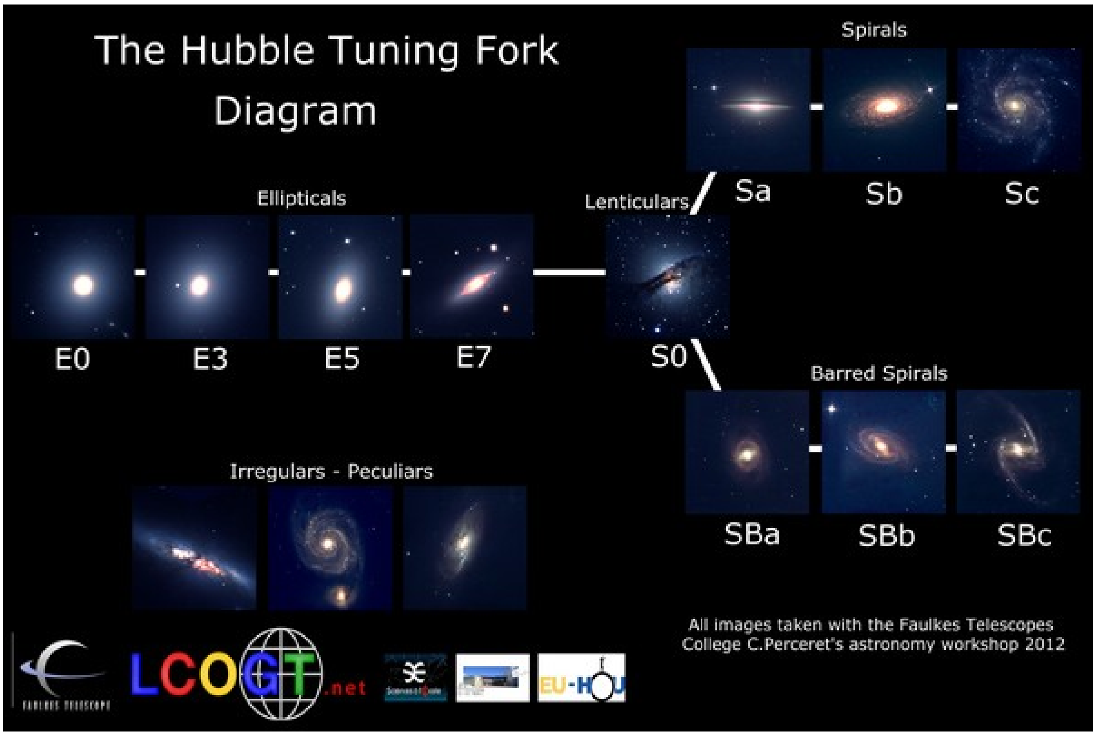

Figure 1.3: The Huble Sequence, also known as the Hubble Tuning Fork (Hubble, 1936). This diagram shows the evolutionary sequence from spheroids to disks. Credit: Las Cumbres Observatory, Global Telescope Network.

1.1.1 Local and distant Universe, and the notion of cosmological redshift

In 1929, Edwin Hubble demonstrated that the Universe is expanding (Hubble, 1929), by observing that “extra-galactic nebulæ” (which were later understood to be other galaxies) were drifting away from each other, and that the recession velocity was larger for objects located further from one another. This translates as the well-known Hubble law:

$$v = H_0.d, \tag{1.1}$$

where v is the recessing velocity of the galaxy in km.s^{-1}, d is the distance to the galaxy in Mpc, and H_0 is a proportionality constant, dubbed the “Hubble constant”. Today, thanks to the Planck satellite, we know that this constant is equal to 67.8 ±0.9 km.s^{-1}.Mpc^{-1} (Planck Collaboration, 2015), in agreement with other earlier missions such as COBE (COsmic Background Explorer) or WMAP (Wilkinson Microwave Anisotropy Probe). This constant means that a galaxy located at 1 Mpc from us is recessing at $\sim$ 68 km.s^{-1} because of the expansion of the Universe.

A direct consequence of this expansion is that the light emitted by distant galaxies undergoes a dilation of its wavelength as it propagates towards us. The more a galaxy is distant from us, the more the photons emitted by this galaxy get their wavelength increased as they propagate, and the redder they appear once they reach us. This phenomenon is called the cosmological redshift, symbolized by the letter z, and is defined as the ratio between the recession velocity v of an object and the speed of light c, under the assumption that the recession velocity is much smaller than the speed of light:

$$z = \frac{v}{c}. \tag{1.2}$$

From Equations 1.1 and 1.2, we can deduce an expression of the distance of observed galaxies:

$$d = \frac{z.c}{H_0}. \tag{1.3}$$

In astronomy, the farther we observe in space, the farther we observe in time, because the velocity of photons is finite. Thus, we see distant galaxies as they *were*, sometimes billions of years ago, when they emitted the photons we receive now. Taking into account that light is shifted towards the red part of the spectrum by the expansion of the Universe as it travels towards us, one can deduce the epoch at which we see an object. Distant galaxies in which I am interested are located at redshift 2, which means that they were formed approximately 10 Gyr ago (3 Gyr after the Big Bang), that their angular size on the sky is less than 3 arcsec and that they are located about 3,600 Mpc.h^{-1} from us, where h is the reduced Hubble constant, $H_0/(100$ km.s^{-1}.Mpc$^{-1})$.

1.1.2 Differences between local and distant galaxies

Observations of typical distant galaxies in the Hubble Ultra Deep Field are depicted in Figure 1.4, and are to be compared to observations of local disk galaxies such as NGC 1672 and M104 (see Figure 1.1). As high-redshift galaxies are located much farther than the galaxies in Figure 1.1, a much higher resolution is needed to probe details inside them. The Hubble Ultra Deep Field is such a high-resolution survey taken in 2003-2004, but it cannot reach the level of details needed to understand the internal physics of these objects. Today, complex high-performance-computing (HPC) simulations (see Figure 1.5) allow astrophysicists to study galaxies at high resolution (down to pc-scale, or even lower for interstellar medium simulations), independently of the redshift.

Due to the huge amount of time (10 Gyr, almost 77 % of the age of the Universe) between the epoch where redshift 2 galaxies are observed and today, where local galaxies live, distant galaxies and nearby galaxies are very different from each other. While they are both made of stars, gas, dust and dark matter, and are both distributed among star-forming disks (e.g. Labbé et al., 2003) and red ellipticals (e.g. Pentericci et al., 2001), their physical properties differ. Table 1.1 summarizes different typical parameters for local and high-redshift galaxies.

Redshift z	Gas fraction g (%)	Surface density Σ_{gas} (M$_\odot$.pc^{-2})	Velocity dispersion σ_{gas} (km.s^{-1})	Jeans length L_J (pc)	Jeans mass M_J (M$_\odot$)
0	$\sim$ 10	5 - 10	5 - 10	10 - 100	$10^{5\text{-}6}$
2	$\sim$ 50	100	50	300 - 1000	$10^{8\text{-}9}$

Table 1.1: Main differences between high-redshift and nearby star-forming galaxies.

Compared to local galaxies and focusing on star-forming disks, high-redshift galaxies:

- are more compact, i.e.: their total mass is comparable to that of nearby galaxies but their size is significantly smaller (see e.g. Daddi et al., 2005; Williams et al., 2014; Davari et al., 2014). This likely comes from the fact that galaxies are building up their outer parts over time to become larger, rather than adding mass to their centers (see e.g. Carrasco et al., 2010; Van Dokkum et al., 2010);
- have a lower fraction of stars with respect to their total mass (and thus a higher gas fraction), because most stars observed in local galaxies did not have time to form *yet* at high redshift. The gas fraction is $\sim$ 50 % in high-redshift disks (see e.g. Daddi et al., 2010; Tacconi et al., 2010, 2013), compared to $\sim$ 10 % in nearby spirals (see e.g. Blanton & Moustakas, 2009).

The measurements of the gas fraction at high redshift presented in Daddi et al. (2010); Tacconi et al. (2010, 2013) are used to calibrate the simulations introduced here and come from CO observations, with their known uncertainties and variations of the CO-to-H_2 conversion factor x_{CO} (see e.g. Narayanan et al., 2012; Bolatto et al., 2013; Sargent et al., 2014). However, measurements of x_{CO} from dust with Herschel PACS/SPIRE give similar results (see e.g. Magnelli et al., 2012), and the 50 % gas fraction is self-consistent in our simulations since we recover observed values of x_{CO} for typical star-forming galaxies (Bournaud et al., 2015).

In galactic disks, the velocity dispersion of the gas is compensated by the gravitational energy; the system is thus in a roughly stable equilibrium. This is translated by a Toomre factor Q (Toomre, 1964, see also Safronov 1960) of about 1:

$$Q = \frac{\kappa \sigma}{\pi G \Sigma} \sim 1, \tag{1.4}$$

where κ is the epicyclic frequency (i.e. the frequency at which a radially displaced fluid parcel oscillates), σ is the velocity dispersion of the gas, G is the gravitational constant and Σ is the surface density of the gas. The larger fraction of gas in high-redshift galaxies makes them more subject to violent instabilities than their local counterparts. This leads to the creation of big clumps of gas, and prevents the formation of spiral arms (see e.g. Bournaud, 2016). Typically, high-redshift disk galaxies contain a few very massive giant clumps, whereas low-redshift galaxies contain several small (10 - 100 pc) and less massive giant molecular clouds (see e.g. Murray et al., 2010). It is here reminded that the Toomre factor was developped for idealized disks (i.e. arbitrarily thin, smooth and rotating disks, e.g. Toomre, 1964; Frank & Shlosman, 1989) and does not apply to realistic disks, with hydrodynamics, dissipation, a relative thickness and non-axisymmetry. Therefore, the critical value of 1 is more of a guide than of a rule and numerical simulations have to be performed in order to take all the aforementioned effects into account.

The typical size of the clumps in a high-redshift galaxy is given by the value of the Jeans' length. A gaseous cloud becomes unstable and starts to collapse if the internal gas pressure force cannot com-

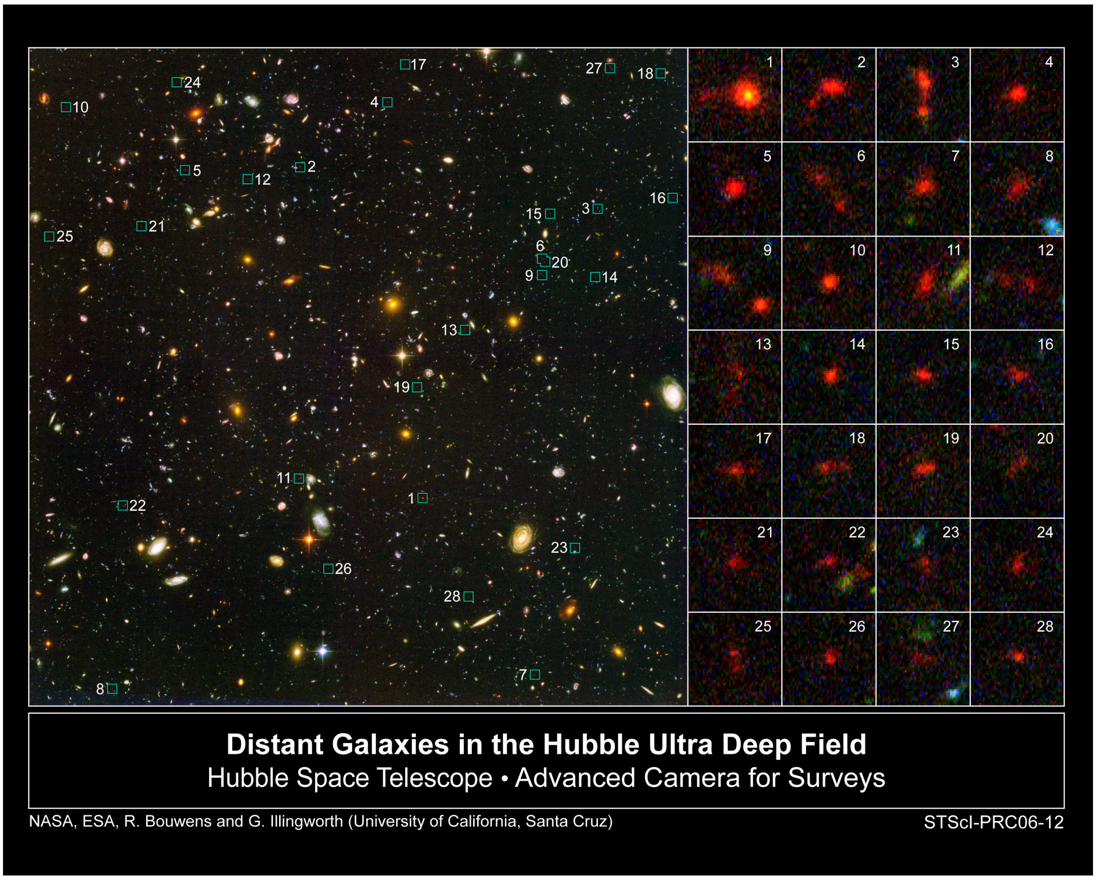

Figure 1.4: Some of the 10,000 galaxies of the Hubble Ultra Deep Field (HST/ACS), at redshift up to 8, most galaxies being around 1.5. Credit: R. Bouwens & G. Illingworth.

pensate its gravity, namely if the free-fall time t_{ff} is larger than the time t_s needed for sound waves with a velocity c_s to cross the cloud (see Equation 1.5). The critical radius above which the cloud collapses is the Jeans' radius R_J (Jeans, 1902):

$$t_{ff} = t_s = \frac{R_J}{c_s}. \tag{1.5}$$

For a perfect gas of hydrogen, $c_s = \sqrt{\frac{C_p . p}{C_v . \rho}}$, where C_p and C_v are the specific heats of a gas at a constant pressure and of a gas at a constant volume, p is the pressure and equals $\rho kT/m_H$, with k the Boltzmann constant, ρ the mass density of the gas and T its temperature, and m_H is the mass of hydrogen. Thus:

$$t_{ff} = t_s = \frac{R_J}{\sqrt{\frac{kT}{m_H}}}. \tag{1.6}$$

To solve Equation 1.6 for Jeans' radius, let's calculate the free-fall time from the second law of Newton for a cloud of mass M and radius R, and a massless particle inside it :

$$\frac{d^2r}{dt^2} = -\frac{GM}{r^2} = \frac{d}{dt}v(r) = \frac{dr}{dt}\frac{dv}{dr} = v\frac{dv}{dr} = \frac{1}{2}\frac{dv^2}{dr}, \tag{1.7}$$

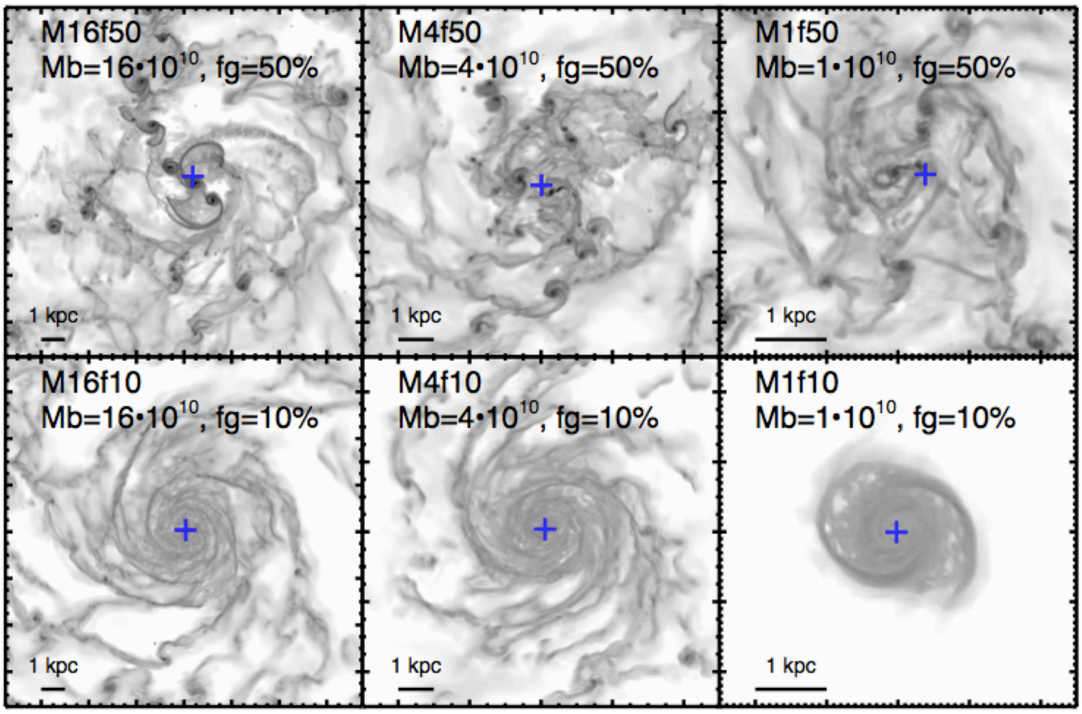

Figure 1.5: Simulated disk galaxies from the local (bottom) and distant (top) Universe seen face-on. The color gradient shows the mass-weighted gas density. The blue cross shows the location of the central black hole. Mb is the baryonic mass in $M_\odot$ and fg is the gas fraction. While local disk galaxies have well-defined spiral arms, distant galaxies have giant clumps and are more unstable. Credit: Gabor & Bournaud (2013).

where v is the velocity of the particle and r is its position in the cloud. After integrating, and knowing the initial conditions $v(t=0)=0$ and $r(t=0)=R$, we find :

$$v = \frac{dr}{dt} = \pm\sqrt{2GM\left(\frac{1}{r}-\frac{1}{R}\right)}. \tag{1.8}$$

We choose the negative solution because the cloud is collapsing, we substitute $s=r/R$, and with $\rho = 3M/4\pi R^3$ for a spherical and homogeneous cloud, we integrate again:

$$t_{ff} = \sqrt{\frac{3}{8\pi G\rho}} \int_{s=1}^{0} \sqrt{\frac{s}{s-1}}\, ds. \tag{1.9}$$

With $s = \sin^2\theta$, we finally have :

$$t_{ff} = \sqrt{\frac{3\pi}{32G\rho}} = R_J\sqrt{\frac{m_H}{kT}}. \tag{1.10}$$

The Jeans' length is thus:

$$L_J = 2R_J = \sqrt{\frac{3\pi kT}{8G\rho m_H}}. \tag{1.11}$$

With a gas number density of typically 1 - 10 cm^{-3} and a temperature of 10^4 K, the Jeans' length and typical size of the clumps is thus of the order of $\sim$ 300 - 1,000 pc. However, in a high-redshift disk galaxy, turbulence is of the order of the sound speed or higher (see e.g. Agertz et al., 2009), and the total dispersion must be accounted for. Furthermore, realistic gas clouds are neither spherical nor homogeneous. Nevertheless, the values given by this simplistic calculation have the correct order of magnitude (see e.g. Elmegreen et al., 2007, 2009).

1.1.3 Galactic outflows

In the Universe, less than 20 % of all baryons (in the form of gas, stars and dust) are found inside galaxies (Sommer-Larsen, 2006). Only a small fraction of the rest of them is found around the most massive galaxies. This "missing bayons problem" is in apparent contradiction with the universal law of gravitation, according to which all baryons should have fallen in galaxies by now (see Chapter 4 for further details). Hence, models create galaxies too massive compared to observational data (see e.g. Croton et al., 2006). To solve this discrepancy, efficient expelling mechanisms, such as powerful galactic outflows removing gas from galaxies, are needed.

Galactic-scale outflows of gas (see Figure 1.6) have been detected both in ionized and molecular gas, at all redshifts for which interstellar absorption features are accessible (Steidel et al., 2010). Such galactic outflows, or galactic winds, are mostly generated by two sources of feedback located inside the host galaxy, in the form of energy or momentum injection in the interstellar medium (e.g. Costa et al., 2014). These sources are the stars, and the supermassive black hole located at the center of the host galaxy. Their outflow characteristics are further described in Sections 1.2.6, 1.3.4, 3.1 and 4.2.2.

Alternatively, it is possible to boost feedback processes and outflows in the numerical models, in order to get galaxies with quite realistic masses at our epoch (see e.g. Oppenheimer et al., 2010). However, this requires the onset of powerful feedback processes very early in the cosmic history and induces other tensions: the formation of massive galaxies with high star formation rates is needed too early compared to observations, and their gas is removed with a quenching happening too soon (e.g. Dekel & Mandelker, 2014). Therefore, artificially boosting current models of feedback at very early epochs cannot solve the problems entirely (Genel et al., 2014), and further research has to be done on the feedback sources and the propagation of outflows.

Finally, apart from outflows, another mechanism can explain why some baryons are found outside of galaxies. Indeed, gas can be periodically prevented from falling inside galaxies by a powerful source of energy, and accumulate in the circumgalactic medium. The following section explains why both mechanisms can explain the death of galaxies.

1.1.4 Quenching and starvation

In the Universe, we observe massive red and dead galaxies (mostly ellipticals but also some spirals) which have no (or almost no) star formation anymore (see e.g. Croton et al., 2005; Croton & Farrar,

Figure 1.6: Galactic outflows in the Cigar Galaxy, M82. A burst of star formation was triggered in M82 as its neighbour M81 passed close to it, and generated the galactic-scale outflows. Hydrogen emission in the H_α band is depicted in red, over an optical observation of the galaxy. In this image, outflowing gas extends for more than 3 kpc. Credit: NASA, ESA, and The Hubble Heritage Team (STScI/AURA).

2008). They cannot sustain high rates of star formation despite the possible presence of cold gas inside them (e.g. Lees et al., 1991) and around them (e.g. Thom et al., 2012), and appear red because of their old stellar populations (e.g. Labbé et al., 2005). Two evolutionary tracks can explain the existence of such red and dead galaxies: quenching, and slow starvation (Schawinski et al., 2014).

- Quenching is a sudden and rapid mechanism leading to the abrupt stop of all star formation processes in a galaxy (e.g. Gonçalves et al., 2012), for example by removing all its gas content in a few million years with powerful outflows.
- On the opposite, starvation is a long-term process. Galaxies are thought to be fed on cosmological scales by cold inflows along the cosmic web (e.g. Birnboim & Dekel, 2003; Kereš et al., 2005; Ribaudo et al., 2011). If accretion of such cold flows on a galaxy is prevented, for example if the halo is kept hot enough for a long time and shocks develop between the hot circumgalactic medium (CGM) and the cold inflows (Dekel & Birnboim, 2006), the galaxy slowly depletes its gas by turning it into stars, until the time when there is too few gas to sustain star formation (a few Gyr later, under the assumption that no merger occurs). According to Dekel & Birnboim (2006), slow starvation is dominant in massive galaxies ($M_{\rm halo} \geq 10^{12}$ $M_\odot$) at redhift below 2.

The presence of cold gas around red and dead galaxies (and sometimes even inside them) suggests that quenching and/or starvation mechanisms have to be maintained over extended periods of time, or happen relatively frequently, to prevent gas from falling back in and star formation processes from starting again. The contrary would lead to the so-called rejuvenation of dead galaxies, as tentatively observed by e.g. Fang et al. (2012).

Due to observational, theoretical and numerical considerations (see Section 1.2 and Chapter 3), supermassive black holes and active galactic nuclei have been accused of playing a role in both quenching and slow starvation in galaxies.

1.2 *Supermassive Black Holes and Active Galactic Nuclei*

Supermassive black holes (SMBHs) are the most massive type of black holes known in the Universe, with a mass of the order of 10^{6-10} $M_\odot$, and are found at the center of most of the massive galaxies known today (see e.g. Magorrian et al., 1998; Kormendy & Ho, 2013). Our own Milky Way also hosts a supermassive black hole, which is called Sagittarius A* (e.g. Reynolds, 2008).

It has been observed that the mass of a supermassive black hole is linearly related to that of the bulge of the host galaxy (see Figure 1.7, Magorrian et al. (1998) and references in Chapter 3). This relation, also known as the Magorrian relation, suggests the existence of a relation of co-evolution between the supermassive black hole and the host galaxy (see however Greene et al., 2010).

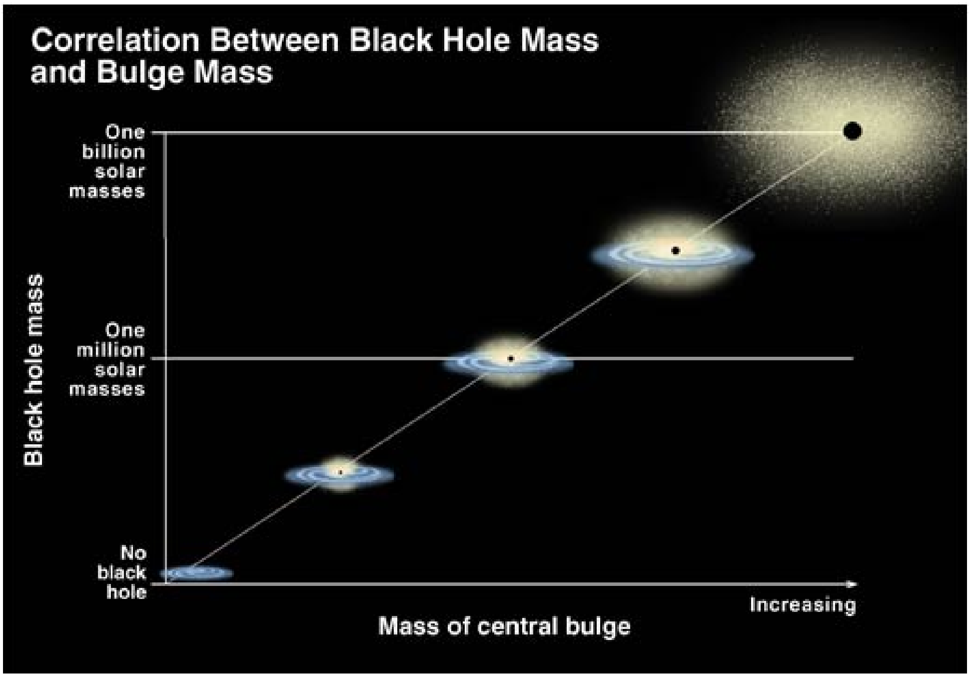

Figure 1.7: The observational relation between the mass of the central black hole and that of the bulge of the host galaxy, also known as the Magorrian relation, after Magorrian et al. (1998). This relation is valid over a wide range of orders of magnitude (from dwarf galaxies to massive ellipticals), and up to high redshift. Credit: Tim Jones/UT-Austin, after K. Cordes & S. Brown (STScI).

Supermassive black holes are not only the most massive objects known in the Universe, but also the most compact ones: the radius of a black hole, which is called the Schwarzschild radius (see Equation 1.13), is only of 3 km per solar mass. To give a sense of the compactness with a concrete example, a black hole of the mass of the Earth ($6.0 \,.\, 10^{24}$ kg) would fit inside a sphere of radius 9 mm.

To derive the Schwarzschild radius based on simple assumptions, let's consider that the escape velocity of a body of mass m from the gravitational potential of a black hole of mass M and radius R is given by the equality between the kinetic energy and the gravitational potential energy:

$$E_{kin} = E_{grav} \Leftrightarrow \frac{1}{2} m v_{esc}^2 = \frac{GmM}{R} \Leftrightarrow v_{esc} = \sqrt{\frac{2GM}{R}}. \tag{1.12}$$

For a black hole, the gravitational potential is so deep that nothing can escape, even photons: $v_{esc} = c$[1], where c is the speed of light. Thus, the Schwarzschild radius is:

$$R_{Sch} = \frac{2GM}{c^2}. \tag{1.13}$$

Even if the reasoning is simple, this solution is correct. For a more accurate way of deriving the Schwarzschild radius, see Karl Schwarzschild's original paper, Schwarzschild (1916).

1.2.1 Formation of Supermassive Black Holes

Up to now, several hypotheses were made regarding the formation of supermassive black holes, but none of these scenarios has been observationally proven yet. The main reasons are that the hypothetical seeds (i.e. the progenitors of supermassive black holes) have not been directly observed; or that the scenario does not explain the high mass of such black holes at high redshift, for the seeds are too light and do not have time to accrete enough mass between the predicted formation epoch and the observed redshift.

Among scenarios of supermassive black hole formation, we find:

- collapse of Population III stars, the first stars in the Universe (metal-free and with a mass of $\sim 100\ M_\odot$, see e.g. Tumlinson, 2002; Shapiro, 2004; Ricotti & Ostriker, 2004), and then mergers with other black holes (see e.g. Yoo & Miralda-Escudé, 2004; Shapiro, 2005b) and accretion of matter (e.g. Soltan, 1982). The distribution between the two latter is respectively 10 % and 90 % (Combes, 2006);
- direct collapse of a massive gas cloud ($> 10^5\ M_\odot$, Micic, 2007) into a disk, or via a supermassive star (if fragmentation of the cloud into stars can be avoided, see e.g. Loeb & Rasio, 1994);
- collapse of a star cluster (see e.g. Binney & Tremaine, 1987).

---

[1] The gravitational well of a black hole is so deep that photons trying to escape it are redshifted to such an extent that the time needed for them to leave the sphere of influence of the black hole goes to infinity.

The collapse of Pop III stars most likely happened in the early Universe, even though the mass of the seed is too light to explain the mass of local supermassive black holes, for it would require an extended period of super-Eddington accretion (see above, and e.g. Valiante et al., 2016). For the two other scenarios, the mass of the seed is high enough so that it does not require super-Eddington accretion, since the mass of the seed corresponds to an intermediate-mass black hole. However, the existence of such intermediate-mass black holes remains uncertain, since they only have been theorized (see e.g. Colbert & Mushotzky, 1999), but not observed yet.

For further details, comprehensive reviews about supermassive black holes and their formation can be found in e.g. Rees (1978); Volonteri (2010); Volonteri & Bellovary (2012).

1.2.2 Growth of Supermassive Black Holes

Black holes are known to grow by two mechanisms: accretion of matter (e.g. Soltan, 1982) and mergers (e.g. Yoo & Miralda-Escudé, 2004; Shapiro, 2005b). The following subsections describe what we know and what is still problematic about both mechanisms.

1.2.2.1 Accretion

Accretion onto a supermassive black hole is the most efficient mechanism known to release energy. As matter falls inside the gravitational potential well of a supermassive black hole, it distributes into an accretion disk. Friction and turbulent viscosity appear in this accretion disk and matter orbiting the black hole (gas, stars, dust, and whatever was close enough to the event horizon of the black hole) loses most of its kinetic energy through these dissipative processes.

This kinetic energy is converted into thermal energy: matter is heated to such an extent that it starts to radiate in the ultra-violet (UV) and X, creating a corona of hot gas around the accretion disk, which in turn emits X-rays (see Figure 1.8). The maximum accretion rate, and therefore the maximum luminosity, is defined by the Eddington accretion rate (or luminosity, Eddington, 1926), above which the radiation pressure from the photons escaping the accretion disk prevents the material from falling in.

The mechanisms bringing matter from galaxy scale (a few kpc) down to the central region (a few pc) by evacuating their angular momentum are well-known, but those fueling the gas from the central pc down to the supermassive black hole (sub-pc) are still debated:

- In high-redshift galaxies, violent disk instabilities at large scale (a few kpc) can drive matter inwards to a few parsecs in a few dynamical times. Low-redshift galaxies are more stable and gas is fueled towards the center through torques created by spiral waves and bars, instead of large-scale disk instabilities (e.g. Combes, 2001; Bournaud, 2016). Still, those large-scale processes do not remove enough angular momentum to drive gas to sub-pc scale directly into the sphere of gravitational influence of the supermassive black hole. Instead, it can be trapped in a nuclear ring (the inner Linblad resonance, see e.g. Binney & Tremaine, 1987).

- At smaller scale, viscous torques (which are not efficient at large scale), friction of giant molecular clouds with stars, and cloud collisions are at play, making the gas clouds lose energy so that their galactocentric distance shrinks and they spiral towards the nucleus (Combes, 2001).
- At sub-pc scale, several mechanisms have been proposed to fuel supermassive black holes, among which tidal distorsions, through which dense nuclear star clusters have their envelopes dispersed (e.g. Hills, 1975; Frank & Rees, 1976); stellar collisions (e.g. Spitzer & Saslaw, 1966; Colgate, 1967; Courvoisier et al., 1996; Rauch, 1999); and nuclear starbursts, through winds coming from young stars and supernova explosions (see Section 1.3.3 and e.g. Norman & Scoville, 1988; Williams et al., 1999; Combes, 2001).

While kpc- (see Chapters 3 and 4) and pc-scales (see Chapter 4) are resolved in the simulations I used during my thesis, sub-grid models are still needed for accretion at the sub-pc scales (Bondi accretion, see Section 2.1.4.2), as in most current galaxy simulations. The accretion onto the black hole is therefore not computed from basic physical principles, but from a recipe mimicking the behaviour of the system at the resolution of the simulation. However, it is known that the black hole accretion rate is linked to the accretion rate in the central parsecs (i.e.: from gravitational considerations, we can assume that a given fraction of the matter arriving in the central parsecs will eventually fall on the black hole at sub-pc scale). The Bondi prescription relies on this assumption and is therefore a good proxy for the actual black hole accretion rate in parsec-scale resolution simulations.

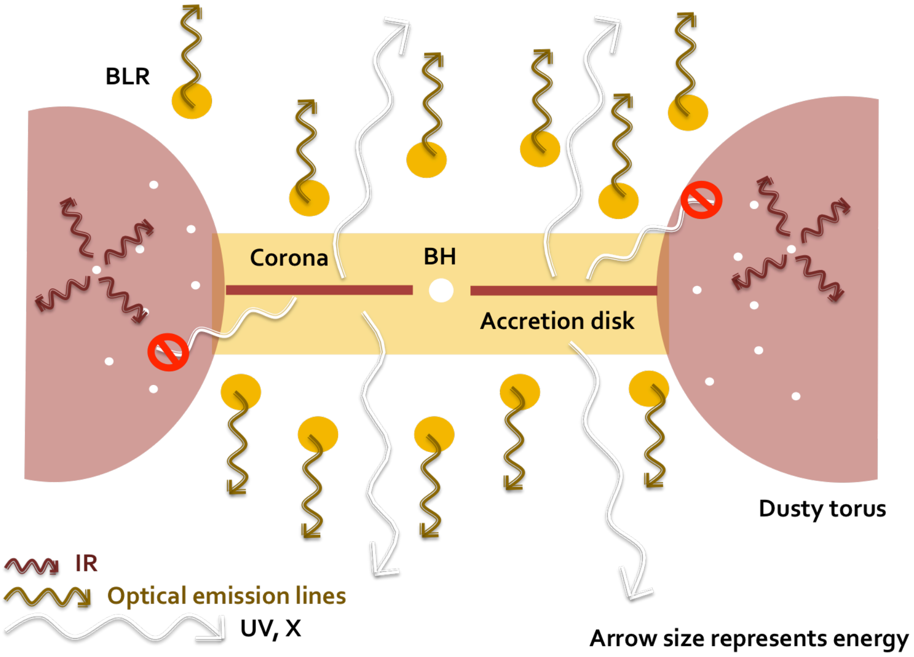

Figure 1.8: Edge-on view of the components of an AGN spectrum according to the Unified Model of Urry & Padovani (1995): while the BH does not actually emit light, the accretion disk and its corona emit UV and X photons due to friction and illuminate BLR clouds, which in turn emit optical lines. The dusty torus blocks UV and X photons in the azimuthal directions and re-emits isotropically in the infrared (IR, see Section 1.2.4.3).

1.2.2.2 Mergers

Galaxy mergers are common in the life of most massive galaxies (see e.g. Lotz et al., 2011), and, as the merger of two galaxies leads to a new more massive galaxy (whether spiral or elliptical depending on the gas fraction and masses of the two initial bodies), it also leads to the coalescence of the two supermassive black holes located at each of their centers (see e.g. Treister et al., 2010; Primack, 2010) — although the resulting supermassive black hole can also be kicked out of the galaxy in case of asymmetries (see e.g. Peres, 1962; Bekenstein, 1973; Blecha et al., 2016).

Galaxy interactions and mergers produce strong torques, efficiently removing the angular momentum of matter. Mergers also cause a complete geometrical redistribution of the gas, bringing most of it to the center of the galaxy (see e.g. Combes, 2001). They can trigger powerful starbursts (see Figure 1.6), particularly in the case of two massive galaxies merging together. Most of the time, the gas inflowing towards the center because of the merger also contribute to the growth of the supermassive black hole, either directly or via the winds and supernovæ generated by a powerful starburst (see previous section, Combes, 2001, and references therein).

Up to recently, it was still unclear whether black holes could merge, but the recent detection of gravitational waves (LIGO Collaboration, 2016) from the collapse of two black holes proves not only the existence of black holes, but also that (stellar) black hole mergers are possible on time-scales smaller than the age of the Universe, despite the final-parsec problem encountered in simulations (see e.g. Vasiliev et al., 2015). Among the solutions proposed to solve this numerical problem, we find interactions of the black hole binary with the surrounding interstellar medium, allowing the binary to lose momentum and eventually coalesce (see e.g. Merritt, 2013).

1.2.3 Active Galactic Nuclei

During episodes of accretion on the supermassive black hole, the nuclear region of a galaxy becomes so luminous that it can outshine the host and release a tremendous amount of energy in the surrounding medium. Such episodes of intense activity at the nucleus of a galaxy are called AGNs, Active Galactic Nuclei, and have a short duration (a few 10^7 yr) compared to the life-time of the galaxy, though they can be recurrent (e.g. Combes, 2001). Depending on the accretion regime (high or low), energy is released in the form of large-scale winds or jets (see Figure 1.9). In addition to these, observations suggest that AGN radiation escapes the host from both sides of the galactic disk, ionizing the surrounding material with a biconical shape, thus creating large-scale ionization cones (see Figure 1.10 and e.g. Müller-Sánchez et al., 2011).

All massive galaxies are believed to host a supermassive black hole at their center, up to high redshift (see e.g. Magorrian et al., 1998; Graham, 2016). Nevertheless, few actually host an AGN, especially at low redshift (e.g. Eastman et al., 2007). A possible explanation to this is that local galaxies have a smaller gas fraction and smaller clumps: thus, they do not fuel the black hole as frequently or as efficiently as high-redshift galaxies do, and most of the time the black hole is in a quiescent phase

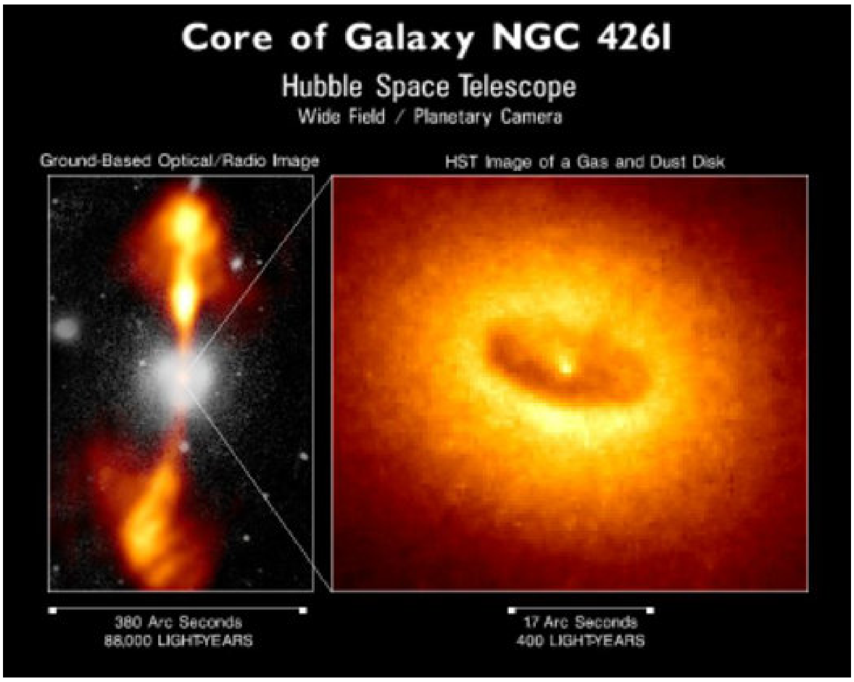

Figure 1.9: *Left:* the elliptical galaxy NGC 4261, observed in the optical, with its large-scale jets, observed in the radio, from the ground. *Right:* the gas and dust disk located in the central region of NGC 4261, observed with the HST. The AGN producing the jets is located at the very center of the galaxy (the nucleus); it is not resolved. Credit: HST/NASA/ESA.

or the AGN is faint or heavily obscured, hence not detectable.

1.2.4 Classification of AGNs

There are several classifications of AGNs, based on observational features. Here, I describe three of them: the Seyfert/quasar classification, the radio-emission classification, and the Unified Model. All three categories can overlap because they are based on (relatively) independent parameters.

1.2.4.1 Quasars and Seyferts

In the literature, AGNs can be referred to as Seyfert (or Sy) galaxies and quasars, or QSOs (quasi-stellar objects). The quasars are the most luminous AGNs, and are far more luminous than the Seyferts: the bolometric luminosity of typical quasars is observed to be about 10^{46-47} erg.s^{-1}, compared to $10^{43.5-44.5}$ erg.s^{-1} for typical Seyfert galaxies (Osterbrock & Ferland, 2006).

1.2.4.2 Radio-quiet and radio-loud AGNs

AGNs are also dubbed radio-loud or radio-quiet, depending on the value of their luminosity in the radio. Radio-loud AGNs have strong radio jets, whereas radio-quiet AGNs are believed to have very weak to no jets. Similarly to X-ray binaries, very collimated jets are supposed to be created by inefficient phases of accretion. On the opposite, phases of efficient accretion create outflows, which are less collimated than jets.

1.2.4.3 The Unified Model of AGNs

The Unified Model of AGNs (see Figure 1.10) was proposed by Urry & Padovani (1995) to describe the characteristics of all observed AGNs according to their inclination angle, and explain the collimation of their ionizing radiation observed at large scale.

According to this model, the accretion disk around the SMBH thickens to become a torus of gas (see Figures 1.8 and 1.10) approximately at the sublimation radius of dust — which is roughly 0.1 pc for a temperature of ~ 1,400 K (Hönig & Kishimoto, 2010). Hence, the torus is dusty but the inner region (accretion disk and corona) is so hot that dust evaporates and thus it contains no grains.

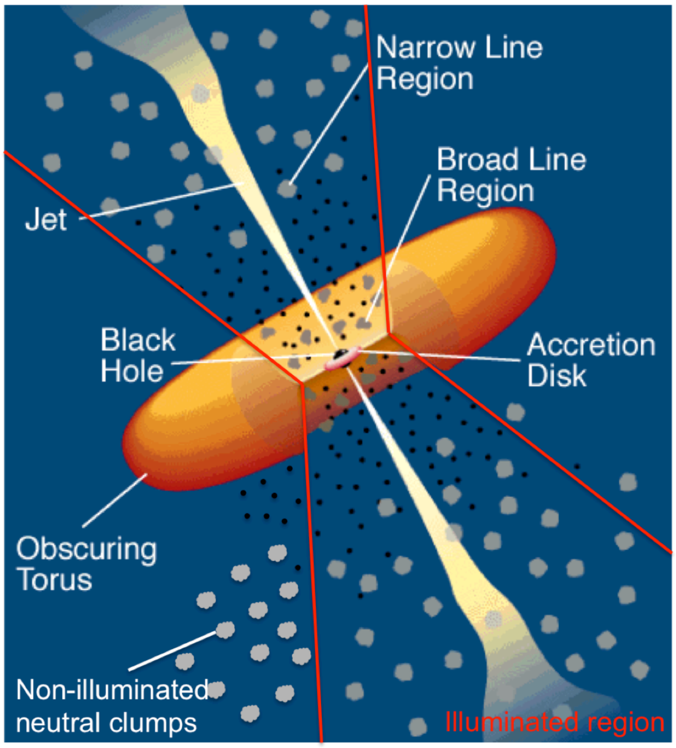

Figure 1.10: Schematic structure of an AGN according to the Unified Model of Urry & Padovani (1995). I modified the original illustration to add the emission cone (red) and the non-illuminated clumps that remain neutral. Close to the SMBH, clumps are highly ionized by the AGN emission and emit broad lines. They belong to the Broad Lines Region (BLR). Farther from the SMBH, clumps of gas are still illuminated but ionized to a lesser extent. They emit narrow lines and are part of the Narrow Lines Region (NLR). According to the model, the dusty torus is able to collimate AGN radiation at very small (sub-pc) scale.

Furthermore, small clumps of gas are distributed on both sides of the accretion disk (see Figures 1.8 and 1.10): some are illuminated, and therefore more or less ionized, and some are outside the emission cone, and remain neutral. The clumpy region close to the black hole ($r < 1$ pc) is called the Broad Lines Region (BLR), from the broad width of the emission lines (H I, He I and He II) that are observed in the spectra of BLRs — more than 1,000 - 5,000 km.s^{-1} (Osterbrock & Ferland, 2006). The outer clumpy region, located a little further from the supermassive black hole ($100 < r < 1{,}000$ pc), is called the Narrow Lines Region (NLR), from the narrow width of the emission lines in the observed spectra, roughly 200 - 400 km.s^{-1} (Osterbrock & Ferland, 2006). The intermediate region is called the Coronal Lines Region (CLR) because light is scattered as it travels through the corona of hot gas that surrounds the accretion disk. A fraction of the light emitted by AGNs can be obscured by interstellar gas and dust close to the accretion disk. In turn, the obscuring gas and dust will emit optical lines and infrared light respectively.

Depending on whether both narrow and broad lines are observed in their spectra, galaxies with AGNs are divided into several categories, from 1.0 to 2.0. AGNs of type 1 are oriented face-on with respect to the observer, and therefore we can see both narrow and broad lines in the observed spectra (see Figure 1.11). On the contrary, AGNs of type 2 are oriented edge-on with respect to the observer, and we can only see the narrow lines, since broad lines are hidden by the torus (see Figures 1.11 and 1.8). Intermediate categories cover all the inclination range, so that for quasars and Seyferts 1.5, for instance, we see narrow lines plus attenuated broad lines that come from scattered light.

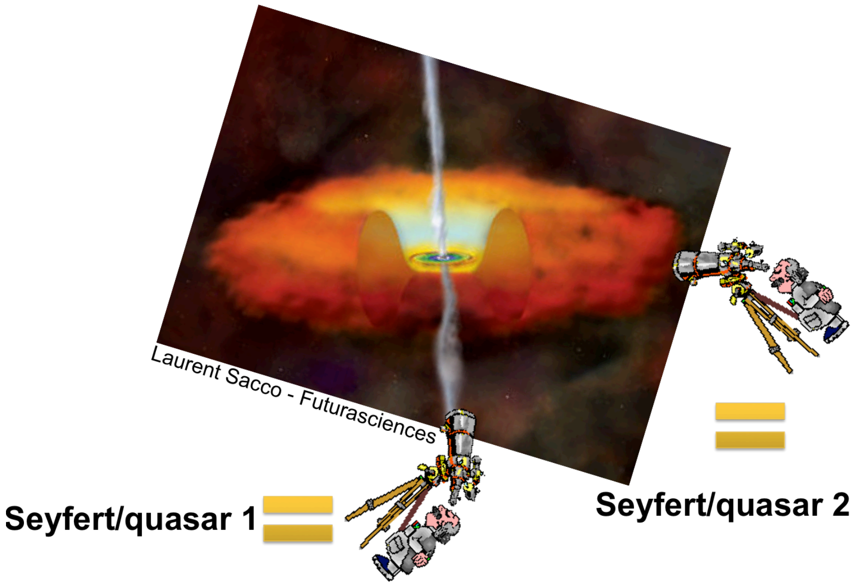

Figure 1.11: Classification of AGNs from type 1 to 2. Type 1 AGNs are oriented face-on with respect to the observer, while type 2 AGNs are oriented edge-on. The whole spectrum of inclination angles is described with AGN types from 1.0, 1.1, 1.2, . . ., 1.9, 2.0. Based on a picture by L. Sacco from Futurasciences.

However, this model was not fully proven when I started my PhD, especially regarding the presence of a torus, its geometry and opening angle, and its behaviour with AGN luminosity (see e.g. Netzer, 2015, for a recent review), and other tentative models, such as the "receding torus" model (Lawrence, 1991), have been proposed to explain tensions with observations. Also, in the Unified Model of AGNs, the conical shape of the ionizing radiation of the AGN is explained by a collimation at sub-pc scale, by the dusty torus. This might not be necessary, since I showed in Roos et al. (2015) that the interstellar medium of high-redshift galaxies is able to collimate AGN radiation at large scale (a few hundreds of pc) to some extent, without requiring the presence of a torus.

1.2.5 Feedback from AGNs in star-forming galaxies

While galaxies feed their central AGN with gas, stars, and dust, the AGN in turn *feeds back* onto its host galaxy. The intensity of this feedback depends on the coupling between the tremendous amounts of energy released by AGNs and the interstellar medium of their host galaxy. This energy comes from accretion of matter onto the most compact objects known in the Universe, which is the most efficient mechanism to produce energy: approximately 1 % of the accretion energy is released, which leads to AGNs with luminosities from $10^{43.5}$ erg.s^{-1} for the faintest ones, to 10^{46-47} erg.s^{-1} for the most luminous ones.

Due to these extremely high numbers, AGNs have long been accused of being responsible for quenching galaxies (see Section 1.1.4). However, I showed with high-resolution simulations (6 pc) and accurate radiation modelling, that even though AGNs are often pointed at as cosmic killers due to theoretical considerations, the impact of AGN winds and ionization on star formation is actually negligible (see Chapter 3 and Roos et al., 2015), possibly even when accurate stellar feedback is accounted for (see Chapter 4 and Roos et al., 2016, submitted to ApJ).

AGN feedback can be seen as two physical mechanisms acting together: first, heating and second, ionization (see King & Pounds, 2015, for a recent review). These models are briefly described in the following sections. Another aspect of AGN feedback is related to the release of cosmic rays. It is described briefly in Section 1.2.5.3 because it was not accounted for in this thesis.

1.2.5.1 Heating

Photons released in the central region of a galaxy transfer their energy to the surrounding material. This energy transfer can translate as an increase of the temperature of the gas. This heating leads to gas dilution, and creates bubbles of diffuse gas. By simple buoyancy — just as CO_2 bubbles rise to the surface of your glass of Crémant d'Alsace at New Year's Eve — these bubbles tend to move away from the galactic disk. Because of high pressure gradients (e.g. Balsara & Krolik, 1993; Woods et al., 1996; Chelouche & Netzer, 2005), these bubbles are accelerated, entraining some more material with them (see Section 1.2.6 for further details), and possibly reach the escape velocity of the gaseous halo, and even of the dark matter halo. The implementation of this thermal feedback in the RAMSES simulations is described in Section 2.1.4.2.

1.2.5.2 Ionization

As for heating, photons released in the central region of a galaxy transfer their energy to the surrounding material. Some of these photons have a really high energy and are able to eject electrons from the atoms they encounter. Most of the gas in the Universe being hydrogen, the energy needed to ionize it is 13.6 eV. As AGN photons (especially in the UV and X-rays) are very energetic, they are able to ionize several atoms of hydrogen each (this is called multiple scattering). The implementation of long-range photo-ionization is described in Section 3.2.2.

This phenomenon is not physically separated from heating: both happen at the same time and are linked to one another. However, for technical reasons (see Chapter 3), they are treated as separate models in simulations, which furthermore do not necessarily account for both.

1.2.5.3 Cosmic rays

At the same time they release photons in the central region of their host galaxy, AGNs are also known to produce cosmic rays, i.e.: particles such as protons and atomic nuclei, accelerated to relativistic velocities along magnetic field lines. AGNs are not the only source of cosmic rays in the interstellar medium of a galaxy: massive stars are also known to release them, as they explode as supernovæ. Such particles are known to drive winds in hot magnetized gas by growing magnetic fluctuations and transfering momentum and energy from the cosmic rays to the gas (see e.g. Ruszkowski et al., 2016).

However, cosmic ray feedback was not accounted for in this thesis because the simulations I used are hydrodynamics simulations, whereas treating cosmic rays necessites the use of magnetohydrodynamics simulations. We chose not to add magnetic fields in order to be able to reach the highest spatial resolution possible (down to 1.5 pc) and treat the AGN and the stellar outflows at the same time. This does not impact the results about AGN outflows, stellar outflows, and the coupling between the two. Nonetheless, for comparison with observed galactic winds, we have to keep in mind that we have neglected an ingredient whose role in the outflow driving (and whose coupling with other feedback models) is currently not well-known.

1.2.6 AGN outflows

In this thesis, I focus on star-forming galaxies at high redshift, where the accretion onto the supermassive black hole is dominated by efficient phases, and the energy released by AGNs in the central regions of galaxies generates galactic-scale outflows of gas (instead of jets). These AGN outflows have typical velocities of 3,000 - 30,000 km.s^{-1} (e.g. Chartas et al., 2014), but generally small gas densities and outflow rates (e.g. Gabor & Bournaud, 2014).

Even though these AGN outflows are well observed at large scales, their launching mechanisms are still debated. Among the current models of wind launching, we find thermal pressure gradient, radiative pressure and shielding, magnetic stresses and cosmic rays:

- Thermal pressure can drive winds with velocities up to 1,000 km.s^{-1}, if the temperature is high enough (see previous section and e.g. Balsara & Krolik, 1993);
- Continuum and line radiation pressure can efficiently accelerate existing AGN outflows (e.g. Arav, 1996; Everett, 2005), if shielding of the central continuum reduces the ionization level of the gas (e.g. Chelouche & Netzer, 2003), for instance with magnetic stresses (see next item);
- Magnetic stresses: open magnetic field lines can produce fast centrifugally-driven winds in accretion disks (e.g. Blandford & Payne, 1982);
- Cosmic rays (see above).

Real AGN outflows are most likely a combination of these different launching mechanisms, all the more since there is evidence that global galactic winds are composed of multi-phase outflows (e.g. Everett et al., 2002; Chelouche & Netzer, 2005; Steenbrugge et al., 2005).

1.3 *Stars and Star Formation*

Stars are spherical, gravitationally-bound bodies made of plasma, and get their energy from the thermonuclear reactions in their core, which make them shine: the fusion of hydrogen creates helium, and then the fusion of the helium produced by the first reactions creates heavier elements. The lifetime of stars is inversely proportional to their mass, which determines their whole evolution.

Beside the supermassive black hole — be it in an active phase or not, the stars are the most important component of a galaxy (see Figure 1.12 for on-going star formation), since their presence makes a galaxy observable:

- through the light of the stars themselves first: massive stars emit mostly in blue and UV when they are young, while stars with smaller and smaller initial mass emit more and more towards the red part of the spectrum (up to the near infrared);
- but also through the consequences of this emission: gas and dust are illuminated, heated or even ionized, and in turn emit infrared light and optical lines.

The following sections describe the physical processes at play in the birth of stars, the major events of the life of a star depending on its mass, and how stars can affect their surroundings.

1.3.1 *Formation of stars*

Stars are formed in clusters (see Figure 1.12), after a giant molecular cloud fragments into smaller cores that will eventually become stars. Figure 1.13 describes the different steps of the formation process.

Destabilized by local turbulence, a shock wave from a nearby event (a supernova explosion, for instance), a more distant event (a galaxy merger, maybe), or simply reaching Jeans' mass by accretion of gas, a dense and cold clump of molecular gas starts to collapse under its own mass. As it collapses, the original cloud can fragment into smaller and smaller molecular cores in a hierarchical way. Each fragment with size of the order of the Jeans' length (see Equation 1.11) becomes a self-gravitating core and starts to rotate, and the collapse goes on as matter distributes in an accretion disk, fueling each of the protostars. As accretion from each gas cloud is still on-going, jets are launched from the poles of the rotating protostar, starting to clear out its surroundings. The temperature in each protostar rises due to the gravitational collapse, and when the temperature is high enough so that thermonuclear reactions ignite and balance the gravitational collapse, the new stars are born. Photons emitted by the young stars finish clearing out the remains of the cloud, and the accretion disks disappear once all the remaining gas has fallen onto the stars. The whole process takes a few million years, which is almost instantaneous on cosmological time scales.

Figure 1.12: The NGC 60 star cluster and the N 90 star-forming cloud. This picture is a composite image of many different exposures taken with the Advanced Camera for Surveys on the Hubble Space Telescope using several filters. Credit: NASA, ESA, and the Hubble Heritage Team (STScI / AURA).

1.3.2 *Life cycles of stars*

The life of a star is completely determined by its initial mass and metallicity (i.e.: the amount of elements other than hydrogen and helium). Figure 1.14 describes the evolutionary tracks of solar-mass stars and massive ($\sim 10\ M_\odot$) stars. The higher the initial mass, the shorter the life of the star and the more spectacular its death. This trend is enhanced by the presence of metals inside the star at its formation.

Solar-type stars spend their long life (about 10 Gyr) burning their hydrogen fuel. When all hydrogen in the core of the star has been converted to helium, the core of Sun-like stars collapses while their envelope (where the last hydrogen atoms still burn) expands: the star becomes a red giant. The temperature increases in the core, allowing helium to be converted to carbon and oxygen for about 100 million years. After this phase, the envelope is so extended that, for comparison, that of our Sun would reach Jupiter. Due to continuous expansion, solar-type stars lose their envelope in a few 10 thousand years, leaving a naked core of carbon. Radiation from this hot core ionizes the remaining gas of the envelope, creating a "planetary nebula" while the carbon core, which is called a white dwarf, slowly cools down as it emits very dim light.

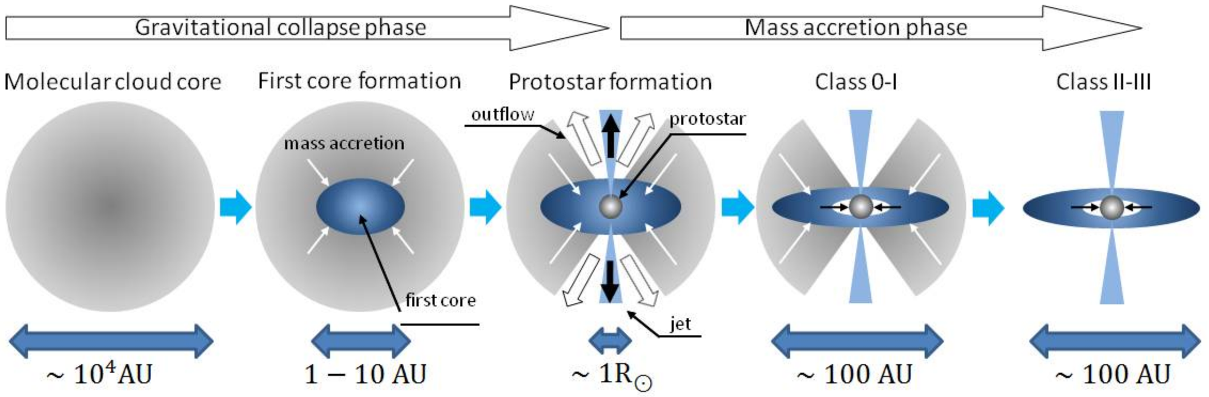

Figure 1.13: The different phases of star formation. 1 AU = 1.50 . 10^{11} m. Credit: Tsukamoto/Nagoya University.

Massive stars live the beginning of their life quite similarly to lower-mass stars, though they burn their hydrogen and helium much faster (10 Myr on average). Thanks to their high mass, the nuclear reactions continue when the star runs out of helium: the carbon core contracts further and reaches a temperature high enough to create oxygen, neon, silicon, sulfur and iron. Once the core is mainly composed of iron — the most stable element, fusion reactions stop and the iron core cools down. It then collapses until it reaches densities of the order of atomic nuclei, causing electrons to merge with atomic nuclei to form a neutron star. Meanwhile, the envelope falls back on the core and bounces off it. This creates a supernova explosion, produces all elements heavier than iron, and releases a large amount of neutrinos. The fate of the neutron star depends on its mass: if it is more than 1.44 $M_\odot$ (a limit known as the Chandrasekhar mass, Chandrasekhar, 1984), collapse will continue until the central object becomes a black hole; otherwise, the neutron star will merely cool down.

In terms of numbers, low-mass stars are far more numerous than their massive sisters (see e.g. Salpeter, 1955; Chabrier, 2003). However, according to initial mass functions (IMFs) such as Salpeter's and Chabrier's, even though low-mass stars live for a very long time, they enclose only a small fraction of the total stellar mass of the Universe. This is also true for remnants of massive stars such as neutron stars and stellar black holes. Therefore, most stellar matter is recycled by successive generations of massive stars. Indeed, when massive stars explode, they release a significant fraction of their mass in the interstellar medium (the remainder being (1) turned into energy during the explosion and (2) enclosed into either a neutron star or a black hole), along with all the metals created during their life and at their death. Stars are thus the origin of almost[2] all metals present in the Universe, including those composing human bodies (and the Earth, for that matter): as André Brahic used to say, "we are all made of stardust".

---

[2] According to the Standard model of Cosmology, a fraction of the metals up to lithium were created during the primordial nucleosynthesis, just after the Big Bang.

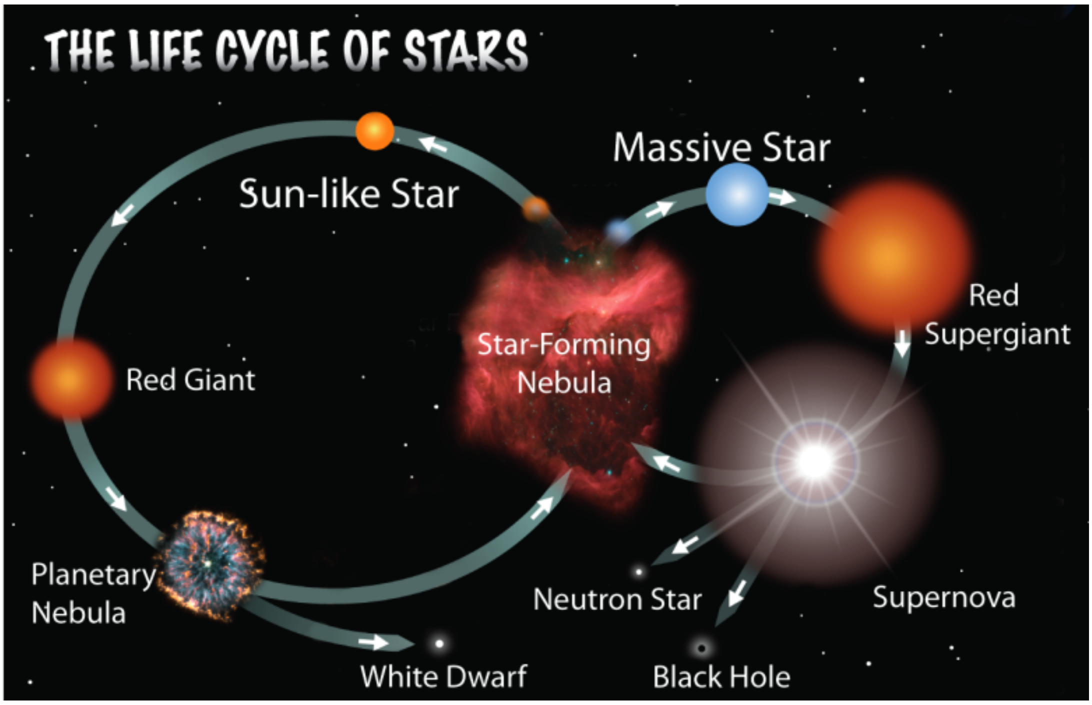

Figure 1.14: Life cycles of stars according to their initial mass. The higher the initial mass of the star, the shorter its life and the more spectacular its death. Credit: B. Dietschi.

1.3.3 Feedback from stars

As for supermassive black holes, the gas of the host galaxy feeds the stars at their formation, and the stars *feed back* on their host. This feedback happens mainly at two stages of the life of massive stars: their youth, and their death. Young massive stars emit strong winds which can entrain the surrounding gas with them, heat it and ionize it, while supernova explosions produce shock waves releasing a huge amount of energy in the surrounding medium. This energy release is also able to create a wind and heat and ionize gas. Both processes are described in the following sections.

1.3.3.1 Heating and ionization from young stars

Just like AGNs, young stars emit photons which heat and/or ionize the surrounding gas. They create regions of ionized gas (also known as HII regions since most atoms in the Universe are hydrogen atoms), whose size is determined by the equilibrium between ionizing processes and recombinations, and which expand because of radiative pressure. However, the energy released in the interstellar medium by a single star is several orders of magnitude lower than that released by an AGN. Nevertheless, there are billions of stars in a typical galaxy, and the winds created by several stars in a cluster can combine to form super-bubbles of a few pc of radius (see e.g. Liu et al., 2015).

1.3.3.2 Supernovæ

As described in Section 1.3.2, massive stars finish their life when their envelope collapses on their core, creating a gigantic explosion called a (core-collapse) supernova[3]. Like AGNs, supernovæ are known to produce cosmic rays (see e.g. Shapiro, 2005a; Girichidis et al., 2016).

Supernova explosions last only a few seconds but they can remain visible for several weeks (like SN 1987A), outshining their whole host galaxies in the same manner as AGNs. Each supernova releases a remarkably universal value of energy of 10^{51} erg in the interstellar medium. The blast wave created by the explosion generates shocks in the interstellar medium and releases thermal as well as kinetic energy. As for star clusters, several supernovæ exploding one after another in a small region of the interstellar medium can combine their energy and create super-bubbles (see e.g. Sharma et al., 2014).

1.3.4 Stellar outflows

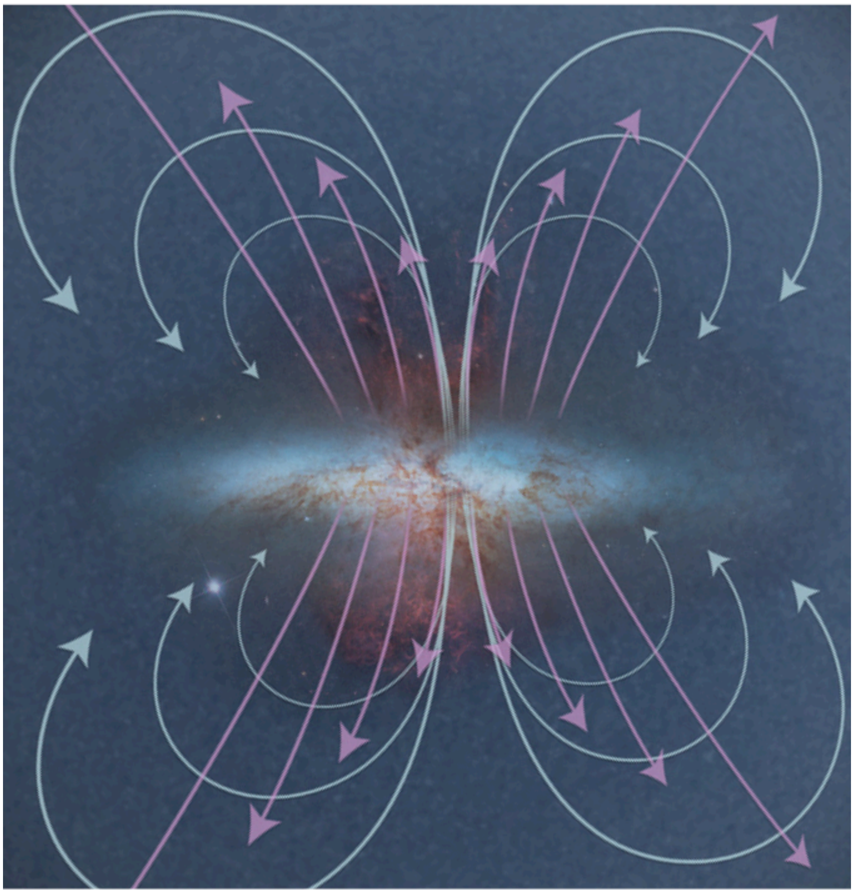

Figure 1.15: Powerful stellar outflows leaving the starburst galaxy M82 (in pink) compared to stellar fountains (in blue), redistributing the gas from the center of the galaxy to its outskirts (Binney & Tremaine, 1987). Credit: NASA/STScI/A. Field (modified).

---

[3] Other mechanisms can create supernovæ, such as accretion of matter from a giant companion onto a white dwarf or a neutron star, which in turn reaches the Chandrasekhar mass.

From observations, young stars and supernovæ are known to drive outflows with a high mass outflow rate, but a limited velocity of 100 to 500 km.s^{-1} (e.g. Bournaud et al., 2014). Nonetheless, in extreme but rare cases like starburst galaxies, where a major episode of star formation is triggered by the encounter of another galaxy, for instance, more powerful outflows can be created for a short period of time (see Figure 1.6).

Though, in typical star-forming galaxies of the Main Sequence, and especially in massive galaxies — i.e. galaxies with a deep gravitational potential well, stellar outflows are weak and the gas lifted by the winds rapidly falls back on the disk, in what we call galactic fountains (see Figure 1.15). A simple geometrical reasoning shows that such stellar fountains redistribute the gas from the center of the galaxy to its outskirts (Binney & Tremaine, 1987). They also recycle a fraction of the gas in the circumgalactic medium, by entraining it back on the galactic disk.

* * *

Chapter 2

Numerical techniques in Astrophysics

Contents

2.1 Numerical simulations

In astrophysics, it is particularly hard — or even impossible — to reproduce cosmic conditions (density, temperature, gravity field, etc.) in a laboratory. To study the evolution of planets, stars and galaxies, we instead use numerical simulations as a test bed. Hence, in the field of galaxy evolution, we are able to simulate distant and nearby galaxies, including our Milky Way, and galaxy mergers such as the Antennae (see Figure 2.1). Such numerical simulations are particularly useful to study the long-term evolution of cosmic objects such as galaxies on several hundreds of million years — which is not humanly possible with observations, as well as to explore the parameter space (e.g. mass, gas fraction, merger configurations, modified gravity, etc.).

Performing numerical simulations can be compared to cooking : we need a dish (the simulation box), ingredients to put in it (initial conditions), and instructions to follow (physical equations and models). As would an oven do, a super-computer then makes the system evolve with time. Due to limited computational power, numerical simulations only include the relevant ingredients and instructions (or initial conditions and models). Indeed, computing the metallicity of all planets in a galaxy is not meaningful when you want to understand its orbit in a galaxy cluster, and vice-versa. Hence, numerical simulations are not meant to reproduce the whole Universe as it is, but rather to test our current theories: we make predictions, and compare them to observations so that we can falsify them.

Figure 2.1: Simulations compared to observations. *Left:* the Milky Way simulation from F. Renaud and the Milky Way artist's conception based on observations of the Galaxy and several local galaxies such as M51, by N. Risinger. *Right:* the Antennae simulation from F. Renaud and H_αR-L-RGB observations of the Antennae at the Cerro Tololo Inter-American Observatory (CTIO) by J. Thibert. Credit: F. Renaud.

There are mainly three types of hydrodynamic codes which can be used to perform numerical simulations in astrophysics: the first uses a fixed grid on which the coordinates of the fluid parcels are projected (eulerian coordinates); the second one uses a non-fixed grid moving along with the fluid parcels (lagrangian coordinates); the third uses unstructured grids. Mathematically, all coordinate systems give the same solutions to a given equation, but numerically, some differences arise (see Section 2.1.2 and e.g. Kim et al., 2014). The following sections present the simulation code I used during my thesis, Ramses, other examples of simulation codes, and the typical initial conditions, equations and sub-grid models usually included in simulations. The last section presents the radiative transfer code I used to compute AGN photo-ionization in simulations of galaxies (see Chapter 3), Cloudy.

2.1.1 The Ramses code

Ramses (Teyssier, 2002) is a eulerian simulation code used to compute the time evolution of the equations of hydrodynamics on a cartesian mesh with adaptive refinement, and to compute N-body gravitation. Dark matter and stars are treated as collisionless particles, and gas is treated as a fluid. For gravitation, Poisson's law is applied to the gravitational potential for each cell of the mesh, and the acceleration of each particle in the gravitational field is computed from the gravitational potential at its position. For the gas, the equations of hydrodynamics are solved on the grid. There are other similar simulation codes in the field of galaxy evolution, e.g. Enzo (O'Shea et al., 2004).

At t = 0, the simulation box contains a disk of 50 % of gas and 50 % of stars — defined by exponential radial and vertical profiles, surrounded by an homogeneous gaseous halo, and a dark matter halo. The galaxy hosts a supermassive black hole (represented by a sink particle) at its center. As time evolves, clumps of gas condensate to form a typical redshift 2 star-forming galaxy.

2.1.1.1 Adaptive mesh refinement

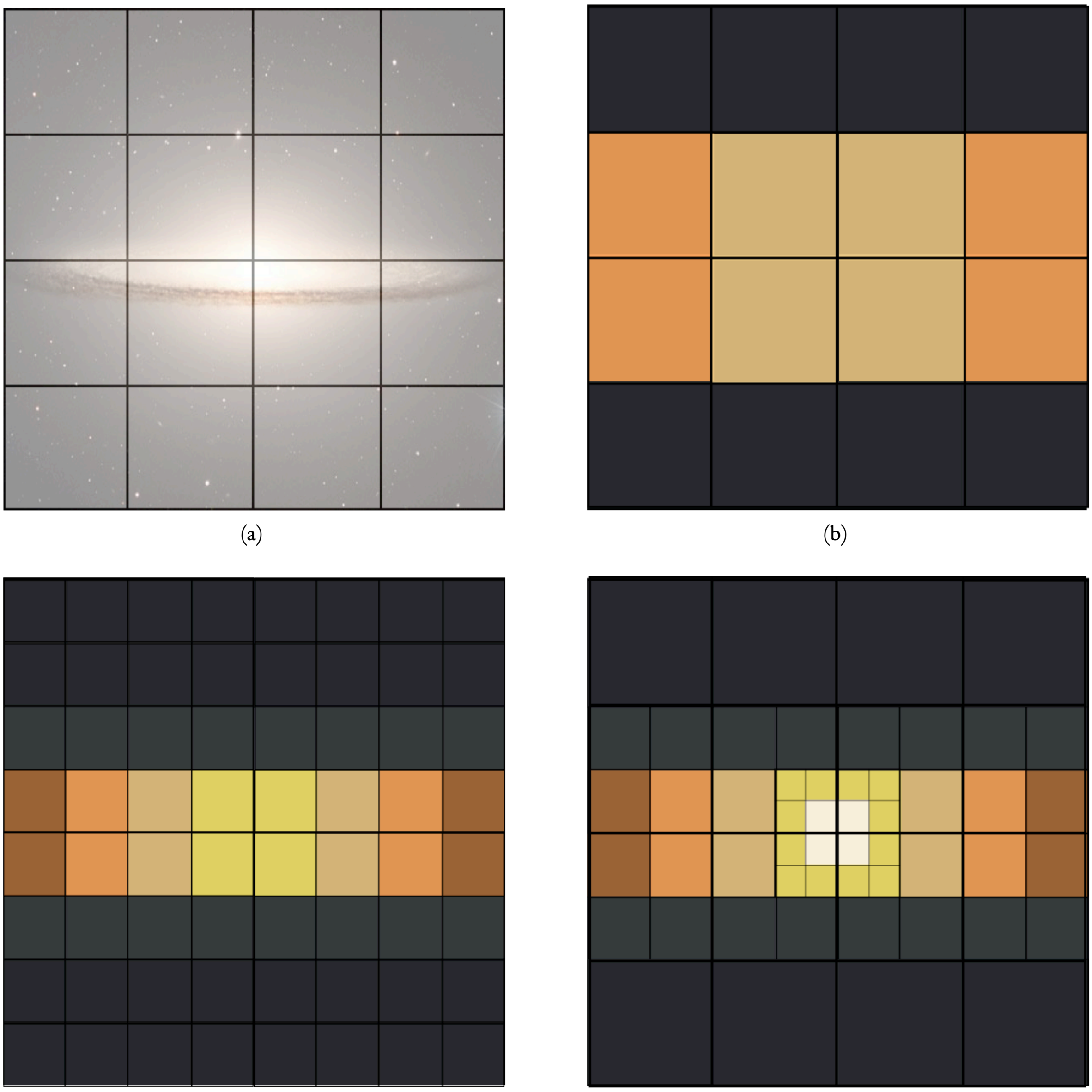

(a) (b) (c) (d)

Figure 2.2: (a) A galaxy to be represented on a 2D grid (the Sombrero galaxy, M104, see Figure 1.1. Credit: ESO). (b) A 2D cartesian grid with coarse resolution. The resolution is not high enough to render the galaxy accurately. (c) A 2D cartesian grid with fine resolution. The galaxy is better rendered but a cartesian grid with a fine resolution takes a much longer time to compute, compared to a coarse grid. (d) An adaptive mesh refinement (AMR) 2D grid with fine resolution where needed and coarse resolution elsewhere. Refinement is adapted on-the-fly and fine resolution is computed only in the regions of interest, which saves computation time. Here, 3 levels of refinement are represented. The principle is the same in 3D.

Ideally, to best describe a structure, the higher the resolution, the better, since the elements describing it are smaller and more numerous (see Figure 2.2a, b and c). However, current supercomputers do not have the power to compute a huge grid of, e.g., 200 kpc length with 1 pc cells. To solve this problem, one can increase resolution only in the regions of physical interest, such as high gas density, large gradients, or any meaningful discriminating criterion (Figure 2.2d). This adaptive mesh refinement (AMR) is done dynamically during the execution of RAMSES simulations. AMR allows us to have a better resolution in the most interesting regions (here, the densest regions of the interstellar medium, where star formation occurs) and simultaneously save computing time with a smaller resolution in the regions where well-known physical processes occur at large scales (e.g. hot and diffuse gas in the gaseous halo).

The initial grid of the simulation box is a cartesian mesh in 3D. It is set up at the coarsest level of refinement l_{min}, and there are $2^{l_{min}}$ cells per side. Each of these cells may be refined, that is to say that each cell meeting a given criterion is splitted into $2^{n_{dim}}$ nested cells (where n_{dim} is the number of dimensions), down to a maximum level of refinement specified in the code. The largest cells are at the coarsest level l_{min}, while the smallest cells are at the finest level l_{max}, and the size Δx of any cell at a level l in a simulation box of size L is given by the formula:

$$\Delta x = \frac{L}{2^l}. \tag{2.1}$$

AMR has an oct-tree approach, i.e.: each group of refined cells is an oct which is arranged in cartesian coordinates; each cell being identified by the oct identifier and the coordinates inside the oct. Neighboring cells must not differ by more than one level of refinement. Non-refined cells are called leaf cells and octs are called parent cells, or grids. The total flux is conserved throughout the tree structure since mass, momentum and energy fluxes of each leaf cell are summed and passed to their parent cell (Berger & Colella, 1989).

In my simulations, the refinement criteria are based on (see Section B.2 for more details):

- a maximal number of particles (dark matter or stars) per cell,
- a maximal gas mass per cell,
- a minimal number of cells to resolve Jeans' length (Truelove et al., 1997).

The first two criteria are physical and allow resolving physical phenomena of interest, while the last criterion is both physical and numerical. First, the resolution of Jeans' length is ensured so that the densest cells are artificially heated according to a density-dependent temperature floor (the so-called Jeans' polytrope), in order to prevent numerical fragmentation. This effect is taken into account in the exploitation of the results. Second, ensuring the resolution of Jeans' length allows us to refine cells in advance, so that the formation of self-gravitating structures is permitted.

The AMR technique is the result of the combination of two earlier techniques, known as particle mesh codes, and tree codes. These techniques have been used to simulate galaxies with the limited computation resources available in the 1980's. Current AMR astrophysics code, like RAMSES and ENZO, were built thanks to these two kinds of precursors, and still use some of the techniques developed for them. We now describe these two techniques in more detail.

Particle mesh codes

A galaxy can be basically described as a set of $\sim 10^{11}$ stars — which can be treated as a collisionless fluid since their cross-section is small, and gas. This fluid approach is however way too expensive in memory to implement, since the Poisson equation must be solved for 6 dimensions (3 of space and 3 of velocity). In elliptical galaxies, as the system is roughly spherically symmetric, it is possible to replace the exact 3D approach on velocities by gaussian distributions of velocities, and therefore solve the evolution in 3 dimensions of space. This approximation is however not valid for disks.

Another solution to simulate a set of $\sim 10^{11}$ stars with gas is the N-body approach, resolving each particle individually. But for simulations to run in acceptable time-scales, the total number of particles is actually limited to 10^{3-4} and thus this technique is not adapted to galaxy simulations.

In the late 1970's, particle mesh codes have been developed based on the advantages of each of the aforementioned methods. Gas is treated as a fluid on a grid, and stars (and dark matter) as particles moving within a gravitational potential. At each time-step, the Poisson equation and the equations of motion are solved on the grid, forces are then applied to the particles according to their position on the grid to get the gravitational potential, which is in turn used to solve the Poisson equation, and so on and so forth. This hybrid method is faster than computing, for each particle, the interactions due to all other particles because the number of cells is usually smaller than the total number of interactions, and also because the gravitational potential is computed in the Fourier space (James, 1977). Indeed, in the direct space, the gravitational potential φ is the convolution of the gas density ρ and the inverse of the distance r:

$$\varphi(\vec{r}) = -\int \frac{G\vec{\rho}(\vec{u})d^3\vec{u}}{||\vec{r}-\vec{u}||}, \tag{2.2}$$

whereas in the Fourier space, this convolution becomes a product between the Fourier transforms of the density and of the inverse of the distance. Furthermore, the Fourier transform method is exact (within round-off errors). However, this Fourier approach works only for cartesian grids or fixed nested grids, not with AMR. The problem was overcome in ENZO by using a periodic root grid and multigrid techniques on non-periodic sub-grids.

Today, particle mesh codes are not used to study galaxy evolution anymore because they do not model close interactions between particles accurately.

Tree codes

Tree codes were first used in astrophysics by Barnes & Hut (1989). The initial grid is a single cell, which refines according to a simple criterion: each time there is more than one particle per cell, it is refined in $2^{n_{dim}}$ nested cells. Hydrodynamics equations are solved in 3D, whereas the gravitational potential is solved in each oct (set of 8 nested cells in 3D), from the finest levels to the coarsest: at a given level l, the particles at level $l+1$ are replaced by pseudo-particles (one per oct) at level l, so that the gravitational potential at level l is computed only from particles and pseudo-particles at the same level. The position of each pseudo-particle is computed either as the barycenter of the particles in the oct, or as higher order moments. If the gravitational potential is computed from multipolar moments, the method is exact (within round-off errors). However, the oct approach to compute the gravitational potential creates a huge number of pseudo-particles when several levels are nested, and is therefore not used in the RAMSES code.

2.1.1.2 Time-stepping and the Courant-Friedrichs-Lewy condition

In AMR grids, time-steps Δt at all levels are related so that more refined cells have smaller time-steps. Every n fine time-step, all Δt are synchronized so that time remains the same for all levels, according to the Courant-Friedrichs-Lewy (CFL) condition (Courant et al., 1928):

$$\frac{v\Delta t}{\Delta x} \leq \frac{1}{2}, \tag{2.3}$$

where v is the velocity of the gas in a cell of level l, Δt is the time-step at level l and Δx is the cell size at level l (see Equation 2.1).

The CFL condition implies that the content of a cell cannot move of more than half the cell size per time-step. This ensures mass conservation and solver stability. Indeed, if the total mass of a cell was shifted by, say, 3 cells in one time-step, the solver would assign three times the total mass of the cell to its neighbour and a negative mass to the initial cell, which would be problematic. The CFL condition also ensures the resolution of meaningful physical time-scales in the simulation.

2.1.2 Other techniques used to run astrophysical simulations

AMR codes using eulerian coordinates like RAMSES and ENZO are not the only techniques used to study the evolution of galaxies. Among the other techniques, we find codes using lagrangian coordinates, such as Smooth Particle Hydrodynamics (SPH) codes and unstructured mesh codes.

SPH codes, like GADGET-2 (Springel, 2005) and GASOLINE (Wadsley et al., 2003), are particle-based hydrodynamics codes. They split the fluid into a series of particles, each with a given mass. Depending on the density of the fluid, the particles are either clustered together (high density) or spread apart (low density). The fluid density and other properties are determined by smoothing over the radius of a sphere encompassing a given number of neighbouring particles. This radius is called the smoothing length, and depends on the fluid density: it is small in high density regions and large in low density regions. In SPH codes, this smoothing length is needed not to overestimate interactions between close particles.

At low density, SPH smoothing has a poor resolution, and such codes are not able to resolve shocks as well as AMR codes do, because of the smoothing kernel. Furthermore, in contrast with AMR codes, it is not possible to (un)refine based on parameters other than the fluid density, which can be problematic, especially to study diffuse outflows and jets, or shocks. To get around the problem, an artificial viscosity term has been implemented in the momentum and energy equations of

SPH codes. This artificial viscosity acts as a resistive pressure when particles get close to each other, mimicking a shock by thermalising kinetic energy.

For my PhD thesis, AMR codes are more adapted than SPH codes because we want to resolve the generation, propagation and coupling of outflows, and the shocks between the outflowing gas and the CGM, with a resolution of at least 100 to 150 pc — which is not achievable with SPH codes. Moreover, SPH codes poorly resolve Kelvin-Helmoltz instabilities and turbulence[1]. According to Agertz et al. (2007), this comes from the fact that SPH introduces spurious pressure forces on particles in regions where there are steep density gradients. Nevertheless, in my thesis, a good resolution is important since such mechanisms regulate the infall on the black hole (which is resolved in the POGO project — resolution down to 1.5 pc, see Chapter 4). Last but not least, AMR codes also scale much better on large numbers of CPUs compared to SPH codes. This last aspect is particularly important to run ambitious simulations projects within the three years of a PhD thesis.

Apart from SPH and AMR, a third method using moving unstructured mesh can be used to study the evolution of galaxies. For instance, the code AREPO (Springel, 2010) uses an unstructured mesh defined by the Voronoi tessellation of a set of discrete points. Even though AREPO is more precise than RAMSES for a given set of physical equations and models, RAMSES scales better on a large number of CPUs. In a given amount of time, RAMSES thus allows for better resolution. This good scaling was crucial for my PhD project, as aforementioned.

2.1.3 Initial conditions

Due to limited computational power, only the ingredients which are relevant to the scope of the study are included in numerical simulations. The purpose of simulations is not to reproduce the Universe with all its physics, but rather to test models by controlling the parameter space, and to confront them to observations. In cosmological runs, the simulation box represents a large portion of the Universe, and the resolution is therefore quite low (a few hundreds of pc). At such scales, only dark matter (N-body codes) or dark matter and large-scale baryonic physics (N-body + hydrodynamics codes) are included. For galaxy-scale runs, usually dark matter, gas, star clusters and black holes are taken into account. Dust or metals are included only if they are part of the parameter space of the study. For intra-galactic simulations, the idea is the same. The higher the resolution, the more physics can be resolved and the more small-scale ingredients can be accurately accounted for.

Most of the time, some ingredients are necessary to the physics of the simulation even though they are not resolved (e.g.: stars and star formation in cosmological and galactic-scale simulations). These are then treated with approximate recipes mimicking the behaviour of the physical phenomenon at the resolution of the simulation (see Section 2.1.4.2).

The distribution and spatial configuration of the initial content of the simulation also depend

---

[1] The resolution has improved since the implementation of the artificial viscosity, but SPH codes are still less accurate than AMR codes for such instabilities (see e.g. Hu et al., 2014).

on the spatial scale of the simulation, and are generated with specific codes. Initial conditions (ICs) for cosmological runs are computed according to the Standard Model of Cosmology ΛCDM with dedicated codes, such as GRAFIC2 (Bertschinger, 2001) or MUSIC (Hahn & Abel, 2011). For isolated galaxy runs, the initial disk often has radial and vertical exponential profiles. Idealized initial conditions such as bulges and disks can also be computed using DICE (Perret et al., 2014). For intragalactic runs, idealized interstellar medium or observed probability density functions of the gas are used as initials conditions.

2.1.4 Physical equations

Current computational power does not allow us to include all physical laws, from strong field gravity to quantum mechanics, in our simulations, and resolve the corresponding scales. We therefore have to select only those which are useful for the computation (see Section 2.1.4.1).

Also, in most simulations, the resolution does not allow to resolve some physical processes which are known to play a role in the evolution of the system. This is especially the case for star formation and black hole physics in isolated galaxy and cosmological runs. To take them into account, we have to rely on simplified sub-grid models mimicking the behaviour on the resolved scales (see Section 2.1.4.2). Dark matter-only simulations, however, do not rely on any sub-grid recipe and are exact (within round-off errors).

2.1.4.1 Resolved physics : gravitation, hydrodynamics

In the case of resolved physics, the physical equations are implemented in the code, and their temporal evolution is solved step by step. These computations are exact (within round-off errors). For simulations in the field of galaxy evolution, these are mostly gravitation and hydrodynamics.

Gravitation

Gravitation is computed according to Poisson's law :

$$\nabla^2 \varphi = 4\pi G \rho, \tag{2.4}$$

with φ the gravitational potential, G the gravitational constant and ρ the density of matter. In RAMSES, the Poisson equation is solved using a relaxation method: in each cell, a value of the Laplacian of the gravitational potential φ is assumed, and compared to the actual value of $4\pi G\rho$.

The value of the Laplacian is iteratively modified until it reaches a given precision on the expected density value ($4\pi G\rho$). Several relaxation methods exist, such as the Jacobi method for differential equations, and the conjugate gradient method, which is used in RAMSES (Guillet et al., 2010).

Hydrodynamics

The complete system of fluid dynamics equations can be written in the following compact form:

$$\frac{\partial}{\partial t}\vec{U} + \vec{\nabla}.\vec{F} = \vec{S}, \tag{2.5}$$

with:

$$\vec{U} = \begin{bmatrix} \rho \\ \rho u \\ \rho v \\ \rho w \\ E \end{bmatrix}, \vec{F} = \begin{bmatrix} \rho u & \rho u^2 + P & \rho v u & \rho w u & u(E+P) \\ \rho v & \rho u v & \rho v^2 + P & \rho w v & v(E+P) \\ \rho w & \rho u w & \rho v w & \rho w^2 + P & w(E+P) \end{bmatrix} \text{ and } \vec{S} = \begin{bmatrix} m' \\ F'_x \\ F'_y \\ F'_z \\ E' \end{bmatrix},$$

where $\vec{U}$ is the state vector of the fluid and $\vec{F}$ is the flux vector (mass, momentum, energy), ρ is the gas volumic density of mass, u, v and w are the three components of the velocity $\vec{v}$, E is the volumic density of total energy (thermal and kinetic), and P is the pressure. $\vec{S}$ is the source term, describing all external forces $\vec{F'} = (F'_x, F'_y, F'_z)$, masses m' and energies E' which are not directly related to the fluid, e.g. gravity, stellar and AGN feedback, etc.

2.1.4.2 Sub-grid physics: star formation, feedback, BH accretion, etc.

For scales below the resolution of the simulations, we use sub-grid recipes which approximate the behaviour of the system on the resolved scales. For instance, star formation laws are always implemented as sub-grid models, since we cannot resolve the scales at which stars form (less than 1 AU) in a galaxy simulation (several tens to hundreds of kpc), even with AMR.

Star formation

In the RAMSES simulation code, the prescription for star formation is based on the empirical Kennicutt-Schmidt law (Kennicutt, 1998):

$$SFR_{cell} = \varepsilon \sqrt{\frac{32G}{3\pi}} \rho_{gas}^{n} V_{cell} \text{ if } T_{gas} < T_{thr} \text{ and } \rho > \rho_{thr}, \tag{2.6}$$

where ρ_{gas} is the volumic density of the gas, n is the Kennicutt index, V_{cell} is the volume of the cell and T_{gas} is the gas temperature. The efficiency of star formation ε is empirical and is set to 3 % (Zuckerman & Evans, 1974; Krumholz & Tan, 2007). So that a new star particle can be created, the temperature in a given cell must be below $\mathrm{T_{thr}} = 10^4$ K, and the density must be above $\rho_{\mathrm{thr}} = 100\ \mathrm{cm^{-3}}$.

The temperature threshold distinguishes easily ionized gas (which most likely does not form stars) and gas which is dense or cold enough to recombine, while the density threshold distinguishes diffuse gas from dense star-forming clumps, and is chosen according to the peak of the probability distribution function of gas density in the simulation. It is recalled here that the density of the Sun is $10^{23}\ \mathrm{cm^{-3}}$, and that $100\ \mathrm{cm^{-3}}$ is well below observed molecular cloud densities, where star formation actually occurs in the Universe (e.g. Burkert & Hartmann, 2013). This value is thus motivated by the inability of our simulations to fully resolve interstellar medium densities.

As the empirical value of the Kennicutt index n is around 1.5, the star formation prescription is equivalent to the mass of gas able to collapse per free-fall time t_{ff} (see Equation 1.10):

$$SFR = \varepsilon \frac{\rho_{gas} V_{cell}}{t_{ff}}. \tag{2.7}$$

The SFR per cell is limited to a maximum value, computed to account for the fact that molecular clouds generally do not turn more than 30 % of their gas into stars during their 10 – 100 Myr lifetime (see e.g. Matzner & McKee, 2000; Elmegreen, 2002; Renaud et al., 2012).

Black hole accretion

In RAMSES simulations, the black hole is represented by a special collisionless sink particle which is able to accrete matter. The black hole accretion rate is computed according to the Bondi prescription (Bondi & Hoyle, 1944; Bondi, 1952) :

$$\dot{M}_{BH} = \frac{4\pi G^2 M_{BH}^2 \rho}{\sqrt{c_s^2 + v^2}^3}, \tag{2.8}$$

where M_{BH} is the black hole mass, G the gravitational constant, ρ the gas density, c_s its sound speed, and v the velocity of the gas with respect to the black hole. The radius of the accretion region is four times the size of the smallest cells in the simulation: $\frac{4.L}{2^{l_{max}}}$, where L is the size of the box and l_{max} is the maximal level of refinement. In the accretion region, gas properties (e.g. the mass removed from the cell) are weighted proportionally to the inverse of the distance to the black hole (see Krumholz et al., 2004).

Due to the balance between the radiation force and the gravitational force, the black hole accretion rate is limited by the Eddington accretion rate, given by:

$$\dot{M}_{Edd} = \frac{4\pi G M_{BH} m_p}{\varepsilon_r \sigma_{Th} c}, \tag{2.9}$$

where m_p is the mass of a proton, σ_{Th} the Thomson scattering cross-section, c the speed of light, and $\varepsilon_r = 10$ % (Teyssier et al., 2011) is the efficiency with which accreted matter is converted into luminous energy. This efficiency is to be compared to the efficiency of thermonuclear reactions in stars, which is of the order of 0.7 %.

At each fine time-step dt, gas is removed from the accretion region according to the aforementioned Bondi black hole accretion rate (limited to the Eddington rate), and the aforementioned weighting scheme, provided that the removed mass is less than 50 % of the total gas mass in the cell, in order to avoid negative gas densities.

Thermal AGN feedback

Thermal energy injection from the AGN is indexed on the black hole accretion rate defined in the above section. At each coarse time-step, thermal energy is injected in the four cells surrounding the black hole according to the formula:

$$E_{thermal} = \varepsilon_r \varepsilon_c \dot{M}_{BH} c^2 \Delta t, \tag{2.10}$$

where $\dot{M}_{BH}$ is defined in Equation 2.8, c is the speed of light, Δt is the duration of a coarse time-step, ε_c is the efficiency of the coupling between matter and the radiation, and ε_r is defined above. For ε_c, we use the fiducial value of 0.15, calibrated with the observed relation between the black hole mass and the velocity dispersion of the bulge (Booth & Schaye, 2009; Teyssier et al., 2011).

While thermal energy is too low to heat the injection region at a uniform pressure above a minimum temperature of 10^7 K, it is stored until the next time-step. When the minimum energy is reached, the AGN burst occurs efficiently enough so that the energy is not radiated away too fast to affect the surrounding gas. To prevent arbitrary small time-steps due to the CFL condition in very diffuse and hot gas, the injected energy is limited so that the injection region cannot be heated above the maximum temperature allowed in the code (here, 5.10^9 K). If this temperature is to be reached in any cell of the injection region, energy is tentatively redistributed with an iterative loop before injection, and is actually injected only if all cells have their temperature below the threshold. In the rare cases where the loop does not converge, the radius of the injection region is multiplied by a factor of 1.25 until all cells meet the temperature criterion. This happens rarely and, in such cases, the radius is multiplied by less than a factor of 2 on average (Gabor & Bournaud, 2013).

Feedback from young massive stars

This sub-grid model represents the feedback from young stars (OB-types), of mass > 4 $M_\odot$, whose winds and radiation account for most of the feedback sources related to the life of stars.

Young and massive stars emit photons which ionize their surroundings (essentially UV photons), leading to the creation of HII regions and the driving of outflows, through the transfer of kinetic energy to the surrounding gas. Physically, the size of the HII regions is determined by the balance between all ionizing and recombination processes. In RAMSES, HII regions are approximated by Strömgren spheres, and their size is computed at each coarse time-step according to the mass and age of the star particles (and hence their luminosity), and the temperature of the surrounding gas. The overlap of several Strömgren spheres is also accounted for.

Furthermore, at each coarse time-step, momentum mimicking radiative pressure injection is deposited as a radial velocity kick in each sphere. In the real interstellar medium, a fraction of the ionizing photons travel farther than $r_{\text{Strömgren}}$, and some have enough energy to ionize several atoms (multiple scattering). This is accounted for, not by enlarging the radius of the Strömgren sphere, but by injecting a few times the computed momentum of the ionizing photons.[2]

In the code, radiative pressure is much more important in terms of feedback, compared to ionization. Nonetheless, computing the radius of HII regions is useful to get a physical scale on which momentum should be injected. Therefore, it helps constraining radiative pressure feedback in the same way that AGN photo-ionization feedback helps constraining the scale on which thermal AGN feedback should be injected (see Section 3.2.2.4). This feedback model was developed by Florent Renaud and is described in further details in Renaud et al. (2013).

Kinetic and thermal supernova feedback

After a lifetime of about 10 Myr on average, massive stars responsible for the winds and ionization described above explode as supernovæ. The implementation of supernova feedback in Ramses was done by Dubois & Teyssier (2008).

Kinetic energy is injected in the form of spherical Sedov blast waves whose size is about two cell sizes. Thermal energy injection by supernovæ is modelled as a polytropic equation of state for the cold gas, with a density-dependent polytropic index. Following the resolution study of Martizzi et al. (2012), the energy released by supernova bursts is injected in the simulation at 90 % in the form of kinetic energy and at 10 % in the form of thermal energy.

2.2 The radiative transfer code Cloudy

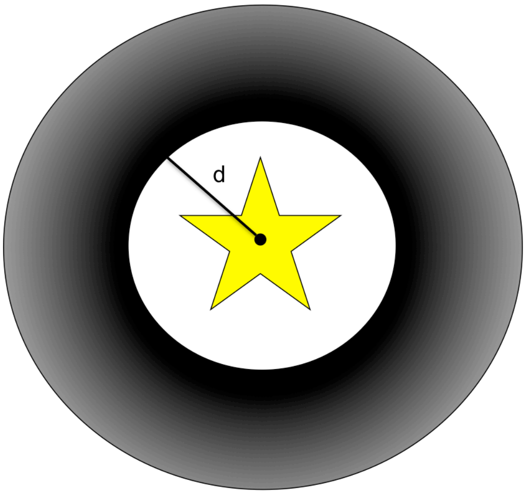

Figure 2.3: Sketch illustrating the input parameters for the Cloudy radiative transfer code. The star represents the ionizing source, whose nature and luminosity are specified as input parameters. The grey area represents a shellular cloud with a radial exponential profile. The width, density profile, metallicity and filling factor of the gas cloud can be specified as input parameters. The last input parameter is the distance d between the ionizing source and the inner boundary of the cloud.

---

[2] The approximation is consistent since the radius of the enlarged sphere taking into account photons traveling farther than the Strömgren sphere is of the same order of magnitude as the reference Strömgren sphere.

Cloudy is a large-scale spectral synthesis code designed by G. Ferland to compute the radiative transfer and the atomic and molecular chemistry along various 1D density profiles. It has been created to simulate physical conditions in the dense clouds surrounding an accretion disk and a supermassive black hole, namely a broad line region (see Section 1.2.4.3 and Figure 1.10). It also works for very low densities, where thermodynamical equilibrium is not reached, because it calculates all parameters (ionization, level populations, kinetic temperature, etc.) step by step, by balancing recombination and ionization processes. I used version C13.02, described in Ferland et al. (2013). A more complete description, based on the previous wide-spread version (C90), is available in Ferland et al. (1998).

The input parameters of Cloudy (see Figure 2.3) are the nature and luminosity of the ionization source (an AGN with a bolometric luminosity of $10^{44.5}$ erg.s^{-1}, for example) and the density, composition, and geometry of the gaseous cloud irradiated by the source, as well as the distance between the two. Cloudy divides the cloud into a set of concentric thin shells centered on the ionization source. These shells are referred to as "equilibrium zones", and their thickness is computed dynamically so that physical conditions remain constant across them. For each zone, Cloudy calculates the balance of all ionization processes (photo-ionization, collisions, charge transfer, etc.) versus recombination processes (radiative and charge transfers, etc.), and outputs the resulting spectral energy distributions (SEDs) and physical conditions (ionization fraction of hydrogen, equilibrium temperature, line emission, etc.).

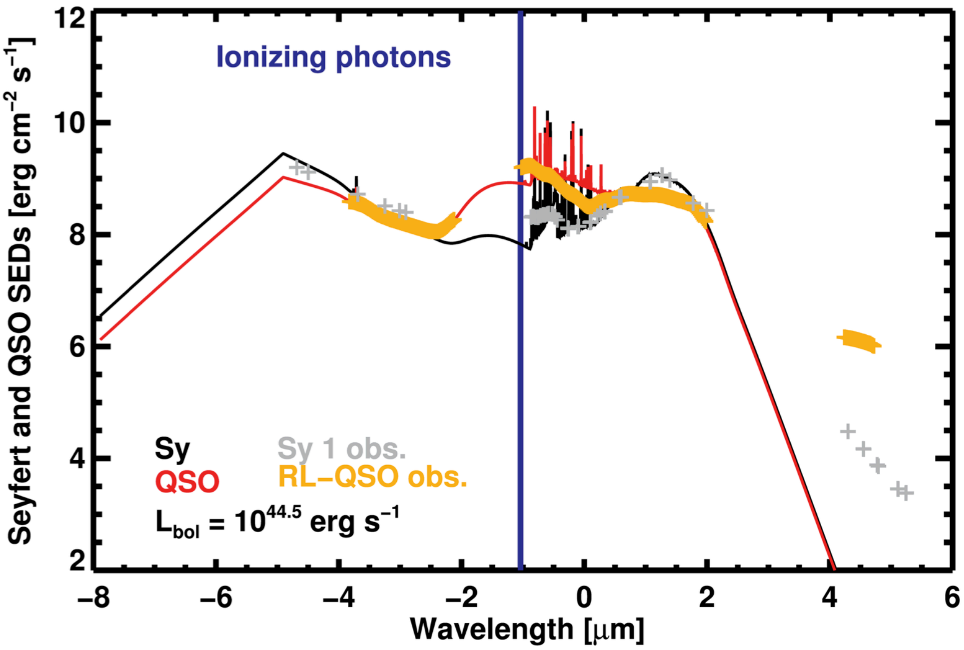

Figure 2.4: The two SEDs used for the Cloudy post-processing method (Roos et al., 2015). The AGN SED is matched to observations of local Seyfert 1 galaxies from Prieto et al. (2010) and the QSO SED is matched to observations of radio-loud quasars from Elvis et al. (1994). The dark blue line is at 911 Å(or 13.6 eV) and divides the ionizing photons on the left from the non-ionizing photons on the right. The FIR parts of our SEDs do not fit the observational data, but since we are interested in ionizing photons, it does not affect the results.

The Cloudy computations used in this thesis include dust with Milky-Way-like distribution and metals with solar-like abundances, and stop when the equilibrium temperature drops under $4 \,.\, 10^3$ K, meaning that the rest of the line of propagation is neutral. Figure 2.4 shows the Seyfert and quasars SED used in the "Cloudification method" to compute AGN photo-ionization in a galaxy, presented in Roos et al. (2015) and Chapter 3.

Even though the radiative transfer computation can be applied to multiple density profiles, Cloudy is not able to treat interactions between different profiles, or to work with complex 3D structures as is. Besides, a 3D tool based on Cloudy already exists (3D_Cloudy, now re-written in Python and called pyCloudy: Morisset, 2006, 2013), although it only works with analytical shapes of objects. Since here the aim of the study was to compute radiative transfer in a galaxy with realistic interstellar medium and high density contrasts, I had to develop my own tools (see Chapter 3 and Appendix A).

◆

CHAPTER 3

Impact of AGN feedback on the host galaxy

Contents

Quenched galaxies are observed in the Universe (see Section 1.1.4 and e.g. Croton et al., 2005; Croton & Farrar, 2008): their star formation processes are very low or even stopped, and they appear red because of their old stellar populations (e.g. Labbé et al., 2005). However, feedback from stars (in the form of winds, supernova explosions and even starbursts) does not have a magnitude high enough to explain the sudden death of massive galaxies, also known as quenching, since the velocity of the observed winds (100 - 500 km.s^{-1}, e.g. Genzel et al., 2011; Newman et al., 2012) is not high enough for gas to escape the dark matter halo of massive galaxies (Bournaud et al., 2014).

Theoretical arguments show that the amount of energy released by accretion onto supermassive black holes is high enough to blow out the entire gas content of the host galaxy (see Section 1.2.5). Low-resolution simulations tend to confirm this idea (see e.g. Di Matteo et al., 2005) and, therefore, AGNs have long been accused of quenching galaxies. Furthermore, numerical arguments favor the intuition that AGNs play a role in regulating star formation — even though they may not go as far as quenching it, since cosmological simulations which do not include AGN feedback produce too many stars in galaxies, compared to observations (e.g. Croton et al., 2006; Fabjan et al., 2010).

Still, the physical link between galaxy quenching and AGNs was still poorly understood when I started my PhD: the magnitude of AGN feedback was still mainly arbitrary, even though it is known that simulations of galaxies including feedback processes must satisfy some observational constraints, such as the linear relation between the black hole mass and the bulge mass[1] (also known as the Magor-

---

[1] At the highest redshifts, the relation is inferred assuming the total stellar mass is a good proxy for the bulge mass (e.g. Reines & Volonteri, 2015; Volonteri & Reines, 2016), since the latter is not resolved.

rian relation, see Figure 1.7 and e.g. Dressler & Richstone, 1988; Dressler, 1989; Yee, 1992; Kormendy & Richstone, 1995; Magorrian et al., 1998; Marconi & Hunt, 2003, and many more until the recent review of Graham 2016), which gives at least an order of magnitude not to put too much feedback.

The work presented in this chapter aims at studying the interplay between the AGN feedback processes and the star formation activity in typical star-forming galaxies at high redhift. More specifically, redshift 2 was chosen because it is known to be both the peak of cosmic star formation (e.g. Madau et al., 1998; Madau & Dickinson, 2014) and the peak of black hole accretion history (e.g. Richards et al., 2006; Madau & Dickinson, 2014). Therefore, such star-forming galaxies have an intense activity of star formation together with an intense AGN activity. It is thus a relevant epoch to study the interplay between the two physical processes.

The two main feedback mechanisms due to AGNs in typical star-forming galaxies at redshift 2 are energy and momentum injection producing outflows, and photo-ionization (see Section 1.2.5). While the first feedback model is often taken into account in simulations at all scales (cosmological simulations (e.g. Dubois et al., 2012), mergers (e.g. Barai et al., 2014), isolated galaxies (e.g. Gabor & Bournaud, 2013, 2014) — though the implementations, assumptions and parameters may differ from one simulation code to another), long-range radiative effects from AGNs were not commonly included when I started my PhD. This comes from the fact that radiative processes are numerous (ionization processes, recombination processes, line emission, molecular chemistry, dust grains physics, etc.) and must be treated exhaustively to be accurate (e.g. complete treatment of the structure of the H-like and He-like iso-electronic sequences to accurately compute line emission). As taking them all into account (as Cloudy C13.02 does, see Ferland et al., 2013) would take way too long during a simulation, simplified sub-grid models mimicking their effects at the resolution of the simulation were developed. Comparisons with complete treatments of radiative transfer such as that of Cloudy are useful in order to improve them.

During my thesis, I modelled the effects of both thermal and radiative feedback from a typical AGN on the star formation activity of a Main Sequence galaxy at redshift 2, to see whether or not they are able to quench it (Roos et al., 2015). We used the standard recipe for thermal AGN feedback (see Section 2.1.4.2 and Booth & Schaye, 2009; Teyssier et al., 2011), and chose to study the effects of AGN photo-ionization in post-processing, using the "complete simulation of the microphysics of gas and dust over the full range of density, temperature, and ionization encountered in astrophysics" (Ferland, 2014) provided by Cloudy C13.02 (see Section 2.2 and Ferland et al., 2013). The following sections describe the known effects of standard thermal AGN feedback on their host galaxy, the motivations to study long-range radiative effects in addition to the latter, the implementation of radiative AGN feedback, and finally, the effects of the combination of the two on the star formation activity and gas ionization fraction of the host galaxy.

3.1 Effects of thermal AGN feedback on the star formation activity of the host

Gabor & Bournaud (2013, 2014) performed high-resolution simulations of isolated typical redshift 2 star-forming galaxies, with resolution down to 6 pc — thus resolving the sites of star formation (giant molecular clouds, GMCs), and used them to study the effects of AGN outflows on the star formation activity of the host galaxy.

Unlike earlier studies such as Di Matteo et al. (2005), Gabor & Bournaud (2013, 2014) simulated typical redshift 2 disk galaxies of the Main Sequence of star formation, hosting standard AGNs (as opposed to extreme QSOs, which, contrarily to typical AGNs, are rare in such galaxies, see e.g. Mullaney et al., 2012; Juneau et al., 2013). Not only the gas distribution is different since the AGN lives in a disk of gas, as opposed to an elliptical galaxy resulting from the merger, but also the resolution is much higher and allowed them to resolve high density contrasts in the interstellar medium. Therefore, the coupling between the energy released by the AGN and the gas in the interstellar medium is different, since high density contrasts are not affected the same way as smooth gas by AGN outflows. Also, higher resolution allows them to better resolve gas supplies onto the AGN, which is important since the bulk of the black hole accretion comes from typical (and frequent) AGNs, and not from extreme (and rare) quasars. Typical galaxies of the Main Sequence are therefore the main mode of black hole growth, which shapes the Magorrian relation (Mullaney et al., 2012).

Gabor & Bournaud showed that typical recipes of thermal AGN feedback and black hole accretion rate produce powerful winds in redshift 2 disks (see Figure 3.1, originally published in Gabor & Bournaud, 2014), without the need of having extreme quasar-level AGN activity. While these outflows have a high velocity of several 10^3 km.s^{-1} and the mass of gas in the outflows is equivalent to 10 to 100 % of the total star formation rate (SFR) of the galaxy, they showed that the outflowing gas is mainly hot and diffuse, that is to say too hot and too diffuse to form stars, whether the AGN is here or not. Thanks to the high resolution of the simulations (6 pc), they also showed that the clumpy, dense and cold star-forming gas in the galactic disk was neither heated, nor expelled by the AGN outflows at large scale, and that the outflowing gas preferentially takes the paths of least resistance.

Those results are valid on time-scales for which gas depletion due to star formation and black hole accretion is not important for the gas distribution in the interstellar medium (a few hundreds of million years), since the galaxy is isolated and therefore out of its cosmological context (no gas inflows, no mergers, initial diffuse and smooth circumgalactic medium). They are thus not in contradiction with longer-term simulations showing that, once a black hole mass threshold is reached, the AGN becomes powerful enough to maintain the halo hot and prevent cold inflows from replenishing the interstellar medium of the galaxy (hence inducing a slow starvation, see Section 1.1.4 and e.g. Dekel & Birnboim, 2006).

Such results are in contrast with the conclusions of lower-resolution simulations (e.g. Di Matteo et al., 2005; Dubois et al., 2013), according to which the coupling of AGN thermal energy with the

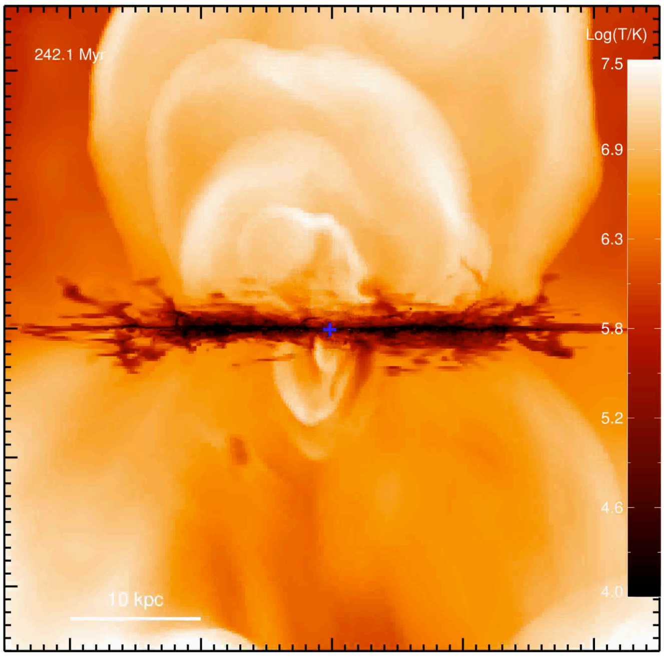

Figure 3.1: Thin slice of the galactic disk seen edge-on, showing the powerful outflows produced by thermal feedback from a typical AGN. The color gradient shows the mass-weighted gas temperature and the blue cross shows the location of the supermasive black hole. Despite the presence of fast outflows ($\sim 10^3$ km.s^{-1}) entraining 10 to 100 % of the amount of gas turned into stars each year, the dense star-forming disk is not affected. This figure comes from Gabor & Bournaud (2014).

interstellar medium of the galaxy is so high that all of it is blown away in a few million years, resulting in the quenching of the galaxy. Contrarily to high-resolution simulations resolving the density contrasts in the interstellar medium, such simulations have a hot and smooth interstellar medium which can be easily expelled by AGN outflows according to Gabor & Bournaud (2014), and lack the dense and cold phase which is not affected.

3.2 Coupling of thermal and radiative AGN feedback

The work presented here was originally published as Roos et al. (2015) and aims at quantifying how radiative AGN feedback changes the physical conditions of the gas, and thus its ability to form stars, giving new clues about the co-evolution of galaxies and their central black hole.

Following the work of Gabor & Bournaud (2013, 2014), I studied the coupling between AGN winds and AGN photo-ionization, to check whether it could change the effect of the AGN on the star formation activity of the host, or not. To do that, I studied how AGN radiation impacts the ionization fraction of the gas phase in star-forming galaxies, by post-processing one of the redshift 2 galaxy simulations of Gabor & Bournaud (2013, 2014). Simulations were performed with Ramses (see Section 2.1.1 and Teyssier, 2002), radiative transfer was computed with Cloudy (see Section 2.2 and Ferland et al., 2013), and I built an interface to use one with the other in post-processing.

This section describes the motivations of this study, and the method developed to compute the ionization state of an entire galaxy simulation due to AGN radiation. This chapter ends with the published article, and a short presentation of the conclusions of the study.

3.2.1 Why does radiative AGN feedback matter ?

Before the beginning of my thesis, it was not known whether energy injected by a typical AGN in the central region of a typical Main Sequence galaxy was able to quickly expel all of its gas content and quench it, or not. Gabor & Bournaud (2013, 2014) showed that *thermal winds* from a typical AGN did not affect star formation and were not able to expel all of the gas content (they entrain only hot and diffuse gas), because the outflows take the path of least resistance, and thus escape the disk mostly in the polar directions.

Still, winds are not the only manifestation of AGN feedback: radiative effects could also be of great importance for star formation (either positively by triggering it, see e.g. Fabian, 2012, or negatively by suppressing it, see e.g. Springel et al. 2005b; Farrah et al. 2012) and for outflow driving (see Section 1.2.6), or black hole fueling (e.g. Springel et al., 2005b; Farrah et al., 2012). However, they are often not included because of the complexity of the equations (see Section 2.2), or taken into account with simplified sub-grid models. Also, radiative transfer is important to constrain feedback with observations, because it leads to the computation of ionization fractions and line ratios, which were mostly unavailable for simulated galaxies including interstellar medium with high density contrasts, when I started my PhD.

Finally, the study of several models of AGN feedback, like thermal feedback and radiative feedback (which are separated in simulations for memory and computation time reasons, whereas they are two aspects of the same physical process), at the same time in a simulation is crucial (1) to compare with observations, since all feedback processes happen simultaneously in real galaxies, and (2) because the interplay between several feedback models implies non-linear processes which can have a higher (or lower) impact than astrophysicists would have guessed by naively summing the results of two separated simulations, each including one feedback model.

3.2.2 Computation of long-range AGN photo-ionization

This section describes the method I developed to compute the ionization state of a simulated galaxy irradiated by an AGN. First, the simulations of typical redshift 2 star-forming galaxies are presented, then the spectra used as ionizing sources for Cloudy are described. The method itself is then presented and its advantages, drawbacks, and the constraints it gives on thermal AGN feedback are discussed.

3.2.2.1 Presentation of the post-processed simulations

The simulation I post-processed is M4f50, as labelled on the second top panel of Figure 1.5 (also described in Gabor & Bournaud, 2013, 2014). It represents a redshift 2 Main Sequence galaxy hosting a typical AGN, and has a total baryonic mass of 4.10^{10} $M_\odot$ and a gas fraction of about 50 %. The box length is 50 kpc, and the size of the smallest cells is 6 pc. The simulation box contains 23 million leaf cells on average. Regularly, a snapshot of the simulation is taken and all parameters are printed out in order to be post-processed.

Thermal AGN feedback (see Section 2.1.4.2) produces powerful winds that do not impact star formation (see Figure 3.1 and previous section). A complementary simulation, where thermal AGN feedback is shut down a few million years before starting the study, was also considered. This allowed us to study the short-term effects of the absence of thermal AGN feedback in a high-redshift disk galaxy, and to compare the role of radiative AGN feedback in the presence and in the absence of thermal AGN feedback.

3.2.2.2 *Models of Seyferts and QSO spectra to use as ionizing sources in Cloudy*

As the simulation I use can only resolve a region of a few parsecs around the central black hole (the size of the smallest cells is 6 pc), I built a model of the spectrum coming out of this region as a whole, which means that the effect of the material surrounding the AGN (clumps, dust, etc.) on the SED, such as attenuation, reflection and scattering, was taken into account.

Modelling the accretion disk, the corona, the dusty torus and the BLR clouds

The components of the spectral energy distribution (SED) of the nuclear region of a galaxy are complex, according to the Unified Model of AGNs (see Sections 1.2.2.1, 1.2.4.3 and Figure 1.8). The accretion disk around the supermassive black hole (i.e.: the AGN) emits UV and X photons, and the corona of hot gas surrounding the accretion disk emits X photons. This radiation strikes the BLR clouds and the dusty torus, which are heated by absorbing a fraction of it. Heated dust re-emits in the IR and FIR. In order not to assume strong hypotheses about the geometry of the torus, only its emission is accounted for, not the absorption of UV and X photons. UV and X photons have their energy higher than the ionization potential of hydrogen, 13.6 eV, and are therefore able to ionize the clumps they encounter to some extent, depending on their size and distance from the AGN. When the gas recombines, optical (and UV) lines are emitted. Finally, the BLR clouds are so dense that they attenuate light dramatically between EUV and optical.

To model the spectrum of the nuclear region as a whole, I therefore took the spectrum of the AGN itself, added dust emission to model the torus, and computed the transmitted spectrum of a typical BLR (see Figure 2.4 for comparison with observations of local Seyferts and quasars):

- The spectrum of the AGN is built with the *agn* command of Cloudy, based on the parameters used in Ferguson et al. (1997), and modified to match observed SEDs of nearby Seyferts (Müller-Sánchez et al., 2011) and radio-loud quasars (Elvis et al., 1994). We study three luminosities, corresponding to three AGN regimes: $10^{44.5}$ erg.s^{-1} (a typical AGN), $10^{45.5}$ erg.s^{-1} (a strong AGN) and $10^{46.5}$ erg.s^{-1} (a typical quasar).
- The dust located in the central region of the galaxy is assumed to have solar abundance and the grains to be composed of silicates and graphites in the same proportions as the interstellar

medium of the Milky Way. Dust emission is modelled with 6 blackbodies, with temperature ranging from 90 to 2,900 K. Dust sublimation and grains depletion are taken into account.

- The BLR is composed of homogeneous clumps of gas, with a uniform hydrogen density of 10^9 cm^{-3} (Mathews & Capriotti, 1985) and a filling factor of 10^{-3} (Osterbrock & Ferland, 2006). Cloudy was used to compute the spectrum transmitted by such a region when it is illuminated by the aforementioned AGN. The inner and outer radii of the BLR are defined so that the dust sublimation radius is crossed during the computation.

The FIR part of the spectrum, which corresponds to cold dust, does not match the observations (see Figure 2.4). As such photons cannot ionize gas and do not heat it efficiently, this discrepancy does not affect our results.

Seyferts and QSOs of type 1

As the central region of the simulated galaxy is not resolved, choices must be made regarding the role of the different components of the central parsecs: dusty torus, BLR geometry, etc. We chose to emit Seyfert 1 and quasar 1 (see Section 1.2.4.1) spectra isotropically, which means that no torus is blocking or attenuating UV and X photons. Despite this, dust emission in the IR is included isotropically. This means that we assume that the emission is not collimated or blocked by the torus at sub-pc scale. The effects seen with the post-processing method therefore show an upper limit compared to the presence of a realistic torus. Since the results indicate a very small effect, including a torus would reduce them even more. Such a choice also allowed us to check that the interstellar medium is efficient at collimating the AGN radiation at galactic scale (to some extent), without needing the presence of an obscuring torus (Roos et al., 2015).

To build a hyper-realistic model, we could have set an arbitrary emission cone with observed parameters, and used a Seyfert/QSO 1 SED inside it so that the photons escaping the AGN nearly perpendicularly to the galactic plane only encounter dust and clumps at large scale, and a Seyfert/QSO 2 SED outside it, so that the photons escaping the AGN towards the torus are much more attenuated, but not arbitrarily blocked. However, this supposed to have realistic constraints for the opening angle of the ionization cone and the orientation and geometry of the putative torus, which was not available when I started my PhD (e.g. Müller-Sánchez et al., 2011; Netzer et al., 2016; Liu et al., 2016).

3.2.2.3 Post-processing method to compute AGN photo-ionization

During my PhD, I developed a method to compute the ionization state due the AGN radiation in a high-resolution (6 pc) simulation of galaxy, in post-processing. It was applied to a RAMSES simulation with 5 levels of refinement ($l_{min} = 8$, $l_{max} = 13$) and 23 million leaf cells per output (with a size of about 5 GB each). Nevertheless, the method can be applied to outputs produced by any code (AMR or other) at any resolution, provided that the position, velocity, gas density, gas temperature, and size of all cells (or particles) in the output to post-process are listed in an ASCII file. The different steps of the "Cloudification process" are listed below. Unless otherwise specified, the duration of each step is given for a typical laptop (with 16 GB of RAM).

- The first step (and only code-depending step) is to export the ASCII list of cells from the output as described above. *Duration: 2 - 3 minutes.*
- This list is then read to build a given number of lines of propagation (LOP) with a 3D distribution, in the simulation box. From our experience, ~ 3,000 lines are enough to sample a 200 kpc-size AMR simulation box with resolution down to 6 pc. If AMR is used, the lines are first sampled with the highest resolution, and then only one point is kept per AMR cell, in order not to oversample the LOP. A temporary output file containing the density profile is written for each LOP. *Duration: 1 - 2 hours.*
- Density profiles are then re-written to be understandable for Cloudy: the commands defining the ionizing source, computation radii and output parameters are added. Due to Cloudy's maximum number of pairs, LOPs are truncated to 500 pairs of density and depth in the cloud[2]. *Duration: 2 - 3 minutes.*
- The next step is to run Cloudy on each of the 3,000 LOPs. For my thesis, it was done in parallel on the Curie super-computer. Each LOP computation is independent and the "Cloudifications" can be done with less cores if needed. *Duration per LOP on Curie: from a few minutes*[3] *to more than 24 hours*[4].
- Re-run problematic lines, such as truncated LOPs (mentioned above) and lines with large gas density gradients. For the latter, the variations of density are so sharp that Cloudy fails to compute the radiative transfer along the line. Such lines are rare (2 - 3 out of 3,072) and need to be smoothed for the computation to succeed. *Duration: same as above (if needed).*
- To compute the SFR and relative temperature change compared to the initial output, I resampled the "Cloudified" data to the original AMR sampling. This step is not necessary to plot the ionization fraction of hydrogen due to AGN radiation because all gas in the simulation box is assumed to be initially neutral[5].

Further details about the codes I developed for the post-processing method to compute long-range AGN ionization (the so-called "Cloudification") are available in Appendix A.

3.2.2.4 Constraints on thermal AGN feedback

Studying the impact of radiative AGN feedback is useful to get constraints on the modelling of thermal AGN feedback in the simulation. Indeed, the modelling of thermal AGN feedback is still mainly arbitrary because the scale on which energy should be re-injected, and hence the size of the cavity it

---

[2] Such lines are rare (4 - 5 out of 3,072) and need to be relaunched by hand with the end of the profile, if necessary (i.e. if the LOP is not still fully ionized at the 500th pair, in which case it will most likely stay ionized until the end of the line).

[3] For the densest LOPs : the column density above which (or equilibrium temperature under which) gas becomes neutral is reached almost immediately, and the calculation stops.

[4] For the most diffuse LOPs : such lines are fully ionized, and balancing recombination and ionization processes along the whole line takes a long time.

[5] This is not true since most gas in the gaseous halo is likely ionized. A fraction of the gas in the disk is also ionized by stars, supernovæ and the release of thermal energy from the AGN. The information is however not available in the simulation. This assumption does not impact the study because we focused on gas which could be ionized by AGN radiation, if it was not already ionized by something else (see Roos et al., 2015, for further details).

creates, is unknown. The injection region is arbitrarily defined in the simulation to match the size of the smallest cells around the black hole. If the region ionized with the post-processing radiative transfer method was much smaller or much larger than this cavity, this would show that thermal feedback is either too strong or too weak, creating an oversized or undersized cavity.

In this work, the AGN is able to ionize the gas in the entire cavity created by the thermal feedback model, and to keep it ionized. Thus, it suggests that the energy re-injected by thermal AGN feedback at the center of the galaxy spreads to form a cavity whose size is realistic. Though, cautions must be taken because depositing energy into the few central cells has a maximal effect, since the amount of heated gas is small, and thus the heating is more efficient. The cooling time is then longer and the diffuse gas inside the cavity is easier to ionize and to keep ionized (because of the low recombination rate) than the gas around it. This tends to show that the energy might have to be re-distributed in all the cells of the cavity, and not just in the few cells surrounding the black hole, so that the heating is a little less efficient.

3.2.2.5 Advantages and drawbacks of the method

Like most techniques used in astrophysics, the post-processing method presented here has its advantages and drawbacks. Among the advantages, we find:

- Cloudy includes a complete treatment of radiative transfer, as described in Section 2.2;
- the method computes radiative transfer along density profiles with high density contrasts representative of a typical redshift 2 star-forming galaxy, thanks to a high-resolution simulation;
- the ionizing source is matched with observed Seyfert and quasar SEDs on a wide range of wavelengths (from IR to X-rays).

While these advantages allow for a remarkably accurate treatment of the radiative transfer along each line, the method also has several drawbacks:

- LOPs are independent from one another: no shadowing, or scattering between lines can be accounted for. We argue that shadowing and scattering in and out of each line cancel out on the scale of the galaxy;
- Gas is not pushed away by radiative pressure because the method is static. This is problematic since radiative pressure is known to be an efficient mechanism to produce outflows (see Section 2.1.4.2);
- The ionization state of the galaxy is computed instantaneously and results cannot be re-injected from one time-step of the simulation to the other because the process is far too long;
- LOPs must have a common origin: only one ionizing source can be considered, and it needs to be at the center of the system (i.e. not applicable to the stars in the galaxy).

Despite these drawbacks, this post-processing method is useful to constrain and improve simplified sub-grid recipes directly implemented in the simulation codes, such as RAMSES-RT (Rosdahl et al., 2013), or thermal AGN feedback (see previous section).

3.3 Effects of thermal and radiative AGN feedback on star formation

This section includes the article published in the Astrophysical Journal in February 2015 (see Roos et al., 2015). The conclusions of the paper are as follows:

- The AGN affects only diffuse gas in the halo and in the disk (which is heated and/or ionized), but not the dense and cold star-forming gas.
- As dense star-forming gas is mostly left unaffected, the instantaneous SFR reduction due to AGN photo-ionization is less than 4 %, even for a quasar bolometric luminosity of $10^{46.5}$ erg.s^{-1}.
- High density contrasts in the interstellar medium of high-redshift galaxies play a major role in the propagation of AGN radiation: dense star-forming clumps block radiation immediately whereas holes allow it to propagate up to kpc-scale inside the disk.
- Taking into account a typical duty cycle of 1/3 for AGN activity, typical and strong AGNs are not likely to affect star formation on a time scale of a few hundreds of million years. However, an extended period of quasar activity could affect star formation more efficiently.

From these results and from Gabor & Bournaud (2013, 2014), it is therefore argued that normal AGNs (i.e.: not extremely luminous — and rare — quasars) cannot be responsible for galaxy quenching, even though they are indeed a good mechanism to remove gas from galaxies. Nevertheless, the AGN outflows obtained from these simulations — even if their velocities are comparable to observations, do not seem to reach mass outflow rates high enough to explain the “missing baryons problem” (Sommer-Larsen, 2006), i.e. 4 to 5 times the star formation rate of the host.

* * *

The Astrophysical Journal, 800:19 (24pp), 2015 February 10 doi:10.1088/0004-637X/800/1/19

THERMAL AND RADIATIVE ACTIVE GALACTIC NUCLEUS FEEDBACK HAVE A LIMITED IMPACT ON STAR FORMATION IN HIGH-REDSHIFT GALAXIES

Orianne Roos, Stéphanie Juneau, Frédéric Bournaud, and Jared M. Gabor
CEA-Saclay, F-91190 Gif-sur-Yvette, France; orianne.roos@cea.fr

Received 2014 May 28; accepted 2014 November 6; published 2015 February 5

ABSTRACT

The effects of active galactic nuclei (AGNs) on their host galaxies depend on the coupling between the injected energy and the interstellar medium (ISM). Here, we model and quantify the impact of long-range AGN ionizing radiation—in addition to the often considered small-scale energy deposition—on the physical state of the multi-phase ISM of the host galaxy and on its total star formation rate (SFR). We formulate an AGN spectral energy distribution matched with observations, which we use with the radiative transfer (RT) code Cloudy to compute AGN ionization in a simulated high-redshift disk galaxy. We use a high-resolution (∼6 pc) simulation including standard thermal AGN feedback and calculate RT in post-processing. Surprisingly, while these models produce significant AGN-driven outflows, we find that AGN ionizing radiation and heating reduce the SFR by a few percent at most for a quasar luminosity ($L_{\rm bol} = 10^{46.5}$ erg s^{-1}). Although the circumgalactic gaseous halo can be kept almost entirely ionized by the AGN, most star-forming clouds ($n \gtrsim 10^{2-3}$ cm^{-3}) and even the reservoirs of cool atomic gas ($n \sim 0.3$–10 cm^{-3})—which are the sites of future star formation (SF; 100–200 Myr), are generally too dense to be significantly affected. Our analysis ignores any absorption from a putative torus, making our results upper limits on the effects of ionizing radiation. Therefore, while the AGN-driven outflows can remove substantial amounts of gas in the long term, the impact of AGN feedback on the SF efficiency in the interstellar gas in high-redshift galaxies is marginal, even when long-range radiative effects are accounted for.

Key words: galaxies: active – galaxies: high-redshift – galaxies: star formation – ISM: clouds – methods: numerical – radiative transfer

Supporting material: tar.gz file

1. INTRODUCTION

The impact of active galactic nucleus (AGN) feedback on star-forming galaxies (SFGs) remains an open question: contradictory answers are found in both simulations and observations. The amount of energy released by AGNs is theoretically high enough to blow all the gas out of their host galaxies or to maintain the surrounding gas at high temperatures (Croton et al. 2006; Ciotti & Ostriker 1997; Matsuoka 2012). Curran & Whiting (2012) also show that there is always a finite ultraviolet (UV) luminosity above which all the gas in a radio galaxy or quasar host is ionized, up to redshift $\gtrsim$3. This makes AGNs good candidates to quench star formation (SF) through outflows and ionization (“quasar mode”) or through jets (“maintenance” or “radio” mode), which occurs in many simulations (e.g., Sijacki et al. 2007; Martizzi et al. 2012; Dubois et al. 2012, 2013). Simulations also predict that galaxy mergers create starbursts and feed quasi-stellar objects (QSOs), which produce shock waves, expel the interstellar medium (ISM), and prevent it from falling back on the galaxy (e.g., Di Matteo et al. 2005; Hopkins et al. 2006; Li et al. 2007). However, mergers are rare and QSO phases are extreme events, and the gas expulsion depends on the coupling between the AGN and the ISM (e.g., DeBuhr et al. 2011). In contrast, other simulations show that AGN jets can trigger large-scale SF by creating blast waves that compress the gaseous clouds of the interstellar/intergalactic medium (Gaibler et al. 2012; Dugan et al. 2014).

On the observational side, most X-ray selected AGNs up to redshift 3 are located in normal star-forming (main sequence) disk galaxies (Mullaney et al. 2012b) and normal SFGs frequently host an AGN up to redshift ∼1–2 (Mullaney et al. 2012a; Juneau et al. 2013; Rosario et al. 2013), which suggests limited AGN impact on SF, under the assumption that their SF history is steady (Elbaz et al. 2011). Nonetheless, there is evidence for AGNs quenching local elliptical galaxies (Schawinski et al. 2007) or suppressing SF without necessarily quenching it (Karouzos et al. 2014). At higher AGN luminosities, molecular outflows have been observed in local quasars (Feruglio et al. 2010) or ultra-luminous infrared galaxies (Cicone et al. 2014; Veilleux et al. 2013), however, without necessarily affecting the star formation rate (SFR; Spoon et al. 2013). Finally, Keel et al. (2012) observed giant AGN-ionized clouds in low-redshift (mostly) interacting or merging galaxies, which could also impact the SFR of the hosts. On the other hand, there is observational evidence for AGNs triggering SF (e.g., Begelman & Cioffi 1989; Graham 1998; Klamer et al. 2004; Croft et al. 2006; Feain et al. 2007; Elbaz et al. 2009), and some studies show that the hosts of more powerful AGNs have higher nuclear SFR but similar global SFR as those of less powerful AGNs, up to intermediate redshift (Diamond-Stanic & Rieke 2012; LaMassa et al. 2013; Esquej et al. 2014). Finally, Hickox et al. (2014) take into account the rapid variability of AGNs and find that, averaged over a period of ∼100 Myr, *every* SFG hosts at least one active episode and the long-term black hole accretion rate (BHAR) is perfectly correlated with the SFR of the host, reproducing the observed weak correlation between the AGN luminosity and the global SFR. A plausible explanation for this apparent discrepancy (both in simulations and observations) in the role of AGN feedback in SF would be that AGN feedback works both ways depending on the current accretion mode (Zinn et al. 2013) and on the timescale considered.

To determine if AGN feedback can reduce SF, we need to know whether the gas expelled and/or ionized would have formed stars in the absence of an AGN. In this paper, we will focus on the impact of thermal and radiative AGN feedback on the physical state of the gas and therefore on its ability to form stars in a simulation representative of a high-redshift star-forming disk galaxy from Gabor & Bournaud (2013).

AGN feedback is often implemented in simulations in the form of local (at the resolution scale) deposition of energy (see Wurster & Thacker 2013 for a comparison of five models of AGN feedback). It has recently been shown that such AGN feedback creates outflows without impacting the disk (e.g., Gabor & Bournaud 2014). However, due to the lack of resolved small-scale observations of those mechanisms at high-redshift, the recipes remain quite arbitrary and do not have strong constraints on the scale at which energy should be re-injected.

Until now, long-range effects of AGN radiation are rarely included because simulations cannot afford both high resolution and a complete treatment of the radiative transfer (RT) due to the cost in terms of computational time and memory. For instance, Vogelsberger et al. (2013, 2014), in their simulation Illustris, use the moving-mesh code AREPO to treat cosmological simulations including standard AGN and stellar feedback plus a prescription for radiative electromagnetic AGN feedback. Also, Rosdahl et al. (2013) implemented RT into RAMSES (RAMSES-RT). However, the resolution of the ISM structure of a galaxy is degraded, and effects of ionization on small-scale structures such as giant molecular clouds (GMCs) cannot be considered. The effect of long-range AGN radiation may, however, have a great impact on the structure of the ISM since most of AGN radiation is emitted in the optical, UV, and X-ray wavelengths and is able to heat and/or ionize the surrounding ISM, which could change the physical properties of the clouds (Proga et al. 2014). Furthermore, the fraction of ionizing photons emitted by the AGN that remains trapped in the ISM depends on the distribution of the gas into clumps (Yajima et al. 2014) and could in return change the properties of the ISM (Maloney 1999) and of the AGN-driven winds (Dove et al. 2000). Many authors already attempted to predict such effects with simple models (see Section 2.3), but due to the complexity of the ISM in a real galaxy and the broad wavelength range of observed AGN spectra such models are not sufficient and RT calculations need to be performed.

To do that, we post-process the results of our high-resolution simulation with a complete treatment of the RT and study the large-scale effect of AGN ionization on SF. Therefore, we are not able to treat coupling to longer-term dynamical effects, but the ISM structure of the high-redshift disk galaxy allows us to probe which ISM phases can be impacted as a function of the AGN luminosity. While it is known that very diffuse gas ($n \lesssim 10^{-3}\,\mathrm{cm}^{-3}$; e.g., in the circumgalactic medium) can be entirely ionized by an AGN, and dense gas ($n \gtrsim 10^{2-3}\,\mathrm{cm}^{-3}$) is self-shielding (Liu et al. 2013a), the impact of AGN radiation on other gas phases, such as atomic gas ($n \sim 0.3$–$10\,\mathrm{cm}^{-3}$; which will form stars on a timescale of a few hundreds of Myr), has not been studied extensively. Moreover, the effects of a clumpy distribution of gas inside a dense galactic disk on the propagation of AGN radiation are hard to determine with a simple model. In Section 2, we describe the galaxy simulation and our method to predict the distribution of the gas photoionized by the AGN in the galaxy. Section 3 shows maps of heated/ionized gas and star-forming regions, total reduction of SFR, and fractions of the total mass and volume of the gas that is heated/ionized by the AGN. Finally, in Section 4 we study the dependence of the SFR reduction on the structure of the ISM, give clues about long-term effects on SF, and the typical size and density of ionized regions. Finally, we try to account for other sources of ionization (e.g., stars, UV background). Our conclusions are in Section 5.

2. METHOD

Using radiative transfer calculations applied in post-processing to a high-resolution simulation of an isolated disk galaxy, we study the effects of photoionization by an AGN on the ISM. Our procedure allows us to quantify the impact of AGN radiation on the SFR of well-resolved star-forming clouds in the galactic disk. In this section we describe the hydrodynamic galaxy simulation, the AGN SED used as the only ionizing source (hypothesis discussed in Section 4.4), and the radiation transfer procedure.

2.1. Sample of Simulated Galaxy Snapshots

The simulation, described fully by Gabor & Bournaud (2013), is an unstable clumpy disk representing an isolated $z \sim 2$ disk galaxy with a well-resolved ISM (see, e.g., Elmegreen et al. 2008 for a comparison of such clumps with observations). Such clumpy galaxies are predicted to efficiently fuel their central black hole (BH), resulting in frequent active phases (Bournaud et al. 2011), which is observationally supported up to intermediate redshift (Bournaud et al. 2012). The simulation is a cube of 50 kpc length using the adaptive mesh refinement (AMR) code RAMSES (Teyssier 2002).

Stars, gas, and dark matter are included. The total baryonic mass is $4 \times 10^{10}\,M_\odot$, and the gas fraction is initially set to $\sim$50%. A cell is refined if its mass exceeds $6 \times 10^5\,M_\odot$, if there are more than 30 dark matter particles in the cell, or if the Jeans length is not resolved by at least four cell widths (Truelove et al. 1997). The maximal resolution of the simulation, taken as the size of the smallest cells, is about 6 pc. Thus, GMCs, where stars are supposed to form (Waller et al. 1987), are resolved. SF is allowed for cells denser than $100\,m_H\,\mathrm{cm}^{-3}$ (see Appendix C for discussion) and colder than $\sim 10^4$ K (Renaud et al. 2012). A thermal model for supernova (SN) feedback is included (see Gabor & Bournaud 2013 for details). The distribution of clouds in the simulation depends on the numerical noise and is therefore stochastic. Furthermore, SF contains a random module for the mass distribution of new stars, which will affect the mass, shape, size, and movements of the clumps. Nevertheless, the simulations used all have the same statistical behavior since they have the same probability density function (PDF) and power spectrum density (PSD) for gas density.

AGN feedback is twofold: gas is heated, diluted, and pushed away by the AGN directly in the simulation (thermal AGN feedback) and RT is added afterward in six successive snapshots of the simulation (AGN photoionization), using version 13.02 of Cloudy (last described by Ferland et al. 2013) to study the large-scale effect of AGN ionization on SF. Thermal AGN feedback is based on Booth & Schaye (2009) and consists of local (10 pc scale) energy re-deposition at a uniform pressure if it is sufficient to heat the gas to an average temperature of 10^7 K, otherwise energy is stored until the next time-step. Corrections to this method were added to prevent too high energy storage when the BH is embedded in very dense clumps. The maximum temperature allowed in the region where energy is re-deposited by the AGN is 5×10^9 K. In the very infrequent case when this maximum temperature is reached, the radius of the re-deposition region is enlarged by a factor of 1.25 until the temperature drops below the maximum temperature. When this happens, the radius is multiplied by a factor $\lesssim 2$ on average. These prescriptions

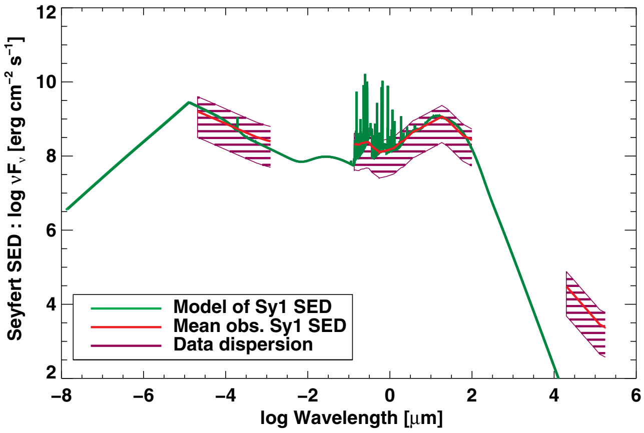

Figure 1. AGN SED model of the emission arising from the vicinity of a Seyfert 1 nucleus (i.e., AGN, dust, and BLR clumps; in green). The red curve is the mean observational Seyfert 1 SED taken from Prieto et al. (2010), and the dark hatched area is the data dispersion.

Table 1
Properties of AGN Luminosity Regimes

Regime	Luminosity	Frequency	BHAR/SFR	$r_{\rm ion}$
Typical AGN	$10^{44.5}$	∼30%	1.7×10^{-3}	20–60
Strong AGN	$10^{45.5}$	∼3%	1.7×10^{-2}	50–120
Typical QSO	$10^{46.5}$	Rare	1.7×10^{-1}	100–260

Notes. Bolometric luminosity in erg s^{-1}. Values are given for $10^{10} < M_* < 10^{11}$ $M_\odot$ typical SFGs. BH accretion rates (BHARs) are derived from the formula given by Mullaney et al. (2012a). $r_{\rm ion}$ is the predicted Strömgren radius in parsecs and was derived from the calculation used by Curran & Whiting (2012) for gas at 10^3 cm^{-3} and 20 or 2000 K respectively.

only apply to the very central region (10 pc scale) of the galaxy and do not directly impact the large-scale gas structure and SF in the intermediate and outer regions of the disk (see Section 2.2.2 of Gabor & Bournaud 2013 for details).

The simulation shows high-velocity AGN-driven outflows, with mass outflow rates between about 10% and 100% of the SFR of the galaxy (∼30 $M_\odot$ yr^{-1}). These outflows are mostly hot and diffuse and do not impact large scale (>100 pc) SF within short (10–20 Myr) timescales (Gabor & Bournaud 2014).

We used two runs of the simulation with the same initial conditions, which develop a clumpy irregular ISM structure. The runs are identical until AGN feedback is shut down in one of them. This moment is defined as $t = 0$. After that, both runs evolved separately. SN feedback remains in both runs. A series of six pairs of successive snapshots was studied, ranging from $t = 0$ to 88 Myr. Among all the snapshots studied, the maximum number density of hydrogen is ∼10^6 cm^{-3} due to both the spatial resolution and the temperature floor. Ionization was added to the snapshots of the simulation including AGN feedback, and the corresponding snapshots of the simulation with no AGN feedback were used to measure an uncertainty on the SFR. The ionization calculation is done on static snapshots of the simulation, and therefore the effect we see is instantaneous and indicates in which phases of the ISM the AGN radiation is absorbed and whether it reaches high-density star-forming regions.

2.2. *Realistic Seyfert SED*

To study the effects of AGN radiation on the surrounding gas, we first require a realistic source spectral energy distribution (SED). In this work, we span a large range of wavelengths (from far-infrared (FIR) to X-rays), and match observational data in the wavelength domains of interest for this study. Hence, several bands of ionizing photons are taken into account (X-rays, extreme-UV (EUV), UV), rather than a simple power-law model. We formulated such an AGN SED for use in Cloudy, as shown in Figure 1. The so-called AGN spectrum used in the study is composed of radiation from the AGN itself (accretion disk and corona) but also takes into account the emission of dust and clumps surrounding the AGN, which are not resolved in our simulation. The input spectrum is described in more detail in Appendix A. It was adjusted to the observational mean SED of the inner region of Seyfert 1 galaxies described by Prieto et al. (2010).

We chose to model the AGN spectrum of an unobscured (Type 1) Seyfert galaxy, i.e., the spectrum coming out of the central region seen face-on. The AGN radiation is propagated isotropically—we neglect the partial absorption of UV and X-ray photons by a dusty torus that would occur according to the Unified Model (Urry & Padovani 1995). We make this assumption because the geometry and orientation of any such torus is unknown, and there are currently not enough resolved observations to be confident about them (Sales et al. 2014; Ricci et al. 2014a, 2014b). Consequently, our results are upper limits to the instantaneous impact of AGN radiation on SF in high-z disk galaxies—including an obscuring torus would only decrease the amount of ionizing radiation emitted into the ISM.

We note here that the FIR part of the spectrum does not match the observations. Nonetheless, those photons are not of a great interest in this study because they cannot ionize gas. We also verified that the presence of emission lines in the broad-line region (BLR) spectrum did not affect our further results.

The normalization of the SED we used to perform the analysis is set to explore three luminosity regimes, as shown in Table 1. The bolometric luminosities are not related to the AGN luminosity inferred from the BHAR in the simulation and we analyze the effects of each luminosity separately. The lowest luminosity regime corresponds to the typical bolometric luminosity observed for an AGN in a $10^{10} < M_* < 10^{11}$ $M_\odot$ normal SFG, which is of a few 10^{44} erg s^{-1} at a redshift of ∼2 (Mullaney et al. 2012a). Such AGNs are hosted by roughly 30% of the standard main-sequence galaxies in the same mass range (Mullaney et al. 2012b; Juneau et al. 2013). The second luminosity we used is reached by ∼10% of all AGNs (Mullaney et al. 2012b), which are hosted by ∼3% of the SFGs. The last luminosity we studied corresponds to a QSO, which is quite uncommon in normal star-forming disks.

Mullaney et al. (2012a) show that typical AGNs up to redshift ∼2 have an average BHAR to SFR ratio of $\lesssim 10^{-3}$. Considering the same definition of the BHAR:

$$\dot{M}_{\rm BH} = (1 - \epsilon)\frac{L_{\rm bol}}{\epsilon c^2}, \qquad (1)$$

where $L_{\rm bol}$ is the bolometric luminosity of the AGN, c is the speed of light, ϵ is the radiative conversion efficiency set to 0.1 (Merloni 2004; Marconi et al. 2004); and an average SFR of 30 $M_\odot$ yr^{-1} for the simulation. We find that our lower-luminosity regime has a BHAR to SFR ratio roughly corresponding to the observed average. The middle- and higher-luminosity regimes are respectively 10 and 100 times above (see Table 1), which is consistent with them being less frequent.

As QSOs and lower-luminosity AGNs do not have the same SED shape, a radio-loud quasar-matched SED was also formulated, using the Elvis et al. (1994) mean SED as a reference. The results are insensitive to the choice of the SED, and therefore we used the Seyfert spectrum in all luminosity regimes. We note here that even more luminous quasars have been observed (e.g., Stern et al. 2014) but since they are even rarer than the QSOs we studied, they might not impact normal star-forming disk galaxies in general.

2.3. *Expectations from Simple Models*

Several simple models have been introduced by many authors to infer the effects of AGN radiation on their host galaxies. Some of them are addressed here. For instance, according to Proga et al. (2014), in optically thin clouds dominated by absorption opacity, radiation propagating through gas at constant density and pressure will uniformly heat the cloud, which will uniformly expand but will not be accelerated whereas for optically thin clouds dominated by scattering opacity, the radiation will uniformly accelerate the cloud away from the emitting source, without changing its size or shape, and inducing no mass loss. On the other hand, when a cloud is optically thick and is exposed to weak radiation, only a thin layer on the irradiated part of the cloud will be heated, inducing a slow mass loss. They find that BLR clouds—which are very dense ($\sim 10^9$ cm^{-3}; Matews & Capriotti 1985), typically become optically thin in less than a sound-crossing time, are weakly accelerated, and that their structure, shape, and size change before they can travel a significant distance. A realistic ISM made of dense clumps and diffuse interclump medium would be a complex combination of the above trivial cases and RT needs to be treated in order to determine the impact of AGN irradiation on such a realistic multi-phase ISM.

As another example, Curran & Whiting (2012) have shown that a UV luminosity of $L(1216\ \text{Å}) \sim 10^{23}$ W Hz^{-1} = 10^{30} erg s^{-1} Hz^{-1} is able to ionize the cold neutral medium with gas densities typical of GMCs ($n \sim 10^3$ cm^{-3}), up to ∼50–100 pc in the galactic disk, around the BH. For our three AGN luminosity regimes, we find $L(1216\ \text{Å}) \sim 10^{29}$, 10^{30}, and 10^{31} erg s^{-1} Hz^{-1} respectively. If we were using a constant density of 10^3 cm^{-3}, we would thus expect the ionization front to be located at the sub-kiloparsec scale around the BH for gas temperatures between 20 and 2000 K (see Table 1).

Finally, a simple calculation of the optical depth in the UV gives an even lower value of this radius: if the UV opacity is $\sim 10^3$ cm^2 g^{-1} (Cayatte et al. 1994; Schaye 2001), the critical value of the column density above which the gas becomes self-shielding is 10^{-3} g cm^{-2}. In this case, if the inner region close to the BH is at a uniform density of 10^3 cm^{-3}, the UV emission is expected to be blocked within the first ∼0.2 pc.

However, these models are valid in idealized conditions such as smoothed galactic profiles or single-band AGN SEDs. In this study, we demonstrate the effect of a broad observationally-matched AGN spectrum, coupled to AGN-driven winds, on a realistic multi-phase distribution of the ISM. Applied to a disk galaxy with turbulent multi-phase ISM, these predictions of the ionization radius can vary by an order of magnitude since most of the gas volume in our high-resolution clumpy ISM has a density low enough not to be opaque to AGN radiation, while a few dense clumps are able to completely block the radiation—which can significantly change the escape fraction of photons emitted by the AGN.

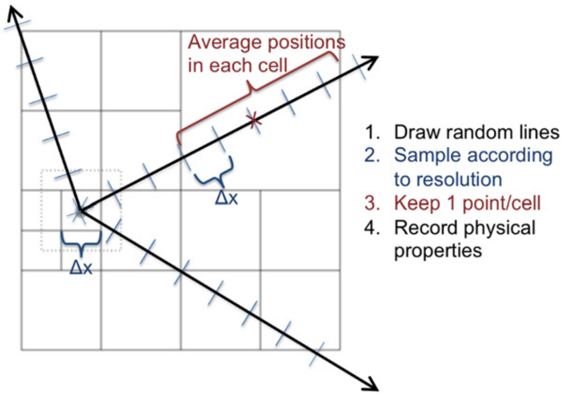

Figure 2. Sketch illustrating the procedure to create the LOPs in the AMR box. First, random lines are cast in the simulation box, from the location of the BH. They are then sampled with points separated by the size of the smallest cells. The positions of all points inside a given cell are averaged in order to keep only one point per cell and per LOP. For each point, relevant physical properties (gas density, temperature, etc.) are recorded. This figure is based on the sketch in the FLASH Users' Guide (ver. 4), from J. B. Gallagher.

Nonetheless, to account for dynamical effects such as mass loss or radiative pressure pushing clouds away, RT calculations need to be performed during the simulation, which is not the purpose of our post-processing treatment. However, the comparison between complete radiative treatment in post-processing and simplified but dynamical RT could help improve both methods, by developing accurate subgrid models.

2.4. *Ionizing the Simulated Galaxy*

We estimate the effects of AGN photoionization on the gas in the simulated galaxy under the assumption that our AGN SED emerges isotropically from the location of the BH. We cast about 3000 lines of propagation (LOPs) in all directions outward from the BH, and calculate the RT along each LOP independently using Cloudy, a code designed to compute the RT and the atomic and molecular chemistry along one-dimensional lines.

2.4.1. *LOP Building*

The first step of our analysis is to build the LOPs, as illustrated by the sketch in Figure 2. For each snapshot, LOPs are distributed as follows. The simulation box is sampled with 512 LOPs randomly cast into the entire box, plus 512 randomly cast LOPs restrained into the 30° half-opening angle cone of revolution perpendicular to the disk. In addition to that, the plane of the galactic disk is sampled with 512 randomly cast LOPs (see Figure 3(a), right). Finally, two arbitrary planes of the simulation box, perpendicular to the galactic disk, are sampled with 768 LOPs each (see Figure 3(a), left, for one of these planes with its 768 LOPs). A third of these lines is cast randomly into the entire plane, another third in the projection of the cone on the plane, and the remainer into the galactic disk. All points of a given LOP are initially separated by the size of the smallest cells (see Figure 2). As shown on the sketch, the positions of all points inside a given cell are then averaged so that only one LOP point is kept per cell and per LOP. For each LOP point, all relevant physical properties (gas density, temperature, etc.) are recorded. The hydrogen number density (hereafter, density) of the cell and its distance to the BH are used to build the density profile along each LOP (see Figure 4 for two examples).

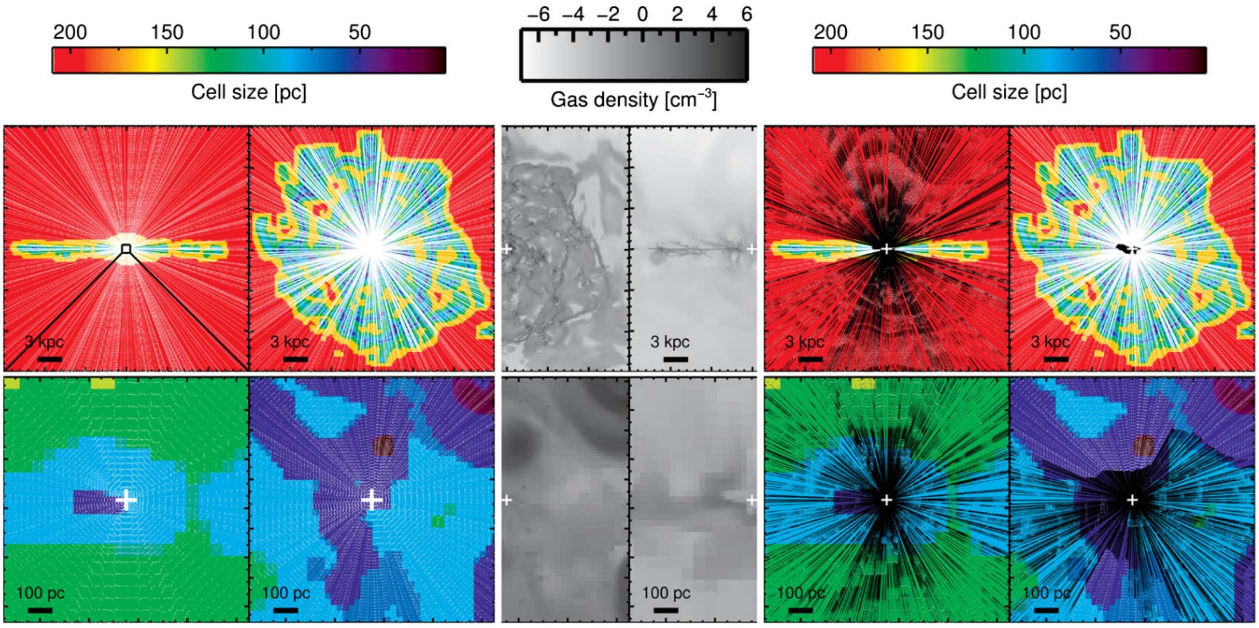

(a) (b) (c)

Figure 3. (a) Large (top row) and zoomed-in (bottom row), edge-on (left column), and face-on (right column) views of the simulated galaxy showing the size of the cells. The points (white dots) of the LOPs located in each plane are superimposed. The sampling is that before propagating the AGN radiation with Cloudy. The white cross shows the location of the BH. Thanks to the mass refinement criterion, substructures are well sampled (see (b)). (b) Comparison with the mass-weighted density maps. The views and zooms are the same, but only half of each map is displayed, for comparison with the maps located on the cropped side. Small AMR cells trace substructures (see Section 2.1). (c) Same key as (a). During the computation, Cloudy resamples the LOPs according to LTE zones. The original AMR LOP is sampled with lower density where the physical conditions are alike, whereas it is sampled with higher density where AGN radiation induces significant and rapid changes. The computation stops when the temperature drops under 4000 K (roughly where there are no more ionizing photons left) or at the end of the line. The Cloudy sampling (black) is superimposed to the original one (white). For the LOP regions located past the point where Cloudy stopped, the original sampling is used. The Cloudy sampling depends on the AGN luminosity. Here, we show that of the typical AGN regime ($L_{\mathrm{bol}} = 10^{44.5}$ erg s^{-1}).

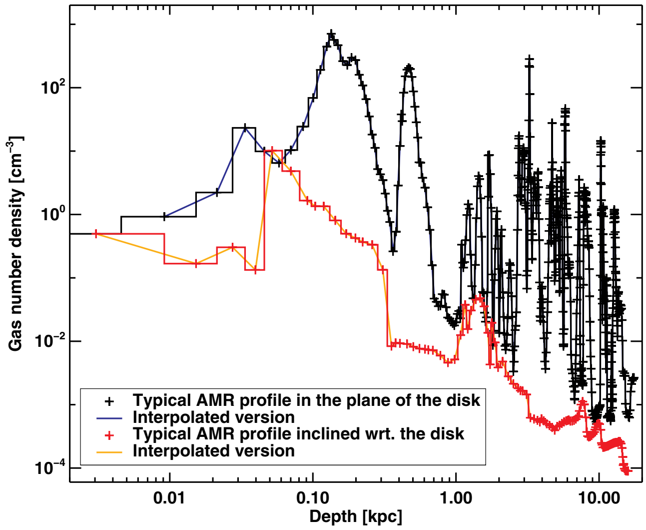

Figure 4. Example of a typical density profile in the plane of the disk (black and dark blue) and outside the plane of the disk (red and orange). The histogram lines (black and red) show the discrete AMR profiles. The lighter (dark blue and orange) curves are the interpolated profiles used in Cloudy. Typical profiles show high density contrasts between the clumps and the interclump medium.

2.4.2. *Cloudy Computations*

Before computing the RT, Cloudy interpolates the discrete density profile coming from the AMR simulation to get a continuous profile (see Figure 4). By comparing the size of the cells (Figure 3(a)) to their density (Figure 3(b)) and from the typical LOP profiles (Figure 4), we know that substructures, namely GMCs, are well sampled along the lines.

The Cloudy computation occurs on a static snapshot and the density profile does not change during the RT computation. The calculation stops either when the computed temperature along the line drops under 4000 K, meaning that the rest of the line is not affected by the ionizing source, or at the end of the line, in which case the line is totally ionized.

When calculating the one-dimensional RT along a single LOP, Cloudy treats the system as a spherically symmetric set of concentric shells (or zones), centered on the ionization source. These zones are dynamically determined with a local thermal equilibrium (LTE) criterion. Thus, the sampling of each line changes during the process and depends on the AGN luminosity (see Figure 3(c) for the sampling at the end of the process for the typical AGN regime): the LOPs are sampled with higher density in regions where AGN radiation induces significant changes, while they are sampled with lower density where the physical properties are similar. The LOP regions where the Cloudy calculation did not occur (because the equilibrium temperature is below 4000 K) keep the initial sampling.

In each zone, ionization processes (photo-ionization, collisions, charge transfer, etc.) and recombination processes (radiative and charge transfers, etc.) are balanced to compute the propagation of radiation along a given LOP, according to the input hydrogen number density profile, filling factor, and radiation source, and gives the resulting SEDs and physical conditions (Ferland et al. 2013). The filling factor is set to 0.2 and accounts for the multi-phase gas distribution along the two other spatial dimensions in the sphere. In each sphere, the flux of the ionizing source is proportional to the inverse square of the distance to the source. To rebuild the galaxy, all computations are assembled using only the radial dependence, and interpolated. This pseudo-three-dimensional ray-tracing approach is similar to that used in Cloudy_3D (Morisset 2006), now re-written in Python and renamed pyCloudy (Morisset 2013). The reflection and scattering between two neighboring LOPs are not considered explicitly. We assume that those phenomena are reproduced on average for the whole galaxy, since reflection and scattering are taken into account inside each individual sphere.

Lastly, the initial temperature along the lines is not used for the calculation, and the gas is considered initially neutral. We do not include the SNe and the UV background in the ionization process. However, they are implemented in the simulation, and from the value of the initial temperature in the cells, we know that they heat the halo and some regions in the disk: gas at $T > 10^6$ K is likely to be ionized and some of the 10^{4-5} K gas is possibly ionized. Such regions could then be transparent to AGN radiation. A test study on a series of LOPs shows that the transparency of such diffuse gas that could be already ionized by other sources has no impact on the effect of AGN radiation on SF (see Section 4.4). Thus, transparent gas is conservatively neglected in the main study. Considering that the gas is initially neutral allows us to study the effect of AGN photo-ionization alone and confront our model of thermal feedback to the ability of the AGN to ionize gas. Here, as the AGN is able to ionize the cavities created by winds entirely, we assume that our model of AGN feedback (thermal + RT) is self-consistent.

2.4.3. Output Parameters for a Given Cell

Temperature. The final temperature of a given cell containing at least one Cloudy point is defined as the maximum between the average equilibrium temperature of the Cloudy points in the cell (corresponding to the temperature gas would reach if it was not externally re-heated), and the initial temperature of the cell.[1] For the points where the computation did not occur (because the temperature on the line dropped under 4000 K), the assumed temperature is the initial temperature. The latter is not necessarily equal to the equilibrium temperature given by Cloudy because gas is constantly heated by thermal AGN and stellar feedback in the simulation. The instantaneous relative temperature change is defined as:

$$\mathrm{RTC} = \frac{T_{\mathrm{final}} - T_{\mathrm{initial}}}{T_{\mathrm{initial}}}, \tag{2}$$

where T_{initial} is the initial temperature of the cell in the simulation (before RT), and T_{final} is the final temperature of the cell defined above. Regions with RTC $< 1\%$ (or $T_{\mathrm{initial}} \leqslant T_{\mathrm{final}} < 1.01 \times T_{\mathrm{initial}}$) are considered not heated.

Star formation rate. A cell is star-forming and has a non-zero value of the SFR if its temperature is below 10^4 K and its density is above a threshold of 10 $m_H\,\mathrm{cm}^{-3}$ (hereafter, m_H will be implicitly assumed). This value distinguishes diffuse gas and dense star-forming clumps and is chosen arbitrarily and independently of the density threshold in the simulation. It is varied in Appendix C. The SFR in each cell i is computed according to the Schmidt–Kennicutt law (Kennicutt 1998) :

$$\mathrm{SFR}_i = \epsilon \sqrt{\frac{32\,G}{3\pi}} \rho_i^N V_i \quad \text{if } T_i < T_{\mathrm{thr}} \text{ and } \rho_i > \rho_{\mathrm{thr}}, \tag{3}$$

where ρ_i is the mass density of cell i, V_i its volume and T_i its temperature before or after RT. The Kennicutt index N is equal to 1.5 and the efficiency ϵ is 1%. T_{thr} and ρ_{thr} are respectively the temperature and density thresholds for SF defined above. The SFR per cell is limited to a maximum value, computed to account for the fact that molecular clouds generally do not turn more than 30% of their gas into stars during their ~10–100 Myr lifetime (Matzner & McKee 2000; Elmegreen 2002; Renaud et al. 2012). The final SFR of the simulated galaxy is the sum of the individual values—interpolated as described below, and is compared: (1) to the initial SFR of the simulation including AGN feedback, (2) to the SFR of the reference simulation, where AGN feedback is shut down. Option (1) allows one to measure the impact of ionization feedback alone, while option (2) allows one to measure the impact of all types of AGN feedback on the SFR.

Neutral fraction of hydrogen. As for the temperature, the fraction of neutral hydrogen in a given cell is defined by averaging the values of all LOP points inside the cell. LOP regions where RT did not occur are assumed to be neutral. A cell is considered ionized if the neutral fraction of hydrogen is smaller than 10%. The fraction of neutral hydrogen, unlike temperature, does not take into account the other heating/ionizing sources (such as stars).

2.4.4. Interpolation onto the Simulation Box

About 3000 LOPs were cast in the simulation box. Even though the box is relatively well covered with LOPs, and due to the Cloudy resampling in LTE zones, all AMR cells in the snapshots do not necessarily contain a LOP point. Thus, values of the physical properties output by Cloudy (temperature, ionization fraction, etc.) need to be interpolated in order to apply to the whole simulation box.

We use the fact that the Jeans length has to be resolved by at least four neighboring cells in the simulation (see Section 2.1)—and therefore their properties are alike—and assume all cells containing no LOP point neighboring a processed cell[2] within a radius of four times the cell size have the same output parameters. With this method, 20% of the total number of cells for each snapshot—equivalent to 20% of the total gas mass in the simulation box (galaxy and gaseous halo)—have known post-RT physical properties. We call these cells "four neighboring cells".

To get the values of the physical properties for the entire grid of the simulation, the properties of the "four neighboring cells" are corrected with respect to the joint histogram of density and cell size. We assume that cells at a given density and a given radius in the galactic disk or gaseous halo are similarly affected by the AGN. Due to the geometry of the simulated galaxy (a disk with a vertical exponential density profile in a diffuse gaseous halo) and the mass criterion of the refinement, the size of the cells (see Figure 3(a)) increases when going away from the galactic disk. This naturally ensures a good sampling of the outer gaseous halo, since fewer LOPs per unit angle are needed to cross larger cells. In a few cases, some density bins are not sampled by the "four neighboring cells" criterion, which is enlarged to eight neighboring cells.

---

[1] If the RT calculation returns a lower temperature, it means that a mechanism other than AGN photoionization (e.g., UV background, SNe, compressive motions, etc.) is already heating the gas at a temperature higher than what the AGN ionization can provide and so these other sources will dominate.

[2] A cell containing either one (or more) LOP point(s) where the Cloudy computation occurred, or one point from LOP regions where the Cloudy computation stopped before the end (because there was no further effect of the ionizing radiation). Two percent of the cells (in mass and in number) contain at least one Cloudy point.

3. RESULTS

The aim of this work is to switch on the AGN located at the center[3] of the simulated galaxy, probe how far gas is ionized by the AGN and whether many star-forming regions are heated and/or ionized and prevented from forming stars. In this section, we compare the ionization, temperature, and SFR of the gas before our RT calculations to those after the RT calculations for the three AGN luminosity regimes presented in Section 2.2.

3.1. Maps of the Ionized Galaxy

After propagating AGN radiation throughout the galaxy, the ionization state of the gas and its new temperature are known, and the new SFRs are computed for all cells. Gas density is the same before and after RT (see Section 2.4). Figures 5 and 6 show edge-on and face-on views of a representative snapshot, and zooms on the central regions are displayed in Figures 7 and 8. Each map is a thin slice of the simulation box, centered on the BH. The maps for some other snapshots are available in Appendix B.

We will first focus on the effect of the lowest AGN luminosity on the galaxy, namely the first two columns of each figure. The impact of the higher luminosities are discussed in next section. The ionization panels of the disk seen edge-on at both large (Figure 5) and small (Figure 7) scales show that the AGN radiation escaping the galaxy has a typical bi-conical shape, as observed by Müller-Sánchez et al. (2011; see Section 4.3 for discussion).

In the central region of the disk, gas at densities of about $10^{1-2}\,\mathrm{cm}^{-3}$ is heated by roughly a factor of 10, though the effect is invisible at a kiloparsec scale. Dense clumps are only slightly heated on the illuminated side but shield themselves and the material behind them. At approximately 500 pc around the BH in the disk, even directly illuminated diffuse gas is not impacted. In the upper outer part of the gaseous halo, and in some diffuse spots above and under the disk, very diffuse gas (10^{-3}–$10^{-6}\,\mathrm{cm}^{-3}$) is relatively inefficiently heated (RTC $<$ 10%) by the AGN. These outer heated regions relatively resemble the upper outer part of the ionization cone. It is, however, important to note that a complete “temperature cone” similar to the ionization cone does not appear here since the measurement of the final temperature takes into account the initial temperature in the simulation (in which gas is already heated by thermal AGN and SN feedback, etc.), whereas ionization is only based on the RT due to the AGN radiation (which assumes the gas was previously neutral, see Section 2.4). We therefore see that the effect of AGN heating dominates the other kinds of feedback only in the outer parts of the halo or in diffuse regions around the galactic disk near the BH.

Finally, only a thin layer (up to ∼40 pc for $10^{1-2}\,\mathrm{cm}^{-3}$; ∼15 pc for $10^{2-3}\,\mathrm{cm}^{-3}$) on the illuminated side of the star-forming regions is heated above the temperature threshold, and most of the ionized regions were not initially forming stars anyway. The remaining star-forming regions shield themselves from the radiation starting approximately at $10^3\,\mathrm{cm}^{-3}$. Around 100 pc away from the BH, even the diffuse star-forming regions remain. The density threshold for SFR is $10\,\mathrm{cm}^{-3}$, but more diffuse clumps would not be self-shielding from the AGN radiation and would contribute negligibly to the total SFR of the galaxy (see discussion in Appendix C).

All snapshots (see Appendix B) show roughly the same behavior, except 6, where the BH is embedded into a very dense clump of gas ($n \sim 10^{4-5}\,\mathrm{cm}^{-3}$). In this case, AGN radiation is blocked within the central clump and regions that could be affected by the AGN are below the resolution limit. Snapshot 3 shows both behaviors since a dense clump just above the BH blocks the radiation above the disk, but not on the other side. Thus, the distribution of the gas into clumps has an important impact on the propagation of the AGN radiation, sometimes preventing it from escaping at all.

3.2. Dependence on AGN Luminosity

In this section, we investigate the effect of increasing AGN luminosities (right two columns of Figures 5–8). As expected, the higher the luminosity, the more extended the ionized and/or heated regions, and the more star-forming regions are suppressed.

In the halo, diffuse gas at $10^{-6}\,\mathrm{cm}^{-3}$ and 10^5 K is heated at 10^6 K in the standard AGN regime and at $10^{6.5}$ and 10^7 K in the strong AGN and QSO regimes. On a small scale in the disk, $10^{1-2}\,\mathrm{cm}^{-3}$ gas is heated from 10^{3-4} to 10^{4-5} K in the normal AGN regime, at approximately 500 pc around the BH. Denser gas or gas located further in the disk is not heated. In the strong AGN regime, gas with the same density and temperature is also heated, but to a higher degree ($10^{4-5.5}$ K) and further away from the BH (up to ∼1 kpc). In the QSO regime, the effect is even more important: diffuse 10^{3-4} K gas is heated to $10^{4-6.5}$ K, within up to ∼10 kpc around the BH, thanks to the diffuse interclump medium allowing the QSO radiation to go past the inner kiloparsec. However, the densest clouds ($>10^4\,\mathrm{cm}^{-3}$) are not heated and shield the gas behind them. The clumpy distribution of gas in the ISM is responsible for the high variability of the maximal radius at which gas is heated by the AGN in the disk, which cannot be probed with smooth density profiles.

As AGN luminosity increases, star-forming regions are suppressed further from the BH. In the strong AGN regime, diffuse star-forming regions close to the BH and not shielded by dense clumps are destroyed up to 300 pc away in the disk. In the QSO regime, this distance increases to 1 kpc and only the $n > 10^3\,\mathrm{cm}^{-3}$ star-forming regions survive at the center. However, most of the SFR lies in the densest star-forming clouds, which are not affected by the AGN radiation.

Snapshot 6 (AGN embedded in a dense clump; see Appendix B) shows a more extreme behavior. Even if AGN radiation escapes the central clump and an ionization cone is visible in the strong AGN and QSO regimes, the reduction of SFR is nearly zero whatever the luminosity of the AGN. This, once again, shows that the gas ionized is mainly not initially star-forming, even at high AGN luminosities.

The idea that star-forming gas is mostly left unaffected even in the strong AGN and QSO regimes is also well presented by the temperature versus relative temperature change diagrams (see Figure 9). The temperature represented is the initial temperature (before RT) and only the gas in the central region of the box—defined as the cylinder of radius 2 kpc and height 4 kpc centered on the BH, is shown. All cells with RTC $<$ 1% are considered not heated and are shown in the first bin ($\log \mathrm{RTC} = -2$). The demarcation line between gas forming stars before RT and remaining below the temperature threshold

---

[3] As the central BH of the galaxy slightly moves during the simulation (Gabor & Bournaud 2013), we use the exact position of the BH particle of the simulation, not the geometrical center of the simulation box.

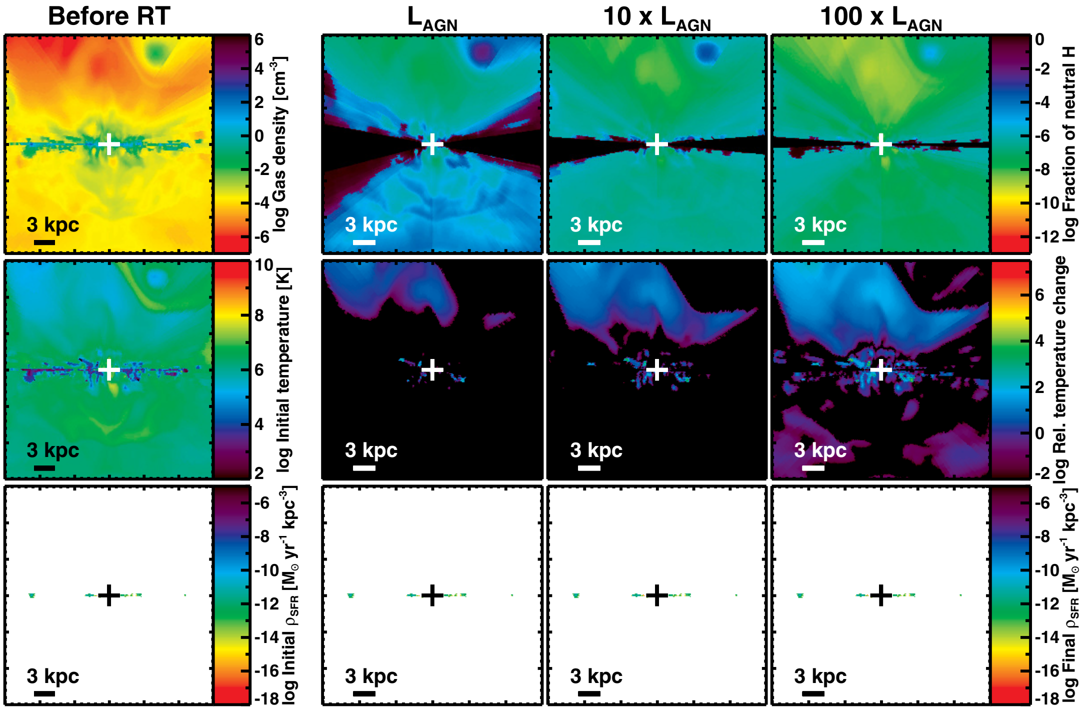

Figure 5. Large edge-on view of the simulated galaxy (snapshot 2). Top row: hydrogen density, fraction of neutral hydrogen after RT. Middle row: temperature before RT, relative temperature change. Bottom row: ρ_{SFR} before RT, ρ_{SFR} after RT. The "+" sign shows the location of the BH and the density threshold for SF is $10\,\mathrm{cm}^{-3}$. Parameters after RT are given for the three AGN luminosities ($L_{\mathrm{AGN}} = 10^{44.5}\,\mathrm{erg\,s}^{-1}$). AGN ionization and heating are more visible in the halo and in diffuse regions surrounding the galactic disk, as AGN luminosity increases.

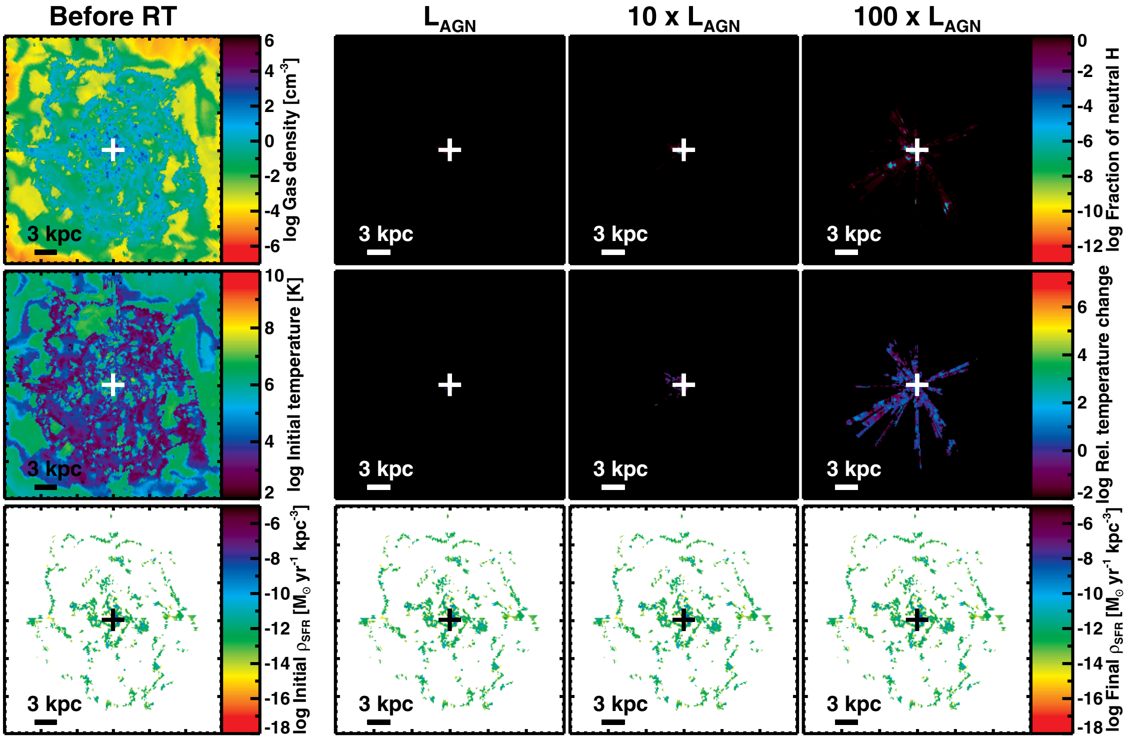

Figure 6. Large face-on view of the simulated galaxy (snapshot 2). Top row: hydrogen density, fraction of neutral hydrogen after RT. Middle row: temperature before RT, relative temperature change. Bottom row: ρ_{SFR} before RT, ρ_{SFR} after RT. The "+" sign shows the location of the BH and the density threshold for SF is $10\,\mathrm{cm}^{-3}$. Parameters after RT are given for the three AGN luminosities ($L_{\mathrm{AGN}} = 10^{44.5}\,\mathrm{erg\,s}^{-1}$). Ionization and heating spots of diffuse gas are visible on a large scale in the disk for the highest AGN luminosity.

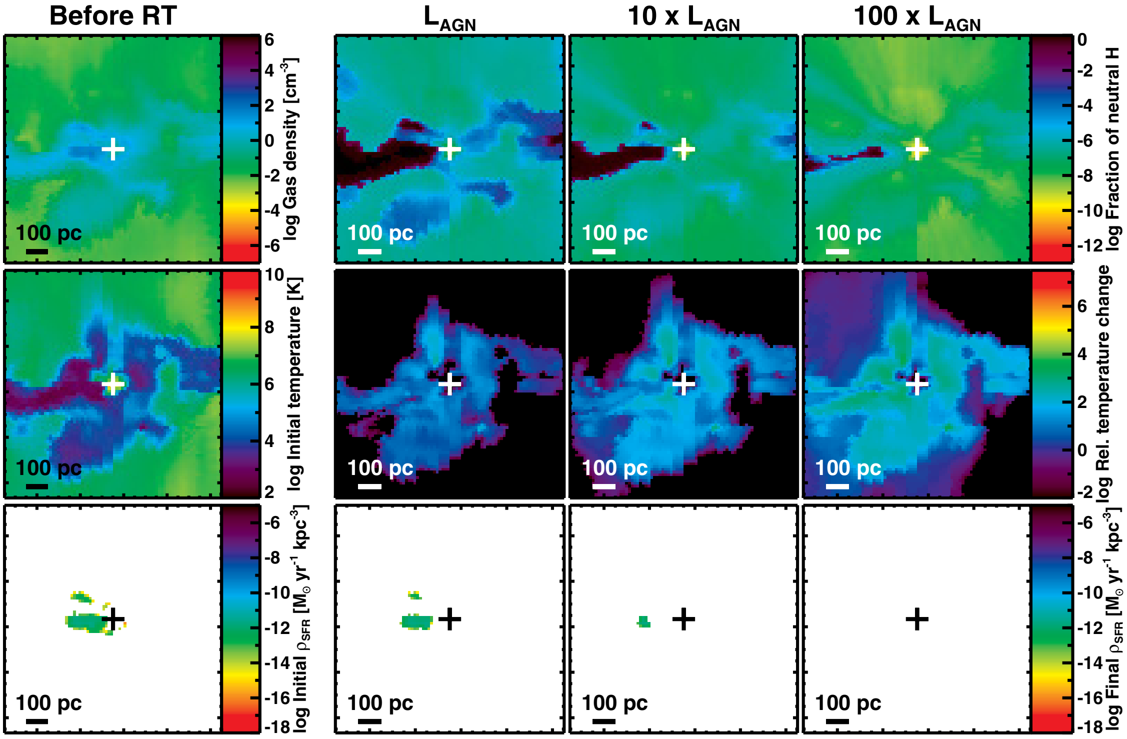

Figure 7. Zoomed edge-on view of the simulated galaxy (snapshot 2). Top row: hydrogen density, fraction of neutral hydrogen after RT. Middle row: temperature before RT, relative temperature change. Bottom row: $\rho_{\rm SFR}$ before RT, $\rho_{\rm SFR}$ after RT. The "+" sign shows the location of the BH and the density threshold for SF is $10\,{\rm cm}^{-3}$. Parameters after RT are given for the three AGN luminosities ($L_{\rm AGN} = 10^{44.5}\,{\rm erg\,s}^{-1}$). On the small scale, diffuse regions are heated above the temperature threshold for SF.

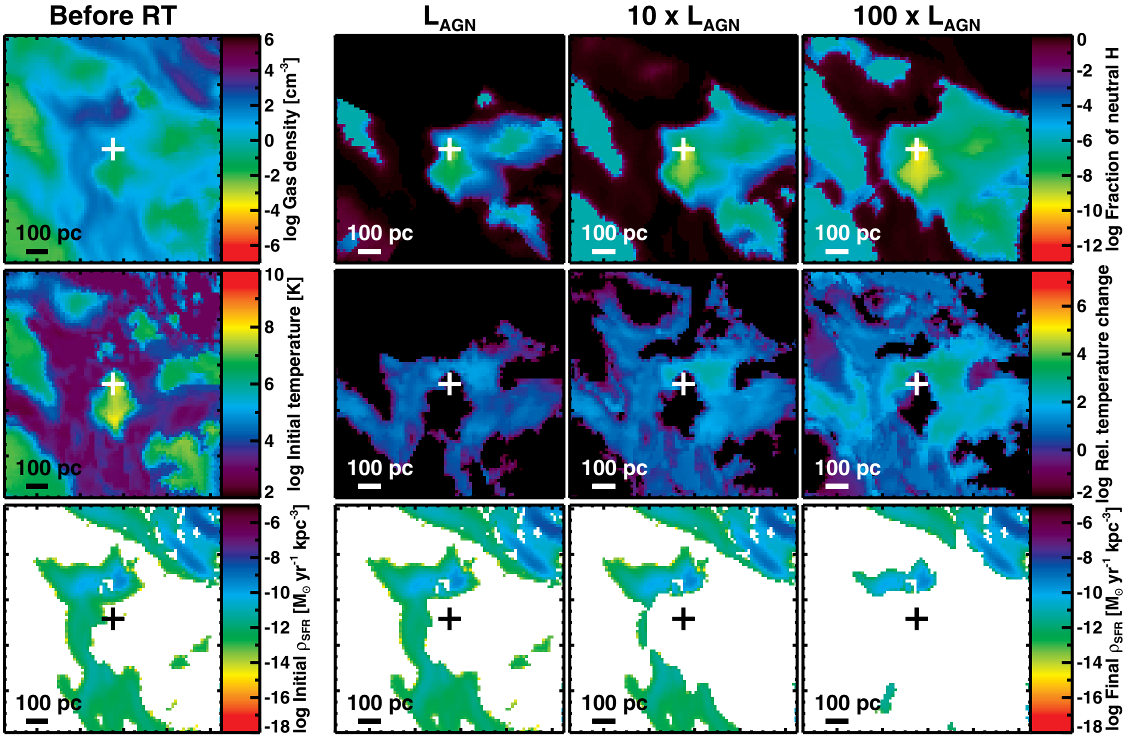

Figure 8. Zoomed face-on view of the simulated galaxy (snapshot 2). Top row: hydrogen density, fraction of neutral hydrogen after RT. Middle row: temperature before RT, relative temperature change. Bottom row: $\rho_{\rm SFR}$ before RT, $\rho_{\rm SFR}$ after RT. The "+" sign shows the location of the BH and the density threshold for SF is $10\,{\rm cm}^{-3}$. Parameters after RT are given for the three AGN luminosities ($L_{\rm AGN} = 10^{44.5}\,{\rm erg\,s}^{-1}$). The densest SF cores are not affected, even with the highest AGN luminosity.

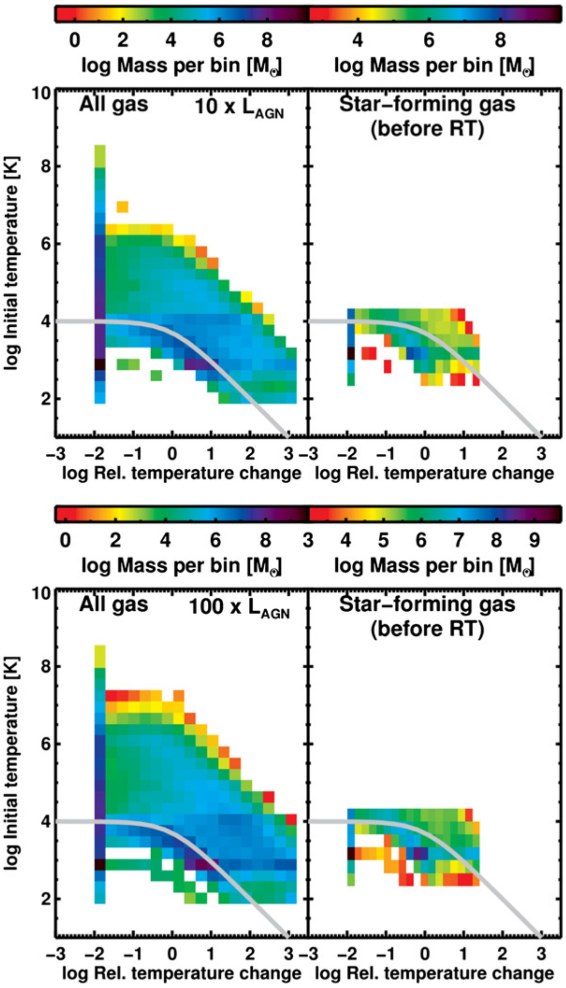

Figure 9. Top: initial temperature of the gas as a function of the relative temperature change for the strong AGN regime. Bottom: same plot for the QSO regime. The left panels show all the gas in the central region of the disk (a cylinder of 2 kpc radius and 4 kpc height, centered on the BH). The right panels show only the gas that forms stars before applying the RT process (in the same region). Each two-dimensional bin is color-coded with its total gas mass. All cells with RTC $< 1\%$ are shown in the lowest RTC bin. Gas above the gray dividing line stops forming stars after the RT process because its temperature crosses the temperature threshold for star formation. The bulk of the gas which is star-forming before RT remains star-forming after the RT process for all AGN luminosity regimes.

for SF after the RT process, and gas forming stars before RT but crossing the temperature threshold after RT is defined as:

$$T_{\rm initial} = \frac{T_{\rm thr}}{\rm RTC + 1}, \tag{4}$$

where $T_{\rm initial}$, $T_{\rm thr}$, and RTC are the quantities defined above. Star-forming gas above the demarcation line defined in Equation (4) is prevented from forming stars due to AGN ionization. Figure 9 clearly shows that, even though a greater amount of gas is heated to a higher degree when increasing the AGN luminosity, the bulk of the star-forming gas is not heated enough by AGN radiation to exceed the temperature threshold for SF.

In summary, increasing AGN luminosity indeed heats a greater amount of gas with densities reaching $10^3\,{\rm cm}^{-3}$ above the temperature threshold for SF. However, given the low density of the gas in most affected regions, we expect the decrease of the total SFR due to photoionization to be relatively small, as quantified below.

3.3. Reduction of the Total SFR

We estimate the global effects of AGN photoionization by summing the SFRs of all cells in the simulation, and calculating total ionized/heated mass and volume fractions (see Section 3.4). Figure 10 shows the evolution of the total SFR as a function of time for the simulation without AGN feedback and the simulation including AGN feedback before and after ionization. Here, the density threshold for SF is $10\,{\rm cm}^{-3}$ (see Appendix C for other thresholds). The slow decrease is due to gas consumption over time—as no new gas is added to the simulation box.

The difference between the SFR without AGN feedback and the SFR with only thermal AGN feedback (before RT) arises due to the fluctuations of the SFR in the simulation, which is highly dependent on the distribution of gas into clumps. As this distribution is stochastic (see Section 2.1), short-term variation and a difference of a few percent between two simulation runs are not surprising and AGN feedback—if it does play a role in this change—is probably not the main driving mechanism. Similarly, the SFR with thermal AGN feedback being greater than the SFR without AGN feedback is most likely due to a random event and is not necessarily a sign of positive AGN feedback (SF triggering).

Figure 10 clearly shows that the impact of RT on the total SFR of the simulation with feedback is small at all luminosities. As the final SFR is based on the final post-RT temperature (defined as the maximum between the Cloudy temperature and the initial temperature; see Section 2.4), it takes into account the effect of the thermal AGN and stellar feedback implemented in the simulation even though these sources are not considered for the RT computation itself. Thus, we conclude that not only does RT change the SFR marginally compared to other feedback models[4] but also, in this particular simulation, the change in SFR due to all kinds of AGN feedback is not significant.

Figure 11 shows the relative reduction of the SFR due to the RT as a function of the AGN luminosity. It is defined as:

$$\Delta_{\rm rel} = \frac{|{\rm SFR}_{\rm final} - {\rm SFR}_{\rm initial}|}{{\rm SFR}_{\rm initial}}, \tag{5}$$

where ${\rm SFR}_{\rm initial}$ is the SFR of the simulated galaxy with thermal AGN feedback before computation of the RT and ${\rm SFR}_{\rm final}$ is the SFR after computation of the RT. The total values of the SFR—both before and after RT—were corrected the same way to account for the resampling induced by the Cloudy computation (see Section 2.4). We see that the effect is indeed very small and although there is an increasing trend at higher luminosities, the overall effect is marginal: a maximum of a few percent in the QSO regime, for the snapshots with the most diffuse inner regions. The lowest curve corresponds to snapshot 6, where no effect is visible on the $\rho_{\rm SFR}$ maps. In the standard AGN regime, the final SFR of this snapshot, which is a rare configuration, is not reduced at all.

We conclude that adding instantaneous AGN photoionization feedback to a simulation containing thermal AGN feedback and stellar feedback changes the SFR of the whole galaxy by only a few percent at most. Moreover, this reduction is much smaller than the difference in SFR between two runs of the same simulation with and without thermal AGN feedback—which represents the fluctuations of the SFR due to the stochastic distribution of clouds—and shows that AGN feedback does not have a significant impact on the SFR on short time-scales.

---

[4] All simulations include SN feedback.

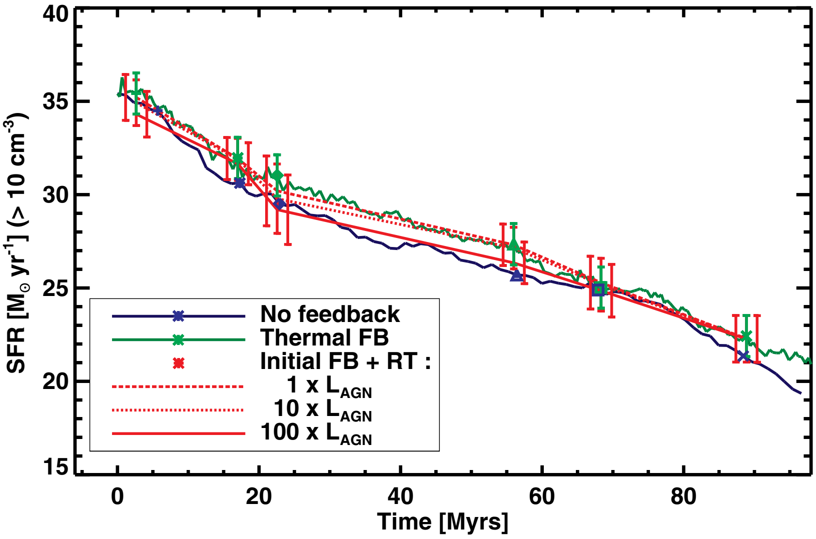

Figure 10. Star formation rate as a function of time for the simulation with no AGN feedback (blue) and the simulation including thermal AGN feedback before and after ionization (green and red respectively). Each line style corresponds to an AGN luminosity, as labeled. Each symbol corresponds to a given snapshot. For clarity, the error bars of the typical AGN regime have been shifted 1.5 Myr to the left, and those of the QSO regime 1.5 Myr to the right. The difference between the reference curve (blue) and the initial feedback one (green) gives the error on the value of the SFR (green error bars). The additional errors are due to the correction of the SFR obtained after the Cloudy computations (described in Section 2.4). The red error bars are the sum of the latter and the stochastic errors (green error bars). The AGN does not have a significant impact on the instantaneous SFR of the whole galaxy along time, even with the highest AGN luminosity.

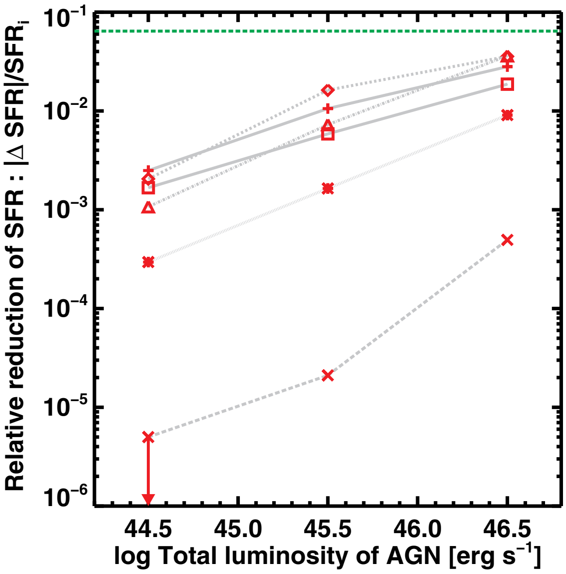

Figure 11. Relative reduction of the star formation rate after radiative transfer as a function of AGN luminosity. Each symbol represents the same snapshot as in Figure 10. They are linked for clarity. The green line shows the maximal relative difference between the simulations with and without AGN feedback. The lower curve corresponds to snapshot 6, where the BH is embedded in a very dense clump. The change in SFR due to the AGN is of a few percent at most.

3.4. Fractions of Heated and/or Ionized Gas

From the small reduction of the SFR, we expect the gas mass fraction that is heated or ionized by the AGN to be small. Figure 12 shows the volume and mass fractions of the gas in the galactic disk (2 kpc thick layers on each side of the median plane of the box) that is ionized by the AGN, as a function of the luminosity. The ratios are defined as follows:

$$m_{\rm ion} = \frac{M_{\rm ionized,corrected}}{M_{\rm total,corrected}}; \quad v_{\rm ion} = \frac{V_{\rm ionized,corrected}}{V_{\rm total,corrected}}. \qquad (6)$$

As for Equation (5), both the pre- and post-RT parameters are those of the simulation with AGN feedback respectively before and after photoionization, and were corrected the same way to account for the resampling due to the Cloudy computation. We consider gas to be ionized if its neutral hydrogen fraction is below 10%. Contributions from OB stars and SNe or thermal AGN feedback are not included since Cloudy computes the RT as if the BH was the only ionizing source and the gas was initially neutral (see Section 2.4). Given that the halo is initially set in the simulation to have very diffuse gas (10^{-5} cm^{-3}), the halo component is highly ionized by the AGN, but would be easily ionized by another source such as OB stars and SN feedback or UV background (see Section 4.4 for discussion). The simulation is not designed to study the gaseous halo properties and one would need to account for cosmological context or at least close environment and satellites. Restraining the study to the gas in the disk reduces this effect but does not cancel it entirely and thus this value shows an upper limit to the amount of neutral gas that could be ionized by an AGN.

We see that even though the fraction of volume ionized by the AGN is large (from 5% to 40% in all representative snapshots depending on the luminosity regime), the corresponding mass fraction is low: from 0.1% to 3% at most. This confirms the intuition that, even though some regions that are ionized have a large spatial extent, they are not significant contributors to the total mass of the galaxy and therefore to the total SFR.

Figure 13 shows the heated mass and volume fractions of gas in the disk. The ratios are similar to Equation (6). Gas is heated if the equilibrium temperature given by Cloudy is greater than the initial temperature in the simulation, meaning that the AGN ionization alone is able to heat the cell above the temperature at which it has been heated by all the other kinds of feedback (thermal AGN and stellar) in the simulation. Thus, heated gas takes into account the "feedback history" of the snapshot (contrarily to ionized gas) and traces the regions where heating due to the AGN photoionization outweighs the other kinds of feedback. However, the behavior is very similar

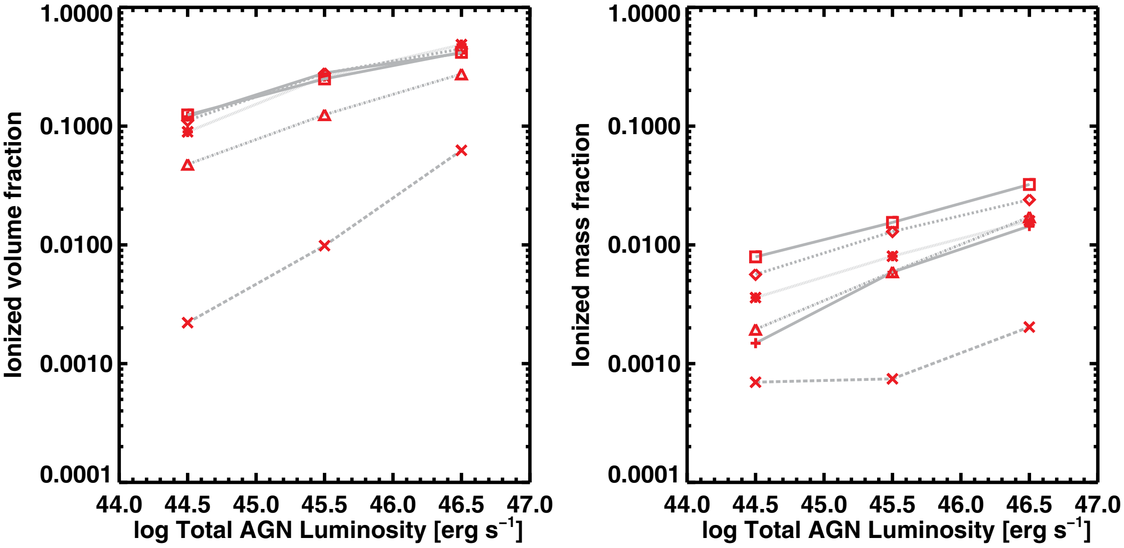

Figure 12. Ionized volume fraction (left) and mass fraction (right) of the gas in the galactic disk as a function of the AGN luminosity (same symbols as Figure 10). The word "ionized" refers to the gas ionized by the single AGN ionization feedback. Before RT, the whole galaxy is assumed to be neutral. Even if the volume fraction of ionized gas in the galactic disk is high, the corresponding mass fraction remains low, meaning that only diffuse gas is ionized by the AGN.

to that of ionized gas, and even when the photoionization has a stronger effect than the other forms of feedback together, the SFR is only slightly impacted because most of the affected gas is not initially star forming.

4. DISCUSSION

In the following, we discuss the dependence of our results on the structure of the ISM. We also deduce a trend for the 100 Myr scale effects on SF and develop our study of the ionization cones. Finally, we try to account for the gas that would already be ionized by other sources before applying RT.

4.1. *Role of ISM Structure*

The profiles used in the LOPs have complex structures with large contrasts between the clump and inter-clump densities (see Figure 4). In order to study the role of the ISM structure on the propagation of AGN radiation, we used Cloudy to calculate the propagation of the three AGN regimes we used before along homogeneous LOPs, using the inner and outer radii of a typical LOP in the plane of the disk and the same filling factor (see Figure 14). We compared the resulting neutral hydrogen fractions to that of a typical LOP in the plane of the disk (as shown in black in Figure 4), whose mean density is $\sim$40 cm^{-3}. We only show the typical AGN and QSO luminosities and note that the strong AGN case is intermediate, as expected.

The ionization profile of the LOP inside the plane of the disk used in the main study is located between those of the constant LOP at 10 cm^{-3} and at 1 cm^{-3}, whereas its mean density is $\sim$40 cm^{-3}. For all constant profiles (except for the 10 cm^{-3} in the typical AGN regime), the radius at which gas becomes less than 10% ionized is larger than for the main study LOP, showing that ionization and heating by the AGN goes deeper in the disk than for the typical disk plane LOP. However, in the uniform-density case, the ionization fraction decreases smoothly whereas that of the main study LOP is not monotonic and regions of highly ionized gas are found far in the disk in the strong QSO regime (see Section 4.3). Such spikes correspond to diffuse interclump regions that are ionized by the AGN. In the QSO regime, they are located at radii up to $\sim$8 kpc in the disk (see Figure 6). This suggests that typical high-redshift disk galaxies are on average dense enough to screen AGN radiation and that holes between the dense clumps are necessary for radiation to go past the inner kiloparsecs.

A smooth exponential density profile enclosing the same mass as the simulated galaxy gave similar results.

We conclude that the ISM structure plays a major role in the propagation of AGN radiation since holes explain that ionization often reaches large distances in the disk or in the halo, whereas dense clumps are not necessary to explain the low ionized mass fraction, since the average density is high enough for the gas to be self-shielding.

4.2. *Long-term Effects on Star Formation*

Long-term effects on SF can be deduced from our instantaneous study by looking at the H I reservoirs in the envelope of GMCs and in the atomic clouds around them ("proto-GMCs"), which are composed of 0.3–10 cm^{-3} ISM (Dobbs et al. 2008).

Indeed, the first step to launch SF is to form a dense cloud of molecular gas (a GMC) out of diffuse ISM. Such GMCs are believed to be created by spiral-wave-induced shocks (Heyer & Terebey 1998; Dobbs et al. 2008) and live about 15–40 Myr (Murray 2011) until they are disrupted by the stars that formed inside them and their envelope is dispersed (Elmegreen 2007). In the absence of external heating, those 0.3–10 cm^{-3} regions form proto-GMCs which gradually fall under 10^4 K. These are likely to collapse due to shocks and create new GMCs, which in turn induce the formation of new stars in the next 100–200 Myr, and the cycle continues.

However, if this gas phase is kept hot or ionized by the AGN, it cannot cool down and collapse and future SF is suppressed on a time-scale shorter than that necessary to refuel the interclump medium with cold infalling gas. The instantaneous effect of the three luminosity regimes on atomic gas is computed the same way as before (see Section 3.4) but accounts only for the gas at densities 0.3–10 cm^{-3} and is displayed in Table 2.

From Table 1, AGN radiation is emitted at $10^{44.5}$ erg s^{-1} about 30% of the time and at $10^{45.5}$ erg s^{-1} about 3% of the time, considering an AGN duty cycle of 1/3.

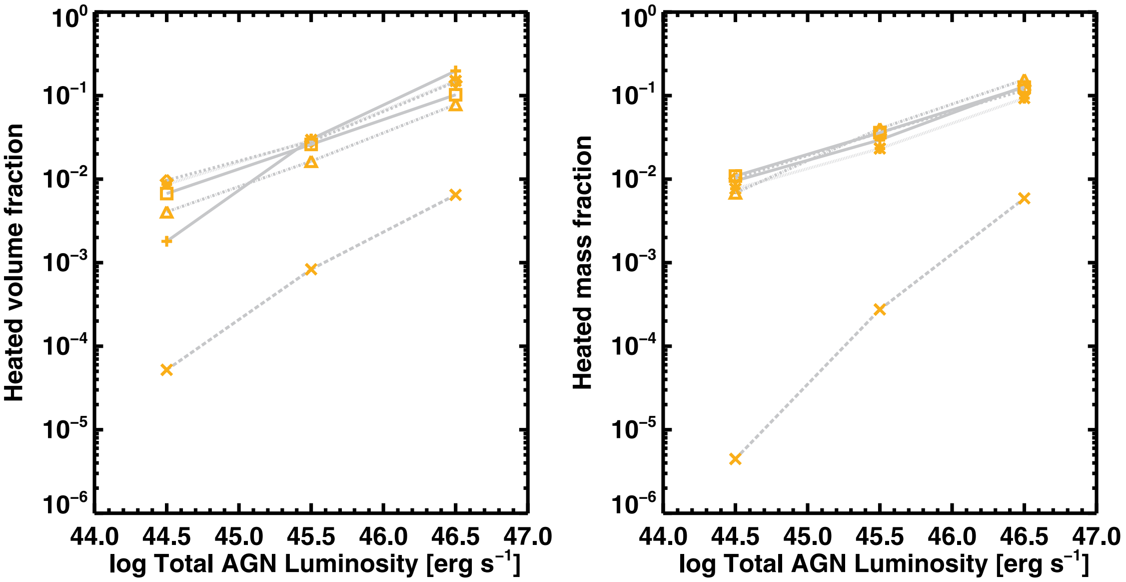

Figure 13. Heated volume fraction (left) and mass fraction (right) of the gas in the galactic disk as a function of the AGN luminosity (same symbols as Figure 10). The word "heated" refers to the gas heated by the single ionization feedback above the temperature at which it has been heated by all other kinds of feedback implemented in the simulation (thermal AGN FB, stellar FB). The volume and mass fraction of heated gas are low, which means that AGN ionization overwhelms all kinds of FB implemented in the simulation for only a small amount of the diffuse gas.

Instantaneously, the heating/ionization of the GMCs due to the AGN in such regimes is negligible (see Table 2), and therefore it is highly unlikely that cumulative effects will become important in the following 100–200 Myr and thus no SF quenching is expected. Even if the AGN were emitting 100% of the time, the results would not change for both the typical and strong AGNs. However, in the case where a QSO would be emitting for an extended period of time because of, e.g., a merger, GMCs would more likely be impacted and cumulative effects could significantly reduce future SF.

The longer-term ($\gtrsim$200 Myr–1 Gyr) SFR evolution depends on the ability of the AGN to keep the gaseous halo warm or ionized. Indeed, keeping the halo hot over an extended period of time could prevent inflows from reaching the disk and starve the galaxy by suppressing its gas supplies (Dubois et al. 2012). However, the simulation we used is an isolated galaxy and its initial gaseous halo is not designed to be realistic and thus we cannot predict whether the AGN is able to quench the galaxy on a time-scale of a few Gyr.

4.3. Distribution of Ionized Gas

This section focuses on the ionization maps in Figures 5–8. In the typical AGN regime, the inner part of the disk surrounding the AGN is ionized up to 50–700 pc, depending on the location of the nearest dense clumps ($n > 10^3\,\mathrm{cm}^{-3}$), which shield themselves, block the AGN radiation, and protect the diffuse material behind them. The galactic disk remains neutral at a larger scale. The LOPs that do not cross dense clumps are ionized until the end, meaning that the material in the halo is not able to stop the radiation. However, this simulation was not designed to have a realistic gaseous halo and is not in its cosmological context.

At small scales around the BH, the limit between neutral and ionized gas goes from 1–10 cm^{-3} in the typical AGN regime, to 10 and 100 cm^{-3} in the strong AGN and QSO regimes respectively. With increasing AGN luminosity, the distance at which clumps are able to shield the diffuse regions behind them is larger, allowing ionization to go further within the disk. Though, it does not affect the densest clumps or the disk itself, which remains neutral.

In the strong AGN and QSO regimes, not only are the ionized regions more extended, but also the fraction of remaining neutral hydrogen is smaller by a factor ~10–100 in the regions that were already ionized in the typical AGN regime. In the QSO regime, ionized spots are visible at large scale within the disk (up to 8 kpc from the BH), though SFR is not impacted since those regions are mostly not initially star forming.

Clearly, the impact of AGN photo-ionization is greater than expected for a simple model (see Section 2.3), showing that the multi-phase distribution of the gas plays a key role in the propagation of AGN radiation: while dense clumps can block the ionizing radiation at a very small scale-length depending on their distance to the BH, QSO radiation is allowed to propagate past the inner kiloparsecs thanks to the diffuse interclump medium. The morphology of the galaxy may also be of great importance since the calculation done by Curran & Whiting (2012) reproduces observations of (most likely) elliptical radio galaxies and quasar hosts (Curran et al. 2006, 2008) up to redshift 3, but fails to reproduce the propagation of AGN radiation in a simulated star-forming disk at redshift ~2.

Ionized gas (AGN ionization only) and heated gas (AGN ionization stronger than thermal AGN and SN feedback) have distinct distributions, showing that, in the simulation presented here, AGN ionization itself does not overwhelm all other forms of feedback and ionization from other sources—at least instantaneously—for the three luminosity regimes.

Yet, our study reproduces the observed biconical shape of AGN emission (see Figure 5), even though the propagation of AGN light is isotropic. This shows that the simulated ISM is able to collimate the AGN radiation to some degree. These ionization cones may be larger-scale analogs to those predicted by the AGN Unified Model of Urry & Padovani (1995). Furthermore, as the AGN is the only ionizing source, we show that other sources of ionization such as stars are not needed for AGN radiation

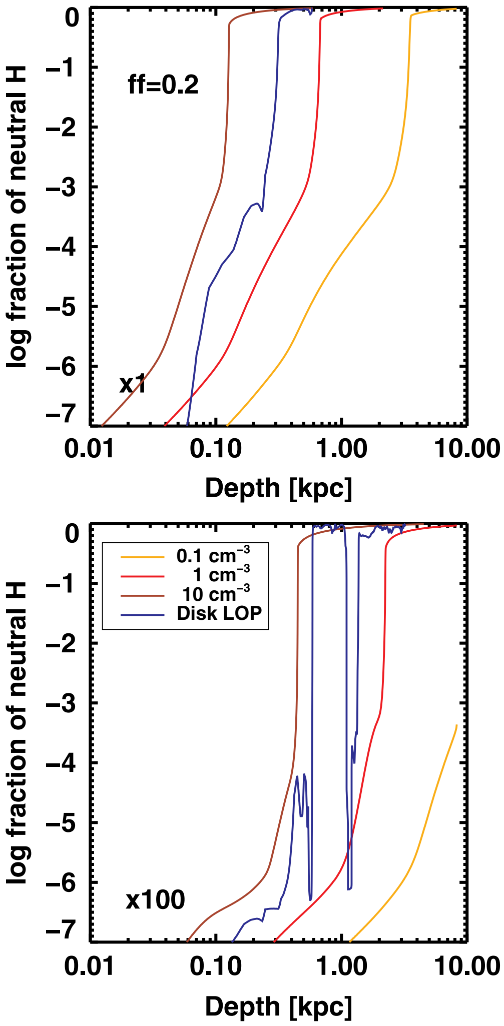

Figure 14. Fraction of neutral hydrogen for three constant density profiles at 0.1, 1, and 10 cm^{-3} and a typical LOP in the disk plane (mean density of 40 cm^{-3}). The top panel shows the typical AGN luminosity and the bottom panel shows the strong QSO luminosity. In a uniform galactic disk at 10 cm^{-3}, a QSO would only ionize the central few hundreds of parsecs.

to escape the galaxy, which is consistent with AGNs being the main drivers of ionization cones. Accounting for these other sources of ionization would only favor the escape of photons emitted by the AGN.

The bases of the cones are not circular and are not necessarily centered on the BH. Their shape depends a lot on the cloud distribution. With a higher AGN luminosity, the ionization cones are wider and their basis is larger, which is in broad agreement with Hainline et al. (2013) in the sense that the size of the narrow-line regions (NLRs) increases with AGN luminosity. Finally, the inclination of the cones with respect to the galaxy spin axis decreases for a higher AGN luminosity. The diffuse and almost entirely ionized gaseous halo may also be consistent with the observations of nearly circular NLRs in radio-quiet quasars by Liu et al. (2013b).

4.4. *Other Sources of Ionization*

As the simulation contains several heating sources (stars, UV background, thermal AGN feedback, etc.; see Section 2.4), a large volume fraction of the gas in the ISM or in the halo is already very hot before the RT process (see Table 3), and is likely to be ionized. This gas could then be transparent to the AGN radiation during the RT process, whereas in our model, all the gas is supposed to be initially neutral. Some of the AGN photons are then artificially absorbed because they interact with gas they should not encounter.

Table 2
Effect of AGNs on Future (100–200 Myr) Star Formation

Regime	Heated Mass Rate (%)	Ionized Mass Rate (%)
Typical AGNs	0^{a}–4	0^{a}–2
Strong AGNs	0.2–9	0.01–3
Typical QSOs	2–30	0.1–8

Notes. Rates are given for atomic gas (0.3–10 cm^{-3}).
[a] Rate is zero for snapshot 6.

To see if the AGN radiation would have a bigger impact if encountering transparent gas, we ran a series of LOPs, in which the number density is set to an arbitrarily low value (10^{-6} cm^{-3}) in every cell whose initial temperature is above a given threshold (5×10^4, 10^5, 10^6, and 10^7 K). These values are set in order to probe different transparency levels, since the ionization state is not explicitly computed in the simulation: at our resolution, gas at $T > 10^6$ K is very likely to be ionized, while gas at a few 10^4 K could be ionized, depending on its density, or due to shocks.

Among the series of LOPs studied, we present the results for the propagation of the QSO radiation along a typical LOP in the plane of the galactic disk (see Figure 15). We compare ionization and temperature along such "semi-transparent" lines to those along the original density profile used in the main study.

Transparent regions are more heated and more ionized than their original counterparts which are essentially not forming stars, even before RT. However, such differences may not be physically relevant, since (1) such regions are heated to 10^8 K, a value that entirely depends on the value of the density we chose for the transparent regions, and (2) the fraction of neutral H is very low ($\lesssim 10^{-4}$) in both cases. In the semi-transparent configuration, a few more ionized spots exist at intermediate radius in the disk compared to the typical LOP, but dense ("opaque") clumps do not seem to be more affected, whatever the AGN luminosity. Furthermore, most star-forming regions are located beyond the range of ionization computed with Cloudy. As accounting for transparent regions does not allow radiation to go further in the disk compared to the original LOPs (because it does not increase the radius at which the temperature drops under 4000 K), taking transparent gas into account has no major effect on SF.

Quantitatively, LOPs that are not star-forming before the RT process stay non-star-forming after the RT process for all transparency criteria (i.e., $\mathrm{SFR}_f = \mathrm{SFR}_i = 0$). For LOPs that are star-forming before the RT process, we compute the relative change of the SFR reduction Δ_{rel} (see Equation (5)), defined as:

$$\Delta_{C-T} = \frac{\Delta_{\mathrm{rel},C} - \Delta_{\mathrm{rel},T}}{\Delta_{\mathrm{rel},C}}, \qquad (7)$$

where $\Delta_{\mathrm{rel},T}$ is the relative reduction of SFR for the different transparency criteria and $\Delta_{\mathrm{rel},C}$ is that of the original profile. Δ_{C-T} can be seen as an error bar on the relative reduction of SFR shown in Figure 11. The values for the different AGN regimes are gathered in Table 3. The standard deviations are large due to the small sample, and there is a high discrepancy between enhancement of the SFR reduction ($\Delta_{C-T} > 0$) and attenuation of the SFR reduction (which is only due to resampling errors

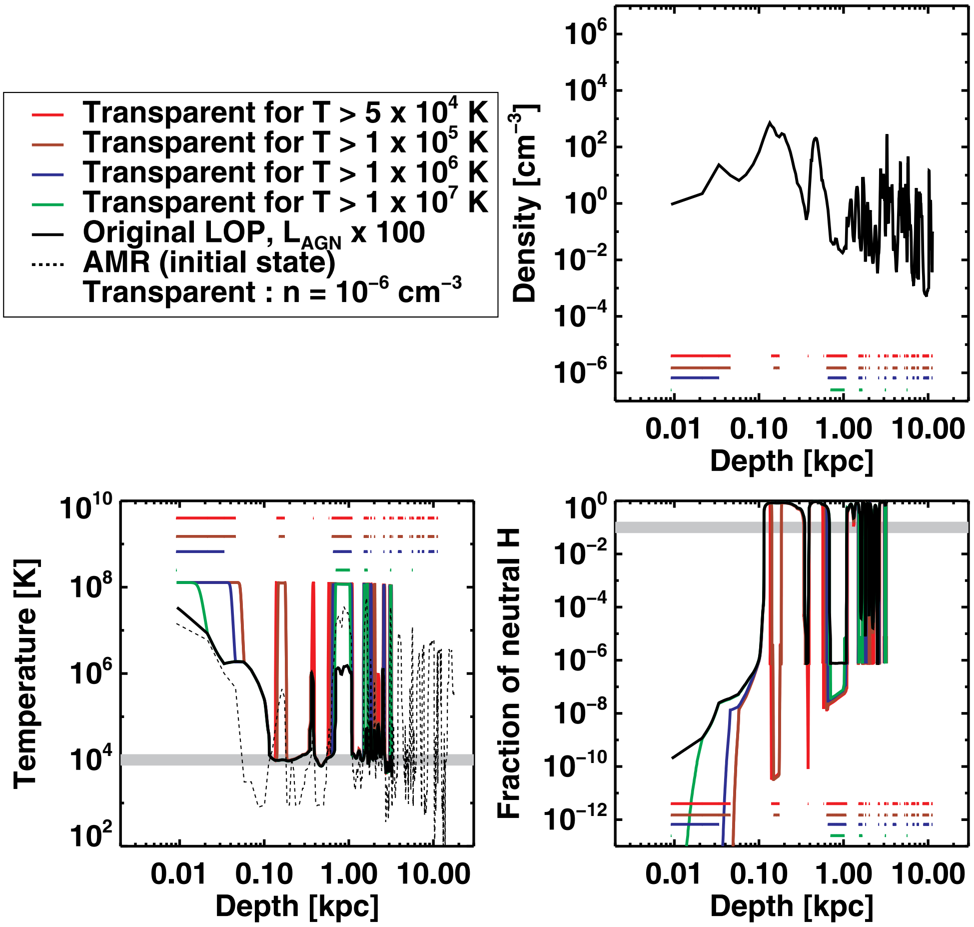

Figure 15. Density (top), temperature (left), and neutral hydrogen fraction (right) profiles for the original LOP (black) and the transparent LOPs, with transparency criteria as labeled. Transparency criteria are shifted for the sake of visibility on the density panel, and reproduced on the two other panels to make the plots easier to read. The gray lines show the temperature threshold for star formation and the ionized gas demarcation used throughout the paper. This LOP is a typical LOP of the galactic disk. Accounting for gas ionized by other sources does not change the physical properties in the star-forming regions.

Table 3
Mean Mass and Volume Fractions of Hot Gas and Mean Relative Change of $\Delta_{\rm rel}$ due to Hot Gas

Transparency Criterion	$T > 5 \times 10^4$ K	$T > 10^5$ K	$T > 10^6$ K	$T > 10^7$ K
Mean mass fraction[a]	4.00 (±0.38)%	2.80 (±0.42)%	1.23 (±0.42)%	0.15 (±0.15)%
Mean volume fraction[a]	98.57 (±0.54)%	98.22 (±0.80)%	74.71 (±7.06)%	6.13 (±5.30)%
Mean Δ_{C-T} for the typical AGN[b]	−6.00 (±16.90)%	−7.79 (±18.50)%	−2.20 (±22.47)%	3.65 (±14.30)%
Mean Δ_{C-T} for the strong AGN[b]	3.81 (±6.70)%	−5.10 (±20.43)%	5.66 (±9.53)%	2.01 (±5.82)%
Mean Δ_{C-T} for the typical QSO[b]	−25.00 (±55.90)%	−18.20 (±41.92)%	13.57 (±33.25)%	−0.61 (±1.72)%

Notes.
[a] Mass and volume fractions take into account the entire galaxy (disk and gaseous halo). The mean is done on the six snapshots studied.
[b] Δ_{C-T} is the relative change between the $\Delta_{\rm rel}$ of the semi-transparent line (T) and the original $\Delta_{\rm rel}$ used for comparison (C), where $\Delta_{\rm rel}$ is the relative reduction of SFR defined in Equation (5). A negative value indicates enhanced SFR suppression compared to the original LOP; a positive value indicates that the relative reduction of SFR is smaller for the semi-transparent line. As SF-triggering cannot be probed with our method (see footnote 5), the latter is only due to the resampling of the lines. The mean is done on the LOPs of the sample that are star-forming before the RT process. Values between parentheses correspond to the standard deviation.

since we cannot probe SF triggering[5]; $\Delta_{C-T} < 0$) for the different transparency criteria. From this, the change in the SFR reduction induced by transparent gas is consistent with zero at all AGN luminosities. Furthermore, a variation of 25% at most of the relative reduction $\Delta_{\rm rel}$ (shown in Figure 11) is marginal. We therefore neglect all ionizing sources other than the AGN in the main study.

5. CONCLUSIONS

In order to determine the effect of AGN long-range photoionization and local thermal energy re-deposition on SF, we used

---

[5] During the RT process, the temperature either increases or remains constant, and the density profile is constant as well (see Section 2.4). Thus, a small decrease of the SFR can only be due to the resampling of density and temperature along the LOP.

Cloudy to propagate AGN radiation from the BH located at the center of a simulated high-redshift disk galaxy through the ISM and the gaseous halo. We built a model of a Seyfert 1 SED spanning a large range of wavelengths and used it as ionizing source in Cloudy. RT was computed through the whole galaxy using LOPs emerging from the central BH in all directions with a good spatial coverage. We tested three different AGN luminosities, corresponding to three "AGN regimes"—typical AGNs ($L_{\rm bol} = 10^{44.5}\,{\rm erg\,s^{-1}}$), strong AGNs ($L_{\rm bol} = 10^{45.5}\,{\rm erg\,s^{-1}}$), and QSOs ($L_{\rm bol} = 10^{46.5}\,{\rm erg\,s^{-1}}$)—and studied how AGN photoionization heats/ionizes the different gas phases in the galactic disk and halo, and how that temperature increase might impact the SFR of the whole galaxy. Our results are as follows.

1. The AGN mainly affects the diffuse phase of the ISM and the gaseous halo. Indeed, the AGN is able to ionize a large volume fraction of the gas in the galactic disk, 5%–40%, depending on the AGN regime, and in the gaseous halo, 30%–90%. However, the corresponding mass fraction remains very low (0.1%–3%), showing that most of the ionized and/or heated gas is diffuse, while GMCs are left unaffected.
2. As the bulk of star-forming gas occurs in dense clumps, the decrease of the total SFR due to local AGN heating and distant AGN radiative effects is marginal, even if there is an increasing trend with luminosity. The maximum relative reduction of SFR is of a few percent in the most diffuse cases at a QSO luminosity.
3. Gas distribution in the simulated high-redshift disk plays a major role on the propagation of AGN radiation: dense star-forming clumps shield themselves and the diffuse material behind them against AGN X-ray to UV ionizing radiation and optical heating radiation, while holes allow it to propagate further in the disk or in the halo. In the QSO regime, diffuse regions of gas in the interclump medium are heated and/or ionized up to ~8 kpc around the BH. Furthermore, the clumpiness of the ISM induces a high variability of the maximal radius at which the AGN is able to heat/ionize gas in the disk, which is not predicted by smooth distributions of gas.
4. Atomic gas around the GMCs and in their envelopes—thought to be the reservoir of future SF—is not strongly impacted by a typical or strong AGN, whether through winds or photoionization. Taking into account a standard AGN duty cycle, we show that the cumulative effects of AGN feedback on SF are small on a timescale of a few hundreds of million years. Thus, in a standard configuration, not only is AGN radiation unable to substantially affect the dense molecular regions that dominate instantaneous SF, but it is also inefficient at destroying cool atomic reservoirs ($\sim 10\,{\rm cm^{-3}}$) for the future sites of SF.

Our detailed calculations suggest that the coupling between AGN radiation and the star-forming ISM is very weak, at least in the most typical SFGs at high redshift. We showed that well-resolved dense star-forming clumps shield themselves against AGN UV radiation—which has been hypothesized by, e.g., Vogelsberger et al. (2013, 2014) in their simulation Illustris at lower resolution, but also against X-ray emission while diffuse gas is affected by the AGN at a large scale in the gaseous halo and even at a large scale inside the galactic disk for the QSO regime.

This study, in association with the results of Gabor & Bournaud (2014), supports the idea that frequent AGNs in high-redshift SFGs are a promising mechanism to regulate or remove the mass of galaxies, without impacting SF even on relatively long timescales of hundreds of Myr, i.e., preserving the steady-state evolution with relatively constant SF histories.

Finally, due to the high variability of the ionization radius induced by the well-resolved ISM, we expect that simple Strömgren spheres do not correctly model the impact of AGN ionizing radiation on the physical state of the gas. We recommend a more complex subgrid model to treat RT without explicitly implementing it in the simulations, including at least non-smoothed gas density (spherical symmetry is not valid in a clumpy ISM), gas column density and distance from the AGN; and AGN luminosity, inferred from the BHAR.

We acknowledge support from the EC through grants ERC-StG-257720 and the CosmoComp ITN. Simulations were performed at TGCC and IDRIS under GENCI allocations 2013-GEN2192 and 2014-GEN2192. We thank the anonymous referee for valuable comments, which improved the content and clarity of this paper.

APPENDIX

The appendices gather more detailed explanations about our study and describe some secondary tests that we did to check the consistency of our model. They are organized as follows: a detailed description of the AGN spectrum and its components is available in Appendix A, maps of ionized/heated gas and $\rho_{\rm SFR}$ for three other snapshots are displayed in Appendix B, and we also present a study of the value of the density threshold for SF (see Appendix C) and of the filling factor (see Appendix D). Finally, we compare the results of our analysis to a lower-resolution simulation (see Appendix E).

APPENDIX A

SEYFERT SED

The input SED can be interpreted in the framework of the Unified Model of AGNs, according to which the supermassive BH is surrounded by an accretion disk, which thickens to become a torus approximately at the sublimation radius of dust. Our AGN SED is composed of (1) UV radiation from the accretion disk and X-rays from the accretion disk's corona, (2) a linear combination of blackbodies corresponding to the heated dusty torus, and (3) illuminated BLR clumps. These different components are defined as follows.

1. The AGN component was built using the *agn* command in Cloudy, defining a multi-component continuum similar to that observed in typical AGNs:

$$F_\nu = \nu^{\alpha_{\rm UV}} e^{-\frac{h\nu}{kT_{\rm BB}}} e^{-\frac{kT_{\rm IR}}{h\nu}} + A\nu^{\alpha_{\rm X}}, \qquad \text{(A1)}$$

where $T_{\rm BB}$ is the cut-off temperature of the blue bump, so that it peaks at 10 microns and $T_{\rm IR}$ is the IR cut-off temperature. $\alpha_{\rm UV}$ and α_X are the exponents in the UV and in the X fields, respectively. Coefficient A was adjusted so that the optical to X-ray spectral index α_{OX} had the specified value, defined by:

$$\frac{F_\nu(2\,{\rm keV})}{F_\nu(2500\,{\rm \AA})} = \left(\frac{\nu_{2\,{\rm keV}}}{\nu_{2500\,{\rm \AA}}}\right)^{\alpha_{OX}}. \qquad \text{(A2)}$$

We used the following parameters: $T = 5.5 \times 10^5$ K, $\alpha_{OX} = -0.7$, $\alpha_{\rm UV} = -0.3$, $\alpha_X = -0.48$. These were initially based on the parameters taken by Ferguson et al. (1997) but then modified to match observed data.

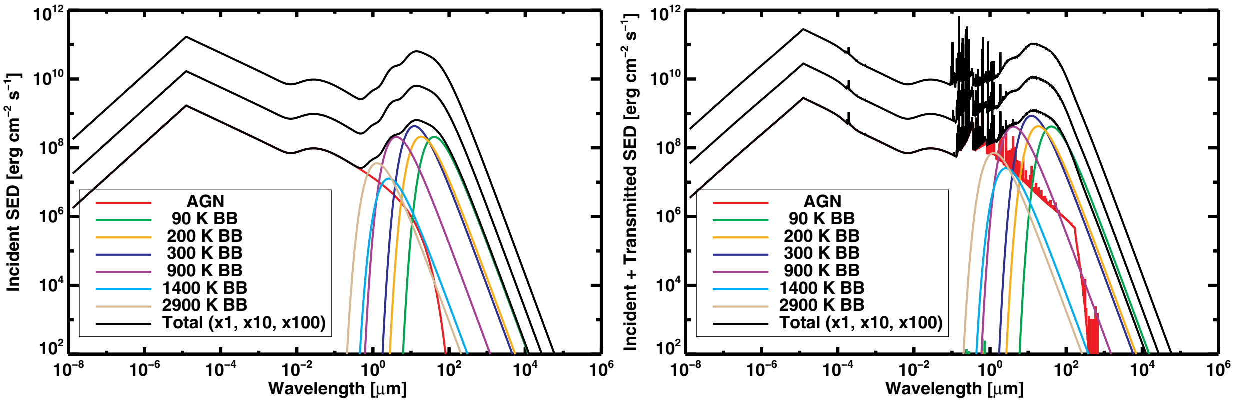

Figure A1. Left: incident SED of the inner region of an Sy 1 galaxy, i.e., the sum (black) of the AGN (red) and the dust (blackbodies; other colors) incident emissions. Right: emergent SED of the inner region of an Sy 1 galaxy, i.e., the sum the incident SED and the radiation transmitted through the BLR. The total SEDs for the three luminosity regimes are shown (black); the components are those of the typical AGN regime.

2. Dust was assumed to have solar abundance and the ISM to be Milky-Way-like. Cloudy computes all processes relevant for the treatment of dust grains: photons absorption and scattering, stochastic heating, photoelectric effect, Auger emissions in X-ray environments, electron and ion collisional charging, collisions between gas and dust and resulting energy exchange, etc. As the radiation field is propagated, gas and dust opacities affect photons, while photons change the properties of grains after absorption. Dust sublimation and grain depletion were taken into account (see Section 2.5 of Ferland et al. 2013 and the online Cloudy documentation Hazy for further details). Often, dust emission is described as a graybody (see Rathborne et al. 2010 for instance). Because graybodies cannot be implemented in Cloudy, we used a linear combination of blackbodies with temperatures ranging from 90 to 2900 K. However, heated dust does not contribute to the ionization of gas and thus the accuracy on the IR part is not crucial for this study. The inner and outer radii of the computation were defined so that RT occurred through the dust sublimation zone—roughly 0.1 pc when the temperature is about 1400 K (Hönig & Kishimoto 2010).
3. The transmitted spectrum of the BLR was computed by propagating the incident AGN SED with Cloudy, through clumps of gas representing a typical BLR, i.e., homogeneous clumps of gas with a hydrogen density of 10^9 cm^{-3} (Matews & Capriotti 1985), and a filling factor of 10^{-3} (Osterbrock & Ferland 2006).

These components are shown in Figure A1 for the typical AGN regime. The strong AGN and QSO regime SEDs are also shown for comparison, but not their components. The input scripts that led to this Seyfert SED and the QSO SED (not shown) are available as supporting material.

APPENDIX B

MAPS FOR OTHER SNAPSHOTS

This section gathers the maps for three of the other snapshots studied in the simulation including AGN feedback, in order to illustrate how the distribution of clumps affects the propagation of AGN radiation. The density threshold for SF is 10 cm^{-3}. As the distribution of clouds evolves with time and the BH moves (see Gabor & Bournaud 2013), the snapshots look similar but are not exactly identical.

The different configurations clearly modify the propagation of the ionizing radiation :

1. Figure A2 shows the maps corresponding to snapshot 1, which is representative of the evolution of the galaxy. In this snapshot, the BH is located slightly above the galactic disk: the typical AGN radiation going downward is mainly blocked, and the lower ionization cone is small. However, in the two other regimes, AGN radiation is energetic enough to go through the center of the galactic disk.
2. Figure A3 displays the maps for snapshot 6, where the BH is embedded into a dense clump ($n > 10^4$ cm^{-3}). This configuration is not frequent because the number of dense clumps in the disk is not large, though it boosts the accretion rate of the BH. In this snapshot, the typical AGN luminosity regime is too weak to ionize the gas. In the strong AGN and QSO regimes, the fraction of photons that escape the central clump increases and an ionization cone with a very small basis appears. The impact on SF is the lowest among all snapshots studied and the changes $\rho_{\rm SFR}$ are below the resolution limit.
3. Finally, Figure A4 shows the maps of snapshot 4, where a dense clump lies on the above edge of the BH. In all luminosity regimes, AGN radiation is blocked in the upper half of the simulation box, similarly to snapshot 6, whereas the lower part behaves like snapshots 1 and 2.

APPENDIX C

DENSITY THRESHOLD FOR STAR FORMATION

The density threshold above which a cell is able to form stars is 100 cm^{-3} in the simulation but the value used for the analysis is 10 cm^{-3}. Such a change does not affect the efficiency of SF, but plays the role of a delimiter between star-forming and non-star-forming regions (Kraljic et al. 2014). In the post-processing, we tested three values of this threshold: 1, 10, and 100 cm^{-3}. With a low threshold, the star-forming regions are much more extended than with a higher threshold (see Figure A5, for 1 and 100 cm^{-3}), though the additional star-forming clouds are so diffuse that the total SFR of the entire galaxy remains comparable (see Figure A6). For QSO luminosities (see the right column of Figure A6), diffuse regions are ionized and the spatial extent of the remaining star-forming regions in the very center of the galaxy hardly depends on the value of the threshold we varied.

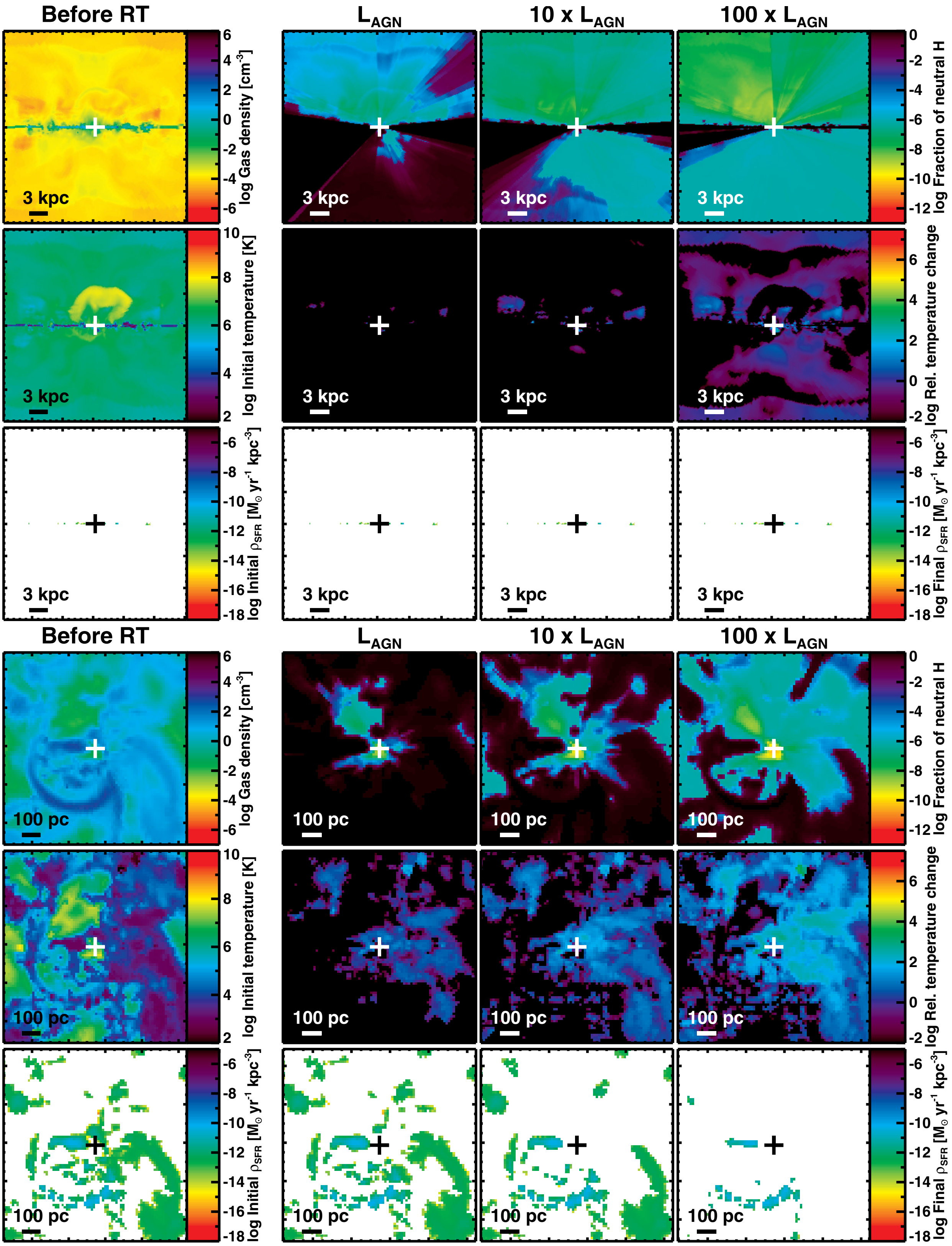

Figure A2. Large edge-on and zoomed face-on views of the simulated galaxy (snapshot 1). Top row: hydrogen density, fraction of neutral hydrogen after RT. Middle row: temperature before RT, relative temperature change. Bottom row: ρ_{SFR} before RT, ρ_{SFR} after RT. The "+" sign shows the location of the black hole and the density threshold for SF is $10\,\mathrm{cm}^{-3}$. Parameters after RT are given for the three AGN luminosities ($L_{\mathrm{AGN}} = 10^{44.5}\,\mathrm{erg\,s}^{-1}$).

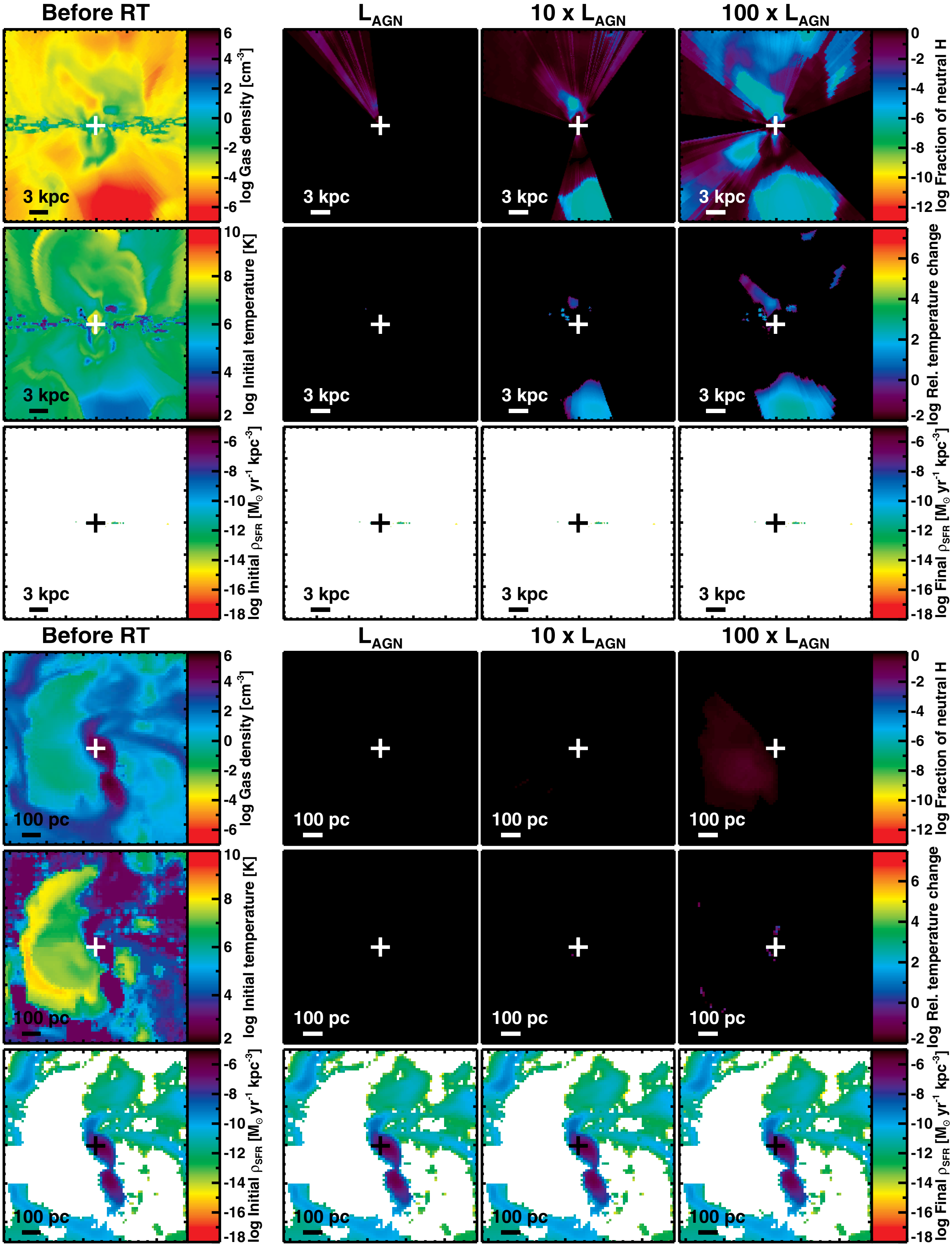

Figure A3. Large edge-on and zoomed face-on views of the simulated galaxy (snapshot 6). Top row: hydrogen density, fraction of neutral hydrogen after RT. Middle row: temperature before RT, relative temperature change. Bottom row: $\rho_{\rm SFR}$ before RT, $\rho_{\rm SFR}$ after RT. The "+" sign shows the location of the black hole and the density threshold for SF is $10\,{\rm cm}^{-3}$. Parameters after RT are given for the three AGN luminosities ($L_{\rm AGN} = 10^{44.5}\,{\rm erg\,s}^{-1}$).

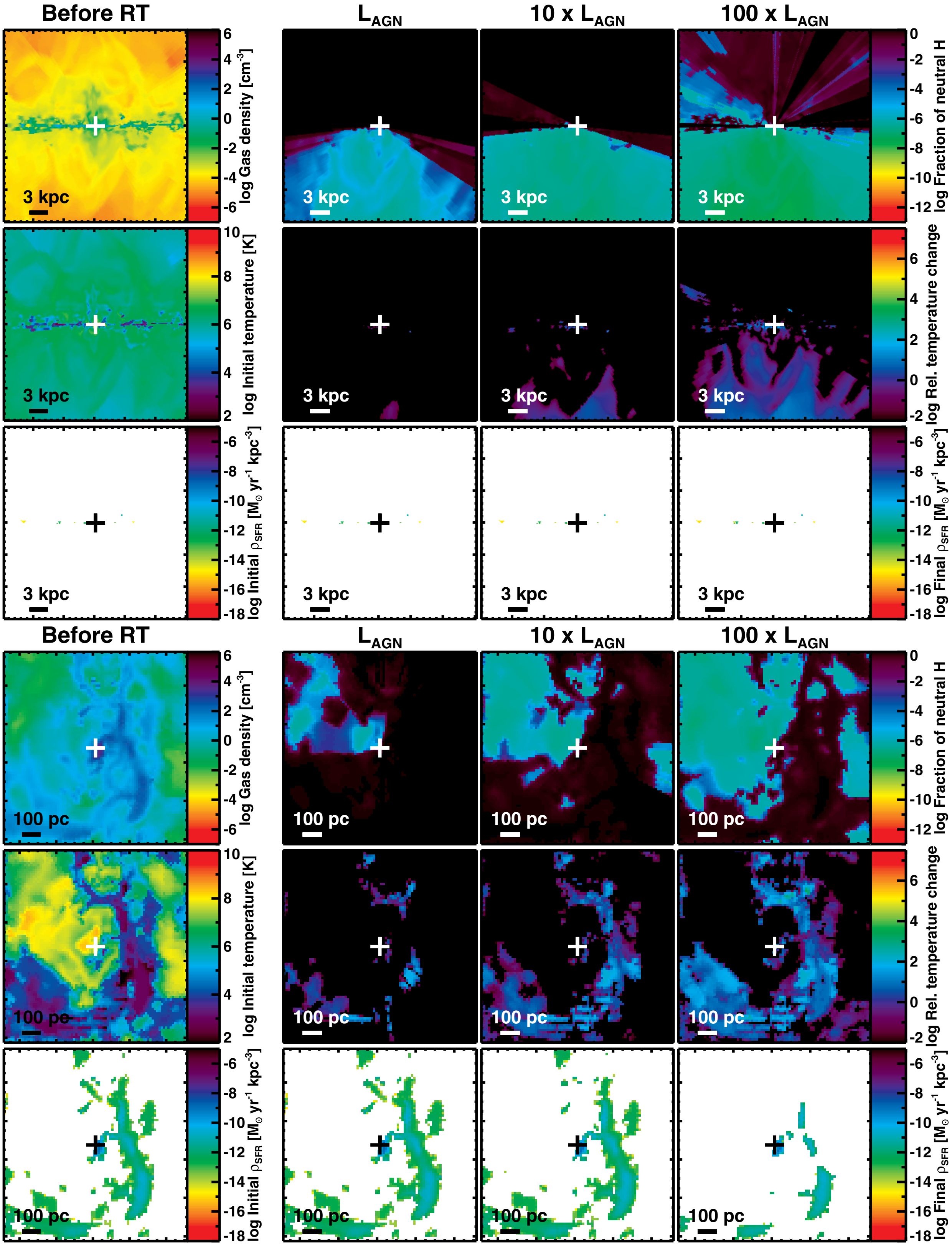

Figure A4. Large edge-on and zoomed face-on views of the simulated galaxy (snapshot 4). Top row: hydrogen density, fraction of neutral hydrogen after RT. Middle row: temperature before RT, relative temperature change. Bottom row: $\rho_{\rm SFR}$ before RT, $\rho_{\rm SFR}$ after RT. The “+” sign shows the location of the black hole and the density threshold for SF is $10\,{\rm cm}^{-3}$. Parameters after RT are given for the three AGN luminosities ($L_{\rm AGN} = 10^{44.5}\,{\rm erg\,s}^{-1}$).

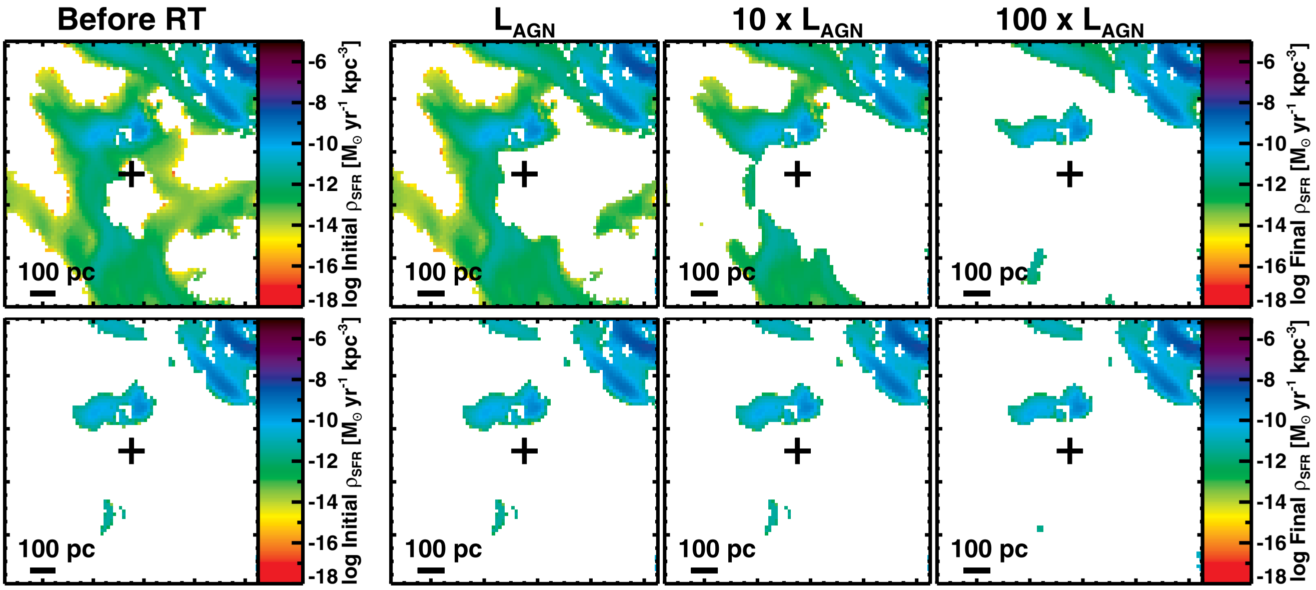

Figure A5. SFR density maps before RT (left column) and after RT (right three columns) for the three AGN luminosities. Top line shows a density threshold for star formation of 1 cm^{-3}, bottom line of 100 cm^{-3}. $L_{\rm AGN} = 10^{44.5}$ erg s^{-1}. With a lower threshold, star-forming regions are more extended but the extra contribution to the total SFR is small (see Figure A6).

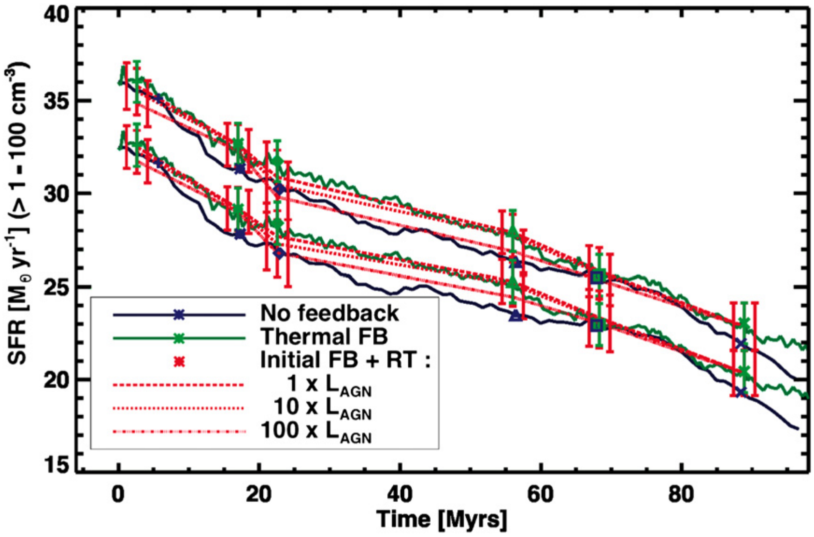

Figure A6. Star formation rate as a function of time. Same key as Figure 10. This figure differs from Figure 10 in that we test different SF thresholds: the lower group of curves corresponds to a density threshold for star formation of 100 cm^{-3}, and the upper one to a threshold of 1 cm^{-3}. The star-forming regions that are cut with a higher threshold are minor contributors to the total SFR along time (<7%).

This weak dependency is also expected from Figure A7, showing the fraction of initial SFR per density bin: most of the SFR lies in the densest cells and cutting at 1, 10, or 100 cm^{-3} does not influence the total SFR calculation much. The shape of this SFR-weighted gas density PDF, dominated by high densities, is typical for simulations of standard SFGs (Teyssier et al. 2010). Hence, whatever the value of the threshold (1, 10, or 100 cm^{-3}, as long as it is low enough not to include the bulk of the star-forming phase; see Figure A7), the fraction of missed SFR is very small, and the behavior is identical.

APPENDIX D

ROLE OF THE FILLING FACTOR

In the Cloudy calculation, the filling factor is set to account for the clumpiness of the gas in the sphere based on the one-dimensional profile. When considering a sphere containing a set of gas condensations separated by empty regions, the filling factor ff corresponds to the fraction of volume occupied by the condensations (Osterbrock & Flather 1959). The specified density is that in the condensations. The mass of the galaxy is given by:

$$M = \sum_i \rho_i^{\rm sim} \times V_i = \sum_i \left(ff_i \times \rho_i^{\rm cloudy}\right) \times V_i, \qquad \text{(D1)}$$

where M is the total mass of the galaxy and ff_i, $\rho_i^{\rm sim}$, and V_i are respectively the filling factor, original mass density and volume of cell i and $\rho_i^{\rm cloudy}$ is the density specified for Cloudy runs. To conserve the mass of the galaxy, the density in each cell is divided by the filling factor before the Cloudy computation (see Equation (D1)). All densities output by Cloudy are multiplied

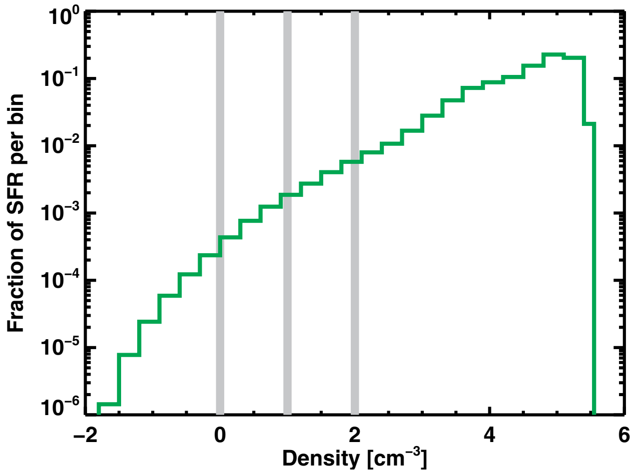

Figure A7. Fraction of SFR per density bin before RT. The vertical gray lines are the three varied density thresholds for star formation. The major contributors to the total SFR have densities above 10^3 cm^{-3} and to cut at 1, 10 or 100 cm^{-3} makes no significant changes.

back by the filling factor before performing the next step of the analysis. In the main study, the value of the filling factor is set to 0.2, which is small enough to account for the clumpiness of the ISM, but still in agreement with the mass refinement criterion (i.e., multiplying the density by five will not change the level of refinement of the cell).

D.1. Constant Density Profile

To study the role of the filling factor, we use the constant density profiles presented in Section 4.1 and compare three values of the filling factor (1, 0.2, and 10^{-3}). We also study the difference between profiles with the original density (conservation of density) versus density divided by the filling factor (conservation of mass):

1. At constant density, the smaller the filling factor, the further the ionization gets into the disk, favoring the hypothesis that the holes between the clumps are necessary for AGN radiation to propagate past the central kiloparsecs.
2. At constant mass, the smaller the filling factor, the closer the ionization is stopped in the disk. This can easily be understood by considering the column density of the encountered gas. Indeed, the first cloud encountered is denser and its recombination time is shorter if the filling factor is smaller. The critical column density needed to stop the AGN radiation is thus reached closer to the BH when decreasing the filling factor, even if the condensations are less numerous and the fraction of volume occupied is smaller.

Both behaviors can also be explained from the theoretical point of view. From Osterbrock & Ferland (2006), the number of recombination Q for hydrogen is proportional to the proton density n_p, the electron density n_e and the filling factor ff:

$$Q \propto ff \times n_p \times n_e. \tag{D2}$$

In the conserved density case, the number of recombinations only depends on the filling factor and thus decreases accordingly. This is consistent with the ionization front being located further in the disk. In the conserved mass case, since the densities are divided by ff, Q goes with the inverse of the filling factor and is larger for a smaller filling factor.

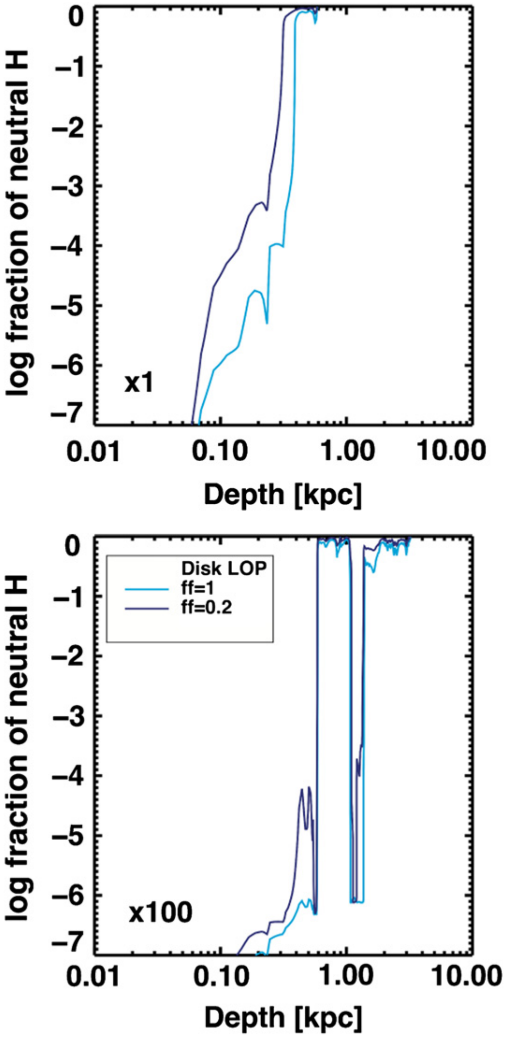

Figure A8. Fraction of neutral hydrogen for a typical LOP in the plane of the disk (as shown in Figure 4) with $ff = 1$ (light blue) and $ff = 0.2$ (dark blue). Same panels as Figure 14. Changing the filling factor does not affect dense star-forming regions but allows diffuse regions to be ionized to a greater extent.

D.2. Typical LOP

We also study the effect of the filling factor on a typical profile of a LOP in the disk plane (see Figure A8 for $ff = 1$ and 0.2; the low filling factor (10^{-3}) was not studied because it would conflict with the mass refinement criterion). At all AGN luminosities, the diffuse regions of the LOP ($n < 10^1$ cm^{-3} regions located less than 500 pc away from the BH and the ionization spots defined in Section 4.3) are ionized to a greater extent when ff is larger, whereas the denser parts show no significant differences. This is easily understood since, in diffuse regions, the density is smaller when ff is larger (since mass is conserved) and the path length needed to reach the column density that stops AGN radiation is larger. Thus AGN ionization goes further in the disk and gas is ionized to a greater degree. In contrast, the density in dense regions is large enough to shield the gas, whatever the filling factor. Therefore, we do not expect the effect of AGN radiation on SF to depend on the filling factor.

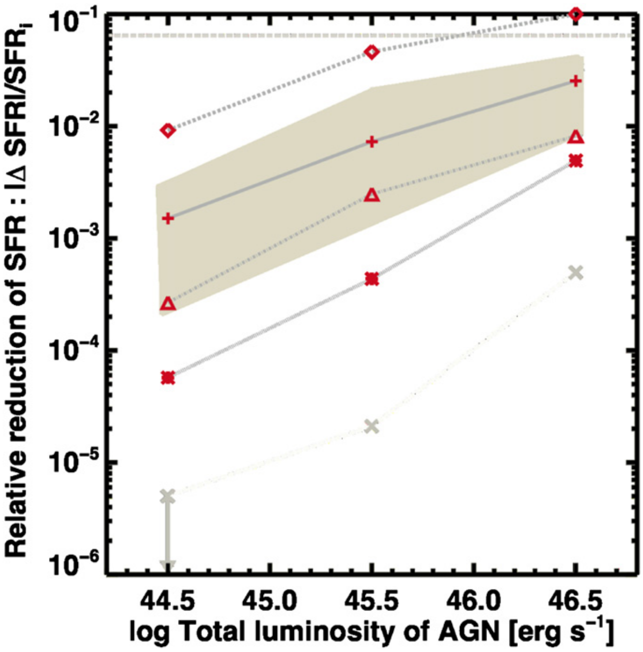

Figure A9. Relative reduction of the star formation rate after radiative transfer as a function of AGN luminosity. Each symbol represents a low resolution snapshot. They are linked for clarity. The beige shaded area, curve, and points recall the data for the high resolution snapshots shown in Figure 11. The median of the relative reduction of the SFR at each luminosity regime is the same as for the high resolution run.

APPENDIX E

EFFECT OF RESOLUTION

In our simulations, the GMCs are resolved, which means that some internal structure is visible, and that they are not at the numerical limit. Furthermore, the SFR of such a simulated galaxy is converged with resolution since the comparison of simulations at ~1 pc resolution (Bournaud et al. 2010) and 0.05 pc resolution (Renaud et al. 2013) shows no difference in the internal parsec-scale substructures of GMCs. Thus, with a higher resolution, we would not get smaller and denser clumps separated by more numerous holes, and the PSD of the ISM would remain the same.

However, as suggested by the study of the filling factor, degrading the resolution could induce significant changes by reducing the number of holes between the clumps. We ran the simulation with AGN feedback from $t = 0$ to 88 Myr with a ~12 pc resolution (one level of refinement less than the runs used in the main study) and chose a few snapshots, close in time to those of the high-resolution run. The simulation is run over the same period of time as the high resolution one in order to have comparable gas consumptions. However, one has to wait for the GMCs to be disrupted and re-grown at lower resolution, which is why we only study four snapshots, close in time to the last 4 snapshots of the high resolution run. The star-forming clumps are thus consistently grown at both resolutions. The PSDs of both high and low resolution snapshots are alike, which means that the intensity of the density fluctuations does not change with resolution. Thus, each pair of high/low resolution snapshots has a similar, though not identical, distribution of gas, and the series of snapshots have to be compared on average.

The low resolution simulation lacks very dense clumps ($n \sim 10^6$ cm^{-3}) compared to the high resolution run and, as the mass of the galaxy is the same, clouds are more extended. Dense clumps at $n \sim 10^{4-5}$ cm^{-3}, as that located on the BH in snapshot 6 of the high resolution run, are present in both high and low resolution runs since the resolution is high enough to reach such densities. However, such configurations are rare, which is why we do not have such a configuration among the low resolution snapshots.

The SFR is lower since there are fewer very dense star-forming clumps. However, the relative reduction of the SFR can be compared in both high and low resolution simulations and that of the low resolution run is shown in Figure A9. Even though the dispersion is larger for these particular low resolution snapshots compared to the high resolution ones, the median is the same as that of the high resolution snapshots, making both results compatible. This tends to show that degrading the resolution of a factor two has no impact on the analysis.

REFERENCES

Begelman, M. C., & Cioffi, D. F. 1989, ApJ, 345, 21
Booth, C. M., & Schaye, J. 2009, MNRAS, 398, 53
Bournaud, F., Dekel, A., Teyssier, R., et al. 2011, ApJL, 741, L33
Bournaud, F., Elmegreen, B. G., Teyssier, R., Block, D. L., & Puerari, I. 2010, MNRAS, 409, 1088
Bournaud, F., Juneau, S., Le Floc'h, E., et al. 2012, ApJ, 757, 81
Cayatte, V., Kotanyi, C., Balkowski, C., & van Gorkom, J. H. 1994, AJ, 107, 1003
Cicone, C., Maiolino, R., Sturm, E., et al. 2014, A&A, 562, A21
Ciotti, L., & Ostriker, J. P. 1997, ApJL, 487, L105
Croft, S., van Breugel, W., de Vries, W., et al. 2006, ApJ, 647, 1040
Croton, D. J., Springel, V., White, S., et al. 2006, MNRAS, 365, 11
Curran, S. J., & Whiting, M. T. 2012, ApJ, 759, 117
Curran, S. J., Whiting, M. T., Murphy, M. T., et al. 2006, MNRAS, 371, 431
Curran, S. J., Whiting, M. T., Wiklind, T., et al. 2008, MNRAS, 391, 765
DeBuhr, J., Quataert, E., & Ma, C.-P. 2011, MNRAS, 412, 1341
Di Matteo, T., Springel, V., & Hernquist, L. 2005, Natur, 433, 604
Diamond-Stanic, A. M., & Rieke, G. H. 2012, ApJ, 746, 168
Dobbs, C. L., Glover, S. C. O., Clark, P. C., & Klessen, R. S. 2008, MNRAS, 389, 1097
Dove, J. B., Shull, J. M., & Ferrara, A. 2000, ApJ, 10, 846
Dubois, Y., Devriendt, J., Slyz, A., & Teyssier, R. 2012, MNRAS, 420, 2662
Dubois, Y., Gavazzi, R., Peirani, S., & Silk, J. 2013, MNRAS, 433, 3297
Dugan, Z., Bryan, S., Gaibler, V., Silk, J., & Haas, M. 2014, ApJ, 796, 113
Elbaz, D., Dickinson, M., Hwang, H. S., et al. 2011, A&A, 533, A119
Elbaz, D., Jahnke, K., Pantin, E., Le Borgne, D., & Letawe, G. 2009, A&A, 1374, 1359
Elmegreen, B. G. 2002, ApJ, 577, 206
Elmegreen, B. G. 2007, ApJ, 668, 1064
Elmegreen, B. G., Bournaud, F., & Elmegreen, D. M. 2008, ApJ, 688, 67
Elvis, M., Wilkes, B. J., McDowell, J. C., et al. 1994, ApJS, 95, 1
Esquej, P., Alonso-Herrero, a., González-Martín, O., et al. 2014, ApJ, 780, 86
Feain, I. J., Papadopoulos, P. P., Ekers, R. D., & Middelberg, E. 2007, ApJ, 662, 872
Ferguson, J. W., Korista, K. T., & Ferland, G. J. 1997, ApJS, 110, 287
Ferland, G. J., Porter, R. L., van Hoof, P. A. M., et al. 2013, RMxAA, 49, 137
Feruglio, C., Maiolino, R., Piconcelli, E., et al. 2010, A&A, 518, 155
Gabor, J. M., & Bournaud, F. 2013, MNRAS, 434, 606
Gabor, J. M., & Bournaud, F. 2014, MNRAS, 441, 1615
Gaibler, V., Khochfar, S., Krause, M., & Silk, J. 2012, MNRAS, 425, 438
Graham, J. A. 1998, ApJ, 502, 245
Hainline, K. N., Hickox, R., Greene, J. E., Myers, A. D., & Zakamska, N. L. 2013, ApJ, 774, 145
Heyer, M. H., & Terebey, S. 1998, ApJ, 502, 265
Hickox, R. C., Mullaney, J. R., Alexander, D. M., et al. 2014, ApJ, 782, 11
Hönig, S. F. F., & Kishimoto, M. 2010, A&A, 523, A27
Hopkins, P. F., Hernquist, L., Cox, T. J., et al. 2006, ApJS, 163, 1
Juneau, S., Dickinson, M., Bournaud, F., et al. 2013, ApJ, 764, 176
Karouzos, M., Im, M., Trichas, M., et al. 2014, ApJ, 784, 137
Keel, W. C., Chojnowski, S. D., Bennert, V. N., et al. 2012, MNRAS, 420, 878
Kennicutt, R. C. 1998, ApJ, 498, 541
Klamer, I. J., Ekers, R. D., Sadler, E. M., & Hunstead, R. W. 2004, ApJ, 612, 97
Kraljic, K., Renaud, F., Bournaud, F., et al. 2014, ApJ, 784, 112

LaMassa, S. M., Heckman, T. M., Ptak, a., & Urry, C. M. 2013, ApJL, 765, L33
Li, Y., Hernquist, L., Robertson, B., et al. 2007, ApJL, 665, L187
Liu, C., Yuan, F., Ostriker, J. P., Gan, Z., & Yang, X. 2013a, MNRAS, 434, 1721
Liu, G., Zakamska, N. L., Greene, J. E., Nesvadba, N. P. H., & Liu, X. 2013b, MNRAS, 430, 2327
Maloney, P. R. 1999, Ap&SS, 266, 207
Marconi, A., Risaliti, G., Gilli, R., et al. 2004, MNRAS, 351, 169
Martizzi, D., Teyssier, R., & Moore, B. 2012, MNRAS, 420, 2859
Matsuoka, Y. 2012, ApJ, 750, 54
Mathews, W. G., & Capriotti, E. R. 1985, in Astrophys. of Active Galaxies and Quasi-stellar Objects (Mill Valley, CA: Univ. Sci. Books), 185
Matzner, C. D., & McKee, C. F. 2000, ApJ, 10, 364
Merloni, A. 2004, MNRAS, 353, 1035
Morisset, C. 2006, in IAU Symp. 234, Planetary Nebulae in Our Galaxy and Beyond, ed. M. J. Barlow & R. H. Mendez (Cambridge: Cambridge Univ. Press), 467
Morisset, C. 2013, in Astrophysics Source Code Library, pyCloudy: Tools to Manage Astronomical Cloudy Photoionization Code, ascl:1304.020
Mullaney, J. R., Daddi, E., Béthermin, M., et al. 2012a, ApJL, 753, L30
Mullaney, J. R., Pannella, M., Daddi, E., et al. 2012b, MNRAS, 419, 95
Müller-Sánchez, F., Prieto, M. A., Hicks, E., et al. 2011, ApJ, 739, 69
Murray, N. 2011, ApJ, 729, 133
Osterbrock, D. E., & Ferland, G. J. 2006, Mercu, 35, 40
Osterbrock, D. E., & Flather, E. 1959, ApJ, 129, 26
Prieto, M. A., Reunanen, J., Tristram, K. R. W., et al. 2010, MNRAS, 402, 724
Proga, D., Jiang, Y.-F., Davis, S. W., Stone, J. M., & Smith, D. 2014, ApJ, 780, 51
Rathborne, J. M., Jackson, J. M., Chambers, E. T., et al. 2010, ApJ, 715, 310
Renaud, F., Bournaud, F., Emsellem, E., et al. 2013, MNRAS, 436, 1836
Renaud, F., Kraljic, K., & Bournaud, F. 2012, ApJL, 760, L16
Ricci, C., Ueda, Y., Ichikawa, K., et al. 2014a, A&A, 142, A142
Ricci, T. V., Steiner, J. E., & Menezes, R. B. 2014b, MNRAS, 440, 2419
Rosario, D. J., Santini, P., Lutz, D., et al. 2013, ApJ, 771, 63
Rosdahl, J., Blaizot, J., Aubert, D., Stranex, T., & Teyssier, R. 2013, MNRAS, 436, 2188
Sales, D. A., Ruschel-Dutra, D., Pastoriza, M. G., Riffel, R., & Winge, C. 2014, MNRAS, 441, 630
Schawinski, K., Thomas, D., Sarzi, M., et al. 2007, MNRAS, 382, 1415
Schaye, J. 2001, ApJ, 562, 95
Sijacki, D., Springel, V., Di Matteo, T., & Hernquist, L. 2007, MNRAS, 380, 877
Spoon, H. W. W., Farrah, D., Lebouteiller, V., et al. 2013, ApJ, 775, 127
Stern, D., Lansbury, G. B., Assef, R. J., et al. 2014, ApJ, 794, 102
Teyssier, R. 2002, A&A, 385, 337
Teyssier, R., Chapon, D., & Bournaud, F. 2010, ApJL, 720, L149
Truelove, J. K., Klein, R. I., Mckee, C. F., et al. 1997, ApJ, 489, 179
Urry, C. M., & Padovani, P. 1995, PASP, 107, 803
Veilleux, S., Meléndez, M., Sturm, E., et al. 2013, ApJ, 776, 27
Vogelsberger, M., Genel, S., Sijacki, D., et al. 2013, MNRAS, 436, 3031
Vogelsberger, M., Genel, S., Springel, V., et al. 2014, MNRAS, 444, 1518
Waller, W. H., Clemens, D. P., Sanders, D. B., & Scoville, N. Z. 1987, ApJ, 314, 397
Wurster, J., & Thacker, R. J. 2013, MNRAS, 431, 2513
Yajima, H., Li, Y., Zhu, Q., et al. 2014, MNRAS, 440, 776
Zinn, P.-C., Middelberg, E., Norris, R. P., & Dettmar, R.-J. 2013, ApJ, 774, 66

Chapter 4

Impact of stellar and AGN feedback on the host galaxy

Contents

The baryonic mass budget of the present Universe is well-known, and is inferred for instance from the primordial nucleosynthesis (e.g. Boesgaard & Steigman, 1985; Olive et al., 2000), according to which the majority of light elements (hydrogen, deuterium, helium, lithium) were produced from a few seconds to a few minutes after the Big Bang. However, models accounting for this baryonic mass budget create galaxies which are too massive compared to observations, and also produce too many stars (see e.g. Sommer-Larsen, 2006; Croton et al., 2006; Silk, 2011; Taylor & Kobayashi, 2015). This discrepancy between observations and models was dubbed the "missing baryons problem".

Some of these "missing" baryons, which account for $\sim 80\,\%$ of the total mass budget, are detected around the most massive galaxies[1] (e.g. Sommer-Larsen, 2006), thanks to their extended soft X-ray emission (e.g. Pedersen et al., 2006). As no efficient mechanism is known to prevent baryons from falling inside galaxies on such time-scales (almost the Hubble time), especially since baryons in the haloes of low-mass galaxies are expected to cool down rapidly (e.g. White & Frenk, 1991; Kereš et al., 2005; Dekel et al., 2009), expelling mechanisms removing baryons from galaxies at a rate of several times their star formation rate are needed (stellar winds in low-mass galaxies and AGN-driven winds at high mass, see e.g. Dekel & Silk, 1986; White & Frenk, 1991; Kereš et al., 2005; Dekel et al., 2009).

Even though outflows are observed to be ubiquitous in star-forming galaxies, the ejected mass rate measurements relying on spectroscopy of the host galaxy can vary by several orders of magnitude because they lack information about the distance of the outflowing gas with respect to the galaxy (see e.g. Heckman et al., 1990, 2000; Pettini et al., 2002; Martin et al., 2012, 2013). However, recently, Bouché et al. (2012); Kacprzak et al. (2015); Schroetter et al. (2015) used background quasars

---

[1] Although still inside the virial radius, defined as the radius enclosing an overdensity of N with respect to the critical density of the Universe at a given redshift. A standard value of N is 200 (e.g. Kravtsov, 2013).

to determine the outflow rate more accurately, with low-ionization absorption lines such as Mg II, and found typical outflow rates of two to three times the instantaneous star formation rate, or lower.

This chapter presents the project of high-resolution (down to 1.5 pc) simulations I set up to study the Physical Origins of Galactic Outflows (POGO). I first describe the coupling between stellar feedback processes, and give the scientific motivations for the study of the coupling between AGN and stellar feedback processes, as well as our aims. The last two sections present the results.

4.1 Coupling of stellar feedback models

In typical galaxies, AGNs are not the only wind source: stars create galactic-scale outflows (see Sections 1.3.3 and 1.3.4) which are quite different from AGN winds: while there is usually only one AGN per galaxy and it is located at its center, there are numerous stars and supernovæ distributed all around the galactic disk. Also, as individual stellar outflows merge to create a global outflow (see Section 1.3.3 and e.g. Sharma et al., 2014; Liu et al., 2015), the geometry of the wind at galactic-scale is different. However, stellar winds in normal Main Sequence galaxies (in contrast with starbursts, which are short and rare events) are less powerful than AGN winds: they propagate slower (100 to 500 $\mathrm{km.s^{-1}}$, see Section 1.3.4 and e.g. Bournaud et al., 2014) and, even though they have a higher mass outflow rate than AGN winds, gas is often not able to escape the dark matter halo of massive galaxies (see Gabor & Bournaud, 2014, though see also Tombesi et al. 2015; Feruglio et al. 2015). In the case of weak stellar outflows in massive galaxies, the gas instead tends to fall back on the galaxy, as galactic fountains (see Section 1.3.4) redistributing the material from the center to the outskirts (Binney & Tremaine, 1987) and recycling some of the gas in the circumgalactic medium.

Low-resolution simulations predict that feedback from massive stars and supernovæ (see Section 2.1.4.2 and Dubois & Teyssier, 2008; Renaud et al., 2013) couple non-linearly to each other to create strong winds (e.g Hopkins et al., 2014; Fierlinger et al., 2016). The non-linear coupling is defined by the fact that supernovæ (outflow rate of 2.6 $\mathrm{M_\odot.yr^{-1}}$ for SNe alone, see Figure 4.1a) and young massive stars (outflow rate of 6.3 $\mathrm{M_\odot.yr^{-1}}$ for young massive stars alone) create outflows much more powerful when they are considered simultaneously (outflow rate of 34.1 $\mathrm{M_\odot.yr^{-1}}$, i.e. about 4 times the sum of the aforementioned outflow rates).

Several hypotheses can be made regarding the origin of the non-linear coupling between stellar feedback processes such as winds and ionization from young massive stars and supernova explosions. Indeed, these feedback processes happen on different time scales: in a given star cluster, massive stars clear the way with their winds during their life, and, after ∼ 10 Myr, some of them explode as supernovæ, often in the diffuse region created by the stars during their life. This can lead to various non-linear aspects:

- mechanical aspects: supernovæ tend to explode in regions which were cleared out by the winds of massive stars. Supernovæ can thus be able to push gas further, since diffuse gas is easier to entrain. Also, clustered star formation leads to the explosion of an average of a few supernovæ in a relatively small region, which enhances the latter effect and can lead to super-bubbles (see Section 1.3.3 and e.g. Sharma et al., 2014; Liu et al., 2015);

- thermal aspects: in the same scenario as above, successive supernovæ explode in diffuse gas, which is heated more efficiently. The cooling time is thus longer and the energy is radiated away less rapidly, resulting in more powerful winds.

Though, to not overestimate this effect, it is important to resolve the propagation of the outflows both spatially (i.e. down to pc-scale) and temporally (accurate CFL condition, see Equation 2.3). Indeed, if the resolution is too low, super-bubbles can be artificially created because the low space and/or time resolution leads to the artificial merging of two flows, which would otherwise have crossed each other, and kept most of their momentum. However, if there is indeed a physical non-linear coupling between stellar feedback processes at high resolution, it is crucial to have an accurate modelling of all stellar feedback processes (among which supernovæ and massive stars) in star-forming galaxies, and account for them simultaneously.

Typically, stellar winds have a rather high mass outflow rate, so they may lift enough mass to explain the “missing baryons problem”, but their expelling efficiency is not sufficient because of their relatively low velocities (100 to 500 $\mathrm{km.s^{-1}}$, see Section 1.3.4 and e.g. Bournaud et al., 2014). Therefore, it is not sufficient to artificially boost stellar outflows to solve the “missing baryons problem”, and another source of outflows is needed.

In contrast with stellar outflows, AGN winds propagate fast (3,000 – 30,000 $\mathrm{km.s^{-1}}$, e.g. Chartas et al., 2014), but they do not entrain much mass compared to stellar outflows. A non-linear coupling between the two feedback sources could create powerful winds which are at the same time fast, and highly mass-loaded, in potential agreement with the amount of baryons located around galaxies. Furthermore, to expel enough gas to explain the “missing baryons problem” in a durable manner, we need to study the interplay between the two feedback sources on the long term, and not just through rare episodes of extreme starbursts or quasars.

4.2 Combination of stellar and AGN feedback

Following the idea that different models of stellar feedback can couple non-linearly to create powerful winds (see Figure 4.1), I wrote a PRACE (Partnership for Advanced Computing in Europe) proposal to study the coupling between stellar feedback and AGN feedback, in order to check whether it could lead to winds powerful enough to eject several times the amount of gas turned into stars.

The PRACE organization federates all the largest super-computing centers in Europe and distributes computation time in many areas of science and industry. PRACE especially promotes the most innovative and high-technology projects. The super-computer Curie — on which were performed all simulations presented here — is hosted at the TGCC (Très Grand Centre de Calcul — Very

Big Computation Center) in Bruyères-le-Châtel, France, and belongs to CEA (the French Commission for Atomic Energy and Alternate Energies). Also, part of the simulations presented here (and those presented in Chapter 3) were performed on Curie at Tier - 1 level, with a GENCI allocation (GENCI: Grand Équipement National de Calcul Intensif — Big National Intensive Computation Equipment, the French HPC agency).

I was granted 11 million hours of computation time as the principal investigator (PI) of the POGO Project, with which I study the Physical Origins of Galactic Outflows at high resolution (from 12 down to 1.5 pc). With this Tier - 0 allocation, I consider typical galaxies on the Main Sequence of star formation at redshift 2, and study whether it is possible to generate outflows with mass outflow rates of a few times their star formation rate (SFR), together with velocities above the escape velocity of the dark matter halo — which could explain the fraction of baryons located outside galaxies to some extent, and if yes, identify the main driver(s).

Thanks to high resolution (down to 1.5 pc), gas fueling on the AGN is resolved at parsec-scale, which was not the case in e.g. Gabor & Bournaud (2013, 2014). Also, the structure of the interstellar medium is resolved on 10 orders of magnitude (from 10^{5-6} cm^{-3} to 10^{-5--6} cm^{-3}) and stars are formed in resolved clumps. Furthermore, an accurate modelling of stellar feedback (kinetic and thermal SN feeback and massive stars radiative feedback) is important because the presence of stellar feedback changes the outflow rate, even though it does not change the SFR much (Renaud et al., 2013). This combination generates a slow outflow, in contrast with high-velocity AGN winds. Taking both accurate stellar feedback and AGN feedback into account is important since non-linear processes between the two feedback models can either enhance or reduce the strength of the galactic wind. Moreover, there are currently few simulations with all these elements at high (12 to 1.5 pc) resolution (see e.g. Booth & Schaye, 2013; Costa et al., 2015; Melioli & de Gouveia Dal Pino, 2015; Hopkins et al., 2016) and the POGO simulations thus bring new insights to the field.

4.2.1 The POGO Project: Physical Origins of Galactic Outflows

With the POGO Project, we study the coupling between the outflows generated by the AGN and by the stars (including young stars and SNe) in a typical Main Sequence galaxy at redshift 2, together with their impact on the host in terms of mass outflow rate and star formation activity.

In the POGO simulations, we use three feedback configurations: AGN feedback only (see Section 2.1.4.2 and Chapter 3), stellar feedback only (see Sections 2.1.4.2 and 4.1), and both feedback models, to identify the main outflow driver(s). The parameters of each run are summed up in Table 4.1 (see Roos et al., 2016, submitted to ApJ, for more details). AGN feedback is a sub-grid energy injection but, thanks to the high resolution of the simulation (12 to 1.5 pc), the propagation of outflows and their loading in mass are resolved. Also, we study three galaxy masses spanning the range of typical Main Sequence galaxies at both low and high redshift (Daddi et al., 2007; Noeske et al., 2007; Elbaz et al., 2011), in order to investigate the relation between the stellar mass of the galaxy, and the mass outflow rates of the galactic winds.

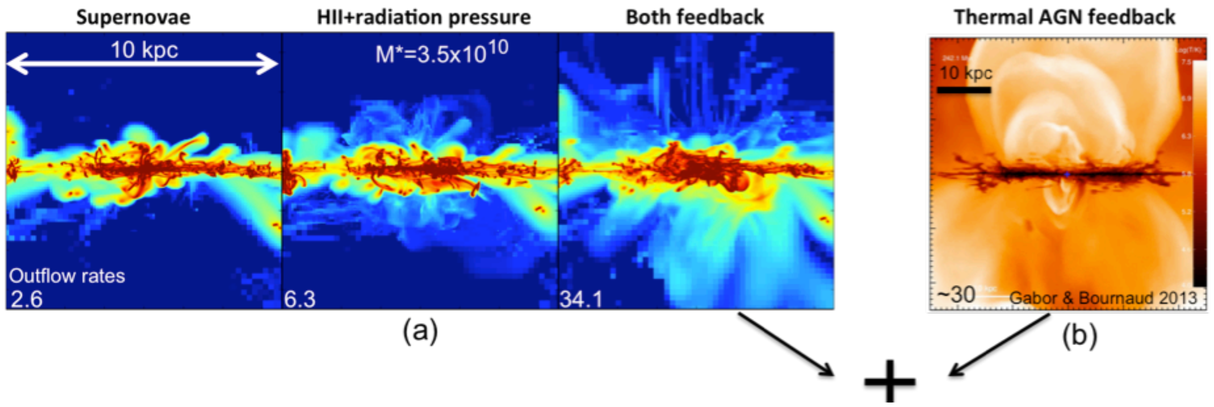

Figure 4.1: Coupling of feedback processes. (a) The three panels show the mass-weighted gas density in a typical star-forming galaxy at redshift 2, seen edge-on. The camera is zoomed on the outskirts of the disk. Outflow rates are indicated in $M_\odot.yr^{-1}$. *Left:* Outflows from kinetic supernova feedback. *Middle:* Outflows from radiative feedback from massive stars. *Right:* Outflows from both models. The coupling between kinetic supernova feedback and radiative pressure feedback from young massive stars is non-linear and generates powerful winds (outflow rate of 34.1 $M_\odot.yr^{-1}$ compared to 2.6 and 6.3 $M_\odot.yr^{-1}$ respectively). (b) Same as Figure 3.1. Depending on the stellar mass of the host, the coupling of AGN and stellar feedback can either enhance the mass outflow rate of the winds (low-mass simulation), or reduce it (intermediate- and high-mass simulations, see Section 4.2.2). This Figure was published in Roos & Bournaud (2015) and is based on simulations by Renaud et al. (2013) and Gabor & Bournaud (2013, 2014).

We use high spatial resolution (12 to 1.5 pc, and 7 levels of refinement) to avoid numerical coupling and measure *physical* coupling: if resolution is not high enough, individual stellar outflows with non-parallel momenta could merge and be artificially coupled, whereas at higher resolution, they would just go through each other and conserve most of their momentum (see above). The same could happen at larger scales with stellar winds and AGN winds.

Also, we follow the propagation of outflows long enough (a few hundreds of million years) to study the steady state of the outflows in a box of size 200 kpc, and check whether we reproduce the outflow acceleration inside the halo that has been recently observed (Schroetter et al., 2015).

At all masses studied, the mass outflow rate is expected to be quite high (several times the SFR of the galaxy), but at both the low- and high-mass ends, one of the two outflow drivers (stars at low mass, the AGN at high mass) could start to dominate the outflow driving (see e.g. Stinson et al., 2013; Hopkins et al., 2014; Keller et al., 2016).

The modelling of the outflows driven by the stars and the AGN together faces a technical difficulty: slow stellar outflows propagate in the circumgalactic medium on long timescales, while AGN winds reach high velocities ($\sim$ 3,000 $km.s^{-1}$ on average) that impose short numerical time-steps. This makes galaxy simulations 4 - 5 times longer, even if computing the AGN-related physics is not expensive itself. Therefore, the use of the latest super-computing facilities is required.

Name	Resolution [pc]	Feedback model(s)	Initial gas mass [$M_\odot$]
M1	1.5	Stellar+AGN	$1.5.10^{10}$
L1	3		
LL1	6		
M1_stellar	1.5	Stellar only	
L1_stellar	3		
LL1_stellar	6		
M1_AGN	1.5	AGN only	
L1_AGN	3		
LL1_AGN	6		
M2	1.5	Stellar+AGN	$4.9.10^{10}$
L2	3		
LL2	6		
M2_stellar	1.5	Stellar only	
L2_stellar	3		
LL2_stellar	6		
M2_AGN	1.5	AGN only	
L2_AGN	3		
LL2_AGN	6		
M3	1.5	Stellar+AGN	$11.5.10^{10}$
L3	3		
LL3	6		
LLL3	12		
LLL3_stellar	12	Stellar only	
LLL3_AGN	12	AGN only	

Table 4.1: The feedback configurations and spatial resolutions of the 24 simulations of the POGO project. The simulations runs are named according to their mass (M1, M2, M3), their feedback models (fiducial, AGN only, stellar only), and their resolution, with L1 standing for low-resolution M1 (one level of refinement less), LL1 for low-low-resolution M1 (two levels of refinement less), and so on. The gas masses span the range of masses of typical Main Sequence disks at both high and low redshift (e.g. Daddi et al., 2007; Noeske et al., 2007; Elbaz et al., 2011). The gas fraction is about 50 % during the runs.

4.2.2 Galactic winds and mass outflow rates in the POGO simulations

The section includes the scientific article about the outflow properties (gas density, temperature and velocity) and mass outflow rates in the POGO simulations, submitted to the Astrophysical Journal (Roos et al., 2016).

The conclusions of the paper are as follows:

- The AGN is the main outflow driver at all masses we studied: the properties of the global outflow (AGN or stellar+AGN) do not depend on the presence of stellar feedback. Depending on the mass of the host, the maximal mass outflow rates of the stellar+AGN configuration range between a few time the star formation rate of the host to 20 time the star formation rate, and velocities reaching several 10^3 km.s^{-1};

- Despite this, stellar feedback must be accurately accounted for since it can either enhance or reduce the mass outflow rate, depending on the mass of the host:
    - at low mass ($M_{gas} = 1.5.10^{10}\ M_{\odot}$), stellar and AGN feedback combined give birth to a wind with a mass outflow rate of about twice that of the wind produced by AGN feedback only. This likely comes from the fact that stellar feedback feeds the central supermassive black hole. Also, dense gas is pushed up by stellar feedback above/under the galactic disk, and then swept by the AGN bursts inside the overall wind, therefore adding mass into the global outflow. Finally, between two AGN bursts, stellar outflows have time to rise again in a diffuse and hot circum-galactic medium, which could enhance their outflow rate compared to the case where the circum-galactic medium is not regularly cleared out by AGN bursts;
    - at intermediate mass ($M_{gas} = 4.9.10^{10}\ M_{\odot}$), stellar outflows do not feed the black hole as efficiently as in the low-mass case, redistribute the gas from the center of the galaxy to its outskirts and are too weak to lift gas high and/or long enough for the AGN to sweep it into the global outflow. While this gas redistribution also happens for the low-mass simulations, the weakness of stellar outflows at higher mass does not (over-)compensate the loss of gas to be expelled. This results in a stellar+AGN winds less mass-loaded than the AGN wind;
    - at high mass ($M_{gas} = 11.5.10^{10}\ M_{\odot}$), the mass outflow rate of the stellar winds, AGN winds, and stellar and AGN winds seem of the same order of magnitude. However, we caution that the results at high mass could be biased due to the short duration of the run and the presence of stellar+AGN outflows at the beginning of the simulations.
- AGN outflows and outflows from stellar and AGN feedback speed up in the gaseous halo of the galaxy, from 1 kpc above the galactic disk to the limits of the box, in remarkable agreement with Schroetter et al. (2015);
- AGN and stellar+AGN outflows fill the circum-galactic medium with successive expanding bubbles of gas which are hotter than the ambiant gas. The circum-galactic medium thus quickly becomes inhomogeneous in both temperature and density. Therefore, assuming that galactic outflows are smooth is not a good approximation.
- The velocity of the expanding bubbles is larger than the escape velocity of the halo and, at large scale, they shock against the hot and diffuse gas (with velocity smaller than the escape velocity) of the initial circumgalactic medium.

4.2.3 Additional impact of AGN photo-ionization on star formation in the POGO simulations

Given the results described in Section 3.2 and in Roos et al. (2015), we expect the additional effects of AGN photo-ionization (computed using the "Cloudification" method described in Section 3.2.2.3 and Roos et al., 2015) on the star formation activity of the POGO galaxies to be negligible. The reasons are as follows:

- the gas distribution and the behaviour of the outflows with respect to it is the same, i.e.: the outflowing gas leaves the galactic disk through the paths of least resistance and does not affect the star-forming regions at large scale (see Figure 1 of Roos et al., 2016),
- the expelled gas is too hot and too diffuse to form stars (i.e.: densities lower than 100 cm^{-3} and temperatures higher than 10^4 K, see Figure 4 of Roos et al., 2016).

Nevertheless, the comparison of the "Cloudification process" with simulation runs using RAMSES-RT (Rosdahl et al., 2013) is relevant, first to improve the sub-grid recipes of RAMSES-RT and second, to overcome the drawbacks of the "Cloudification process" (see Section 3.2.2.5), such as the lack of outflow driving due to AGN radiative pressure (staticity of the method), and the impossibility to re-inject the ionization properties in the simulations from one time-step to the next (too long).

Thus, the computation of AGN photo-ionization is planned for some snapshots of the POGO simulations, in order to compare with short RAMSES-RT post-production runs (with hydrodynamics disabled) on the same snapshots.

* * *

SUBMITTED TO THE ASTROPHYSICAL JOURNAL
Preprint typeset using LaTeX style emulateapj v. 04/17/13

MASS OUTFLOW RATES OF WINDS FROM ACTIVE GALACTIC NUCLEI AND STARS IN REDSHIFT ~ 2 STAR-FORMING GALAXIES

ORIANNE ROOS[1*], FRÉDÉRIC BOURNAUD[1], FLORENT RENAUD[2], JARED M. GABOR[1,3], YOHAN DUBOIS[3], JOAKIM ROSDAHL[4], VALENTIN PERRET[5] AND ROMAIN TEYSSIER[5]
[1]Laboratoire AIM Paris-Saclay, CEA/IRFU/SAp, CNRS, Université Paris-Diderot, F-91191 Gif-sur-Yvette Cedex, France
[2]Department of Physics, University of Surrey, Guildford, GU2 7XH, United Kingdom
[3]Institut d'Astrophysique de Paris, UMR 7095, CNRS, UPMC Université Paris VI, 98bis boulevard Arago, F-75014, Paris, France
[4]Leiden Observatory, Leiden University, PO Box 9513, NL-2300 RA Leiden, the Netherlands and
[5]Institute for Computational Science, University of Zurich, CH-8057 Zürich, Switzerland

(Received receipt date; Revised revision date; Accepted acceptance date)
submitted to the Astrophysical Journal

ABSTRACT

Galactic-scale outflows are ubiquitous in observations of star-forming galaxies up to high redshift, and are a good candidate to remove an amount of gas of a few times the star formation rate from their host. Such galactic outflows are generated by internal sources of feedback: young stars, supernovæ and active galactic nuclei (AGNs). However, the physical origins of such outflows are not well understood yet, and their major driver(s) are still debated. Up to now, most simulations still fail to reproduce all observed parameters at the same time, such as the mass outflow rate and the velocity of the winds. In this paper, we present the POGO project: Physical Origins of Galactic Outflows. With this suite of 24 simulations, we model AGN and stellar feedback simultaneously and based on physical assumptions at high resolution (1.5 - 12 pc), and study their impact on the properties of the outflows of the host-galaxy. Here, we show that AGN and stellar feedback couple non- linearly, but that the AGN remains a major outflow driver at all galaxy masses we studied ($M_* = 1.3$, 4.4 and $10.3 \cdot 10^{10}$ $M_\odot$), which is surprising at low mass. We show that the mass outflow rate depends on the mass of the host, which is crucial to account for in simulations because the coupling between AGN and stellar feedback can be either positive compared to AGN feedback only, and increase the mass outflow rate of the wind (low-mass simulation); or negative, and decrease it (intermediate-mass simulation).

Keywords: galaxies: active – galaxies: high-redshift – galaxies: star formation — galaxies: outflows — methods: numerical

1. INTRODUCTION

Up to now, numerical models accounting for the well-known baryonic mass budget in the present Universe (inferred e.g. from the primordial nucleosynthesis, see Boesgaard & Steigman 1985; Olive et al. 2000) create galaxies which are too massive compared to observations, and also produce too many stars (see e.g. Sommer-Larsen 2006; Croton et al. 2006; Silk 2011; Taylor & Kobayashi 2015). This discrepancy between models and observations — according to which only ~ 20 % of all the baryonic mass is located inside galaxies (Sommer-Larsen 2006) — was dubbed the "missing baryons problem". Here, we study efficient expelling mechanisms included in the models, to check if they can remove baryons from galaxies at a rate of several times their star formation rate (SFR). These expelling mechanisms are thought to be stellar winds in low-mass galaxies and active galactic nucleus (AGN)-driven winds at high mass, (see e.g. Dekel & Silk 1986; White & Frenk 1991; Kereš et al. 2005; Dekel et al. 2009).

From observations, we know that there are ubiquitous outflows at galactic-scale in star-forming galaxies (SFGs) at all redshifts for which interstellar absorption features are accessible (Steidel et al. 2010). However, most simulations to date still fail to reproduce all observed outflow properties at the same time. For example, the velocity of simulated AGN-driven winds matches observations (3,000 - 30,000 km$\cdot$s^{-1}, see e.g. Chartas et al. 2014), but not the mass outflow rate (see Gabor & Bournaud 2014, though see also Tombesi et al. 2015; Feruglio et al. 2015), and vice-versa for young stars and supernovæ (SNe) wind models, which drive outflows with a high mass outflow rate, but a limited velocity of 100 - 500 km$\cdot$s^{-1} (e.g. Bournaud et al. 2014). Also, the outflow speed-up recently observed a few tens of kpc away from the galactic disk in the gaseous halo (Schroetter et al. 2015) is often not reproduced. Furthermore, as opposed to high-resolution simulations of isolated galaxies, most cosmological simulations have wind models which are tuned to reproduce the observed outflow properties (e.g Oppenheimer & Davé 2008; Barai et al. 2013), since the resolution is too low to resolve their propagation and loading in mass. Therefore, cosmological simulations cannot investigate the origin of galactic outflows as we do here, but they are relevant to study the large-scale effects of such outflows on the intergalactic medium (IGM), and provide insights on the representativity of the studies based on isolated galaxies or isolated mergers at large scale.

Currently, the measurements of the observed mass outflow rates of the winds in galaxies rely on the spectroscopy of the host galaxy, and can vary by several orders of magnitude, because of the lack of information about the distance of the outflowing gas with respect to the galaxy (see e.g. Heckman et al. 1990, 2000; Pettini et al. 2002; Martin et al. 2012, 2013). Such measurements were recently improved by using background

---

[*]orianne.roos@cea.fr

quasars and low-ionization absorption lines such as Mg II to determine the outflow rate more accurately. With this method, Bouché et al. (2012); Kacprzak et al. (2015); Schroetter et al. (2015) found typical outflow rates of two to three times the instantaneous star formation rate (SFR) of the host, or lower.

In this paper, we consider typical galaxies of the Main Sequence of star formation at redshift 2, and study whether it is possible to generate outflows with mass outflow rates of a few times the SFR, together with velocities above the escape velocity of the dark matter halo, in potential agreement with the low fraction of baryons inside galaxies. If such outflows are produced, we also aim at identifying their major driver(s).

In contrast with other recent studies of the interplay between AGN and stellar feedback (e.g. Novak et al. 2012; Hopkins et al. 2016), we resolve gas fueling on the AGN at parsec-scale. Therefore, the propagation of the outflows and their loading in mass are resolved, even though AGN feedback is still a sub-grid energy injection (see Section 3). Also, the structure of the interstellar medium (ISM) is resolved on 10 orders of magnitude (from $10^{-5\,-\,-6}$ cm^{-3} to $10^{5\,-\,6}$ cm^{-3}), and stars (stellar particles) are formed in resolved clumps. Finally, the combination of all stellar feedback processes generates a slow outflow, and an accurate modelling of stellar feedback (e.g. kinetic and thermal SN feeback, plus radiative feedback from massive stars) is important because the presence of SN feedback changes the outflow rate (even though it does not change the SFR much). This combination is all the more necessary since it has been shown in some simulations that stellar feedback processes couple non-linearly to produce stronger outflows than when they are taken separately (see e.g. Hopkins et al. 2014; Fierlinger et al. 2016; Roos & Bournaud 2016, and Section 4).

Similarly, the coupling of stellar and AGN winds could lead to the creation of powerful outflows, with velocities and mass outflow rates potentially high enough to give clues about the "missing baryons problem". Based on this and on studies (e.g. Lau et al. 2015) of broad line profiles in the circum-galactic medium (CGM) suggesting that the CGM has non gravitational kinematics and likely comes from galactic winds, we ran a series of simulations to check this hypothesis. This paper presents the first results of the POGO simulations and is organized as follows: we first introduce the POGO suite of simulations (Section 2) and the AGN and stellar feedback models we used (Section 3). We then describe the potential mechanisms leading to the non-linear coupling of stellar outflows (Section 4) and describe our results on the coupling between AGN and stellar outflows in terms of mass outflow rate (Section 5), and the dependence of the mass loading factors on the galaxy mass (Section 6). We finish this paper with a discussion of these results (Section 7) with respect to convergence with resolution, black hole accretion rate, and the long term effects of non-linear coupling between the different sources of outflows in typical galaxies. Our conclusions are in Section 8.

2. THE POGO SUITE OF SIMULATIONS

Table 1
The POGO suite of simulations.

Name	Resol. [pc]	Feedback	Init. M_* [$M_\odot$]
M1	1.5	Stellar+AGN	$1.3{\cdot}10^{10}$
L1	3		
LL1	6		
M1_stellar	1.5	Stellar only	
L1_stellar	3		
LL1_stellar	6		
M1_AGN	1.5	AGN only	
L1_AGN	3		
LL1_AGN	6		
M2	1.5	Stellar+AGN	$4.4{\cdot}10^{10}$
L2	3		
LL2	6		
M2_stellar	1.5	Stellar only	
L2_stellar	3		
LL2_stellar	6		
M2_AGN	1.5	AGN only	
L2_AGN	3		
LL2_AGN	6		
M3	1.5	Stellar+AGN	$10.3{\cdot}10^{10}$
L3	3		
LL3	6		
LLL3	12		
LLL3_stellar	12	Stellar only	
LLL3_AGN	12	AGN only	

Note. — The feedback configurations and spatial resolutions of the 24 simulations of the POGO project. The simulations runs are named according to their mass (M1, M2, M3), their feedback models (fiducial, AGN only, stellar only), and their resolution, with L1 standing for low-resolution M1 (one level of refinement less), LL1 for low-low-resolution M1 (two levels of refinement less), and so on. The gas masses span the range of masses of typical Main Sequence disks at both high and low redshift (Daddi et al. 2007; Noeske et al. 2007; Elbaz et al. 2011). The gas fraction is about 50 % during the runs, which is representative of a redshift 2 disk (Daddi et al. 2010; Tacconi et al. 2010, 2013).

We present the POGO suite of simulations: Physical Origins of Galactic Outflows. With simulations of isolated star-forming disk galaxies at redshift 2, we model several schemes of AGN and stellar feedback simultaneously, with resolution ranging from 12 to 1.5 pc. Our main goal is to see whether powerful outflows with mass outflow rates of a few times the SFR can be created in Main Sequence galaxies at redshift 2, identify the major outflow driver(s) as a function of stellar mass, and the effects of such outflows on the host-galaxy in terms of star formation (SF). Here, we focus on the physical parameters (density, temperature, velocity) of the outflows and on the mass outflow rates. The characteristics of each of the runs are summed up in Table 1.

2.1. *Simulation set-up*

With the code RAMSES (Teyssier 2002), we ran a suite of 24 simulations with three galaxy masses ($M_* = 1.3$, 4.4 and $10.3 \cdot 10^{10}$ $M_\odot$), four spatial resolutions (1.5, 3, 6 and 12 pc) and three feedback configurations: thermal AGN feedback (hereafter, AGN); thermal and kinetic supernova feedback and radiative feedback from young stars (hereafter, stellar); both (hereafter, stellar+AGN), which is the fiducial feedback configuration (see next sections for further details). In the runs where the resolution is the highest, we consider 8 levels of refinement ($l_{\rm min} = 9$, $l_{\rm max} = 17$), and there are $4 \cdot 10^8$ cells in the grid on average. We use a simulation box size of 200 kpc, to have enough space to let the outflows expand and study them in a steady state. The maximal mass resolution of a cell is typically 125 $M_\odot$. Cooling is allowed down to a temperature floor of 100 K, but dense regions are artificially heated based on a density-dependent temperature floor to prevent artificial fragmention, and ensures that the local Jeans length is always resolved by at least a few cells (Truelove et al. 1997).

To solve the equations of motion, the Poisson equation is solved in each cell, and the acceleration of each particle is computed by interpolating the gravitational potential to the position of each particle within the cell.

Dark matter (DM) and stars are treated as particles and behave as collisionless fluids. There are 2 million particles in the simulation box at t = 0, equally distributed between DM and star particles. The DM particles mass resolution is 5 times the stellar mass resolution.

A cell is refined if it contains more than 50 particles (DM or stars), if the Jeans length is not resolved by at least one cell size (Truelove et al. 1997), and if the gas density is above a density threshold set to mimic a pseudo-cooling equation of state (Bournaud et al. 2010).

To prevent too small time-steps due to high sound speeds, the maximal temperature allowed in the simulations is set to $5 \cdot 10^9$ K, which is about two orders of magnitude higher than the temperature of the outflowing gas in the stellar+AGN and AGN feedback runs.

For more details about the simulation set-up, see Sections 2.1 and 2.2 of Gabor & Bournaud (2013).

2.2. *Physical conditions*

At t = 0, the simulation box of each run contains a disk of gas and stars with exponential radial and vertical profiles. Depending on the mass, the cut-off radius ranges between 3 and 7 kpc, and the cut-off height between 600 and 800 pc. The disk is surrounded by a gaseous halo of initial density contrast of 10^{-4} with respect to the gas density at the cut-off height and radius of the disk. The galactic disk is located in the mid-plane of the box. Both gas and stars are initially rotating with a flat rotation curve.

The dark matter halo has a Burkert profile and a mass such that the DM to baryons mass ratio inside the stellar disk radius is 50 %, for consistency with observed rotation curves of $z \sim 2$ star-forming galaxies: the DM profile is rising in the central kpc and then relatively flat (e.g. Förster Schreiber et al. 2011) and galaxies are not dominated by DM inside the stellar disk radius. The radius of the core of the DM halo is half that of the stellar disk. The DM halo is truncated at 10 times the stellar disk radius so that the propagation of ouflows can be accurately followed in the large-scale DM potential well.

The stellar bulge has a Hernquist profile, its half-mass radius is 10% of the stellar disk radius, and it is truncated at 4 times this half-mass radius. Its mass is 10% of the baryonic mass (i.e.: 20% of the stellar mass).

The galaxy masses (see Table 1) span the range of masses of typical Main Sequence disks at both high and low redshift (Daddi et al. 2007; Noeske et al. 2007; Elbaz et al. 2011). The gas fraction in the simulated disks is about 50 % along the runs, which is typical of redshift 2 galaxies (Daddi et al. 2010; Tacconi et al. 2010, 2013).

We run our simulations for several hundreds of million years, which is long enough to study the steady state of the galactic outflows, while still brief enough not to suffer from the lack of cosmological environment and inflows in the simulations (Dekel et al. 2009; Davé et al. 2012).

2.3. *The black hole and the AGN*

The central supermassive black hole (BH) is traced by a sink particle (i.e. a particle able to accrete mass) and is initially placed at the center of the galaxy. Its position is not fixed. The initial BH mass is set according to the Magorrian relation (Magorrian et al. 1998a), i.e. $M_{\rm BH}$ = 1.3, 4.4 and $10.3 \cdot 10^7$ $M_\odot$ for the low-, intermediate- and high-mass galaxy respectively.

Accretion onto the black hole follows the Bondi accretion prescription (Bondi & Hoyle 1944; Bondi 1952) and is capped at the Eddington rate (see Gabor & Bournaud 2013, for further details). AGN feedback is modelled as thermal energy injection in the four cells surrounding the black hole (see next section for further details).

BH accretion is maintained in all runs; only AGN feedback is shut down in the stellar configuration. Residual thermal supernova feedback (see next section for further details) is maintained in the AGN configuration in order to keep a realistic density probability distribution function (PDF) of the interstellar medium (Bournaud et al. 2011), but with a magnitude small enough so that no stellar outflows are generated.

2.4. *Star formation*

Star formation is computed according to the Schmidt-Kennicutt law (Kennicutt 1998a,b) and occurs with a Poisson random process (Rasera & Teyssier 2006) in cells with gas densities above 100 $\rm cm^{-3}$ (Kraljic et al. 2014) and temperature (corrected for the Jeans' polytrope) under 10^4 K (Renaud et al. 2012), with an efficiency of 0.03 (Zuckerman & Evans 1974; Krumholz & Tan 2007).

3. FEEDBACK MODELS

In the POGO suite of simulations, we account for several models of AGN and stellar feedback simultaneously, with a resolution high enough (12 to 1.5 pc) to resolve the propagation of the outflows in the ISM. We include two schemes for AGN feedback: standard thermal AGN feedback and long-range AGN radiation; and three schemes for stellar feedback: thermal energy injection for supernovæ, kinetic energy injection for supernovæ, and radiative pressure injection for young stars radiation. They are briefly described in the following sections.

The respective magnitudes of these feedback schemes are coherent with observations, since (1) AGN feedback reproduces the $L_X/L_{IR} \sim 10^{-3}$ of typical AGNs from Mullaney et al. (2012) and is thus not "artificially boosted" compared to observational data, (2) supernova feedback schemes follow the prescription on the distribution between kinetic and thermal energy of Martizzi et al. (2015), which is based on observations and high-resolution ISM simulations, and are thus not "artificially hindered" compared to observations.

3.1. *AGN feedback models*

Our AGN feedback model is twofold: we consider standard thermal energy injection directly in the simulation code, and long-range photo-ionization in post-processing. This particular feedback model is part of the POGO project but it has not been applied here yet, since it does not change the physical parameters of the outflows (due to the staticity of the method, see Roos et al. 2015).

Thermal energy is injected according to the Bondi accretion rate of matter onto the black hole (Bondi & Hoyle 1944; Bondi 1952; Krumholz et al. 2004), and is modeled using the standard feedback recipe described by Teyssier et al. (2011); Dubois et al. (2012). Energy is injected in the four cells surrounding the BH at each coarse time-step for which the temperature in the injection region is high enough not to dissipate too quickly ($T > 10^7$ K). Also, the size of the injection region is in agreement with the finding that the AGN is not able to heat the surrounding gas at a large distance (Roos et al. 2015).

In previous papers, we have shown that neither AGN-driven winds (Gabor & Bournaud 2013, 2014), nor AGN photo-ionization coupled to AGN-driven winds (Roos et al. 2015) can quench star formation in typical redshift 2 star-forming disks, on a time-scale of a few hundreds of million years. A secondary goal of the POGO project is to show whether or not this result can change by accurately accounting for the coupling between AGN and stellar feedback, and compare to the high SFR suppression in the nuclear region (a factor of 10 to 30) — but not in the disk — found in several simulations (e.g. Dubois et al. 2013; Hopkins et al. 2016). We leave this study to a later paper.

3.2. *Stellar feedback models*

We combine three stellar feedback schemes: kinetic energy injection from supernovæ, thermal energy injection from supernovæ (from Dubois & Teyssier 2008, modified to enable both simultaneously), and radiative pressure injection from young stars (Renaud et al. 2013).

At our resolution, star particles represent star clusters and a fraction of 0.1 of their initial mass explodes as supernovæ, with 90 % of the total energy of each supernova ($E_{\rm tot} = 10^{51}$ erg) being released in kinetic energy, and the remaining 10 % in thermal energy. Kinetic energy is injected in the form of spherical Sedov blast waves whose size is about two cell sizes. Thermal energy injection by supernovæ is modelled as a polytropic equation of state for the cold gas, with a density-dependent polytropic index. The mass loading factor of the supernova winds depend on the local gas density and energy of the blast.

Radiative feedback from young and massive stars is twofold: the size of HII regions is approximated by the Strömgren radius, and is computed at each coarse time-step according to the mass and age of the star particles (and hence their luminosity) and the temperature of the surrounding gas; also, momentum mimicking radiative pressure injection is deposited as a radial velocity kick in each Strömgren sphere at each coarse time-step. Mutliple scattering is included by injecting a few times the computed momentum of the ionizing photons in the Strömgren sphere (see Renaud et al. 2013, for further details).

4. COUPLING OF STELLAR FEEDBACK

Some low-resolution simulations predict that feedback from massive stars and supernovæ couple non-linearly to each other to create strong winds (e.g Hopkins et al. 2014; Fierlinger et al. 2016; Roos & Bournaud 2016). This non-linear coupling is defined by the fact that supernovæ and young massive stars create outflows with higher mass outflow rates when they are considered simultaneously than separately.

Several hypotheses can be made regarding the origin of the non-linear coupling between stellar feedback processes: in a given star cluster, massive stars clear the way with their winds during their life, and, after ~ 10 Myr, some of them explode as supernovæ. This can lead to various non-linear aspects, among which (1) supernovæ tend to explode in diffuse regions cleared out by the winds of massive stars and are thus able to push gas further, since diffuse gas is easier to entrain, (2) successive supernovæ explode in diffuse gas, which is heated more efficiently. The cooling time is thus longer and the energy is radiated away less rapidly, resulting in more powerful winds. Also, clustered star formation leads to the explosion of an average of a few supernovæ in relatively small regions, which enhances the latter effects and can lead to the formation of super-bubbles (see e.g. Sharma et al. 2014; Liu et al. 2015).

Though, to not overestimate this coupling, it is important to resolve the propagation of the outflows both spatially (i.e. down to pc-scale) and temporally (accurate Courant-Friedrichs-Lewy condition), to avoid the artificial merging of two flows, which would otherwise have crossed each other, and kept most of their momentum.

5. COUPLING OF AGN AND STELLAR FEEDBACK

Typically, stellar winds have a rather high mass outflow rate and may lift enough mass to explain the "missing baryons problem", but their expelling efficiency is not sufficient because of their relatively low velocities (100 to 500 $\mathrm{km \cdot s^{-1}}$, see e.g. Bournaud et al. 2014). Therefore, it is not sufficient to artificially boost stellar outflows to solve the "missing baryons problem", and another source of outflows is needed. In contrast, AGN winds propagate fast (3,000 - 30,000 $\mathrm{km \cdot s^{-1}}$, e.g. Chartas et al. 2014), but they do not entrain much mass compared to stellar outflows. A non-linear coupling between the two feedback sources could create fast and highly mass-loaded winds, in potential agreement with the low amount of baryons located inside galaxies.

We have run our suite of simulations in order to verify this intuition, and now we detail the parameters of the outflows (density, temperature and velocity), the mass outflow rates as a function of time for the low-mass SFG simulation ($M_* = 1.3 \cdot 10^{10}\ M_\odot$), as well as the maximal and mean outflow rates and time averaged mass loading factor for all runs.

5.1. *Determination of mass outflow rates and mass loading factors*

The mass outflow rate, or outflow rate, is defined as the flux of mass crossing the surface of a spherical shell in a given time dt. We consider 22 concentric shells, with radii in the range 2 kpc - 100 kpc, their center being that of the simulation box. The portions of the shells crossing a 2.5 kpc layer on each side of the box mid-plane are removed from the computation of the outflow rates because they belong to the galactic disk. This implies that the outflow rates through shells with smaller radii are less accurate than those computed through larger shells, since the fraction of the sphere that is removed increases with a smaller radius.

As the geometry of AGN outflows is different from that of stellar outflows — the AGN outflows are almost spherical and the stellar outflows are almost planar, stellar outflows are artificially underestimated at small radii. Therefore, the comparison between stellar, stellar+AGN and AGN outflow rates at small radii (< 20 kpc) is problematic. Such small shells are thus not shown here and ignored in the computation of the outflow rates and mass loading factors presented in the following sections.

All the outflow rates shown in this paper are net from inflows, which are negligible compared to the outflow rates at all masses we studied, and for all feedback configurations. We recall here that the simulations are isolated galaxies with diffuse idealized circumgalactic medium (CGM), with an average temperature of 10^6 K and an average density of $10^{-3\,-\,-4}$ cm^{-3}.

For each galaxy mass, the total SFR of the stellar feedback configuration is comparable to that of the stellar+AGN feedback configuration. However, in the AGN feedback configuration, the SFR is higher since stellar feedback has been minimized. The mass loading factor of a given run is defined as the ratio between the outflow rate and the SFR.

5.2. *Physical parameters of the gas in the outflows of the low-mass SFG*

In the low-mass star-forming galaxy, stellar feedback has been active since the beginning of the simulation, and AGN feedback was enabled after 115 Myr of evolution (i.e. after all levels of refinement were enabled and star formation became steady), to save computation time because the fast AGN outflows imply small time-steps.

For both the stellar+AGN and AGN (not shown in this paper) configurations, the outflowing gas has a typical density of $10^{-3} - 10^{-4}$ cm^{-3} and is distributed in successive bursts, with temperature higher than that of the CGM: 10^7 K compared to 10^6 K (see the time sequence in Figure 1 and the density-temperature diagram in Figure 2). The CGM is thus filled with successive bubbles of hot (and sometimes shocked, see Section 5.7) gas and becomes inhomogeneous both in density and temperature. Therefore, assuming galactic outflows (even those mainly driven by the AGN) are smooth is not a good approximation.

The velocity field super-imposed on Figure 1 shows that the outflowing gas expands roughly radially at large distance in the gaseous halo and reaches several 10^3 km·s^{-1}. The properties of the stellar+AGN outflows are in broad agreement with the latest results of the FIRE simulations on outflows (Hopkins et al. 2016). In contrast, outflows generated by stellar feedback only (not shown) do not propagate far in the gaseous halo and have typical velocities of a few 100s of km·s^{-1}, which is of the order of magnitude of the rotation velocity and velocity dispersion of the galaxy.

5.3. *Outflow rates for the low-mass stellar+AGN SFG*

Figure 3 shows the evolution of the net outflow rate as a function of time for the stellar+AGN feedback configuration at 3 pc resolution. The fiducial SFR is overplotted for comparison. The "maximal outflow rate" is defined as the maximum of the outflow rates computed through each shell at a given time and is a proxy for the instantaneous power of the outflow seen in observations. The "mean outflow rate" is defined as the mean of the outflow rates through shells with radii 30 - 50 kpc at a given time. The shell restriction is there in order to avoid (1) artificial variations of stellar outflows at small radii due to the geometry and to the method used to compute the outflow rates (see Section 5.1); (2) biases at large radii coming from the fact that time is needed for the outflows to reach the largest shells. This mean outflow rate shows the long-term evolution of the outflows and the average amount of gas expelled of the galaxy (depending on the escape velocity, the amount of cosmological inflow and the depletion time-scale).

We define the ratio α between the time averaged maximal outflow rate and the time averaged mean outflow rate as:

$$\alpha = \frac{\langle \dot{M}_{max} \rangle_t}{\langle \dot{M}_{mean} \rangle_t}. \tag{1}$$

For all masses and feedback configurations at 3 pc resolution (6 pc resolution for the high-mass galaxy), this ratio is between 1.5 and 3. At 6 pc resolution (12 pc for the high-mass galaxy), this ratio varies between 1.5 and 5. However, it does not vary a lot for outflow rates at different radii in a given run (within the higher variability induced in the outflow rates at low radii, compared to high radii). This ratio is useful to get an order of magnitude of the long-term evolution of outflows, for which we observe only the instantaneous power.

5.4. *Non-linear coupling changes the outflow properties*

Visually, the outflows generated by the AGN only (not shown in this paper) are similar to those generated by the combination of AGN and stellar feedback depicted in Figure 3. Figure 4 shows the typical patterns for the gas density, gas temperature and altitude with respect to the galactic disk as a function of outflow velocity for outflows generated by stellar feedback only, stellar+AGN feedback, and AGN feedback only respectively. In this figure, the distribution of the gas in the temperature and density versus outflow velocity planes differ: the sum of the stellar feedback pattern and the AGN feedback pattern in this plane does not equal the pattern of the stellar+AGN feedback configuration. We therefore argue that this corresponds to non-linear coupling between the two sources of galactic winds in the low-mass SFG — as linear coupling would lead to the addition of the patterns.

Non-linear coupling can be either positive or negative, depending on whether it enhances or reduces the outflow rate. As a positive effect, stellar outflows lift dense gas above the galactic disk, and this dense gas is then swept away by AGN bursts. SNe and OB stars winds can also directly feed the BH by sending gas onto it, therefore enhancing AGN feedback. Between two AGN bursts, stellar outflows have time to rise again. As the CGM has been cleared by the last AGN burst, stellar outflows propagate farther and can be more efficient at expelling gas than if there was no AGN burst to clear

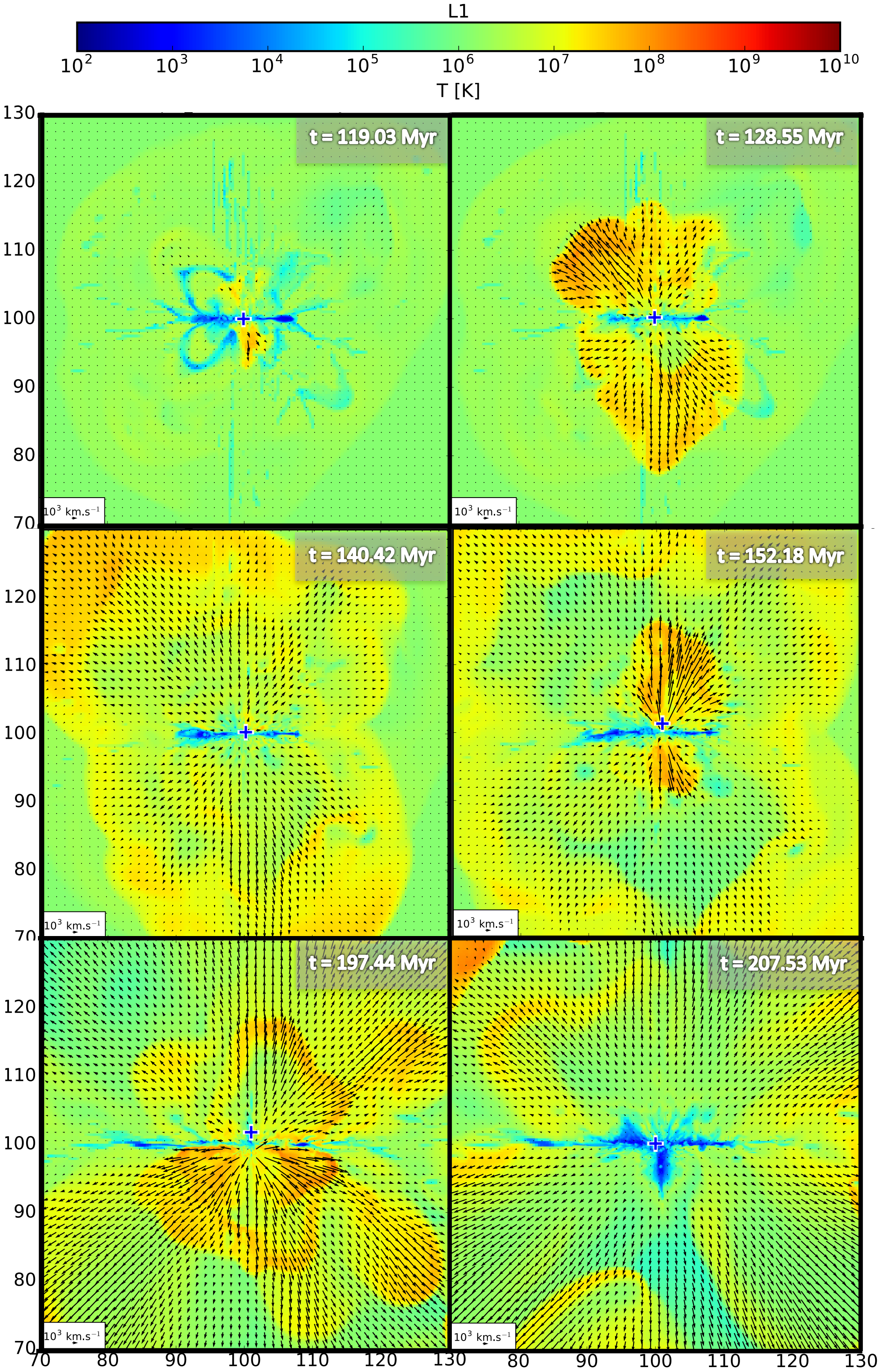

Figure 1. Time sequence of the low-mass stellar+AGN SFG simulation at 3 pc resolution. The maps are slices of the simulation box, with the galactic disk seen edge-on and the velocity field super-imposed. The color gradient shows the mass-weighted gas temperature and the axes are in kpc. The cross shows the location of the BH. AGN feedback was enabled at t = 115 Myr. The outflowing gas in the successive bursts is hotter than the CGM and has a typical velocity of several 10^3 km·s^{-1}. The AGN is the major driver of the outflows since the typical shape does not depend on the presence of stellar feedback. The CGM quickly becomes highly inhomogeneous.

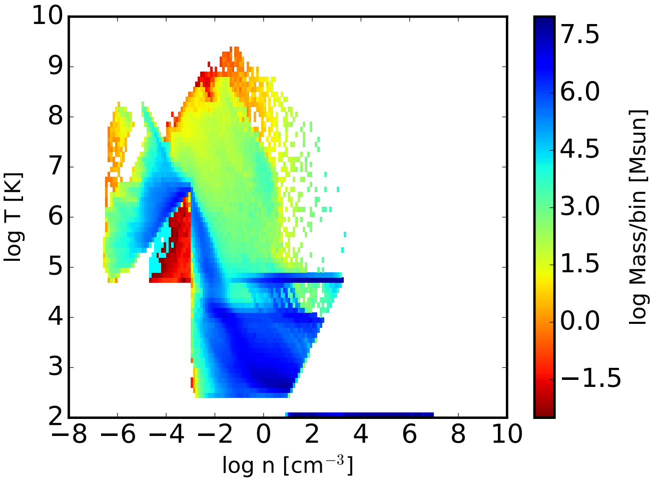

Figure 2. Density-temperature diagram of the gas in the low-mass SFG. The refinement strategies ensure a rough thermal equilibrium following a pseudo-cooling equation of state (Bournaud et al. 2010). Very dense gas is heated according to the density-dependent floor known as the Jeans' polytrope and its temperature is corrected before scientific exploitations (as shown here: cold gas at 100 K). The outflowing gas is heated by the AGN to very high temperatures (10^{7-9} K) and is mainly diffuse (density less than 1 cm^{-3}).

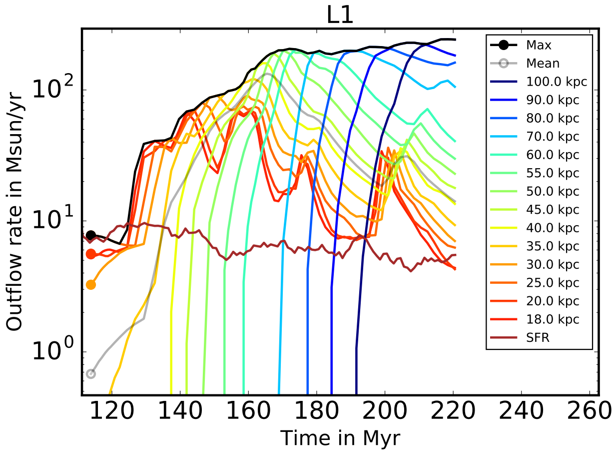

Figure 3. Net outflow rate as a function of time in the low-mass stellar+AGN SFG at 3 pc resolution. The color gradient shows the radius of the shell through which the outflow rate is computed. The black line is the maximal outflow rate for all shells as a function of time and is a proxy for the instantaneous power of the outflows. The gray line shows the mean outflow rate for shells with radii between 30 and 50 kpc and is a proxy for the long-term mass ejection of the outflows. While the SFR (brown) remains roughly constant (with a slow decay due to gas consumption in the isolated galaxy), the successive bursts of outflowing gas reach a maximal outflow rate of several 10^2 $\mathrm{M}_\odot \cdot \mathrm{yr}^{-1}$. The variations in the mean outflow rate closer to the disk reflect the bursty behaviour of AGN accretion and outflows (and star formation, to a lesser degree) due to the shallow gravitational potential well of the low-mass galaxy.

the way. In contrast, AGN outflows can also push stellar fountains back onto the disk, which is a form of negative non-linear coupling. Furthermore, stellar fountains tend to redistribute the gas from the center of the galaxy to its outskirts (Binney & Tremaine 1987), which can leave less fuel for the BH to feed and for the AGN to expel. Lastly, positive effects can turn negative, for example if there is enough dense gas coming from stellar outflows brought inside the AGN outflows, such that cooling is triggered and a fraction of the gas in the outflow starts to fall back on the galaxy instead of leaving it. With the POGO suite of simulations, we aim at identifying which of these non-linear effects appear as a function of the mass of the host.

Figure 4 shows the differences between stellar-, stellar+AGN- and AGN-driven winds in the case of the low-mass SFG: warm gas at 10^{5-6} K has a velocity under 2,000 $\mathrm{km \cdot s^{-1}}$ in the AGN run while it is accelerated to much higher velocities (up to 6,000 $\mathrm{km \cdot s^{-1}}$) in the stellar+AGN configuration. Interestingly, the highest outflow velocity is found in the stellar+AGN run: almost 10^4 $\mathrm{km \cdot s^{-1}}$ compared to 8,000 $\mathrm{km \cdot s^{-1}}$ in the AGN run. This is likely related to the fact that the BH accretes more gas in the stellar+AGN configuration, compared to the AGN configuration (see Section 7.2) and thus the feedback is more efficient. Furthermore, the amount of outflowing gas moving from 6,000 to 8,000 $\mathrm{km \cdot s^{-1}}$ is more important in the AGN run compared to the stellar+AGN run. This shows that very hot and fast gas of the AGN outflow does not couple to dense and cold gas and propagates fast; whereas in the stellar+AGN run, hot gas mixes with colder stellar winds and has a lower velocity.

5.5. *Stellar outflows are swept up by the AGN*

Figure 5 shows a time sequence of the outskirts of the low-mass stellar+AGN disk seen edge-on. From this, we see that the first burst of AGN outflows in the stellar+AGN low-mass simulation sweeps gas in the stellar outflows on the outer parts of the galactic disk. This makes a fraction of the stellar outflows rain back on the disk. However, most of the mass in the stellar outflows is added to the global stellar+AGN outflow, leading to a higher outflow rate compared to the AGN run (see Section 6).

About 30 Myr later, another burst of AGN outflows propagates (see Figure 6). In the meantime, stellar outflows have time to lift gas above the galactic disk again. The fact that they propagate in a diffuse region which was just swept by an AGN burst can also enhance the power of the wind, since it is not encountering the gas lifted there by earlier supernovæ or stars. This gas is then compressed by the next high-velocity AGN burst and a fraction of it is swept away, adding a significant amount of mass in the global stellar+AGN outflow. The rest of the compressed fountains is pushed back on the disk. However, this compression does not result in extra star formation on the time-scales of the study.

5.6. *Outflow speed-up in the gaseous halo*

Recently, a speed-up of galactic outflows has been observed with the VLT/SINFONI in the gaseous halo of nearby SFGs, several kpc away from the galactic disk (Schroetter et al. 2015). Even though the typical velocities of our stellar+AGN outflows are higher than those of the outflows in Schroetter et al. (2015): a few 10^2 $\mathrm{km \cdot s^{-1}}$ in their observations compared to a few 10^3 $\mathrm{km \cdot s^{-1}}$ in our simulations, our stellar+AGN and AGN runs reproduce such a speed-up (top middle and top right panels of Figure 4). This acceleration is typically seen between about 1 kpc and 170 kpc from the galactic disk, which is the maximal distance between the center of the box and

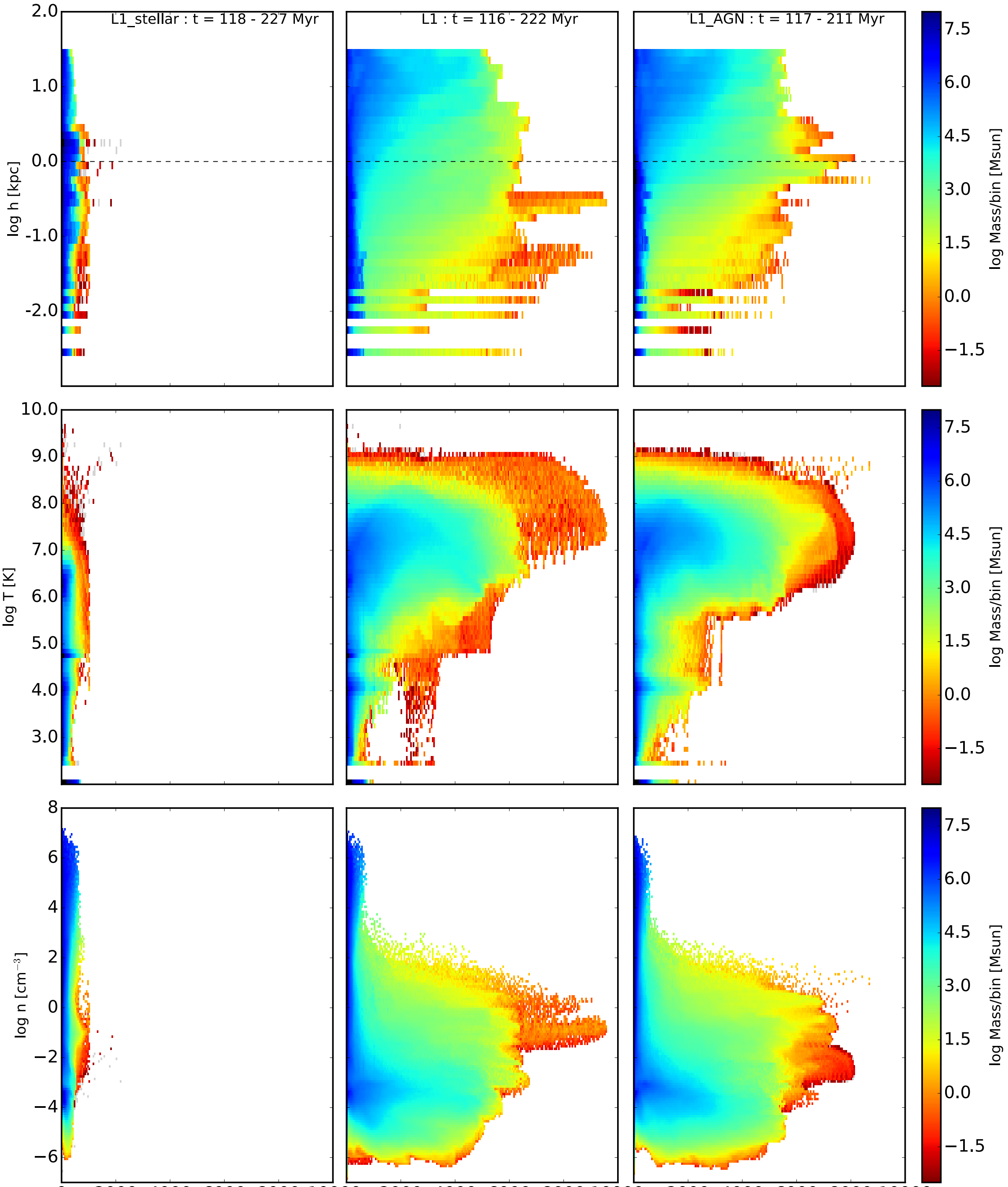

Figure 4. Altitude, temperature and gas density as a function of the outflow velocity for the low-mass typical SFG at 3 pc resolution. The quantities are averaged on several outputs over about 100 Myr. Gas at a few 100s of km·s^{-1} belongs to the galactic disk. *Left:* Typical pattern for outflows generated by stellar feedback. The typical velocity of the outflowing gas is several 100 km·s^{-1}, which is of the order of the galaxy rotation velocity. The bulk of the outflowing gas has a high density (above 1 cm^{-3}). *Middle:* Typical pattern for outflows generated by AGN and stellar feedback. The bulk of the outflowing gas has a velocity of 2 to $4 \cdot 10^3$ km·s^{-1}, a density of 10$^{-4\,-\,-6}$ cm^{-3} and a temperature of 10^7 K. There is a speed-up of outflows from 1 kpc above the galactic disk to the limit of the simulation box. *Right:* Typical pattern for outflows generated by AGN feedback. As for stellar+AGN outflows, the bulk of the outflowing gas has a velocity around 2 - $4 \cdot 10^3$ km·s^{-1}, a density of 10$^{-4\,-\,-6}$ cm^{-3} and a temperature of 10^7 K. The outflow speed-up from 1 kpc above the galactic disk to the limit of the simulation box is also visible. Warm gas (10^{5-6} K) is accelerated to much higher velocities in the stellar+AGN configuration compared to the case where the AGN is the only source of outflows. Also, there is a smaller amount of fastest-moving gas (from 6 to $9 \cdot 10^3$ km·s^{-1}) in the stellar+AGN run compared to the AGN only run because stellar outflows redistribute the gas in the outskirts of the galaxy, clearing the central region. The AGN has thus less gas to push with the same amount of energy (Eddington luminosity, see Section 7.2), and the outflow has a higher velocity.

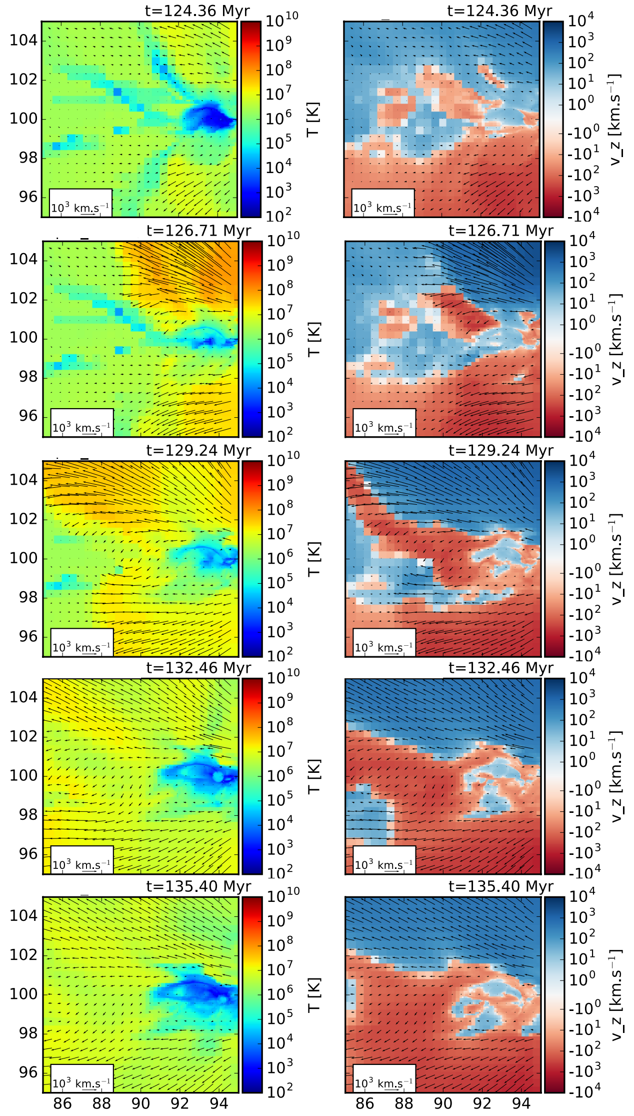

Figure 5. Time sequence of the stellar+AGN low-mass SFG simulation at 3 pc resolution. The maps show slices of the simulation box, with the galactic disk seen edge-on and the velocity field superimposed. The axes are in kpc. The camera is centered on the side of the galactic disk and the axes are in kpc. The BH is located at (100, 100) kpc^2, further on the right of each map. AGN feedback was enabled at t = 115 Myr. *Left:* mass-weighted gas temperature. *Right:* mass-weighted velocity parallel to the galactic rotation axis (ordinate of the maps). From 0 to 100 kpc in the ordinate, outflowing gas is in red. From 100 to 200 kpc in the ordinate, outflowing gas is in blue. As the first burst of the AGN outflow propagates, a fraction of the fountains generated by stellar feedback is pushed back on the galactic disk, while the rest is swept away and adds mass to the overall outflow. This coupling contributes to increase the total outflow rate in the low-mass SFG.

any cell inside it[1]. This acceleration is seen at all masses we studied for stellar+AGN and AGN runs, but not in stellar runs (as expected given the low velocity of stellar fountains compared to AGN winds).

5.7. *Outflow velocity versus escape velocity*

We considered one cell out of 100 in the simulation box as a particle, and computed the interactions between them to get the gravitational potential for each particle.

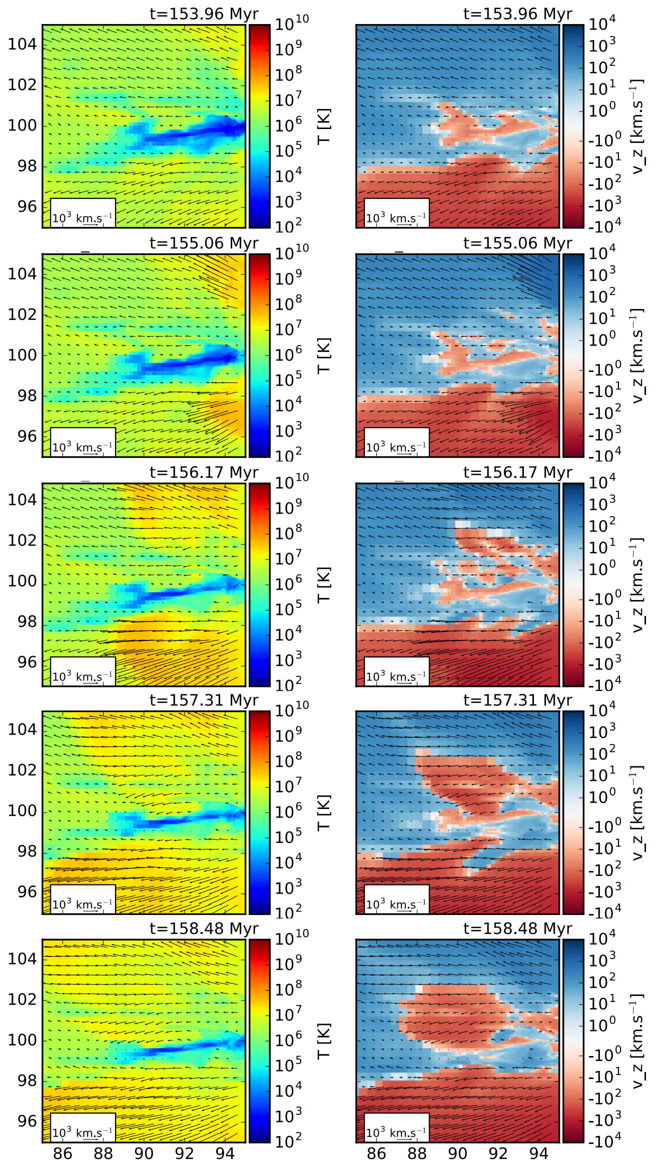

Figure 6. Time sequence as in Figure 5. Between two consecutive bursts of AGN outflows, stellar outflows have time to re-generate, they lose energy and start to fall back on the galactic disk. AGN bursts, as they sweep the gas outward the galactic disk, are able to compress the gas in these fountains, and add mass to the global outflow. In this case also, a fraction of the stellar outflows is pushed back on the galactic disk, as a sign of negative coupling, but most of it is swept inside the global outflow. Here, gas compression does not lead to extra star formation.

From this, we computed the escape velocity for each particle for different snapshots of the simulations. Figure 7 shows the ratio between the gas velocity and the escape velocity for the stellar+AGN low-mass SFG at 3 pc resolution. The corresponding maps for the AGN low-mass galaxy (not shown) are similar. For the stellar low-mass galaxy at 3 pc resolution, all snapshots of the simulation resemble the first one of Figure 7. The galactic stellar+AGN outflows are composed of successive expanding bubbles of outflowing gas. These bubbles are surrounded by an envelope of circum-galactic gas with a velocity inferior to the escape velocity, which is vestigial of the initial circum-galactic medium of the simulation. This envelope is shocked by the encounter of the diffuse bubbles.

---

[1] The size of the box being 200 kpc, this distance is 200 kpc/2$\cdot\sqrt{3}$ = 173 kpc.

Table 2
Time averaged maximal and mean mass loading factors for the POGO simulations.

Run	Max	Mean	Max lores	Mean lores
L1	21.68	6.76	37.22	7.10
L1_stellar	1.01	0.43	1.24	0.76
L1_AGN	5.36	1.99	9.03	2.39
L2	1.33	0.67	1.70	0.47
L2_stellar	0.15	0.00*	0.15	0.00*
L2_AGN	1.07	0.61	1.64	0.84
LL3	2.05	1.28	2.29	1.21
LL3_stellar	-	-	1.43	0.52
LL3_AGN	-	-	2.07	0.96

Note. — The mass loading factor is defined as the ratio between the outflow rate and the corresponding SFR. The time averaged maximal and mean mass loading factors correspond the time averages of the ratio between the mean and maximal outflow rates defined in Figure 3 and Section 5.1, and the star formation rate. *The mean mass loading factor for L2_stellar is zero because the stellar outflows are quite weak and the highest outflowing cells reach only 20 kpc, whereas the mean is computed through shells of radii 30 - 50 kpc. *Lores* means that the maximal resolution is degraded by a factor of 2 between the first two columns and the last two.

For the low-mass SFG, $\sim$ 10 % of the mass in the simulation box has its velocity greater than the escape velocity in the stellar+AGN feedback configuration. The same behaviour is seen in the AGN feedback configuration. Naturally, the stellar feedback configuration shows a different behaviour since the stellar outflows are much less powerful than the AGN outflows : only 1 % of the mass in the simulation box has its velocity above the escape velocity.

6. NON-LINEAR COUPLING OF THE OUTFLOW RATES VERSUS MASS LOADING FACTORS

This section describes the maximal and mean mass outflow rates as well as the corresponding time averaged mass loading factors for all feedback configurations and all masses, at 3 pc (6 pc for the high-mass SFG) and 6 pc (12 pc for the high-mass SFG) resolution. Time averaged mass loading factors are summed up in Table 2.

Figure 8 shows the time average of the maximal mass loading factor of the outflows as a function of the galaxy mass. The maximal mass loading factor is the ratio between the maximal outflow rate (among all shells) and the SFR as a function of time. These values are then averaged with time. Equivalently, Figure 9 shows the time averaged mean mass loading factor as a function of the galaxy mass. Similarly to the observations of Schroetter et al. (2015), we find higher mass loading factors for lower galaxy masses, even though our absolute values are higher. This is in agreement with the theoretical expectations of Murray (2011); Hopkins et al. (2012).

At the low mass studied, the maximal mass-loading factor is high (about 20), and is higher than the sum of the time averaged maximal mass loading factor of the AGN feedback run and the stellar feedback run. At the intermediate and high masses we studied, the mass loading factor of the stellar+AGN winds is of the order of the unity and there is no significant difference between AGN and stellar+AGN runs. The time averaged mean mass loading has the same behaviour at all masses we studied.

At the highest mass we studied, the mass loading factor and outflow rate of the stellar winds is quite high. However, the low-resolution (12 pc) run was created by forking the stellar+AGN run into separate stellar and AGN runs — contrarily to all others, in which the forking happened before enabling AGN feedback. Therefore, when LLL3_stellar was launched, AGN outflows were already in place and the high time averaged maximal mass loading corresponds to AGN winds which did not have time to dissipate.

In the next sections, we describe the non-linear coupling of AGN and stellar feedback processes as a function of the galactic mass, in terms of mass outflow rates.

6.1. *Low-mass $z \sim 2$ SFG*

Figure 10 shows the maximal and mean outflow rates defined in Section 5.1 as a function of time, for the three feedback configurations at 3 pc resolution. The fiducial SFR is superimposed for comparison. In the increasing phase of the outflows, the outflow rate from the AGN run is larger than that of the stellar+AGN run, but the behaviour is the opposite in the steady state: stellar+AGN winds have an outflow rate of twice that of the AGN winds on average. Furthermore, while stellar outflows have a maximal mass outflow rate roughly of the order of the fiducial SFR, stellar+AGN outflows tend to a maximal outflow rate of about 20 times the fiducial SFR. This non-linear coupling (stellar+AGN outflow rate larger than the sum of the two taken separately) is less visible in the mean outflow rates due to the higher variability.

We argue that two phenomena are at play in this positive non-linear coupling: first, the black hole growth is enhanced in the stellar+AGN run compared to the AGN run (see Section 7.2) and thus leads to enhanced AGN feedback and more powerful AGN outflows. This likely comes from the fact that stellar feedback in the central region of the galaxy helps feeding the BH by sending gas directly on it. The second process is the sweeping by the AGN bursts of gas lifted by stellar winds inside the global outflow, possibly enhanced by the fact that stellar outflows propagate more efficiently in a CGM which is regularly cleared by AGN bursts (see Section 5.4).

6.2. *Intermediate-mass $z \sim 2$ SFG*

The mass of the intermediate-mass star-forming galaxy is $M_* = 4.4 \cdot 10^{10}$ $M_\odot$. AGN feedback is enabled after 70 Myr of evolution and all outflows have reached a steady state 20 Myr after that (see Figure 11). In contrast with the low-mass SFG, stellar winds are quite weak (mass outflow rate of about 10 % of the fiducial SFR). As for the low-mass SFG, both AGN and stellar+AGN outflows are powerful (mass outflow rate $\gtrsim$ fiducial SFR), in remarkable agreement with the observations of Bouché et al. (2010). Similarly to the low-mass SFG, AGN outflows grow faster than stellar+AGN outflows at the beginning of the simulation, but once the steady state is reached for both, the behaviour is opposite compared to the low-mass SFG: the mass outflow rate of the stellar+AGN run is *under* that of the AGN run.

Thus, at intermediate mass, non-linear coupling between AGN and stellar feedback acts negatively: contrarily to the low-mass case, combining AGN and stellar outflows actually *decreases* the outflow rate of the global outflow. The main difference compared to the low-mass case is the relative weakness of the stellar outflows compared to the AGN outflows and the SFR. This decrease

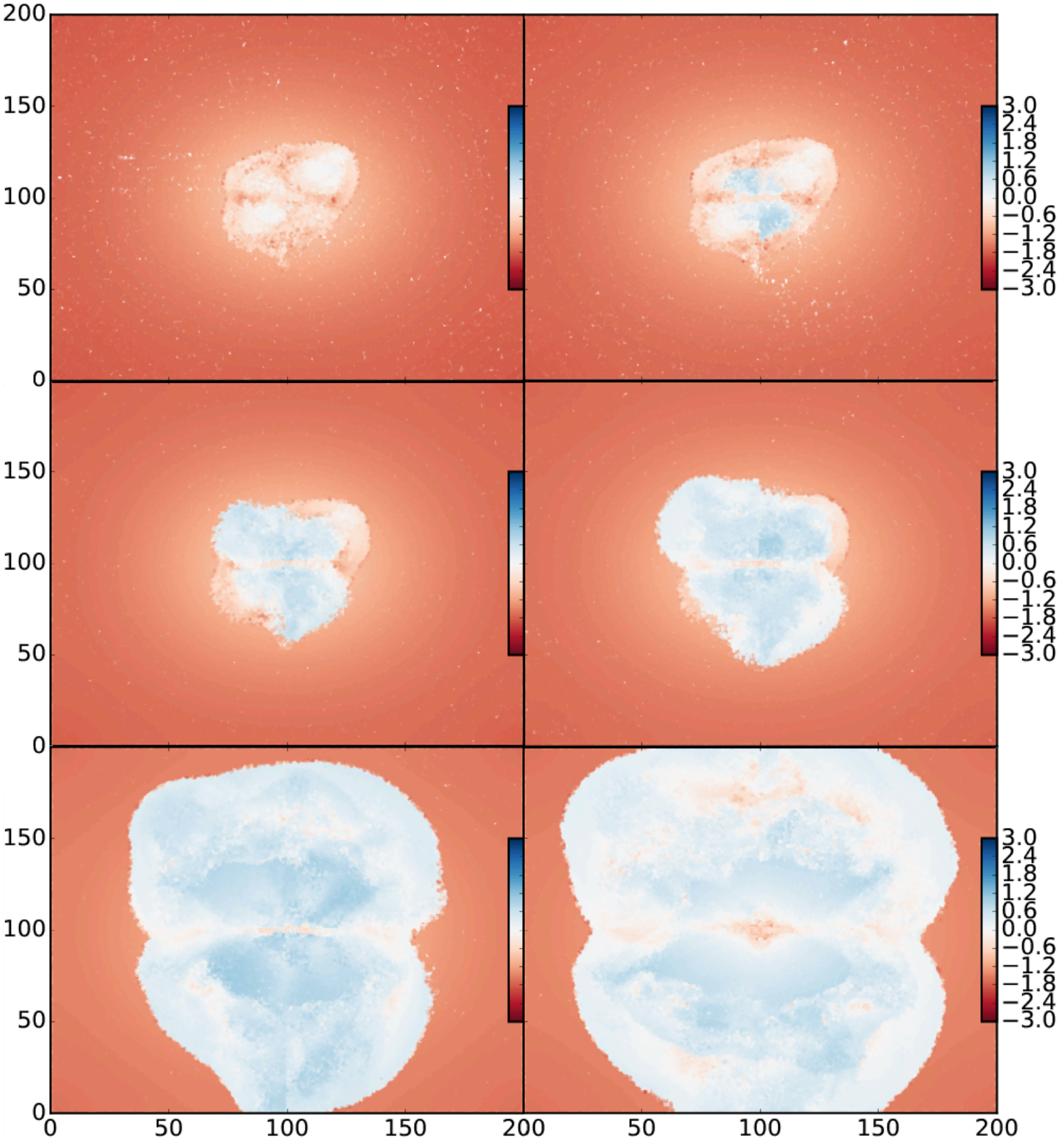

Figure 7. Time sequence of a 20 kpc slice centered on the BH showing the ratio between the velocity and the escape velocity in the low-mass stellar+AGN SFG at 3 pc resolution. The axes are in kpc. Same time-steps as Figure 1. The figure is built by taking 1 cell out of 100 in the simulation box and treating them as particles to compute the gravitational potential at the location of each cell. Each particle is then plotted with its marker size proportional to the mass of the cell it lives in. Fast AGN outflows propagate and encounter the distant CGM (the initial gas of the CGM which has not been mixed with outflowing gas yet). While the outflowing bubbles move faster than the escape velocity, the initial CGM has a velocity smaller than the escape velocity. A shock is created at the boundary between the two.

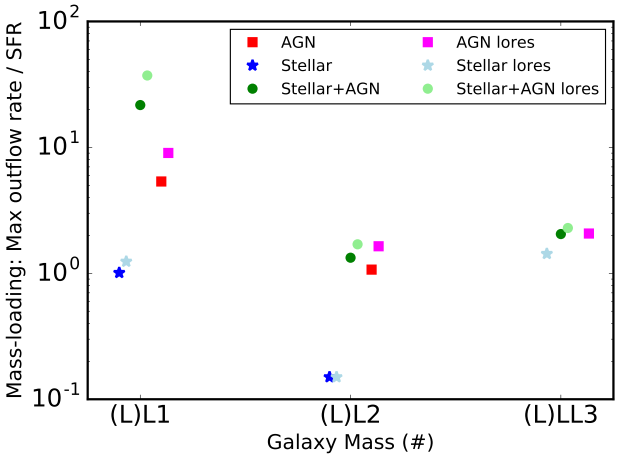

Figure 8. Time averaged maximal mass loading factors as a function of mass for the three feedback configurations: stellar+AGN (green/light green circles), stellar (blue/light blue stars), AGN (red/magenta squares) for two resolutions (3 - 6 pc for the low- and intermediate-mass SFGs, 6 - 12 pc for the high-mass galaxy). The points are horizontally shifted for clarity and the values are summed up in Table 2. The maximal mass loading factor is defined as the ratio between the maximal outflow rate averaged on all shells, and the SFR. The maximal outflow rate measures the current power of the outflow and corresponds to the outflow rate observed in the Universe. The mass loading factors depend on the host mass: at the low mass studied, the mass-loading factor of the stellar+AGN run is high (about 20), and is higher compared to the AGN feedback run. At the intermediate and high masses we studied, the mass loading factor of the stellar+AGN wind is of the order of unity and there is no significant difference between AGN and stellar+AGN.

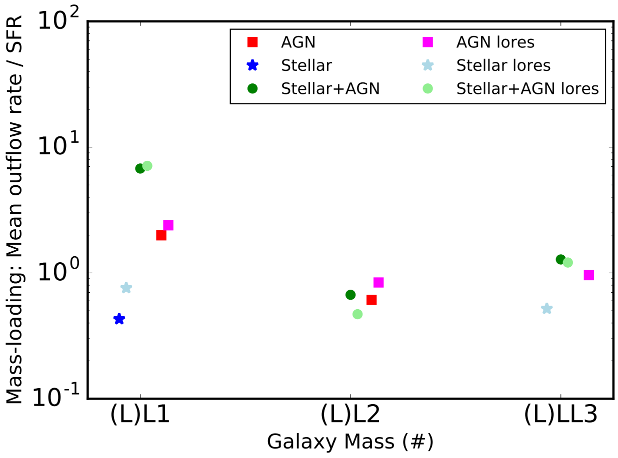

Figure 9. Time averaged mean mass loading factors as a function of mass for the three feedback configurations. Same key as Figure 8. The mean mass loading factor is defined as the ratio between the mean outflow rate averaged on shells, and the SFR. The mean outflow rate determines the average amount of gas ejected from the galaxy on the long term. The behaviour at all masses studied is the same as for the maximal outflow rate.

can have various origins: stellar outflows can remove gas from the central region, and redistribute it in the outskirts of the disk instead (and feed the BH less efficiently, see section 7.2). Thus leading to less powerful winds than in the absence of stellar feedback. Also, stellar feedback is likely too weak to lift enough gas, high enough or long enough for the AGN bursts to sweep it inside the global outflow. The remaining stellar+AGN outflow expels thus less mass than the AGN outflow.

6.3. *High-mass $z \sim 2$ SFG*

For the high-mass star-forming disk ($M_* = 10.3 \cdot 10^{10}$ $M_\odot$) at the highest resolutions (1.5 and 3 pc), we only run the stellar+AGN feedback confguration for a short time (because of the cost in computation time), and run additional simulations at 6 and 12 pc in order to evolve the outflows until they reach a steady state. At 12 pc resolution, we study two additional runs with stellar feedback only and AGN feedback only. Their maximal and mean outflow rates as a function of time are shown in Figure 12. This particular case is problematic for the study of the stellar outflow rate and mass loading factor since the AGN winds had already developed when the stellar run started. In the run, AGN outflows do not have time to dissipate and hide the actual mass outflow rate of the stellar winds (the effect is less severe for the mean mass loading factor).

At high mass, the stellar+AGN outflows are of the order of a few times the fiducial SFR of the galaxy. This is the same for AGN outflows, though the same effects as for stellar outflows (late forking of the runs) can bias the results.

As stellar outflows are usually weaker for higher galaxy masses since the gravitational potential is deeper and thus harder to escape for them, the same negative non-linear coupling as for the intermediate-mass galaxy is possible in this case (though we cannot probe it here because the run may be too short). Thus, it is possible that stellar feedback processes also decrease the strength of AGN winds at high mass.

7. DISCUSSION

In the following sections, we discuss our results by studying the convergence of the results with resolution, the regime of the BH accretion rate and the BH growth in the different feedback configurations, and the long-term consequences of negative non-linear feedback on the intermediate-mass (and potentially the high-mass) star-forming galaxy.

7.1. *Dependence on resolution*

Figures 8 and 9 respectively show the time averaged maximum and mean mass loading factors as a function of mass for the low resolution runs and the higher resolution runs. In all cases (with one exception: the mean mass loading of LL2), lower-resolution runs have absolute values of the mass loading factor which are slightly higher than those at higher resolution (see Table 2) because the mass outflow rate is higher. However, the hierarchy between the values, i.e. the ratio between the stellar+AGN run, the stellar run and the AGN run, remains unchanged whatever the resolution. We therefore argue that the qualitative trends of positive and negative coupling of the mass outflow rates are robust against a change in resolution.

7.2. *Dependence on BH accretion rate*

Figure 13 shows the ratio between the black hole accretion rate and the Eddington accretion rate as a function of time for the three feedback configurations of the low-mass SFG at 3 pc resolution. In the simulations, BH accretion and AGN feedback are capped to the Eddington rate. From this figure, it is obvious that the accretion is

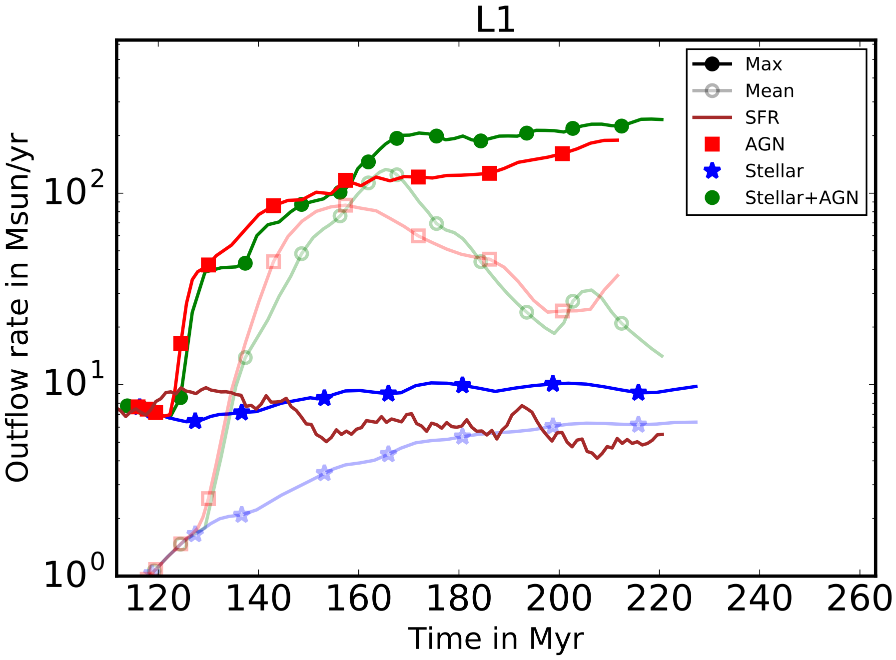

Figure 10. Maximal (solid) and mean (semi-transparent) outflow rates as a function of time in the low-mass SFG for all feedback configurations at 3 pc resolution. Green circles correspond to stellar+AGN feedback, red squares to AGN feedback and blue stars to stellar feedback. The fiducial SFR is shown in brown. The maximal outflow rate in the stellar run is quite weak compared to AGN and stellar+AGN winds (about the fiducial SFR, compared to about 10 times the SFR), and is steady at all times. During the increasing phase of the outflow rates, the AGN run gives slightly more powerful outflows than the stellar+AGN run, however, in the steady state, the maximal outflow rate of the stellar+AGN run is on average twice the outflow rate of the AGN run. Therefore, at our low mass, stellar and AGN feedback clearly couple non-linearly to produce winds with higher mass outflow rates than the sum of the two taken separately. This behaviour is less visible for the mean outflow rates since there are huge variations with time.

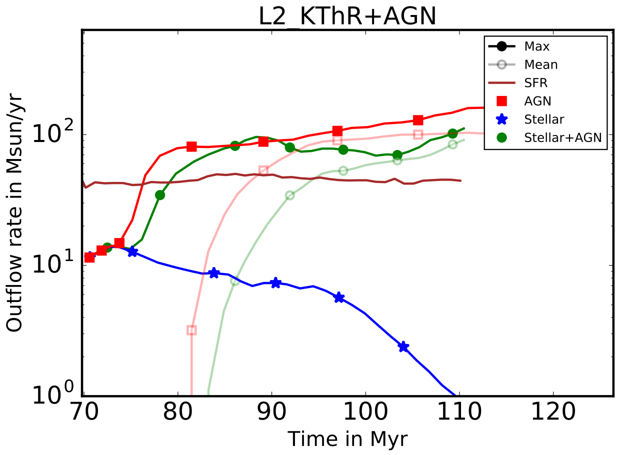

Figure 11. Maximal (solid) and mean (semi-transparent) outflow rates as a function of time in the intermediate-mass SFG for all feedback configurations at 3 pc resolution. Same key as Figure 3. The stellar outflows are very weak (about 10 % of the fiducial SFR on average), while the stellar+AGN and AGN winds have outflow rates of the order of the fiducial SFR. Negative non-linear coupling is at play between stellar and AGN feedback processes, since accounting for both produces winds with a smaller outflow rate on average, compared to the AGN run.

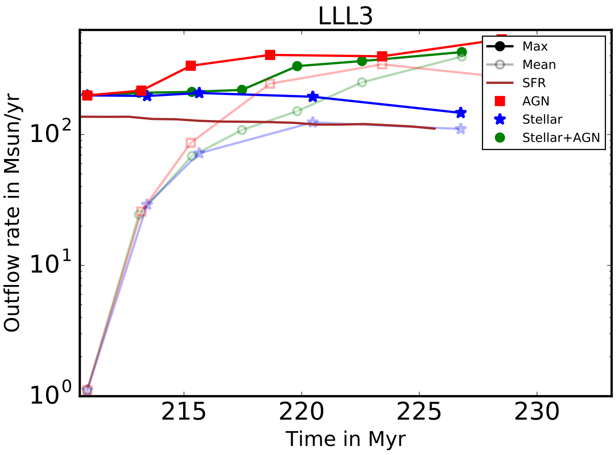

Figure 12. Maximal (solid) and mean (semi-transparent) outflow rates as a function of time in the high-mass SFG for all feedback configurations at 12 pc resolution. Same key as Figure 3. At high mass, the stellar+AGN and the AGN winds have outflow rates of the same order of magnitude. Here, the outflow rate of the stellar winds is quite high due to the vestigies of AGN winds (see text).

Eddington-dominated in all configurations. To be more specific, at low mass, more than 70 % of the time is spent at the Eddington rate. This fraction goes to more than 97 % at higher masses. The values are summed up in Table 3.

However, the very high fraction of time spent at Eddington has to be taken with cautions, since the porosity of the interstellar medium is not resolved while it could regulate the feedback energy that actually propagates away.

Figure 14 shows the average black hole growth rate (defined as the black hole growth divided by the simulation time) as a function of the average star formation rate (defined as the stellar mass growth divided by the simu-

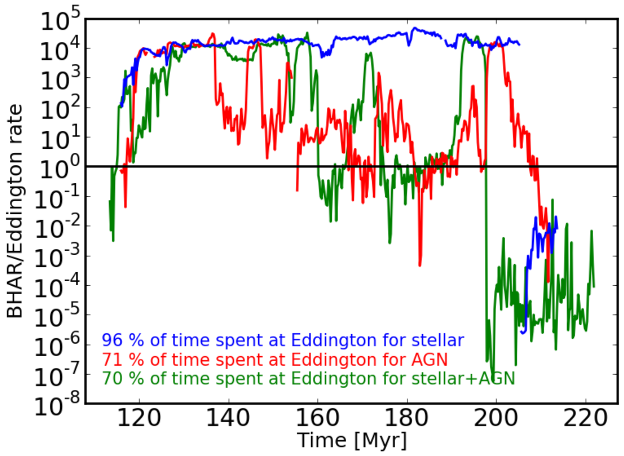

Figure 13. Eddington ratio, i.e. ratio between the BH accretion rate and the Eddington accretion rate, as a function of time for the low-mass SFG at 3 pc resolution. For visibility, the points are averaged in bins of 0.25 Myr. The black solid line shows an Eddington ratio of 1, on which BHARs are capped before use. The stellar+AGN run is plotted in green, the AGN run in red and the stellar run in blue. In the stellar+AGN run, the BH accretion rate is at the Eddington rate 70.36 % of the time, while in the AGN run, it is at the Eddington rate 71.38 % of the time and in the stellar run, it is at the Eddington rate 95.90 % of the time (see Table 3 for the other masses). The BH accretion rate is the highest in the stellar feedback run since there is no AGN outflow to clear the central region and regulate accretion. Interestingly, the BH growth is higher in the stellar+AGN configuration than in the AGN configuration at all masses we studied (see also Figure 14), suggesting the stellar feedback helps feeding the black hole.

Table 3
Fraction of the time spent at the Eddington accretion rate.

Run	% of time spent at Eddington
L1	70.36
L1_AGN	71.38
L1_stellar	95.90
L2	97.17
L2_AGN	97.41
L2_stellar	99.34
LLL3	99.99
LLL3_AGN	98.20
LLL3_stellar	100.00

Note. — Fraction of time where the black hole accretion rate is at the Eddington accretion rate in the different runs containing an AGN.

lation time). At all masses we studied and at fixed SFR, the BH grows the most efficiently in the stellar feedback configuration. This is expected since there is no AGN wind to regulate BH growth. Interestingly, the presence of stellar feedback in the stellar+AGN run enhances the black hole growth, at fixed SFR compared to the AGN run. Thus, we conclude that the BH is fed by violent disk instabilities typical of redshift 2 disks (see e.g. Bournaud 2016) in the AGN configuration, while there is an additional feeding due to stellar feedback (direct capture of gas from SNe and OB stars winds) in the stellar+AGN run.

It is interesting to note that an enhanced black hole growth at fixed SFR (and thus an enhanced AGN feedback) due to the presence of stellar feedback does not necessarily imply more powerful winds, since at intermediate mass there is actually a decrease of the global mass outflow rate.

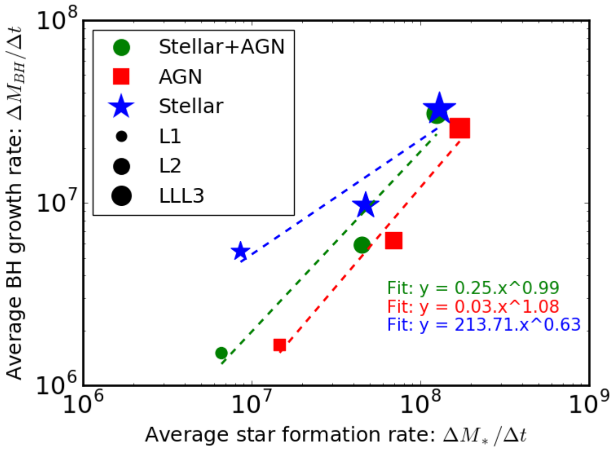

Figure 14. Average star formation rate as a function of average black hole growth rate, in solar masses per million year, for the three galaxy masses (marker size as labelled) and the three feedback configurations (stellar+AGN: green, AGN: red, stellar: blue). In the absence of AGN outflows to regulate its growth, the black hole grows very efficiently. Interestingly, the presence of stellar feedback enhances the black hole growth at fixed SFR, compared to the case with AGN feedback only. All runs show a BH growth which is more efficient than the expected Magorrian relation (see text). We thus argue that some unstable clumpy disks at high redshift are able to feed their black hole more efficiently than the bulk of star-forming galaxies at low redshift.

Figure 14 can be compared to the Magorrian relation (Magorrian et al. 1998b), since the simulation time is constant and provided that the total stellar mass is considered in place of the bulge mass (which is a standard proxy at high redshift, since the bulge is not resolved, see e.g. Reines & Volonteri 2015; Volonteri & Reines 2016). Taking the low-mass SFG as an example, the initial stellar mass is $1.3{\cdot}10^{10}$ $M_\odot$ and the initial black hole mass is set according to the Magorrian relation to $1.3{\cdot}10^7$ $M_\odot$. At the end of the simulations, we know from Figure 14 that both the BH and the stellar mass have grown of a few 10^8 $M_\odot$. This means that the stellar mass has grown of a few percent while the BH mass has been multiplied by 10, way above the Magorrian relation. This very efficient BH growth is in broad agreement with the findings of Wang et al. (2010); Volonteri & Stark (2011), who show that (very) high-redshift quasars can grow faster than today.

As stressed in Section 6.3, we recall here that the LLL3 stellar and AGN configurations might be biased towards the value of the stellar+AGN run.

7.3. *Consequences of the negative non-linear coupling at intermediate mass*

In the intermediate-mass simulation (and possibly in the high-mass simulation too), taking into account stellar outflows reduces the mean and maximal outflow rates by a factor of about 1.2 to 2.5, depending on the resolution.

While this seems small, when integrated from redshift 2 down to redshift 1 or 0, this can change the gas fraction from ~ 50 % at redshift 2 down to 10 or 20 % at low redshift since a significant amount of gas will *not* be removed from galaxies. This behaviour could be of crucial importance in many cosmological simulations, which mostly cannot reproduce the size and morphology distribution of galaxies at low redshift.

Also, the gas fraction in both distant and local galaxies is important to the understanding of the structure of the ISM. Indeed, Fensch et al, in prep show that it is the gas fraction, both at redshift 2 and redshift 0, that determines the lifetime of giant molecular clouds, regardless the strength of the AGN and stellar feedback.

8. CONCLUSIONS

We have run a series of simulations of redshift 2 isolated disk galaxies of the Main Sequence at high resolution (from 12 to 1.5 pc), in order to study the coupling between thermal AGN feedback and stellar feedback (in the form of kinetic and thermal supernova feedback, plus radiative feedback from OB stars) and see whether it could create powerful outflows with velocities larger than the escape velocity and mass outflow rates of the order of 2 to 3 times the star formation rate, and identify the major driver(s) of the outflows. This paper focuses on the outflow properties (density, temperature and velocity) and outflow rates. Our main results are summerized as follows:

- The AGN is a major driver of the galactic outflows at all masses we studied: the typical shape, velocity, gas density and gas temperature of the outflowing gas is the same regardless the presence of stellar feedback. While this was expected for the intermediate and high masses, this is surprising in the low-mass galaxy we studied, where AGNs are supposed to play a minor role;
- Nonetheless, it is important to accurately account for stellar feedback since the mass outflow rate is sensitive to the presence of stellar feedback processes, and to the mass of the host:
  - at low mass ($M_* = 1.3 \cdot 10^{10}$ $M_\odot$), non-linear coupling between stellar and AGN feedback is positive and enhances the maximal mass outflow rate by a factor of 2. This likely comes from the fact that stellar feedback helps feeding the BH, thus enhancing AGN feedback. Also, dense gas is pushed up by stellar feedback above the galactic disk, and then swept away by the AGN bursts, therefore adding mass into the outflows. Between two AGN bursts, stellar outflows have time to rise in a diffuse and hot circum-galactic medium (since regularly swept by the AGN bursts), which can also enhance the outflow rate of stellar winds. All effects combined lead to a more powerful outflow;
  - at intermediate mass ($M_* = 4.4 \cdot 10^{10}$ $M_\odot$), non-linear coupling is still there but negative processes dominate: stellar outflows redistribute the gas from the center of the galaxy to its outskirts and are too weak to lift enough gas for the AGN to sweep into the global outflow. This results in a stellar+AGN with a lower mass outflow rate compared to the AGN case;
  - at high mass ($M_* = 10.3 \cdot 10^{10}$ $M_\odot$), the mass outflow rate of the stellar+AGN wind seems of the same order of that of the AGN wind and of the stellar wind (though we expect some biases in these particular runs).
- AGN outflows and stellar+AGN outflows speed-up in the gaseous halo, from 1 kpc above the galactic disk to the limits of the box, in remarkable agreement with the observations of Schroetter et al. (2015);
- AGN and stellar+AGN outflows are composed of successive hot expanding bubbles of gas with velocities larger than the escape velocity of the galaxy. These bubbles encounter the gas of the initial CGM (with velocity smaller than the escape velocity) and create shocks;
- The AGN and stellar+AGN winds rapidly fill the CGM with inhomogeneous gas (both in density and temperature) and thus assuming the gas in the outflows is homogeneous is not a good approximation.

In all our simulations, the expelled gas is mainly hot and diffuse. However, a significant fraction of molecular gas has been observed in galactic outflows (e.g. Aalto et al. 2012; Cicone et al. 2014). Among the possible explanations to this discrepancy, we find the absence of magnetic fields in our simulations, due to which the outflowing gas likely cannot drag cold gas without disrupting it (see e.g. McCourt et al. 2015), or the lack of radiative cooling of the outflowing gas due to shocks (Zubovas & King 2014), or to the presence of metals in the CGM (Costa et al. 2015). The presence of cosmic rays could also change the velocity and outflow rate of the winds (e.g. Birnboim et al. 2015; Dubois & Commerçon 2016).

Finally, there are galaxies less massive than our least massive galaxy (observed with e.g. MUSE, HST, CANDELS, SINFONI, or ALMA), in which our results may not apply since stellar feedback is known to be very efficient in them (e.g. Ferrara & Tolstoy 2000; Stinson et al. 2009).

We acknowledge support from the EC through grants ERC-StG-257720 and the CosmoComp ITN. Simulations were performed at TGCC and IDRIS under GENCI allocations 2013-GEN2192 and 2014-GEN2192. We also acknowledge PRACE for awarding us access to resource Curie, based in France at Bruyères-le-Châtel.

JR was funded by the European Research Council under the European Unions Seventh Framework Programme (FP7/2007-2013) / ERC Grant agreement 278594-GasAroundGalaxies, and the Marie Curie Training Network CosmoComp (PITN-GA-2009-238356).

REFERENCES

Aalto, S., Muller, S., Sakamoto, K., et al. 2012, A&A, 546, A68
Barai, P., Viel, M., Borgani, S., et al. 2013, MNRAS, 430, 3213
Binney, J., & Tremaine, S. 1987, Galactic Dynamics
Birnboim, Y., Balberg, S., & Teyssier, R. 2015, Monthly Notices of the Royal Astronomical Society, 447, 3678
Boesgaard, A. M., & Steigman, G. 1985, Annual Review of Astronomy and Astrophysics, 23, 319
Bondi, H. 1952, Mon. Not. R. Astron. Soc., 112, 195
Bondi, H., & Hoyle, F. 1944, Mon. Not. R. Astron. Soc., 104, 273
Bouché, N., Hohensee, W., Vargas, R., et al. 2012, Monthly Notices of the Royal Astronomical Society, 426, 801
Bouché, N., Dekel, A., Genzel, R., et al. 2010, Astrophys. J., 718, 1001
Bournaud, F. 2016, Galactic Bulges, 418, 355

Bournaud, F., Dekel, A., Teyssier, R., et al. 2011, Astrophys. J., 741, L33

Bournaud, F., Elmegreen, B. G., Teyssier, R., Block, D. L., & Puerari, I. 2010, Monthly Notices of the Royal Astronomical Society, 409, 1088

Bournaud, F., Valentin Perret, Renaud, F., et al. 2014, Astrophys. J., 780, 57

Chartas, G., Hamann, F., Eracleous, M., et al. 2014, Astrophys. J., 783, 57

Cicone, C., Maiolino, R., Sturm, E., et al. 2014, A&A, 562, A21

Costa, T., Sijacki, D., & Haehnelt, M. G. 2015, Monthly Notices of the Royal Astronomical Society, 448, L30

Croton, D. J., Springel, V., White, S., et al. 2006, Mon. Not. R. Astron. Soc., 365, 11

Daddi, E., Dickinson, M., Morrison, G., et al. 2007, ApJ, 670, 156

Daddi, E., Bournaud, F., Walter, F., et al. 2010, ApJ, 713, 686

Davé, R., Finlator, K., & Oppenheimer, B. D. 2012, MNRAS, 421, 98

Dekel, A., & Silk, J. 1986, The Astrophysical Journal, 303, 39

Dekel, A., Birnboim, Y., Engel, G., et al. 2009, Nature, 457, 451

Dubois, Y., & Commerçon, B. 2016, Astronomy & Astrophysics, 585, A138

Dubois, Y., Devriendt, J., Slyz, A., & Teyssier, R. 2012, MNRAS, 420, 2662

Dubois, Y., Gavazzi, R., Peirani, S., & Silk, J. 2013, Mon. Not. R. Astron. Soc., 433, 3297

Dubois, Y., & Teyssier, R. 2008, Astronomy & Astrophysics, 477, 79

Elbaz, D., Dickinson, M., Hwang, H. S., et al. 2011, Astron. Astrophys., 119, 1

Ferrara, A., & Tolstoy, E. 2000, MNRAS, 313, 291

Feruglio, C., Fiore, F., Carniani, S., et al. 2015, A&A, 583, A99

Fierlinger, K. M., Burkert, A., Ntormousi, E., et al. 2016, MNRAS, 456, 710

Förster Schreiber, N. M., Shapley, A. E., Erb, D. K., et al. 2011, ApJ, 731, 65

Gabor, J. M., & Bournaud, F. 2013, Mon. Not. R. Astron. Soc., 16, 1

—. 2014, Mon. Not. R. Astron. Soc., 13, 1

Heckman, T. M., Armus, L., & Miley, G. K. 1990, The Astrophysical Journal Supplement Series, 74, 833

Heckman, T. M., Lehnert, M. D., Strickland, D. K., & Armus, L. 2000, The Astrophysical Journal Supplement Series, 129, 493

Hopkins, P. F., Kereš, D., Oñorbe, J., et al. 2014, Mon. Not. R. Astron. Soc., 445, 581

Hopkins, P. F., Quataert, E., & Murray, N. 2012, Mon. Not. R. Astron. Soc., 421, 3522

Hopkins, P. F., Torrey, P., Faucher-Giguère, C.-A., Quataert, E., & Murray, N. 2016, MNRAS, 458, 816

Kacprzak, G. G., Churchill, C. W., Murphy, M. T., & Cooke, J. 2015, Monthly Notices of the Royal Astronomical Society, 446, 2861

Kennicutt, R. C. 1998a, Annu. Rev. Astron. Astrophys., 36, 1

—. 1998b, Astrophys. J., 10

Kereš, D., Katz, N., Weinberg, D. H., & Davé, R. 2005, Monthly Notices of the Royal Astronomical Society, 363, 2

Kraljic, K., Renaud, F., Bournaud, F., et al. 2014, Astrophys. J., 784, 112

Krumholz, M. R., Mckee, C. F., & Klein, R. I. 2004, Astrophys. J., 611, 399

Krumholz, M. R., & Tan, J. C. 2007, ApJ, 654, 304

Lau, M. W., Prochaska, J. X., & Hennawi, J. F. 2015, ArXiv e-prints, arXiv:1510.06018

Liu, H.-L., Wu, Y., Li, J., et al. 2015, The Astrophysical Journal, 798, 30

Magorrian, J., Tremaine, S., Richstone, D., et al. 1998a, AJ, 115, 2285

—. 1998b, The Astronomical Journal, 115, 2285

Martin, C. L., Shapley, A. E., Coil, A. L., et al. 2012, The Astrophysical Journal, 760, 127

—. 2013, The Astrophysical Journal, 770, 41

Martizzi, D., Faucher-Giguère, C.-A., & Quataert, E. 2015, Mon. Not. R. Astron. Soc, 450, 504

McCourt, M., O'Leary, R. M., Madigan, A.-M., & Quataert, E. 2015, MNRAS, 449, 2

Mullaney, J. R., Daddi, E., Béthermin, M., et al. 2012, Astrophys. J., 753, L30

Murray, N. 2011, Astrophys. J., 729, 133

Noeske, K. G., Weiner, B. J., Faber, S. M., et al. 2007, ApJ, 660, L43

Novak, G. S., Ostriker, J. P., & Ciotti, L. 2012, MNRAS, 427, 2734

Olive, K. A., Steigman, G., & Walker, T. P. 2000, Physics Report, 333, 389

Oppenheimer, B. D., & Davé, R. 2008, MNRAS, 387, 577

Pettini, M., Rix, S. A., Steidel, C. C., et al. 2002, The Astrophysical Journal, 569, 742

Rasera, Y., & Teyssier, R. 2006, A&A, 445, 1

Reines, A. E., & Volonteri, M. 2015, The Astrophysical Journal, 813, 82

Renaud, F., Kraljic, K., & Bournaud, F. 2012, Astrophys. J., 760, L16

Renaud, F., Bournaud, F., Emsellem, E., et al. 2013, Mon. Not. R. Astron. Soc., 436, 1836

Roos, O., & Bournaud, F. 2016, in IAU Symposium, Vol. 319, Galaxies at High Redshift and Their Evolution Over Cosmic Time, ed. S. Kaviraj, 41–44

Roos, O., Juneau, S., Bournaud, F., & Gabor, J. M. 2015, Astrophys. J., 800, 19

Schroetter, I., Bouché, N., Péroux, C., et al. 2015, Astrophys. J., 804, 83

Sharma, P., Roy, A., Nath, B. B., & Shchekinov, Y. 2014, Monthly Notices of the Royal Astronomical Society, 443, 3463

Silk, J. 2011, in IAU Symposium, Vol. 277, Tracing the Ancestry of Galaxies, ed. C. Carignan, F. Combes, & K. C. Freeman, 273–281

Sommer-Larsen, J. 2006, Astrophys. J., 644, L1

Steidel, C. C., Erb, D. K., Shapley, A. E., et al. 2010, Astrophys. J., 717, 289

Stinson, G. S., Dalcanton, J. J., Quinn, T., et al. 2009, MNRAS, 395, 1455

Tacconi, L. J., Genzel, R., Neri, R., et al. 2010, Nature, 463, 781

Tacconi, L. J., Neri, R., Genzel, R., et al. 2013, ApJ, 768, 74

Taylor, P., & Kobayashi, C. 2015, Monthly Notices of the Royal Astronomical Society, 448, 1835

Teyssier, R. 2002, Astron. Astrophys., 385, 337

Teyssier, R., Moore, B., Martizzi, D., Dubois, Y., & Mayer, L. 2011, MNRAS, 414, 195

Tombesi, F., Meléndez, M., Veilleux, S., et al. 2015, Nature, 519, 436

Truelove, J. K., Klein, R. I., Mckee, C. F., et al. 1997, Astrophys. J., 489, 179

Volonteri, M., & Reines, A. E. 2016, The Astrophysical Journal Letters, 820, L6

Volonteri, M., & Stark, D. P. 2011, MNRAS, 417, 2085

Wang, R., Carilli, C. L., Neri, R., et al. 2010, ApJ, 714, 699

White, S. D. M., & Frenk, C. S. 1991, The Astrophysical Journal, 379, 52

Zubovas, K., & King, A. R. 2014, MNRAS, 439, 400

Zuckerman, B., & Evans, II, N. J. 1974, ApJ, 192, L149

Chapter 5

Conclusions

Contents

When I started my PhD thesis, supermassive black holes in active phases (active galactic nuclei, or AGNs) were mainly invoked as the usual suspects, when it came to galaxy quenching. The purpose of this chapter is to recap the work done in the field of AGNs during the time of this thesis, to sum up the conclusions of my work, and to open it to future perspectives.

5.1 AGN feedback, a state-of-the-art from before my thesis to today

When I started my PhD, the bimodality between galaxies actively forming stars at all observed redshifts and "red and dead" galaxies forming (almost) no stars anymore was already well-known (see Section 1.1.4), even though the physical mechanisms killing galaxies were (and are) still debated. Furthermore, current models predict galaxies which are too massive compared to observations, and do not reproduce the observed fraction of baryons located in the intergalactic medium, thus requiring strong feedback processes to expel gas.

AGNs, with their powerful outflows and extreme luminosities, were often pointed at to explain both the quenching of massive galaxies by the sudden removal of all their gas content, and the presence of 80 % of baryons around them. They were also pointed at to explain the slow starvation scenario, by keeping the halo of massive galaxies hot enough to prevent cosmic inflows on the long term, therefore inducing a slow consumption of the gas in the interstellar medium and the eventual cessation of star formation activity and black hole fueling.

There are two modes of black hole accretion (high-efficiency and low-efficiency), which respectively drive outflows and jets, and are responsible for the so-called "quasar-mode" and "maintance-mode" or "radio-mode" feedback. Both modes were already frequently accounted for in simulations when I started my PhD (e.g. Sijacki et al., 2007; Martizzi et al., 2012; Dubois et al., 2012, 2013). While the latter mode is dominant in massive elliptical galaxies, typical star-forming galaxies rather show large-scale galactic outflows. Here, I focus on the relation between AGNs and star-forming galaxies, and the evolution of theorists' view about quenching from AGNs during the last three years is recapitulated (see Somerville & Davé, 2015, for a recent review).

The earliest 3D simulations of galaxies including AGN feedback (and stellar feedback) were presented in Springel et al. (2005b); Di Matteo et al. (2005), and modelled mergers of idealized disk galaxies inducing extreme quasar episodes. AGN feedback was modelled as a fraction of the bolometric luminosity (inferred from the Bondi accretion rate) deposited as thermal energy into the gas particles around the black holes, and was able to drive strong outflows that eventually stopped black hole accretion. Such outflows removed almost all the gas from the resulting galaxy, leading to the quenching of star formation (Springel et al., 2005a). Since then, a similar approach of AGN feedback has been used in a large number of studies, with increasing resolution and additional physics. Hence, Sijacki et al. (2007) included for the first time both the "quasar-mode" and "maintenance-mode" of AGN feedback in their cosmological simulations. At that time, the approach had to be simplified, because of the relatively coarse numerical resolution. Based on this study, more and more similar approaches have since been implemented, and some of them are briefly described here.

In the first studies, only extreme quasars and mergers in idealized galaxies could be accounted for. But with the improvement of both resolution and models, cosmological simulations were made possible, and astrophysicists started to consider typical AGNs in typical Main Sequence galaxies, both in isolated galaxy simulations and cosmological runs. Among large-scale cosmological simulation projects including AGN feedback, we find:

- OWLS (OverWhelmingly Large Simulations, see Schaye et al., 2010) and EAGLE (Evolution and Assembly of GaLaxies and their Environments, see Schaye et al., 2015), including stellar and AGN feedback. More specifically, they include "stochastic" thermal AGN feedback, in which an average energy injection rate is stored for each black hole, until it can stochastically heat a given threshold number of particles with a given temperature increase. In OWLS, the feedback from AGNs is efficient at high masses, and an increased initial wind model with velocity increasing with gas pressure or halo mass allows to generate galaxy-wide outflows at all masses (Haas et al., 2013). In the EAGLE simulations, sub-grid feedback models were calibrated to the observed present-day galaxy stellar mass function and sizes, and reproduce the observed growth of the stellar mass density to within 20 % (Furlong et al., 2015);
- Dubois et al. (2012) developed a model of AGN feedback for cosmological simulations using a quasar-heating mode when the black hole accretion rate is comparable to the Eddington rate, and a radio-jet mode at lower accretion rates. This feedback model not only deposits energy on the grid, but also mass and momentum. They showed that AGN feedback efficiently prevents the accumulation of gas and efficiently ejects it of galaxies, significantly suppressing star formation. This project is based on early Horizon simulations, and gave birth to the Horizon-AGN simulation project. In this framework, Kaviraj et al. (2016) quantify how feedback from black holes helps shape galaxy stellar-mass growth in the redshift range $0 < z < 6$, particu-

larly in the most massive galaxies, in comparison to Horizon-noAGN. According to Dubois et al. (2016), the merger-enhanced AGN activity is able to durably set the morphological type of the post-merger remnant by quenching its quiescent star formation on extended periods of time. Finally, Volonteri et al. (2016) show that both a central and an off-centre AGN can shine concurrently in some cases, and that this dual AGN population decreases with redshift, in agreement with observations.

- The Illustris simulations (Vogelsberger et al., 2014) use the Bondi accretion model of Sijacki et al. (2007) and a similar feedback scheme, and additionally include a simplified treatment of photo-ionization and photo-heating due to the AGN radiation field. For instance, Sijacki et al. (2015) find that black holes and their host galaxies co-evolve at the massive end, but for low-mass star-forming galaxies no tight relation with either their central black hole masses or the nuclear AGN activity exists.
- Finally, Richardson et al. (2016) developed a project of comparison of cosmological zoom simulations including AGN feedback. They include both adaptive mesh refinement and smoothed particle hydrodynamics simulations modelling a region around a forming galaxy cluster, and they compare the ability of the methods to handle successively more complex baryonic physics.

In addition to large cosmological projects studying the effects of AGN feedback at large scale, simulations of isolated galaxies and/or isolated mergers also developed to study the impact of AGNs at smaller scales, and catch the small-scale processes such as black hole accretion, wind propagation and star formation more accurately. Among them, we find:

- Newton & Kay (2013) found that for each of the stellar and AGN feedback processes, the heating temperature is the dominant parameter, rather than the overall energy budget or timing of heating events;
- Gabor & Bournaud (2013, 2014); Roos et al. (2015) showed that typical AGN winds and radiation modelled without free parameters at high resolution (6 pc) are a good mechanism to regulate the mass of the host-galaxy, but not to quench its star formation activity (see next section for further details);
- Barai et al. (2014) formulated kinetic AGN feedback models for energy- and momentum-driven winds, using only two free parameters: the feedback efficiency and the AGN wind velocity. They found that kinetic AGN feedback generates intermittent bipolar jet-like outflows of gas in the isolated galaxy simulations. In contrast, the thermal AGN feedback model from Springel's team was found to have negligible impact on gas properties. Barai et al. (2014) claimed that the effect seen in previous works is due to gas depletion around the black hole and the creation of an artificial cavity.
- Hopkins et al. (2016) studied the interaction between AGN feedback and a multiphase interstellar medium, in simulations including explicit stellar feedback, multiphase cooling, accretion disk winds, and Compton heating. They found that AGN winds suppress the nuclear star formation rate by factors of 10 to 30, the black hole accretion rate by factors of 3 to 30, and

increase the outflow rate from the nucleus by factors of 10, in agreement with observational evidence for galactic-scale AGN outflows.

- Bieri et al. (2016) focused on the radiative effects of AGNs in star-forming disks with idealized interstellar medium, and showed that quasars ($L = 10^{46}$ erg.s^{-1}) can drive large-scale winds with high velocities and substantial mass outflow rates of about 10^3 $M_\odot$.yr^{-1} for a few million years, in agreement with observations. They favored energy-driven winds via extremely fast nuclear outflows, and interpreted them as being IR-radiatively-driven winds.
- Roos et al. (2016) studied the coupling between AGN and stellar feedback processes, and showed that the mass outflow rate of the outflows depends on the mass of the host and can be either positive compared to AGN feedback alone (low-mass simulation) and enhance the mass outflow rate of the wind, or negative compared to AGN feedback alone (intermediate-mass simulation) and decrease the mass outflow rate of the wind (see next section for further details).

Thanks to these studies, progress has been made in the field of active galactic nucleus feedback. Typical “moderate” AGNs living in most star-forming galaxies are now recognized, and were shown incapable of quenching galaxies. Despite this, we now know they can regulate the total baryonic mass of galaxies through powerful outflows.

5.2 CSI: Cosmic Scene Investigations, lessons learned from a 3-year investigation

During the last three years, my work was to check whether or not typical AGNs are guilty of abruptly ending the star formation processes in typical Main Sequence galaxies at redshift 2, and how important their impact on their host was in terms of mass outflow rate and star formation suppression. Indeed, supermassive black holes in active phases are the ideal culprits of such cosmic crimes, since it is known from low-resolution simulations and theory that they release enough energy to blow out the entire gas content of their host. In this thesis, I desribed the work I did during three years in order to investigate the case. It was made possible by the latest high-performance computing resources and massively parallel computation techniques, which allowed me to run and study simulations of galaxy evolution at high resolution (12 to 1.5 pc), with acccurate modelling of feedback processes from the AGN and the stars.

Even if the AGNs look like the ideal culprits and were often pointed at as cosmic killers when I started my PhD (see above), I showed in Roos et al. (2015), together with Gabor & Bournaud (2013, 2014) that the winds and long-range photo-ionization of typical AGNs living in normal star-forming galaxies cannot be responsible for the sudden death of galaxies. Following the intuition that feedback processes could couple non-linearly to produce fast winds with high mass outflow rates, I wrote a PRACE proposal in which I explained that the stars could be the AGN’s partners in crime, and join in a cosmic criminal conspiracy to kill their host (i.e.: I proposed to study the properties of winds generated by both the AGN and the stars, which could potentially expel gas in the circumgalactic medium efficiently, and quench the star formation activity of their host).

With the POGO simulations, I showed that the interplay between AGN and stellar feedback processes indeed changes the mass outflow rate, depending on the stellar mass of the host. Therefore, despite the fact that the AGN remains the main outflow driver at all masses studied, it is important to account for accurate stellar feedback modelling, to get reliable outflow parameters and mass outflow rates. At low mass (M_{gas} = 1.5.10^{10} $M_{\odot}$), AGN and stellar feedback act together to create a stronger wind than that produced by the AGN alone. Stellar feedback helps feeding the central supermassive black hole, resulting in more efficient feedback and more powerful outflows. Also, gas lifted by the stellar winds is swept up by the AGN before it has time to fall back on the galaxy (as galactic fountains do), therefore adding mass to the global wind. Lastly, stellar outflows propagate in a diffuse and hot circum-galactic medium which is reguarly swept up by AGN bursts, which can enhance their mass outflow rate. At intermediate mass (M_{gas} = 4.9.10^{10} $M_{\odot}$), AGN and stellar feedback act against each other, and the strength of the global wind is reduced. Indeed, stellar outflows re-distribute the gas from the central region to the outskirts, but the gravitational potential well is too deep for the stellar feedback to produce strong outflows. Therefore, the fountains fall back on the disk before the AGN bursts have time to sweep the gas in the global outflow. Moreover, stellar feedback feeds the black hole less efficiently and AGN winds have less material to entrain. This results in a less powerful galactic wind.

To sum up, even though the criminal association leads to powerful winds with maximal mass outflow rates of about 2 to 20 times the star formation rate of their host, the expelled gas is mostly hot and diffuse and the star-forming phase is untouched, as in Gabor & Bournaud (2013, 2014). Therefore, AGN and stellar feedback, even when they are combined, cannot be responsible for the abrupt quenching of star formation in z $\sim$ 2 Main Sequence galaxies at all masses we studied. Nonetheless, the mass outflow rate of AGN and stellar winds is higher in low-mass galaxies, compared to AGN winds. When integrated down to redshift zero, this could significantly change the gas fraction and morphology of local galaxies in the models. However, whether this positive coupling in low-mass galaxies generates outflows powerful enough to account for a significant fraction of the mass located outside galaxies remains to be proven. The results of the POGO simulations are available in Roos & Bournaud (2015), in press, and Roos et al. (2016), submitted to the Astrophysical Journal.

To conclude, the mystery of the death of galaxies is still far from being solved and there is still plenty of research to do, since normal AGNs and stellar outflows only give clues for the removal of some of the gas in low-mass galaxies, and cannot explain quenching at any of the masses studied. Nonetheless, the gang of cosmic rays is not above suspicion, and is now in the firing line of astrophysicists (see next section).

5.3 *Future perspectives*

During this thesis, I studied typical galaxies of the Main Sequence at the apogee of cosmic star formation rate and supermassive black hole growth, i.e. redshift $\sim$ 2. My main research interests are the various internal sub-pc processes that occur inside a star-forming galaxy: star formation, stellar radiation, supernova explosions, supermassive black hole fueling and AGN feedback; and how they affect their host at large scale (a few hundreds of kpc).

I focused on simulations of isolated galaxies including several models of AGN and stellar feedback. It would also be of interest to consider other types of simulations (mergers, cosmological simulations or cosmological zooms, low-redshift galaxies, etc.), and to improve the current implementation of physics at the smallest scales reachable in simulations. This could help us improve our knowledge of their effect at the scale of the entire galaxy (a few tens of kpc), and even the intergalactic medium, in terms of star formation rate, outflow rate, quenching and gas expulsion. The following sections give hints on the ways to achieve this and to expand the scope of the research performed during this PhD thesis.

5.3.1 Compare isolated galaxies to mergers and cosmological zooms

My work is based on isolated galaxy simulations, but it would be interesting to broaden the scope of the work and study two alternate cases: isolated mergers, and cosmological zooms.

In the case of a merger, the spatial distribution of gas changes, and it is possible that the effects of AGN photo-ionization on the star formation activity of the galaxy are stronger compared to the case of an isolated disk, and that the outflow propagation and coupling with interstellar medium is changed. On the one hand, gas gets more fragmented, and on the other hand, it is redistributed spherically. First, if the gas is sufficiently fragmented, the outflows will propagate through the paths of least resistance, as for isolated disks. Therefore, the situation would be similar to that presented in Gabor & Bournaud (2013, 2014); Roos et al. (2015), and AGN outflows and photo-ionization would not affect the star formation activity of the galaxy much. On the other hand, if the gas content becomes a rather smooth interstellar medium distributed spherically, the AGN photons would encounter gas in all directions, and may be able to expel/ionize the majority of it. In contrast with star-forming disks, this could potentially lead to the fast quenching of the resulting elliptical.

Several studies of AGN activity during a merger and its impact on star formation in a smooth interstellar medium have already been performed a few years ago (see e.g. Di Matteo et al., 2005; Newton & Kay, 2013) and were showing a fast quenching of star formation due to the ejection of all the gas of the galaxy. Even though these first simulations at low resolution opened the way to many interesting studies, with the high-resolution simulations available today and the numerous physical processes that were added to them, many non-linear physical phenomena are at stake. Thus, predicting which of the two scenarios is the most probable (outflows efficient at removing all the gas from the host, or not) is difficult without performing new simulations.

Such high-resolution simulations would also help determining what physical process is responsible for the bulk of star formation and supermassive black hole growth: rare events such as major mergers can enhance both of them on short periods of time (leading to starbursts and quasar phases), while secular processes (bars, disk instabilities, etc) are less efficient at forming stars or fueling the central black hole, but act on much longer time-scales.

Finally, contrarily to isolated galaxy simulations or isolated merger simulations, cosmological zooms include a more realistic environment compared to what is observed in the Universe. Having a more realistic gaseous halo around the galaxy and cold streams inflowing onto the galaxy would allow us to predict the effects of AGN outflows and photo-ionization on longer time-scales than in Gabor & Bournaud (2013) and Roos et al. (2015), i.e. a few Gyr. Also, with such simulations, it would be possible to check whether the feedback models used in POGO are able to prevent gas from falling onto the galaxy, by keeping the gaseous halo hot and induce a slow starvation, or not.

5.3.2 Develop more accurate feedback recipes

Another important aspect is to improve all the feedback recipes we already have. Indeed, even if the resolution gets higher and higher in galaxy simulations, feedback processes are still sub-grid recipes (see Section 2.1.4.2 and Appendix B), even in the current highest-resolution isolated galaxy simulations (sub-pc scale). Therefore, effort must be made in order to get input from both lower- (cosmological scale) and higher-resolution (giant molecular cloud scale) simulations, and share all relevant results accross the different fields.

Furthermore, it would be interesting to apply RT post-processing (as in Roos et al., 2015) on several types of simulations (e.g. isolated low-redshift star-forming galaxies, mergers, cosmological zooms), in order to derive a simplified recipe for RT calculation, which could be used in any of these configurations. The comparison with RAMSES-RT runs in each case would also help check its consistency, and improve both methods.

Thermal AGN feedback can also be improved, for example by injecting energy in a non-spherical region of which the dimensions are dynamically determined based on physical assumptions. In Roos et al. (2015), I showed that the AGN is able to entirely ionize the diffuse cavity created by AGN winds at the centre of the galaxy, and to keep it ionized (see Figure 8 of Roos et al., 2015). Therefore, it may be more physical to inject energy inside this whole region rather than in the few cells surrounding the supermassive black hole (see Section 3.2.2.4). This could induce visible changes, since the pressure gradient would be stronger on the contour of the cavity. The size and shape of the injection region should then be computed according to the gas density and AGN luminosity, rather than based on an ad hoc prescription. Nonetheless, a statistical study on several snapshots of various simulations (low and high redshift, various masses, mergers, cosmological zooms, etc.) should be done first, in order to derive a reliable recipe to identify such a region.

To further constrain the shape and size of the injection region, it would be worth comparing the emission lines of the ionized gas in the central region (obtained with Cloudy following the process presented in Roos et al., 2015) to integral field spectroscopy (IFS) of nearby Seyfert nuclei, for example using the Gemini Multi-Object Spectrograph Integral Field Unit (GMOS-IFU) on the Gemini-South telescope (similarly to what Ricci et al. (2015) did for early-type galactic nuclei), or the Spectrograph for INtegral Field Observations in the Near Infrared (SINFONI, see e.g. Carniani et al., 2016) and the Multi Unit Spectroscopic Explorer (MUSE) on the VLT (see e.g. Schroetter et al., 2015).

Eventually, thanks to the high resolution of the simulations, the emission lines of the outflowing gas can also be compared to observations of the circumgalactic medium and outflows, and give clues about the sub-kpc gas clumps observed there by e.g. Crighton et al. (2015).

5.3.3 *Account for cosmic rays*

During my thesis, I combined several feedback sources (AGN, stars) and feedback models (thermal and kinetic energy injection, photo-ionization, radiative pressure injection). However, another source of feedback plays an important role in typical star-forming galaxies, namely: cosmic rays (see Sections 1.2.5.3 and 1.3.3.2). Indeed, improving resolution and existing feedback models is not sufficient if all important sources of feedback are not accounted for.

Cosmic rays are frequently observed in the Universe, and are created during supernova explosions (see Section 1.3.3.2), or by AGN jets or winds (see Section 1.2.5.3). Furthermore, they seem to be of great importance for the chemistry of the interstellar medium (e.g. Viti et al., 2013; Grenier et al., 2015), and many studies on cosmic rays are already on-going in RAMSES simulations of galaxies: see e.g. Birnboim et al. (2015) for simplified non-thermal pressure cosmic ray feedback, see also Dubois & Commerçon (2016) for anisotropic advection-diffusion of cosmic rays in magnetohydrodynamics simulations. In the POGO simulations, it would be interesting to study the coupling between supernovæ, young stars, AGNs and the cosmic rays they produce, as well as their potential impact on outflows and star formation, in collaboration with them.

A first step could be to compute the global effects of a cosmic ray background from supernovæ on the interstellar medium using simplified recipes (see e.g. Jubelgas et al., 2008, for such a study without AGN, see also Pakmor et al. 2016 for a more sophisticated treatement including injection of cosmic rays from supernovæ as well as advective transport, cosmic ray cooling, and cosmic ray transport through isotropic or anisotropic diffusion). But after this preliminary phase, should cosmic rays from supernovæ play a major role in star formation (see e .g. Pfrommer et al., 2007) and outflow driving (as in Pakmor et al., 2016), it would be necessary to eventually upgrade hydrodynamics simulations to magnetohydrodynamics (MHD, see e.g. Dubois & Commerçon, 2016) simulations and study more specifically the episodic production of energetic cosmic rays produced by active galactic nuclei (see also Sijacki et al., 2008).

* * *

APPENDIX A
Useful scripts

A.1 Bash scripts

The following subsections show useful aliases and bash functions I wrote during my thesis to easily (or lazily) handle files for the Cloudy post-processing method (Roos et al., 2015) and for the RAMSES simulations of the POGO Project (Roos & Bournaud, 2015; Roos et al., 2016, submitted to the Astrophysical Journal).

For more details about the “Cloudification process”, see Chapter 3, and for more details about the POGO simulations, see Chapter 4 and Table 4.1.

A.1.1 Aliases

```
alias shout='ls -1 *.out'  #Show *.out files (Cloudy)
alias shin='ls -1 *.in'    #Show *.in  files (Cloudy)
alias cout='shout | wc -l' #Count *.out files (Cloudy)
alias cin='shin | wc -l'   #Count *.in  files (Cloudy)
alias shook='shout | xargs grep -l "exited OK"' #Show OK files (Cloudy)
alias cook='shook | wc -l'                      #Count them (Cloudy)
alias shosww='shout | xargs grep -l "someth"'   #Show NOT OK files (Cloudy)
alias cosww='shosww | wc -l'                    #Count them (Cloudy)

alias output="ls -d output_00*/" #List outputs (RAMSES)
alias stout="store ; output" #List outputs in the cwd and in the corresponding storedir (RAMSES)
alias lastLOGO='simtime_last $LOGO/L*' #Show time of last output for all LOGO sims (RAMSES)

alias ipy='ipython --matplotlib' (Python)
```

A.1.2 Functions

The external Python, IDL or bash routines called by some of the following functions are available online (see next section).

```
#Cloudy
#Separate Cloudified files
cloudified () {
mkdir -p Done/ Sww/
echo Classifying files...
for i in `ls *.out | xargs grep -l 'Cloudy exited OK'` ; do
    echo $i is OK ; mv ${i/\.out/\*} ./Done
done
for i in `ls *.out | xargs grep -l 'something went wrong'` ; do
    echo $i has gone wrong ; mv ${i/\.out/\*} ./Sww
done
}
```

```
#General (Curie)
#Shows equivalent directory in storedir
store () { #to be used in scratchdir only
dir=$(pwd)
dir=${dir//$SCRATCHDIR}
ls -lh $STOREDIR/$dir
}

#RAMSES
#Output time in Myr
simtime () { #if no argument : all outputs in current dir, else specified output(s) in current dir
if [[ "$#" == "0" ]] ; then
    outpts=$(ls -d output_00*/)
else
    outpts=$@
fi
#echo $outpts
for i in $outpts ; do
    i=${i##*_00}
    i=${i%/} #get output number
    tmp=$(cat output_00$i/info_00$i.txt | grep time | awk '{print $3}')
    tm=$(echo "${tmp/E+/*10^}*14.9" | bc -l) #math function
                                             #+ substitutions to get readable number
                                             #+ conversion to Myr
    echo "Time for output_00$i : $(printf '%5.3f' $tm) Myr"
done
}

#Print time of last output
simtime_last () { #if no argument : last output of all sims, else last output of specified sim(s)
dir=$(pwd)
if [[ "$#" == "0" ]] ; then
    files=$(ls -d $SCRATCHDIR/POGO_*/[LM]*/ | grep -v beginning)
else
    files=$@
fi
for i in $files ; do
    cd $i
    tmp=${i##*rooso\/}
    echo $tmp #current directory
    outpt=$(ls -d output/output_00*/ | tail -n 1)
    outpt=${outpt##*_00}
    outpt=${outpt%\/} #get number of last output
    cd output
    if [[ "$tmp" == *"1"* ]] ; then ref_agn='052' ; tot_time='920' ; fi
    if [[ "$tmp" == *"2"* ]] ; then ref_agn='089' ; tot_time='580' ; fi
    if [[ "$tmp" == *"3"* ]] ; then ref_agn='273' ; tot_time='500' ; fi #references
    t_now=$(simtime $outpt | awk '{print $5}')
    t_ref=$(simtime $ref_agn | awk '{print $5}')
    to_go=$(echo "$tot_time-$t_now" | bc -l) #time to go
    elapsed=$(echo "$t_now-$t_ref" | bc -l)   #time elapsed
    ###echo Simulation planned to stop at $tot_time Myr.
   ###echo Time elapsed : $(printf '%5.3f' $t_now) Myr. Time to go : $(printf '%5.3f' $to_go) Myr.
    echo AGN outflows launched $(printf '%5.3f' $elapsed) Myr ago.
    echo ''
done
cd $dir #go back to initial directory
}
```

```
#Count files in specified output
count () { #if no argument : all outputs in current dir, else specified output(s) in current dir
if [[ "$#" == "0" ]] ; then
    outpts=$(ls -d output_00*/)
else
    outpts=$@
fi
for i in $outpts ; do
    i=${i##*_00}
    i=${i%/}
    echo Number of files in output_00$i : $(ls output_00$i/ | wc -l)
done
}

#Count files of last output
count_last () { #if no argument : last output of all sims, else last output of specified sim(s)
dir=$(pwd)
if [[ "$#" == "0" ]] ; then
    files=$(ls -d $SCRATCHDIR/POGO_*/[LM]*/ | grep -v beginning)
else
    files=$@
fi
for i in $files ; do
    cd $i
    tmp=${i##*rooso\/}
    echo $tmp #current directory
    outpt=$(ls -d output/output_00*/ | tail -n 1)
    outpt=${outpt##*_00}
    outpt=${outpt%\/} #get number of last output
    cd output
    count $outpt #count number of files per output
    echo ''
done
cd $dir #go back to initial directory
}

#Speed of runs in Myr/day
speed () { #if no argument : last used logfile, else specified logfile(s)
if [[ "$1" == "" ]] ; then
    echo 'Treating last generated time_elapsed and dt file...'
    ipy -c "%run /fakepath/how_to_compute_physical_speed.py"
else
    for i in `ls $1*` ; do
        echo 'Treating '$i'...'
        ipy -c "%run /fakepath/how_to_compute_physical_speed.py --log $i"
        #echo ''
    done
fi
}

#Check simtime, file number and speed for last output
check_last () { #if no argument : last output of all sims, else last output of specified sim(s)
dir=$(pwd)
if [[ "$#" == "0" ]] ; then
    files=$(ls -d $SCRATCHDIR/POGO_*/[LM]*/ | grep -v beginning)
else
    files=$@
fi
#echo $files
```

```
for i in $files ; do
    tmp=${i##*rooso\/}
    echo $tmp #current directory
    cd $i
    nml=$(ls run_*.log | tail -n 1) #last logfile
    speed $nml #compute speed
    outpt=$(ls -d output/output_00*/ | tail -n 1) #last output
    outpt=${outpt##*_00}
    outpt=${outpt%\/} #get output number
    cd output
    #echo Output number is... $outpt
    if [[ "$tmp" == *"1"* ]] ; then ref_agn='052' ; tot_time='920' ; fi
    if [[ "$tmp" == *"2"* ]] ; then ref_agn='089' ; tot_time='580' ; fi
    if [[ "$tmp" == *"3"* ]] ; then ref_agn='273' ; tot_time='500' ; fi #references
    t_now=$(simtime $outpt | awk '{print $5}')
    t_ref=$(simtime $ref_agn | awk '{print $5}')
    elapsed=$(echo "$t_now-$t_ref" | bc -l)
    echo AGN outflows enabled at output_00$ref_agn. Time elapsed since then : $elapsed Myr.
    #Simulation planned to stop at $tot_time Myr.
    simtime $ref_agn $outpt #compute time
    count $outpt  #count files
    echo ''
done
cd $dir #go back to initial directory
}

#Clean output
cleano () { #Remove all files in specified output, except *.txt
if [[ -d "output_00$1" ]] ; then #if directory exists
    cd output_00$1 ; rm `ls * | grep -v txt` ; ls ; cd .. ; count $1 #clean, show files, count them
else
    echo output_00$1 does no exist. Aborting...
fi
}

#Black hole accretion rate
bhar () { #Get BHAR of specified logfiles
rm accretion.txt #remove previous file if any
for i in `ls $@` ; do
    echo $i
    logfile_extract $i accretion >> accretion.txt #run program and concatenate
done
ipy /fakepath/how_to_compute_BHAR.py #get BHAR
}
```

A.1.3 Stand-alone codes

The job scripts for Curie and bash routines I wrote and used during this thesis are available at `https://bitbucket.org/rooso/jobutils/src`. Some of them rely on a RSA public key to download files from Curie to a local computer automatically.

- `Be_Lazy.sh`: automated process to download all new files from Curie and process them with `Lets_POGO.sh`.
- `EPS_to_MOVIE.sh`: convert separated .eps files to a single movie.
- `Lets_POGO.sh`: download all files generated for a given output from Curie and process them.
- `MASTER_JOB`: single file to run to launch all useful programs.

- `OUTFLOWS_MEAN.txt`: update outflow files and generate plots of the mean.
- `change_file_names.sh`: rapidly change names of a large number of files.
- `clear_empty_eps_files.sh`: rapidly remove all empty .eps files.
- `dl_movies.sh`: download last version of simulation movies from Curie.
- `job_vesc.sh`: download escape velocity files from Curie and process them.
- `make_large_T_maps.sh`: replot all temperature maps.
- `mass_loadings.sh`: compute mass loading factors and generate plot.
- `update_movies.sh`: download relevant files and update movies with `EPS_to_MOVIE.sh`.
- `update_outflows.sh`: download relevant files and update all outflow plots.
- `update_sfr_maps.sh`: download relevant files and update all sfr maps.
- Jobs to be run on Curie:
    - `JOB`: submit this job to run all the following jobs on the last viable output.
    - `job_amr2map.py`: generate all relevant maps.[1]
    - `job_amr2map.tpl`: python template for job script above.
    - `job_movie`: convert fits.gz files to .jpg and wrap to movie.
    - `job_nTv_out.py`: generate density, temperature and velocity file.
    - `job_nTv_out.tpl`: python template for job script above.
    - `job_nTv_out_eps.py`: generate plot with the `nTv_out` file.
    - `job_nTv_out_eps.tpl`: python template for job script above.
    - `job_outflows_shells`: generate outflow files.
    - `job_tar`: tar new outputs and sync them to storedir (initially written by J. Gabor).

The various Python routines called to generate plots are described in the following section.

A.2 Routines in Python, Fortran 90 and IDL

This section recaps all the routines I've been using for my PhD thesis. I wrote most of them but also used routines authored by other people. URLs for where to find the codes are provided and a brief descritpion is given.

A.2.1 Python routines

All Python routines are available at `https://bitbucket.org/rooso/pyutils`.

- `RamsesMovie.py`: treat fits.gz file and format for movie.
- `Vescape.py`: plot escape velocity.
- `avg_sfr.py`: compute time average of star formation rate.
- `fargs.py`: parse a command line and get the arguments (author: F. Renaud).
- `outflows.py`: plot outflow rates as a function of time.

---

[1] This Python code generates job scripts which are then submitted on Curie. Trick used to pass command line parameters.

- `plot_LOP_sample.py`: plot a sample of LOPS.
- `plot_eos.py`: optimize `mass_sph` and `m_refine` for pseudo-cooling equation of state (author: F. Renaud).
- `plot_sfr.py`: plot star formation rate as a function of time (author: F. Renaud).
- `pythonstartup.py`: define plot formatting on start-up.
- `rho_T_diagram_sequential_no-units.py`: plot density-temperature diagram or density, temperature and altitude versus outflow velocity.
- `sfr_map.py`: compute star formation rate map from density and temperature maps.
- `show_fits.py`: plot various maps from fits.gz files.
- `slice.py`: example code to get a slice with Pymses (author: M. Joos, modified by O. Roos).
- `valeska_color.py`: stand-alone example on how to use `find_colors.py` (developed for V. Valdivia).
- Routines in the `utils` module:
    - `CreateMovie.py`: movie wrapper (found as is on the internet and then modified).
    - `__init__.py`: module file.
    - `do_hist2d.py`: build a 2D histogram.
    - `file_len.py`: search file length.
    - `find_colors.py`: find colors for specified range of values.
    - `get_boxlen_lmax.py`: search length of box and maximal level of refinement for a given RAMSES output.
    - `get_dir_name.py`: search the name of the current directory and format for plotting.
    - `get_labels.py`: search labels for given map.
    - `get_sim_time.py`: search time of given RAMSES output.
    - `get_unit.py`: search unit of plotted variable.
    - `jeans_correction.py`: correct for Jeans' polytrope.
    - `my_format.py`: custom number formatting (given as is during Python workshop).
    - `progressbar.py`: customized progress bar (found as is on the internet).
    - `readfast.py`: read big files fast (found as is on the internet).
- Codes to be used on Curie:
    - `how_to_compute_BHAR.py`: compute black hole accretion rate of specified logfile.
    - `how_to_compute_fine_dt.py`: compute duration of fine time-steps.
    - `how_to_compute_physical_speed.py`: compute speed of a run in Myr.day^{-1}.
    - `how_to_compute_time_elapsed.py`: compute physical time elapsed during run and duration of coarse time-steps.
    - `how_to_plot_bhar.py`: plot black hole accretion rate generated with the code `how_to_compute_BHAR.py`.

A.2.2 Fortran 90 routines

All Fortran routines are available at https://bitbucket.org/rooso/f90utils:

- `Makefile`: makefile for `amr2map.f90` and `part2map.f90` (author: R. Teyssier, modified by F. Renaud, J. Gabor and O. Roos).
- `amr2map.f90`: generate hydro maps from Ramses outputs (author: R. Teyssier, modified by F. Renaud, J. Gabor and O. Roos).
- `line_of_prop_cone.f90`: generate LOPs in an AMR cube from ASCII file (author: O. Roos).
- `line_of_prop_plane.f90`: generate LOPs in an AMR cube from ASCII file (author: O. Roos).
- `logfile_extract.f90`: extract various parameters (i.e.: black hole accretion rate) from Ramses logfile (author: J. Gabor).
- `outflows.f90`: generate outflow files from Ramses outputs (author: F. Renaud, modified by O. Roos).
- `part2map.f90`: generate particle maps from Ramses outputs (author: R. Teyssier).
- `post_cloudy_parameters.f90`: find nearest Cloudy point for each cell of a Ramses output (author: O. Roos).
- `sfr_amr.f90`: compute SFR of all cells in a Ramses output (author: O. Roos).

My version of Ramses is available at https://bitbucket.org/rooso/ramses_or.
The official and up-to-date version of Ramses (by R. Teyssier) is available at https://bitbucket.org/rteyssie/ramses.

A.2.3 IDL routines

All IDL routines I developed and/or used for my PhD thesis are available at https://bitbucket.org/rooso/idlutils/. There are too numerous to be all listed here (∼ 110 routines).

The Ramses plot routine mentioned in the previous section is `ramses_movie.pro` (written by J. Gabor), available in the `AMR_stuff` directory. The files `outflow_temp_movie.pro` and `outflow_vel_movie.pro` (same directory), also written by J. Gabor, show examples of use.

* * *

Appendix B

Ramses explained to beginners

Contents

This Appendix is a beginners' guide to simulate galaxies including star formation, supermassive black hole and accretion, stellar feedback, and AGN feedback.

B.1 Preparatory phases for Ramses galaxy simulations

Before launching your simulations in what we will call the "cruise mode", during which you will be able to study different physical parameters, you need to go through some preparatory stages. These stages and their purpose are described in the following sections.

B.1.1 Relaxation phase

This phase is physically motivated and aims at relaxing the hot gas. At $t = 0$, the simulation box contains an exponential disk of gas and stars (possibly with a bulge), inside a halo of gas and a halo of dark matter. Due to the projection on the grid, the disk is truncated. There is no analytical solution to the evolution of such a configuration[1], and the system is out of equilibrium when the simulation starts. Therefore, the initial conditions have to be relaxed. Furthermore, there is no turbulence at t = 0 (this could be implemented, but it would be complex and rely on assumptions), and thus thermal support must be ensured in order to avoid violent instabilities and a Toomre factor Q close to zero (see Equation 1.4).

At the end of the relaxation phase, spiral arms are supposed to have formed and, if a gas ring appeared due to instabilities, it is supposed to have dissipated. The recommended values of the Ramses keywords for this phase are described below.

Characteristics:

- Duration: 2 - 3 rotation periods (100 - 200 Myr) !short in wall-clock time,
- Resolution: low (30 - 50 pc) !since resolution is low.
- EOS (equation of state) parameters:
    - `isothermal = .true.` !temperature is set on the EOS at each coarse time-step.
    - `cooling = .false.` !disable cooling to save computation time.
      WARNING ! `isothermal` and `cooling` should always have opposite values.
    - `T2_star = 2E4 !K` !characteristic temperature of the EOS.
    - `eos_type = 'isothermal'`
      N.B.: `eos_type = 'isothermal'` and `isothermal = .true.` mean that the temperature of each cell is set to `T2_star` at each coarse time-step.
    - `jeans_refine = 0` !do not refine wrt. Jeans' length.
    - `nremap = 10` !do a load balancing every 10 coarse time-steps.
- Star formation is usually disabled during this phase (i.e.: `T2_star` is high enough so that the gas temperature is above 10^4 K, while the low resolution ensures that gas density is below the threshold `n_star`, see Section B.3.1) because the initial burst of star formation (see Section B.1.2.2) can rapidly deplete gas-rich galaxies of their gas during this phase.
- Stellar feedback can be either disabled to save computation time:
    - `f_ek = 0` !disable kinetic SN feedback.
    - `f_w = 0` !set loading factor for SN feedback to 0.
    - `eta_sn = 0` !disable mass loss from SNe.
    - `THII = 0` !disable radiative feedback from massive stars.

  or enabled from the beginning:

    - `f_ek = 0.9` !90 % of E_SN goes to kinetic SN feedback.

---

[1] Only analytical shapes can be in equilibrium from the beginning of a simulation, if the velocity distribution is appropriate. However, analytical shapes are not relevant here, because we want to study realistic galaxies, and model the interstellar medium with high density contrasts.

  - `f_w = -10` !loading factor of 10 for kinetic SN feedback.
    N.B.: the "-" sign means that thermal SN feeback is also enabled, with a fraction 1-`f_ek` of E_SN (see Section B.3.2). E_SN is the total energy of a supernova, 10^{51} erg.s^{-1}.
  - `eta_sn = 0.2` !fraction of stars exploding as SNe.
  - `THII = 6E4 !K` !temperature of the HII regions.
  - `nHII_skip = 200` !radiative feedback is applied on one star in `nHII_skip` stars, with an amplitude multiplied by `nHII_skip`. Increase `nHII_skip` to save computation time when there are too many HII regions to compute.

  N.B.: further explanations on how each stellar feedback model can be enabled or disabled are available in Section B.3.2.

- For a galaxy hosting an AGN, the BH sink particle can be created at the beginning:
  - `sink = .true.` !enable sink particles.
  - `init_black_hole = .true.` !create a BH sink particle at t = 0.

  N.B.: in cosmological runs, for instance, BH sink particles are dynamically created using various criteria (density threshold, velocity, etc., see RAMSES Users' Guide for more details).

- AGN feedback and BH accretion are either disabled to save computation time:
  - `bondi = .false.` !disable calculation of Bondi accretion rate.
  - `do_accretion = .false.` !disable BH accretion.
  - `agn = .false.` !disable AGN feedback.

  or enabled with `Tmax_global` low enough not to generate AGN outflows (also to save computation time[2]):
  - `Tmax_global = 5e7 !K` !maximal temperature allowed.
  - `bondi = .true.` !enable calculation of Bondi accretion rate.
  - `do_accretion = .true.` !enable BH accretion.
  - `agn = .true.` !enable AGN feedback.
  - `level_agn =` *lmax effective* !maximal level at which to compute AGN feedback.
    N.B.: The effective maximal level of refinement is the last level enabled in a given run.

  N.B.: the keyword `smbh = .true.|.false.` is deprecated in the version of RAMSES I use (see Section A.2.2) because it includes the custom BH sink particle and AGN feedback routines written by J. Gabor (see Gabor & Bournaud, 2013).

B.1.2 Transition phase: gradual increase of resolution

This phase is technically motivated and follows the relaxation phase. It is necessary because a direct increase of the resolution would not fit in memory. When increasing the resolution, the minimal temperature allowed in the simulation (`T2_star`) has to decrease, since we want to resolve denser gas. Hot gas thus needs to be allowed to cool down and get denser.

---

[2] AGN outflows propagate fast and thus induce small time-steps, see the CFL condition in Section 2.1.1.

B.1.2.1 First increase

In a first step, two additional levels of refinement are enabled (for how to do this, see Section B.2).

Characteristics:

- Duration: at least 1 load balancing (see Section B.1.4.1). When additional levels of refinement are enabled, gas condenses and many new cells are created, and trigger the creation of new cells around them (and so on) for a few time-steps. One needs to wait for this to stabilize.
- Lower `nremap`: `nremap = 2` (see Section B.1.4.1)
- Resolution: about 10 pc
- `T2_star = 2E3 !K` !gradually decrease to allow gas to cool down.
- `isothermal = .false.` !temperature is not forced on the EOS.
- `cooling = .true.` !enable cooling.
  WARNING ! `isothermal` and `cooling` should always have opposite values.
- `eos_type = 'isothermal'` !with `isothermal = .false.`, temperature is ≥ `T2_star`.
- Enable stellar feedback if not already enabled:
  - `f_ek = 0.9` !kinetic SN feedback (see above).
  - `f_w = -10` !loading factor for SN feedback (see above).
  - `eta_sn = 0.2` !fraction of stars exploding as SNe (see above).
  - `THII = 6E4 !K` !radiative feedback from OB stars (see above).
  - `nlev_sf` = *lmax effective* !maximal level at which star formation can occur (see Section B.3.1).
- Keep `Tmax_global` low to save computation time: `Tmax_global = 5e7 !K`.
- Leave AGN feedback and accretion disabled if not already enabled.

B.1.2.2 Down to maximal resolution (2 levels per step)

After this first increase of resolution, the process goes on down to the maximal level of refinement in the simulation (`levelmax`), with 2 more levels maximum per run.

Characteristics:

- Duration: at least 1 load balancing, wait for the new grid to be stable (see above).
- `T2_star = 300 !K` !decrease `T2_star` down to the temperature floor planned for the simulation.
- `jeans_refine = 4 *` *number of levels enabled* !force the Jeans' length to be refined by at least 4 cells at all enabled levels.
- `level_jeans` = *lmax effective* !level at which Jeans' polytrope is computed.

At this stage, gas is allowed to get dense enough to form stars. This increase in density is sudden because it is generated by the activation of the last level(s) of refinement. Therefore, many cells pass above the density threshold for star formation (see Section B.3.1) at the same time (and trigger the refinement of neighbouring cells, see above). This in turn induces a burst of star formation, which is a numerical artefact. Therefore, before starting the "cruise mode", one needs to wait for star formation to become steady.

At the maximal level of refinement and once star formation is steady:

- Enable BH accretion if not already enabled.
  - `bondi = .true.` !compute Bondi accretion rate (see above).
  - `do_accretion = .true.` !enable accretion (see above).
- Enable AGN feedback if not already enabled.
  - `agn = .true.` !enable AGN feedback (see above).
  - `inject_agn_cold_gas = .true.` !inject energy only in cells where temperature will be lower than `Tmax_AGN`.
  - `expand_agn_blast = .true.` !expand injection region if all cells in the region have their temperature above `Tmax_AGN`.
- `Tmax_AGN = 5E9 !K` !set `Tmax_AGN` high enough for the outflows to develop. WARNING ! `Tmax_AGN` does not supersede `Tmax_global` ! Make sure to set `Tmax_global` ≥ `Tmax_AGN`.
- `reset_accreted_mass_on_startup = 1` !reset mass accreted by the BH in the absence of AGN feedback[3] (otherwise, it can cause problems to eject the accumulated energy). /!\ DO NOT FORGET to disable for following runs.

B.1.3 Make sure everything is consistent

Before launching your simulations in the "cruise mode", do a final check of the value of the keywords in your namelist:

- EOS parameters:
  - `isothermal = .false.` !needs to be the opposite of `cooling`.
  - `cooling = .true.` !allow gas to cool (tabulated values).
  - `eos_type = 'isothermal'` !T ≥ `T2_star`.
  - Other possibility: to save computation time, do not actually use the cooling routine but use a pseudo-cooling EOS (less accurate, no outflow generation):
    - `isothermal = .true.`
    - `cooling = .false.`

---

[3] This applies only if BH accretion was enabled before AGN feedback. Do this if the preparatory phases are particularly long and an overdense clump is starting to form in the nuclear region.

  - `eos_type = 'pseudo_cooling'`

    N.B.: The "pseudo-cooling" EOS is a piecewise polytropic equation of state ensuring a rough thermal equilibrium (Bournaud et al., 2010). The hot and diffuse halo is set to the virial temperature and warm atomic hydrogen at 10^4 K is accounted for with an isothermal regime. Dense gas is at the temperature floor of the simulation. However, to prevent the artificial fragmentation of the densest regions and ensure the Jeans' length is always resolved by at least a few cells (Truelove et al., 1997), a density-dependent temperature floor — the so-called Jeans' polytrope — is implemented above a given density threshold (depending on resolution).

    N.B.B.: Even if actual cooling is used, this "pseudo-cooling" EOS is used to calibrate the gas density thresholds for refinement (see Section B.2).

- For an AGN:
  - Check `Tmax_AGN` is high enough for AGN feedback to work correctly (e.g. `Tmax_AGN = 5E9 !K`) and `Tmax_global` ≥ `Tmax_AGN`.
  - Make sure accreted the mass is not reset at each restart: `reset_accreted_mass_on_startup = 0`.

B.1.4 Optimization of load balancings and level synchronization

In a RAMSES simulation, the computation is distributed among many cores, each treating only a portion of the grid. As cells refine, some cores end up with higher loads while others — in which cells unrefine — end up under-occupied. The purpose of the load balancing is to *balance* the amount of tasks each core needs to treat. It is controlled by the keyword `nremap` (see Section B.1.4.1).

Due to the CFL condition (see Section 2.1.1), each level of refinement in the simulation evolves with a different time. To avoid a significant shift and ensure that time remains the same in the whole simulation box, all levels are regularly synchronized (see Section B.1.4.2).

This section describes how the load balancings and the level synchronization can be optimized to save computation time during a RAMSES run.

B.1.4.1 Load balancings: nremap

A load balancing is done every `nremap` coarse time-steps, i.e.: all CPUs exchange their information and the AMR grid is redistributed among them. This needs to be done regularly in order to avoid memory overloading (e.g. when too many cells refine on 1 CPU). However, doing load balancings too frequently slows down the code. Thus, `nremap` has to be tuned to get an optimal ratio between the duration of a load balancing and the slow down induced by memory overloading, before launching the simulation in "cruise mode" — and checked regularly.

To do that, you can:

- record the time elapsed between successive coarse time-steps — in the shell, type:

```
cat log_ramses | grep 'Time elapsed' > time_elapsed
```

- plot as a function of index using Python:

```
import numpy as np
import matplotlib.pyplot as plt
data = np.genfromtxt('time_elapsed',delimiter=':')
plt.plot(data[:,1])
```

The file `log_ramses` is the RAMSES logfile generated at each run. Its name depends on your RAMSES job script. In the plot, peaks correspond to load balancings[4]. The gradual increase between them corresponds to the increasing amount of data a CPU has to treat. Regularly make sure the ratio between the time needed to remap and the time gained is good.

B.1.4.2 Level synchronization: nsubcycle

At each level, time-steps evolve separately due to the different sizes of the cells and velocities of the gas (CFL condition, see Section 2.1.1). The keyword `nsubcycle` is an array with 1 value per level of refinement, and controls their synchronization: at level i, every $\texttt{nsubcycle}_i$ time-steps of level_i, the latter time-step is reset to:

$$dt_i = \frac{dt_{i-1}}{\texttt{nsubcycle}_i}. \tag{B.1}$$

For example:

- `nsubcycle = 1, 1, 1, 1`: there are 4 levels of refinement and they are all synchronized (single time-stepping).
- `nsubcycle = 2*1, 5*2`: there are 7 levels of refinement. The first two (l_{min} and l_{min}+1) are synchronized. For the following 5 levels, every 2 time-steps of level i, the time-step at level i is set to $dt_{i-1}/2$.

The coarsest levels can be synchronized (i.e.: `nsubcycle = 1, 1, ...`) to save computation time. Often, the relaxation phase (see previous section) has all its enabled levels synchronized.

B.2 Refinement strategies explained to beginners

This section describes the refinement strategies implemented in RAMSES that I used for my simulations. They are complementary with one another and are to be used together.

B.2.1 Refine by number of particles in a cell: m_refine

The first refinement criterion is the number of particles (stars of DM) per cell. While you usually want about 50 DM or star particles per cell, setting `m_refine` to arbitrary high values is the usual way to temporary disable levels of refinement.

---

[4] If the number of CPUs is high, some of these peaks correspond to output generation, not load balancings. Check their frequency with `nremap` and `foutput`.

Ex: `m_refine = 5*50, 2*1E10`: for the first five levels, refine if there are more than 50 DM and star particles in a cell. For the following two levels, refine if there are more than 10 billion DM and star particles in a cell (that is to say: DO NOT refine).

N.B.: `levelmin` and `levelmax` cannot be modified during a run and must be set to their final value from the beginning of the simulation. The *effective* maximal level of refinement is then controlled with `m_refine` and `mass_sph` (see next section).

B.2.2 Refine by gas mass per cell: mass_sph

In complement to the number of particles in a cell, one can refine by gas mass per cell and per particle (DM or star), i.e.: if the mass of gas in a cell is larger than `mass_sph*m_refine`.

Ex: `mass_sph = 2*1.5E-5, 8.8E-6, 5E-6, 3.6E-6, 2*1E10`

N.B.: `mass_sph` is in 1E9 solar masses per particle. In this example, the last two levels are disabled (as for the number of particles per cell, setting an arbitrary high value is the usual way to disable a level of refinement with `mass_sph`).

The threshold density corresponding to the threshold gas mass for level i is:

$$\frac{(\texttt{m\_refine} \times \texttt{mass\_sph})[\mathrm{1E9\ M_\odot}]}{\left(\frac{\texttt{boxlen}\,[\mathrm{pc}]}{2^i}\right)^3} \text{ in 1E9 } \mathrm{M_\odot.pc^{-3}}, \text{ with } 1\ \mathrm{M_\odot.pc^{-3}} \simeq 40\ \mathrm{cm^{-3}}. \qquad \text{(B.2)}$$

The values of `mass_sph` and `m_refine` are optimized for a pseudo-cooling EOS with `T2_star` set to 10^4 K (see Section B.1.3), using Florent Renaud's python tool `plot_eos.py`:

```
plot_eos.py -opt namelist
```

In the above instruction, `namelist` is the namelist you will use for your simulation in "cruise mode" (i.e.: with all levels of refinement enabled). This Python program makes sure the different levels resolve `jeans_refine` Jeans' length (see next section), each with a density threshold roughly corresponding to the equilibrium temperature gas would be at, if it was following the pseudo-cooling equation of state (see Section B.1.3). Even if actual cooling is accounted for, this gives an order of magnitude to set clever refinement thresholds.

N.B.: To use `plot_eos.py`, modify your namelist to account for the pseudo-cooling EOS and remove comments so that the program can read it:

- set `eos_type` to `'pseudo_cooling'` and `T2_star` to 10^4 K, no matter what you actually use (e.g. `cooling = .true.`, `isothermal = .false.`, `T2_star = 300 !K`, `eos_type = 'isothermal'`).

- remove comments behind all values read by the program in the namelist, i.e.: `levelmin` and `levelmax`, `level_jeans`, `boxlen`, `mass_sph` and `m_refine`, `T2_star`, `g_star`, and `eos_type`.

WARNING ! Do NOT use BOTH optimized `mass_sph` AND optimized `m_refine`. The routine gives you optimized `mass_sph` for your input `m_refine`, and vice versa. Choose one to change, usually `mass_sph`.

In some cases, you might want to unrefine coarse levels compared to the pseudo-cooling EOS, in order to save computation time.

B.2.3 Refine by Jeans' length: jeans_refine

Truelove et al. (1997) recommends to always ensure the resolution of Jeans' length by at least a few cells to prevent numerical instabilities and fragmentation — but also to refine cells in advance, so that self-gravitating structures are allowed to form.

Ex: `jeans_refine = 5*4, 2*0`: for the first five levels, refine if the Jeans' length is not resolved by 4 cells. The following two levels are disabled. To avoid numerical instabilities and fragmentation, all cells at `level_jeans` (and above) are arbitrarily heated along Jeans' polytrope (see Section 2.1.4.2).

B.2.4 Interpolation after refinement

When a cell is refined into $2^{n_{dim}}$ nested cells, it is possible to either interpolate the gas properties between the new cells and create a gradient, or divide all parameters by $2^{n_{dim}}$ to get equivalent cells. This is controlled by the keyword `interpol_type`:

```
interpol_type = 0|1|2|3 !(default: 0)
```

The four interpolation methods are the following:

- 0: no interpolation
- 1: MinMod limiter
- 2: MonCen limiter
- 3: Central slope
  WARNING ! Interpolation does not guarantee energy and momentum conservation.

The variables used for interpolation can be chosen with the following:

`interpol_var = 0|1 !(default: 1)`, with:

- 0: conservative variables (density, density times velocity, density times energy, see Equation 2.1.4.1)
- 1: primitive variables (density, velocity, pressure)

N.B.: I do not interpolate after refining, to ensure energy and momentum conservation within round-off errors. For more details about the interpolation methods, see the RAMSES Users' Guide.

B.3 Stars explained to beginners

This section describes the keywords and routines related to stars in the RAMSES code: star formation, supernova feedback and radiative feedback from massive stars.

B.3.1 Star formation

In the simulations, the star formation prescription follows the Schmidt-Kennicutt law with an efficiency `eps_star` of 0.03 (see Section 2.1.4.2). A new star particle is created if the gas density in a cell is larger than `n_star` and the temperature is lower than 10^4 K, with a mass randomly dsitributed around the mean value (Rasera & Teyssier, 2006):

$$M_{star,typical} = \frac{1}{2} \rho \cdot \left(\frac{\texttt{boxlen}}{2^{\texttt{nlev\_sf}}} \right)^3 . \tag{B.3}$$

In this equation, ρ is the mass density of the gas, `boxlen` is the size of the box, and `nlev_sf` is the maximal level at which star formation occurs. The factor of 1/2 ensures that at most half of the gas mass in a given cell is turned into a star particle at a given time-step. The keyword `nlev_sf` is a float controling the mass of new star particles. In isolated galaxy simulations, they are usually of the order of the mass of star clusters (of course, it depends on resolution).

B.3.2 Stellar feedback

This section describes how to enable or disable each stellar feedback model. This supposes you have my version of the RAMSES code (i.e.: with my patch for supernova feedback and F. Renaud's patch for radiative feedback). The meaning of the keywords is described in Section B.1.

Supernova feedback:
`f_ek > 0` and `f_w < 0` ==> thermal + kinetic SN FB (using `-1*f_w` + mass loss in kinetic FB).
`f_ek > 0` and `f_w = 0` ==> thermal SN FB only (+ mass loss in thermal SN FB).
`f_ek > 0` and `f_w > 0` ==> kinetic SN FB only (+ mass loss in kinetic SN FB).
`f_ek = 0` and `f_w = 0` ==> no SN FB (+ mass loss in thermal SN FB /!\).
N.B.: to disable mass loss too, set `eta_sn` (the number of stars exploding to SNe) to 0.

Radiative feedback from massive stars
`eta_sn > 0` and `THII < 0` ==> photo-ionization + radiative pressure (using `-1*THII`),
SN feedback is disabled (but mass loss enabled, see above).
`eta_sn > 0` and `THII > 0` ==> photo-ionization + radiative pressure and SN feedback (as above).
`eta_sn > 0` and `THII = 0` ==> no radiative feedback. SN feedback enabled (controlled as above).
`eta_sn = 0` and `THII = 0` ==> no stellar feedback at all and no mass loss (see above).

B.4 Black holes and AGN feedback explained to beginners

This section is based on J. Gabor's patch for sink particles and AGN feedback and lists all related keywords, their meaning and their recommended value. DO NOT put all keywords to their recommended value at once (see preparatory phases in Section B.1).

Keywords in the namelist:

- RUN parameters:
  - `sink = .true.` !enables treatment of sink particles.
  - `init_black_hole = .true.` !creates a BH at the beginning of the simulation.
- PHYSICS parameters:
  - `bondi = .true.` !compute the Bondi accretion rate (see Equation 2.8).
  - `do_accretion = .true.` !actually do the accretion.
  - `beta_accretion = 0.0` !power law index of Bondi accretion rate boost:

    $$\alpha = \left(\frac{\rho}{\texttt{n\_star}}\right)^{\texttt{beta\_accretion}} \quad \text{if } \rho > \texttt{n\_star}, \text{ else } \alpha = 1. \tag{B.4}$$

    `n_star` is the density threshold for star formation (see above).
  - `reset_accreted_mass_on_startup = 0` !do not reset accreted mass at each restart.
  - `agn = .true.` !enable AGN feedback.
    At each coarse time-step, the energy that would be released by the stored accreted mass is computed. If it is high enough to heat all cells in a radius of four cell sizes above `Tmin_AGN`, the blast wave is released, else it is stored (see Section 2.1.4.2).
  - `Tmin_AGN = 1E7 !K` !minimal temperature for AGN feedback.
  - `Tmax_AGN = 5E9 !K` !maximal temperature at which cells can be heated by the AGN blast wave.
    /!\ DOES NOT supersede `Tmax_global`.
  - `inject_agn_cold_gas = .true.` !within the injection region, energy is deposited only in cells that would be colder than `Tmax_AGN` once heated by the blast wave.
  - `expand_agn_blast = .true.` !in case no cell in the injection region would remain colder than `Tmax_AGN` once heated by the blast wave, the radius of the injection region is iteratively increased.
  - `level_agn` = *lmax effective* !maximal level at which BH accretion and AGN feedback are computed.
  - `radii_measure` = *radii in kpc* !measure the gas mass within spheres of specified radii.
  - /!\ `smbh = .true.` !obsolete keyword replaced by `do_accretion` and `check_smbh_formation_sites` (not used here).

- `INIT_BH parameters:`
  - `bh_x = 0. !kpc` !initial BH position. N.B.: `(0.,0.,0.)` is the centre of the box.
  - `bh_y = 0.`
  - `bh_z = 0.`
  - `bh_vx = 0.!km/s` !initial BH velocity.
  - `bh_vy = 0.`
  - `bh_vz = 0.`
  - `bh_mass = 5E-3 !1E9 Msun`
    N.B.: If more than one BH is needed (e.g.: merger simulation), separate BHs by commas.

B.5 RAMSES movies explained to beginners

This section presents the routines to produce movies during the execution of RAMSES simulations. They have mainly been developed by J. Gabor.

To create movies as you run your simulation (i.e.: you don't have to write more outputs to build your movie), put the following parameters in your namelist.
N.B.: this supposes you have the correct patches in your RAMSES directory (see `movie_param.f90` and `movie_module.f90` in the `patch` directory of your RAMSES distribution).

Keywords in the namelist:

- `OUTPUT parameters:`
  - `movie = .true.` !enable movie making.
- `MOVIE parameters:`
  - `dt_movie =`*n* `!Myr` !time between two snapshots in the movie.
  - `gas_or_parts = 'gas'|'parts'` !show gas or particles.
  - `lmax_movie =`*l* !maximal level of refinement for the snapshots.
  - `typ_m =`*n* !variable to show on the snapshots.
    For `'gas'`, the possible values are:
    1: mass-weighted mean density
    2: mass-weighted x-velocity
    3: mass-weighted y-velocity
    4: mass-weighted z-velocity
    7: mass-weighted temperature
    `-11`: surface density
    For `'parts'`, the only possible value is:
    1: total mass (per pixel)
  - `dir_m = x|y|z` !direction of projection of the snapshots.

- `xmin = [0,1]` !region of interest for the snapshots.
- `xmax = [0,1]`
- `ymin = [0,1]`
- `ymax = [0,1]`
- `zmin = [0,1]`
- `zmax = [0,1]`

  N.B.: The value is a fraction of the total box size `boxlen`.
- `suffix_m =` *string* !suffix added to the file names.
- `age_flag = 0|1|2` !choose which particles to show.

  The flag takes into account:
  - 0: all particles
  - 1: old particles only
  - 2: particles younger than `max_particle_age` only
- `max_particle_age =` n !maximum age of particles for `age_flag = 2`.

N.B.: to create several movies at a time, separate values for each keyword with commas.

These parameters generate one fits.gz file per `dt_movie` Myr for each element in the arrays (here, only one). To wrap them into a movie, run `job_movie` (see Section A.2.1) or try J. Gabor's IDL routine (see Section A.2.3).

* * *

Bibliography

Agertz, O., Teyssier, R., & Moore, B. 2009, Monthly Notices of the Royal Astronomical Society, 397, L64 (cited on page 9).

Agertz, O., Moore, B., Stadel, J., et al. 2007, Monthly Notices of the Royal Astronomical Society, 380, 963 (cited on page 33).

Arav, N. 1996, The Astrophysical Journal, 465, 617 (cited on page 20).

Balsara, D. S., & Krolik, J. H. 1993, The Astrophysical Journal, 402, 109 (cited on pages 19 and 20).

Barai, P., Viel, M., Murante, G., Gaspari, M., & Borgani, S. 2014, Monthly Notices of the Royal Astronomical Society, 437, 1456 (cited on pages 42 and 101).

Barnes, J. E., & Hut, P. 1989, The Astrophysical Journal Supplement Series, 70, 389 (cited on page 31).

Bekenstein, J. D. 1973, The Astrophysical Journal, 183, 657 (cited on page 15).

Berger, M. J., & Colella, P. 1989, Journal of Computational Physics, 82, 64 (cited on page 30).

Bertschinger, E. 2001, The Astrophysical Journal Supplement Series, 137, 1 (cited on page 34).

Bieri, R., Dubois, Y., Rosdahl, J., et al. 2016, ArXiv e-prints, arXiv:1606.06281 (cited on page 102).

Binney, J., & Tremaine, S. 1987, Galactic Dynamics (cited on pages 12, 13, 25, 26 and 76).

Birnboim, Y., Balberg, S., & Teyssier, R. 2015, Monthly Notices of the Royal Astronomical Society, 447, 3678 (cited on page 106).

Birnboim, Y., & Dekel, A. 2003, Monthly Notices of the Royal Astronomical Society, 345, 349 (cited on page 10).

Blandford, R. D., & Payne, D. G. 1982, Monthly Notices of the Royal Astronomical Society, 199, 883 (cited on page 20).

Blanton, M. R., & Moustakas, J. 2009, Annual Review of Astronomy & Astrophysics, 47, 159 (cited on page 6).

Blecha, L., Sijacki, D., Kelley, L. Z., et al. 2016, Monthly Notices of the Royal Astronomical Society, 456, 961 (cited on page 15).

Boesgaard, A. M., & Steigman, G. 1985, Annual Review of Astronomy and Astrophysics, 23, 319 (cited on page 75).

Bolatto, A. D., Wolfire, M., & Leroy, A. K. 2013, Annual Review of Astronomy & Astrophysics, 51, 207 (cited on page 6).

Bondi, H. 1952, Monthly Notices of the Royal Astronomical Society, 112, 195 (cited on page 36).

Bondi, H., & Hoyle, F. 1944, Monthly Notices of the Royal Astronomical Society, 104, 273 (cited on page 36).

Booth, C. M., & Schaye, J. 2009, Monthly Notices of the Royal Astronomical Society, 398, 53 (cited on pages 37 and 42).

Booth, C. M., & Schaye, J. 2013, Nature Scientific Reports, 1738 (cited on page 78).

Bouché, N., Hohensee, W., Vargas, R., et al. 2012, Monthly Notices of the Royal Astronomical Society, 426, 801 (cited on page 75).

Bournaud, F. 2016, Galactic Bulges, 418, 355 (cited on pages 6 and 13).

Bournaud, F., Daddi, E., Weiß, A., et al. 2015, Astronomy & Astrophysics, 575, A56 (cited on page 6).

Bournaud, F., Elmegreen, B. G., Teyssier, R., Block, D. L., & Puerari, I. 2010, Monthly Notices of the Royal Astronomical Society, 409, 1088 (cited on page 120).

Bournaud, F., Valentin Perret, Renaud, F., et al. 2014, The Astrophysical Journal, 780, 57 (cited on pages iii, 26, 41, 76 and 77).

Burkert, A., & Hartmann, L. 2013, The Astrophysical Journal, 773, 48 (cited on page 35).

Carniani, S., Marconi, A., Maiolino, R., et al. 2016, Astronomy & Astrophysics, 591, A28 (cited on page 106).

Carrasco, E. R., Conselice, C. J., & Trujillo, I. 2010, Monthly Notices of the Royal Astronomical Society, 405, 2253 (cited on page 6).

Chabrier, G. 2003, Publications of the Astronomical Society of the Pacific, 115, 763 (cited on page 23).

Chandrasekhar, S. 1984, Science, 226, 497 (cited on page 23).

Chartas, G., Hamann, F., Eracleous, M., et al. 2014, The Astrophysical Journal, 783, 57 (cited on pages iii, 20 and 77).

Chelouche, D., & Netzer, H. 2003, Monthly Notices of the Royal Astronomical Society, 344, 233 (cited on page 20).

—. 2005, The Astrophysical Journal, 625, 95 (cited on pages 19 and 21).

Colbert, E. J. M., & Mushotzky, R. F. 1999, The Astrophysical Journal, 519, 89 (cited on page 13).

Colgate, S. A. 1967, The Astrophysical Journal, 150, 163 (cited on page 14).

Combes, F. 2001, in Advanced Lectures on the Starburst-AGN, ed. I. Aretxaga, D. Kunth, & R. Mújica, 223 (cited on pages 13, 14 and 15).

Combes, F. 2006, Formation and Evolution of Supermassive Black Holes, ed. J. W. Mason, 159 (cited on page 12).

Costa, T., Sijacki, D., & Haehnelt, M. G. 2014, Monthly Notices of the Royal Astronomical Society, 444, 2355 (cited on page 9).

Costa, T., Sijacki, D., & Haehnelt, M. G. 2015, Monthly Notices of the Royal Astronomical Society, 448, L30 (cited on page 78).

Courant, R., Friedrichs, K., & Lewy, H. 1928, Mathematische Annalen, 100, 32 (cited on page 32).

Courvoisier, T. J.-L., Paltani, S., & Walter, R. 1996, Astronomy & Astrophysics, 308, L17 (cited on page 14).

Crighton, N. H. M., Hennawi, J. F., Simcoe, R. A., et al. 2015, Monthly Notices of the Royal Astronomical Society, 446, 18 (cited on page 106).

Croton, D. J., & Farrar, G. R. 2008, Monthly Notices of the Royal Astronomical Society, 386, 2285 (cited on pages 9 and 41).

Croton, D. J., Farrar, G. R., Norberg, P., et al. 2005, Monthly Notices of the Royal Astronomical Society, 356, 1155 (cited on pages 9 and 41).

Croton, D. J., Springel, V., White, S., et al. 2006, Monthly Notices of the Royal Astronomical Society, 365, 11 (cited on pages iii, v, 9, 41 and 75).

Daddi, E., Renzini, A., Pirzkal, N., et al. 2005, The Astrophysical Journal, 626, 680 (cited on page 6).

Daddi, E., Dickinson, M., Morrison, G., et al. 2007, The Astrophysical Journal, 670, 156 (cited on pages 3, 78 and 80).

Daddi, E., Bournaud, F., Walter, F., et al. 2010, The Astrophysical Journal, 713, 686 (cited on page 6).

Davari, R., Ho, L. C., Peng, C. Y., & Huang, S. 2014, The Astrophysical Journal, 787, 69 (cited on page 6).

Dekel, A., & Birnboim, Y. 2006, Monthly Notices of the Royal Astronomical Society, 368, 2 (cited on pages 10 and 43).

Dekel, A., & Mandelker, N. 2014, Monthly Notices of the Royal Astronomical Society, 444, 2071 (cited on page 9).

Dekel, A., & Silk, J. 1986, The Astrophysical Journal, 303, 39 (cited on page 75).

Dekel, A., Birnboim, Y., Engel, G., et al. 2009, Nature, 457, 451 (cited on page 75).

Di Matteo, T., Springel, V., & Hernquist, L. 2005, Nature, 1 (cited on pages 41, 43, 100 and 104).

Dressler, A. 1989, in IAU Symposium, Vol. 134, Active Galactic Nuclei, ed. D. E. Osterbrock & J. S. Miller, 217 (cited on page 42).

Dressler, A., & Richstone, D. O. 1988, The Astrophysical Journal, 324, 701 (cited on page 42).

Dubois, Y., & Commerçon, B. 2016, Astronomy & Astrophysics, 585, A138 (cited on page 106).

Dubois, Y., Devriendt, J., Slyz, A., & Teyssier, R. 2012, Monthly Notices of the Royal Astronomical Society, 420, 2662 (cited on pages 42, 99 and 100).

Dubois, Y., Gavazzi, R., Peirani, S., & Silk, J. 2013, Monthly Notices of the Royal Astronomical Society, 433, 3297 (cited on page 99).

Dubois, Y., Peirani, S., Pichon, C., et al. 2016, ArXiv e-prints, arXiv:1606.03086 (cited on page 101).

Dubois, Y., Pichon, C., Devriendt, J., et al. 2013, Monthly Notices of the Royal Astronomical Society, 428, 2885 (cited on page 43).

Dubois, Y., & Teyssier, R. 2008, Astronomy & Astrophysics, 477, 79 (cited on pages 38 and 76).

Eastman, J., Martini, P., Sivakoff, G., et al. 2007, The Astrophysical Journal Letters, 664, L9 (cited on page 15).

Eddington, A. S. 1926, The Internal Constitution of the Stars (cited on page 13).

Elbaz, D., Daddi, E., Le Borgne, D., et al. 2007, The Astrophysical Journal, 468, 33 (cited on page 3).

Elbaz, D., Dickinson, M., Hwang, H. S., et al. 2011, Astronomy & Astrophysics, 119, 1 (cited on pages 78 and 80).

Elmegreen, B. G. 2002, The Astrophysical Journal, 206 (cited on page 36).

Elmegreen, B. G., Elmegreen, D. M., Fernandez, M. X., & Lemonias, J. J. 2009, The Astrophysical Journal, 692, 12 (cited on page 9).

Elmegreen, D. M., Elmegreen, B. G., Ravindranath, S., & Coe, D. A. 2007, The Astrophysical Journal, 658, 763 (cited on page 9).

Elvis, M., Wilkes, B., McDowell, J., et al. 1994, The Astrophysical Journal Supplement Series, 95, 1 (cited on pages 39 and 46).

Everett, J., Königl, A., & Arav, N. 2002, The Astrophysical Journal, 569, 671 (cited on page 21).

Everett, J. E. 2005, The Astrophysical Journal, 631, 689 (cited on page 20).

Fabian, A. C. 2012, Annual Review of Astronomy and Astrophysics, 50, 455 (cited on page 45).

Fabjan, D., Borgani, S., Tornatore, L., et al. 2010, Monthly Notices of the Royal Astronomical Society, 401, 1670 (cited on page 41).

Fang, J. J., Faber, S. M., Salim, S., Graves, G. J., & Rich, R. M. 2012, The Astrophysical Journal, 761, 23 (cited on page 11).

Farrah, D., Urrutia, T., Lacy, M., et al. 2012, The Astrophysical Journal, 745, 178 (cited on page 45).

Ferguson, J. W., Korista, K. T., & Ferland, G. J. 1997, The Astrophysical Journal Supplement Series, 110, 287 (cited on page 46).

Ferland, G. J. 2014, in American Astronomical Society Meeting Abstracts, Vol. 223, American Astronomical Society Meeting Abstracts #223, 225.03 (cited on page 42).

Ferland, G. J., Korista, K. T., Verner, D. A., et al. 1998, Publications of the Astronomical Society of the Pacific, 110, 761 (cited on pages iv, vii and 39).

Ferland, G. J., Porter, R. L., van Hoof, P. A. M., et al. 2013, Revista Mexicana de Astronomía y Astrofísica, 49, 137 (cited on pages iv, vii, 39, 42 and 44).

Feruglio, C., Fiore, F., Carniani, S., et al. 2015, Astronomy & Astrophysics, 583, A99 (cited on page 76).

Fierlinger, K. M., Burkert, A., Ntormousi, E., et al. 2016, Monthly Notices of the Royal Astronomical Society, 456, 710 (cited on page 76).

Frank, J., & Rees, M. J. 1976, Monthly Notices of the Royal Astronomical Society, 176, 633 (cited on page 14).

Frank, J., & Shlosman, I. 1989, The Astrophysical Journal, 346, 118 (cited on page 6).

Fumagalli, M., Labbé, I., Patel, S. G., et al. 2014, The Astrophysical Journal, 796, 35 (cited on page 3).

Furlong, M., Bower, R. G., Theuns, T., et al. 2015, Monthly Notices of the Royal Astronomical Society, 450, 4486 (cited on page 100).

Gabor, J. M., & Bournaud, F. 2013, Monthly Notices of the Royal Astronomical Society, 16, 1 (cited on pages iv, 8, 37, 42, 43, 44, 45, 50, 78, 79, 101, 102, 103, 104, 105 and 117).

—. 2014, Monthly Notices of the Royal Astronomical Society, 13, 1 (cited on pages iii, iv, 20, 42, 43, 44, 45, 50, 76, 78, 79, 101, 102, 103 and 104).

Genel, S., Vogelsberger, M., Springel, V., et al. 2014, Monthly Notices of the Royal Astronomical Society, 445, 175 (cited on page 9).

Genzel, R., Newman, S., Jones, T., et al. 2011, The Astrophysical Journal, 733, 101 (cited on page 41).

Girichidis, P., Naab, T., Walch, S., et al. 2016, The Astrophysical Journal Letters, 816, L19 (cited on page 25).

Gonçalves, T. S., Martin, D. C., Menéndez-Delmestre, K., Wyder, T. K., & Koekemoer, A. 2012, The Astrophysical Journal, 759, 67 (cited on page 10).

Graham, A. W. 2016, Galactic Bulges, 418, 263 (cited on pages 15 and 42).

Greene, J. E., Peng, C. Y., & Ludwig, R. R. 2010, The Astrophysical Journal, 709, 937 (cited on page 11).

Grenier, I. A., Black, J. H., & Strong, A. W. 2015, Annual Review of Astronomy & Astrophysics, 53, 199 (cited on page 106).

Guillet, T., Teyssier, R., & Colombi, S. 2010, Monthly Notices of the Royal Astronomical Society, 405, 525 (cited on page 34).

Haas, M. R., Schaye, J., Booth, C. M., et al. 2013, Monthly Notices of the Royal Astronomical Society, 435, 2931 (cited on page 100).

Hahn, O., & Abel, T. 2011, Monthly Notices of the Royal Astronomical Society, 415, 2101 (cited on page 34).

Heckman, T. M., Armus, L., & Miley, G. K. 1990, The Astrophysical Journal Supplement Series, 74, 833 (cited on page 75).

Heckman, T. M., Lehnert, M. D., Strickland, D. K., & Armus, L. 2000, The Astrophysical Journal Supplement Series, 129, 493 (cited on page 75).

Hills, J. G. 1975, Nature, 254, 295 (cited on page 14).

Hönig, S. F., & Kishimoto, M. 2010, Astronomy & Astrophysics, 523, A27 (cited on page 17).

Hopkins, P. F., Kereš, D., Oñorbe, J., et al. 2014, Monthly Notices of the Royal Astronomical Society, 445, 581 (cited on pages 76 and 79).

Hopkins, P. F., Torrey, P., Faucher-Giguère, C.-A., Quataert, E., & Murray, N. 2016, Monthly Notices of the Royal Astronomical Society, 458, 816 (cited on pages 78 and 101).

Hu, C.-Y., Naab, T., Walch, S., Moster, B. P., & Oser, L. 2014, Monthly Notices of the Royal Astronomical Society, 443, 1173 (cited on page 33).

Hubble, E. P. 1925, The Astrophysical Journal, 62 (cited on page v).

—. 1929, Proceedings of the National Academy of Science, 15, 168 (cited on page 4).

—. 1936, Realm of the Nebulae (cited on pages 3 and 4).

James, R. 1977, Journal of Computational Physics, 25, 71 (cited on page 31).

Jeans, J. H. 1902, Philosophical Transactions of the Royal Society of London Series A, 199, 1 (cited on page 7).

Jubelgas, M., Springel, V., Enßlin, T., & Pfrommer, C. 2008, Astronomy & Astrophysics, 481, 33 (cited on page 106).

Juneau, S., Dickinson, M., Bournaud, F., et al. 2013, The Astrophysical Journal, 764, 176 (cited on page 43).

Kacprzak, G. G., Churchill, C. W., Murphy, M. T., & Cooke, J. 2015, Monthly Notices of the Royal Astronomical Society, 446, 2861 (cited on page 75).

Kaviraj, S., Laigle, C., Kimm, T., et al. 2016, ArXiv e-prints, arXiv:1605.09379 (cited on page 100).

Keller, B. W., Wadsley, J., & Couchman, H. M. P. 2016, ArXiv e-prints, arXiv:1604.08244 (cited on page 79).

Kennicutt, R. C. 1998, The Astrophysical Journal, 10 (cited on page 35).

Kereš, D., Katz, N., Weinberg, D. H., & Davé, R. 2005, Monthly Notices of the Royal Astronomical Society, 363, 2 (cited on pages 10 and 75).

Kim, J.-H., Abel, T., Agertz, O., et al. 2014, The Astrophysical Journal Supplement Series, 210, 14 (cited on page 28).

King, A., & Pounds, K. 2015, Annual Review of Astronomy & Astrophysics, 53, 115 (cited on page 19).

Kormendy, J., & Ho, L. C. 2013, Annual Reviews of Astronomy & Astrophysics, 51, 511 (cited on page 11).

Kormendy, J., & Richstone, D. 1995, Annual Review of Astronomy & Astrophysics, 33, 581 (cited on page 42).

Kravtsov, A. V. 2013, The Astrophysical Journal, 764, L31 (cited on page 75).

Krumholz, M. R., Mckee, C. F., & Klein, R. I. 2004, The Astrophysical Journal, 611, 399 (cited on page 36).

Krumholz, M. R., & Tan, J. C. 2007, The Astrophysical Journal, 654, 304 (cited on page 35).

Labbé, I., Rudnick, G., Franx, M., et al. 2003, The Astrophysical Journal Letters, 591, L95 (cited on page 5).

Labbé, I., Huang, J., Franx, M., et al. 2005, The Astrophysical Journal Letters, 624, L81 (cited on pages 10 and 41).

Lawrence, A. 1991, Monthly Notices of the Royal Astronomical Society, 252, 586 (cited on page 18).

Lees, J. F., Knapp, G. R., Rupen, M. P., & Phillips, T. G. 1991, The Astrophysical Journal, 379, 177 (cited on page 10).

LIGO Collaboration. 2016, Physical Review Letters, 116, 061102 (cited on page 15).

Liu, H.-L., Wu, Y., Li, J., et al. 2015, The Astrophysical Journal, 798, 30 (cited on pages 24, 76 and 77).

Liu, J., Liu, Y., Li, X., et al. 2016, Monthly Notices of the Royal Astronomical Society, 459, L100 (cited on page 47).

Loeb, A., & Rasio, F. A. 1994, The Astrophysical Journal, 432, 52 (cited on page 12).

Lotz, J. M., Jonsson, P., Cox, T. J., et al. 2011, The Astrophysical Journal, 742, 103 (cited on page 15).

Madau, P., & Dickinson, M. 2014, Annual Review of Astronomy & Astrophysics, 52, 415 (cited on pages iii, vi and 42).

Madau, P., Pozzetti, L., & Dickinson, M. 1998, The Astrophysical Journal, 498, 106 (cited on pages iii, vi and 42).

Magnelli, B., Saintonge, A., Lutz, D., et al. 2012, Astronomy & Astrophysics, 548, A22 (cited on page 6).

Magorrian, J., Tremaine, S., Richstone, D., et al. 1998, The Astronomical Journal, 115, 2285 (cited on pages 11, 15 and 42).

Marconi, A., & Hunt, L. K. 2003, The Astrophysical Journal Letters, 589, L21 (cited on page 42).

Martin, C. L., Shapley, A. E., Coil, A. L., et al. 2012, The Astrophysical Journal, 760, 127 (cited on page 75).

—. 2013, The Astrophysical Journal, 770, 41 (cited on page 75).

Martizzi, D., Teyssier, R., & Moore, B. 2012, Monthly Notices of the Royal Astronomical Society, 420, 2859 (cited on pages 38 and 99).

Mathews, W. G., & Capriotti, E. R. 1985, in Astrophysics of Active Galaxies and Quasi-Stellar Objects, ed. J. S. Miller, 185 (cited on page 47).

Matzner, C. D., & McKee, C. F. 2000, The Astrophysical Journal, 10, 364 (cited on page 36).

Melioli, C., & de Gouveia Dal Pino, E. M. 2015, The Astrophysical Journal, 812, 90 (cited on page 78).

Merritt, D. 2013, Dynamics and Evolution of Galactic Nuclei (cited on page 15).

Micic, M. 2007, PhD thesis, The Pennsylvania State University (cited on page 12).

Morisset, C. 2006, Proceedings of the International Astronomical Union, 2, 467 (cited on page 40).

—. 2013, Astrophysics Source Code Library (cited on page 40).

Mullaney, J. R., Pannella, M., Daddi, E., et al. 2012, Monthly Notices of the Royal Astronomical Society, 419, 95 (cited on page 43).

Müller-Sánchez, F., Prieto, M., Hicks, E., et al. 2011, The Astrophysical Journal, 739, 69 (cited on pages 15, 46 and 47).

Murray, N., Quataert, E., & Thompson, T. A. 2010, The Astrophysical Journal, 709, 191 (cited on page 6).

Narayanan, D., Krumholz, M. R., Ostriker, E. C., & Hernquist, L. 2012, Monthly Notices of the Royal Astronomical Society, 421, 3127 (cited on page 6).

Netzer, H. 2015, Annual Review of Astronomy and Astrophysics, 53, 365 (cited on page 18).

Netzer, H., Lani, C., Nordon, R., et al. 2016, The Astrophysical Journal, 819, 123 (cited on page 47).

Newman, S. F., Genzel, R., Förster-Schreiber, N. M., et al. 2012, The Astrophysical Journal, 761, 43 (cited on page 41).

Newton, R. D. A., & Kay, S. T. 2013, Monthly Notices of the Royal Astronomical Society, 434, 3606 (cited on pages 101 and 104).

Noeske, K. G., Weiner, B. J., Faber, S. M., et al. 2007, The Astrophysical Journal Letters, 660, L43 (cited on pages 3, 78 and 80).

Norman, C., & Scoville, N. 1988, The Astrophysical Journal, 332, 124 (cited on page 14).

Olive, K. A., Steigman, G., & Walker, T. P. 2000, Physics Report, 333, 389 (cited on pages v and 75).

Oppenheimer, B. D., Davé, R., Kereš, D., et al. 2010, Monthly Notices of the Royal Astronomical Society, 406, 2325 (cited on page 9).

O'Shea, B. W., Bryan, G., Bordner, J., et al. 2004, ArXiv Astrophysics e-prints, astro-ph/0403044 (cited on page 28).

Osterbrock, D. E., & Ferland, G. J. 2006, Mercury, 35, 40 (cited on pages 16, 17, 18 and 47).

Pakmor, R., Pfrommer, C., Simpson, C. M., & Springel, V. 2016, The Astrophysical Journal Letters, 824, L30 (cited on page 106).

Pedersen, K., Rasmussen, J., Sommer-Larsen, J., et al. 2006, New Astronomy, 11, 465 (cited on page 75).

Pentericci, L., McCarthy, P. J., Röttgering, H. J. A., et al. 2001, The Astrophysical Journal Supplement Series, 135, 63 (cited on page 5).

Peres, A. 1962, Physical Review, 128, 2471 (cited on page 15).

Perret, V., Renaud, F., Epinat, B., et al. 2014, Astronomy & Astrophysics, 562, A1:1 (cited on page 34).

Pettini, M., Rix, S. A., Steidel, C. C., et al. 2002, The Astrophysical Journal, 569, 742 (cited on page 75).

Pfrommer, C., Springel, V., Jubelgas, M., & Ensslin, T. A. 2007, in Astronomical Society of the Pacific Conference Series, Vol. 379, Cosmic Frontiers, ed. N. Metcalfe & T. Shanks, 221 (cited on page 106).

Planck Collaboration. 2015, ArXiv e-prints, arXiv:1502.01589 (cited on page 4).

Prieto, M., Reunanen, J., Tristram, K., et al. 2010, Monthly Notices of the Royal Astronomical Society, 402, 724 (cited on page 39).

Primack, J. 2010, Science, 328, 576 (cited on page 15).

Rasera, Y., & Teyssier, R. 2006, Astronomy & Astrophysics, 445, 1 (cited on page 124).

Rauch, K. P. 1999, The Astrophysical Journal, 514, 725 (cited on page 14).

Rees, M. J. 1978, The Observatory, 98, 210 (cited on page 13).

Reines, A. E., & Volonteri, M. 2015, The Astrophysical Journal, 813, 82 (cited on page 41).

Renaud, F., Kraljic, K., & Bournaud, F. 2012, The Astrophysical Journal, 760, L16 (cited on page 36).

Renaud, F., Bournaud, F., Emsellem, E., et al. 2013, Monthly Notices of the Royal Astronomical Society, 436, 1836 (cited on pages 38, 76, 78 and 79).

Reynolds, C. S. 2008, Nature, 455, 39 (cited on page 11).

Ribaudo, J., Lehner, N., Howk, J. C., et al. 2011, The Astrophysical Journal, 743, 207 (cited on page 10).

Ricci, T. V., Steiner, J. E., & Menezes, R. B. 2015, Monthly Notices of the Royal Astronomical Society, 451, 3728 (cited on page 105).

Richards, G. T., Strauss, M. A., Fan, X., et al. 2006, The Astronomical Journal, 131, 2766 (cited on pages iii, vi and 42).

Richardson, M. L. A., Scannapieco, E., Devriendt, J., et al. 2016, ArXiv e-prints, arXiv:1605.03589 (cited on page 101).

Ricotti, M., & Ostriker, J. P. 2004, Monthly Notices of the Royal Astronomical Society, 350, 539 (cited on page 12).

Roos, O., & Bournaud, F. 2015, Proceedings of the IAU General Assembly, S319, in press (cited on pages 79, 103 and 107).

Roos, O., Bournaud, F., Renaud, F., et al. 2016, submitted to The Astrophysical Journal (cited on pages 19, 78, 80, 82, 102, 103 and 107).

Roos, O., Juneau, S., Bournaud, F., & Gabor, J. M. 2015, The Astrophysical Journal, 800, 19 (cited on pages iv, vii, 18, 19, 39, 40, 42, 44, 47, 48, 50, 81, 101, 102, 104, 105 and 107).

Rosdahl, J., Blaizot, J., Aubert, D., Stranex, T., & Teyssier, R. 2013, Monthly Notices of the Royal Astronomical Society, 436, 2188 (cited on pages 49 and 82).

Ruszkowski, M., Yang, H.-Y. K., & Zweibel, E. 2016, ArXiv e-prints, arXiv:1602.04856 (cited on page 20).

Safronov, V. S. 1960, Annales d'Astrophysique, 23, 979 (cited on page 6).

Salpeter, E. E. 1955, The Astrophysical Journal, 121, 161 (cited on page 23).

Sargent, M. T., Daddi, E., Béthermin, M., et al. 2014, The Astrophysical Journal, 793, 19 (cited on page 6).

Schawinski, K., Urry, C. M., Simmons, B. D., et al. 2014, Monthly Notices of the Royal Astronomical Society, 440, 889 (cited on pages 3 and 10).

Schaye, J., Dalla Vecchia, C., Booth, C. M., et al. 2010, Monthly Notices of the Royal Astronomical Society, 402, 1536 (cited on page 100).

Schaye, J., Crain, R. A., Bower, R. G., et al. 2015, Monthly Notices of the Royal Astronomical Society, 446, 521 (cited on page 100).

Schreiber, C., Pannella, M., Elbaz, D., et al. 2015, Astronomy & Astrophysics, 575, A74 (cited on page 3).

Schroetter, I., Bouché, N., Péroux, C., et al. 2015, The Astrophysical Journal, 804, 83 (cited on pages 75, 79, 81 and 106).

Schwarzschild, K. 1916, Sitzungsberichte der Königlich Preußischen Akademie der Wissenschaften (Berlin), 1916, Seite 189-196 (cited on page 12).

Shapiro, M. M. 2005a, in Bulletin of the American Astronomical Society, Vol. 37, American Astronomical Society Meeting Abstracts, 1238 (cited on page 25).

Shapiro, S. L. 2004, The Astrophysical Journal, 610, 913 (cited on page 12).

—. 2005b, The Astrophysical Journal, 620, 59 (cited on pages 12 and 13).

Sharma, P., Roy, A., Nath, B. B., & Shchekinov, Y. 2014, Monthly Notices of the Royal Astronomical Society, 443, 3463 (cited on pages 25, 76 and 77).

Sijacki, D., Pfrommer, C., Springel, V., & Enßlin, T. A. 2008, Monthly Notices of the Royal Astronomical Society, 387, 1403 (cited on page 106).

Sijacki, D., Springel, V., Di Matteo, T., & Hernquist, L. 2007, Monthly Notices of the Royal Astronomical Society, 380, 877 (cited on page 99).

Sijacki, D., Springel, V., Di Matteo, T., & Hernquist, L. 2007, Monthly Notices of the Royal Astronomical Society, 380, 877 (cited on pages 100 and 101).

Sijacki, D., Vogelsberger, M., Genel, S., et al. 2015, Monthly Notices of the Royal Astronomical Society, 452, 575 (cited on page 101).

Silk, J. 2011, in IAU Symposium, Vol. 277, Tracing the Ancestry of Galaxies, ed. C. Carignan, F. Combes, & K. C. Freeman, 273 (cited on page 75).

Soltan, A. 1982, Monthly Notices of the Royal Astronomical Society, 200, 115 (cited on pages 12 and 13).

Somerville, R. S., & Davé, R. 2015, Annual Review of Astronomy & Astrophysics, 53, 51 (cited on page 100).

Sommer-Larsen, J. 2006, The Astrophysical Journal, 644, L1 (cited on pages iii, v, 9, 50 and 75).

Spitzer, Jr., L., & Saslaw, W. C. 1966, The Astrophysical Journal, 143, 400 (cited on page 14).

Springel, V. 2005, Monthly Notices of the Royal Astronomical Society, 364, 1105 (cited on page 32).

Springel, V. 2010, Monthly Notices of the Royal Astronomical Society, 401, 791 (cited on page 33).

Springel, V., Di Matteo, T., & Hernquist, L. 2005a, The Astrophysical Journal Letters, 620, L79 (cited on page 100).

—. 2005b, Monthly Notices of the Royal Astronomical Society, 361, 776 (cited on pages 45 and 100).

Steenbrugge, K. C., Kaastra, J. S., Crenshaw, D. M., et al. 2005, Astronomy & Astrophysics, 434, 569 (cited on page 21).

Steidel, C. C., Erb, D. K., Shapley, A. E., et al. 2010, The Astrophysical Journal, 717, 289 (cited on pages iii and 9).

Stinson, G. S., Brook, C., Macciò, A. V., et al. 2013, Monthly Notices of the Royal Astronomical Society, 428, 129 (cited on page 79).

Tacconi, L. J., Genzel, R., Neri, R., et al. 2010, Nature, 463, 781 (cited on page 6).

Tacconi, L. J., Neri, R., Genzel, R., et al. 2013, The Astrophysical Journal, 768, 74 (cited on page 6).

Taylor, P., & Kobayashi, C. 2015, Monthly Notices of the Royal Astronomical Society, 448, 1835 (cited on page 75).

Teyssier, R. 2002, Astronomy & Astrophysics, 385, 337 (cited on pages iv, vii, 28 and 44).

Teyssier, R., Moore, B., Martizzi, D., Dubois, Y., & Mayer, L. 2011, Monthly Notices of the Royal Astronomical Society, 414, 195 (cited on pages 36, 37 and 42).

Thom, C., Tumlinson, J., Werk, J. K., et al. 2012, The Astrophysical Journal Letters, 758, L41 (cited on page 10).

Tombesi, F., Meléndez, M., Veilleux, S., et al. 2015, Nature, 519, 436 (cited on page 76).

Toomre, A. 1964, The Astrophysical Journal, 139, 1217 (cited on page 6).

Treister, E., Natarajan, P., Sanders, D. B., et al. 2010, Science, 328, 600 (cited on page 15).

Truelove, J. K., Klein, R. I., Mckee, C. F., et al. 1997, The Astrophysical Journal, 489, 179 (cited on pages 30, 120 and 123).

Tumlinson, J. B. 2002, PhD thesis, University of Colorado at Boulder (cited on page 12).

Urry, C. M., & Padovani, P. 1995, Publications of the Astronomical Society of the Pacific, 107, 803 (cited on pages 14 and 17).

Valiante, R., Schneider, R., Volonteri, M., & Omukai, K. 2016, Monthly Notices of the Royal Astronomical Society, 457, 3356 (cited on page 13).

Van Dokkum, P. G., Whitaker, K. E., Brammer, G., et al. 2010, The Astrophysical Journal, 709, 1018 (cited on page 6).

Vasiliev, E., Antonini, F., & Merritt, D. 2015, The Astrophysical Journal, 810, 49 (cited on page 15).

Viti, S., Bayet, E., Hartquist, T. W., et al. 2013, in Astrophysics and Space Science Proceedings, Vol. 34, Cosmic Rays in Star-Forming Environments, ed. D. F. Torres & O. Reimer, 7 (cited on page 106).

Vogelsberger, M., Genel, S., Springel, V., et al. 2014, Monthly Notices of the Royal Astronomical Society, 444, 1518 (cited on page 101).

Volonteri, M. 2010, The Astronomy and Astrophysics Review, 18, 279 (cited on page 13).

Volonteri, M., & Bellovary, J. 2012, Reports on Progress in Physics, 75, 124901 (cited on page 13).

Volonteri, M., Dubois, Y., Pichon, C., & Devriendt, J. 2016, ArXiv e-prints, arXiv:1602.01941 (cited on page 101).

Volonteri, M., & Reines, A. E. 2016, The Astrophysical Journal Letters, 820, L6 (cited on page 41).

Wadsley, J. W., Stadel, J., & Quinn, T. 2003, New Astronomy, 9, 137 (cited on page 32).

White, S. D. M., & Frenk, C. S. 1991, The Astrophysical Journal, 379, 52 (cited on page 75).

Williams, C. C., Giavalisco, M., Cassata, P., et al. 2014, The Astrophysical Journal, 780, 1 (cited on page 6).

Williams, R. J. R., Baker, A. C., & Perry, J. J. 1999, Monthly Notices of the Royal Astronomical Society, 310, 913 (cited on page 14).

Woods, D. T., Klein, R. I., Castor, J. I., McKee, C. F., & Bell, J. B. 1996, The Astrophysical Journal, 461, 767 (cited on page 19).

Yee, H. K. C. 1992, in Astronomical Society of the Pacific Conference Series, Vol. 31, Relationships Between Active Galactic Nuclei and Starburst Galaxies, ed. A. V. Filippenko, 417 (cited on page 42).

Yoo, J., & Miralda-Escudé, J. 2004, The Astrophysical Journal Letters, 614, L25 (cited on pages 12 and 13).

Zuckerman, B., & Evans, II, N. J. 1974, The Astrophysical Journal Letters, 192, L149 (cited on page 35).